

## Functional MRI of the lower extremities

***Citation for published version (APA):***

Mazzoli, V. (2017). *Functional MRI of the lower extremities*. [Phd Thesis 1 (Research TU/e / Graduation TU/e), Biomedical Engineering]. Technische Universiteit Eindhoven.

***Document status and date:***

Published: 06/12/2017

***Document Version:***

Publisher's PDF, also known as Version of Record (includes final page, issue and volume numbers)

***Please check the document version of this publication:***

- A submitted manuscript is the version of the article upon submission and before peer-review. There can be important differences between the submitted version and the official published version of record. People interested in the research are advised to contact the author for the final version of the publication, or visit the DOI to the publisher's website.
- The final author version and the galley proof are versions of the publication after peer review.
- The final published version features the final layout of the paper including the volume, issue and page numbers.

[Link to publication](#)

***General rights***

Copyright and moral rights for the publications made accessible in the public portal are retained by the authors and/or other copyright owners and it is a condition of accessing publications that users recognise and abide by the legal requirements associated with these rights.

- Users may download and print one copy of any publication from the public portal for the purpose of private study or research.
- You may not further distribute the material or use it for any profit-making activity or commercial gain
- You may freely distribute the URL identifying the publication in the public portal.

If the publication is distributed under the terms of Article 25fa of the Dutch Copyright Act, indicated by the "Taverne" license above, please follow below link for the End User Agreement:

[www.tue.nl/taverne](http://www.tue.nl/taverne)

***Take down policy***

If you believe that this document breaches copyright please contact us at:

[openaccess@tue.nl](mailto:openaccess@tue.nl)

providing details and we will investigate your claim.

# **Functional MRI of the lower extremities**

**Valentina Mazzoli**

This research was part of the “BioMech Tools” project, funded by the European Research Council within the Seventh Framework Program awarded to Nico Verdonschot. The research was also supported by the European Union COST Action BM1304.

Printing of this thesis was supported by the Department of Radiology of the Academic Medical Center in Amsterdam.

Printed by: Ipskamp Printing, Enschede, The Netherlands  
Cover design: Diana Vaselli

A catalogue record is available from the Eindhoven University of Technology Library  
ISBN: 978-90-386-4390-8

# Functional MRI of the lower extremities

PROEFSCHRIFT

ter verkrijging van de graad van doctor aan de Technische Universiteit Eindhoven, op  
gezag van de rector magnificus prof.dr.ir. F.P.T. Baaijens,  
voor een commissie aangewezen door het College voor Promoties, in het openbaar te  
verdedigen op woensdag 6 december 2017 om 16:00 uur

door

Valentina Mazzoli  
geboren te Sassocorvaro, Italië



Dit proefschrift is goedgekeurd door de promotoren en de samenstelling van de promotiecommissie is als volgt:

voorzitter:	prof. dr. P.A.J. Hilbers
1 <sup>e</sup> promotor:	prof. dr. ir. G.J. Strijkers
2 <sup>e</sup> promotor:	prof. dr. K. Nicolay <sup>†</sup>
copromotor(en):	prof. dr. ir. A.J. Nederveen (AMC Amsterdam)
	prof. dr. N. Verdonschot (Radboud UMC Nijmegen)
leden:	prof. dr. K. Ito
	prof. dr. A. Heerschap (Radboud UMC Nijmegen)
	prof. dr. B.M. Damon (Vanderbilt University)
	dr. J.J. Prompers

*Het onderzoek of ontwerp dat in dit proefschrift wordt beschreven is uitgevoerd in overeenstemming met de TU/e Gedragscode Wetenschapsbeoefening.*

*Dedicated to prof. Klaas Nicolay*



# Table of contents

<b>Chapter 1:</b>	Introduction and thesis outline	<b>1</b>
<b>Chapter 2:</b>	Functional Magnetic Resonance Imaging of the lower extremities: imaging beyond anatomy	<b>11</b>
<b>Chapter 3:</b>	A novel diffusion-tensor MRI approach for skeletal muscle fascicle length measurements	<b>39</b>
<b>Chapter 4:</b>	Assessment of passive muscle elongation using Diffusionon Tensor MRI: Correlation between fiber length and Diffusion coefficients	<b>59</b>
<b>Chapter 5:</b>	Water and fat separation in real-time MRI of joint movement with Phase Sensitive bSSFP	<b>85</b>
<b>Chapter 6:</b>	Accelerated 4D self-gated MRI of tibiofemoral kinematics	<b>107</b>
<b>Chapter 7:</b>	Accelerated 4D Phase Contrast MRI in skeletal muscles contraction	<b>129</b>
<b>Chapter 8:</b>	On the origin of changes in $T_2$ and $T_{1\rho}$ in the meniscus under loading conditions	<b>153</b>
<b>Chapter 9:</b>	Summary and general discussion	<b>171</b>
<b>Appendix:</b>	List of publications	<b>193</b>
	Acknowledgements	<b>197</b>
	Curriculum Vitae	<b>201</b>



# Chapter

Introduction

1

Musculoskeletal diseases affect more than one out of every two persons aged 18 and over, and nearly three out of four aged 65 and over (23). A broad range of different musculoskeletal pathologies have been discovered and categorized, all sharing the symptoms of pain and limited physical function. Trauma, back pain, and osteoarthritis (OA) are the three most commonly reported musculoskeletal conditions. OA is currently the most common cause of disability in adults in the United States. Although the mortality associated to musculoskeletal diseases is in general quite low compared to cardiovascular diseases and cancer (10), they present a higher incidence and in general higher treatment costs. OA alone accounts for nearly half of the causes of hospitalization in the US for the population aged 65 and higher.

In addition to the considerable decrease in quality of life induced by musculoskeletal disease, hospitalization and treatment for musculoskeletal conditions also pose a great economic burden. It is known that the prevalence of these diseases, especially OA, increases dramatically with increasing age and it is strongly linked to overweight and obesity. Due to the general trend of aging population and the increased number of people that are overweight or obese, the expected impact of musculoskeletal disease will keep increasing. In fact, by 2030, the number of adults affected with clinically diagnosed OA is projected to reach 25% of the adult population in the western world.

Due to socioeconomic burdens posed by musculoskeletal diseases, interest is growing in basic science, prevention, as well as methodologies to improve treatments and rehabilitation. In particular, computer models that can be used to simulate normal and abnormal function, as well to predict the effect of intervention, are becoming increasingly popular (1).

The work in this thesis relates to the use of Magnetic Resonance Imaging (MRI) in diagnosis, characterization, and follow-up of musculoskeletal diseases. In the following sections, I will briefly discuss functional MRI in the lower extremities, and subsequently I will discuss its possible applications in biomechanical models, as well as in diagnosis. Finally, I present the aims and outline of my thesis.

## Functional MRI

Magnetic Resonance Imaging (MRI) is a non-invasive imaging modality that exploits magnetic properties of water protons contained within the human body. As compared to other imaging modalities, MRI is characterized by excellent soft tissue contrast. Furthermore, MRI does not involve the use of ionizing radiation and, for most of the applications, it does not rely on the injection of a contrast medium. This makes MRI a

highly suitable option for routine clinical evaluation of many diseases and a common imaging choice in biomedical research, both in clinical and preclinical settings.

MRI is one of the most used imaging modalities to detect abnormalities and pathologies in the lower extremities, together with ultrasonography imaging, CT and X-rays. MRI scans used in the musculoskeletal field allow for depiction of human anatomy with relatively high spatial resolution and for discrimination between different soft tissue structures in great details as a consequence of their different magnetic properties.

Most of the currently used MRI sequences for the evaluation of lower extremities are acquired in a static and unloaded configuration. Therefore, conventional imaging techniques primarily focus on accurate anatomical representation of the tissues of interest, rather than on their actual function.

As opposed to conventional anatomical imaging, functional imaging refers, within the context of this thesis, to a collection of imaging techniques that allow to obtain information on the biomechanical status of a certain tissue within the human body or to measure changes following a certain event. A review about state-of-the-art functional MRI in the lower extremities will be presented in **Chapter 2**.

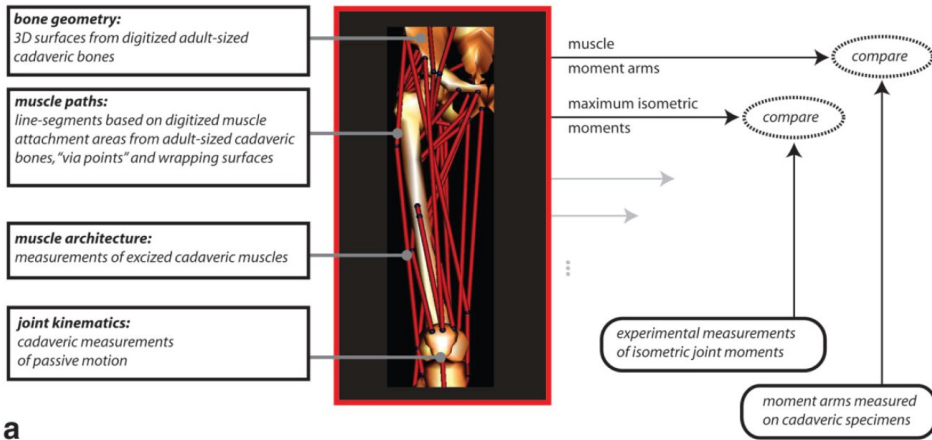
## **A biomechanics perspective**

The etiology of many musculoskeletal diseases is related to biomechanical factors. Currently used imaging diagnostic tools include ultrasound, CT, X-rays and MRI. While these methods can provide detailed information on tissue anatomy, they typically fail to provide adequate assessment of the musculoskeletal status of patients. Image-based techniques are often just “static pictures” and do not provide functional information.

Functional analysis of patients with musculoskeletal pathologies can be done using kinematic analysis. In a clinical environment these analysis are usually performed in a highly subjective manner (based on pure observation or on manual assessment, thus with a high level of variability). In a research environment the functional analysis are more sophisticated and performed using gait laboratory equipment (9, 12, 18). These gait analysis systems are able to quantify kinematic and kinetic parameters of the subject, but a downside is that these methods are scarcely accessible and rather expensive. Furthermore, gait analysis systems based on motion captures provide only limited information as they are based on surface anatomy, while fluoroscopic imaging does not provide information on soft tissues and it involves ionizing radiations.

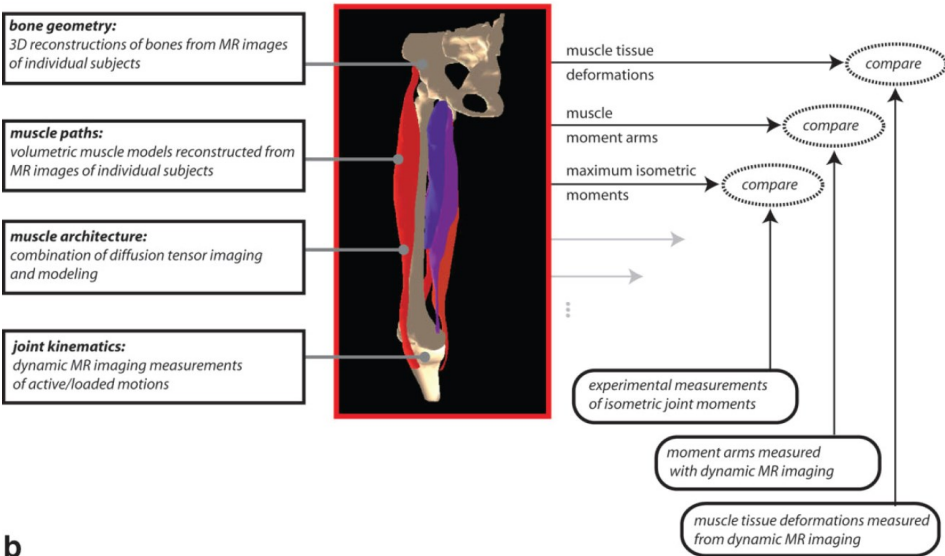


Traditional Musculoskeletal Modeling Pipeline



a

Future Image-based Musculoskeletal Modeling Pipeline



b

**Figure 1:** Traditional (a) and future (b) musculoskeletal modeling pipelines proposed by Blemker et al. (3). Functional MRI techniques, coupled with high-resolution anatomical MRI scan, can be introduced in the musculoskeletal modelling pipeline, both to provide input data to create the models, as well as to validate their outcome. The image is reproduced with permission.

Biomechanical models are used to obtain a high level of understanding of the functioning of the lower extremities (5, 7). Biomechanical computational models are of fundamental importance to simulate specific surgical approaches and to predict the

(long-term) effects of interventions. Models have been used to simulate surgical procedures such as total knee replacement (14, 15, 17), total hip replacement (19), and to gather insight into tissue degeneration (13, 16). Computer simulations can provide more insight into cause-effect relationships, and allow to isolate the role of individual tissues and/or tissue interactions in motion impairment and motion abnormalities.

Despite the great potential of computer modelling in orthopedic biomechanics, the typical output of current models has still limited applicability in individual patients (3). This is because the input data for models often are derived from cadaver measurements (22), which are therefore not specific to a particular patient and not reflecting important features such as geometrical aspects, soft-hard tissue interaction and adequate muscle activation patterns. Although big efforts have been made in order to make use of *in vivo* data in the musculoskeletal modeling pipeline, these models still present a number of heavy simplifications, since several parameters cannot be currently measured *in vivo* in a non-invasive way.

MRI is a very attractive tool to enhance the imaging-based musculoskeletal pipeline, due to its non-invasive nature and excellent soft tissue contrast with a large field-of-view, which can allow to simultaneously monitor different tissues during motion and/or loaded situations (3).

## A radiology perspective

Besides biomechanics, also the field of radiology could benefit from functional MRI. In fact it is believed that pathologies may be missed if the joint is not assessed in different and/or functional conditions (8).

Many musculoskeletal pathologies originate from abnormal loading and motion patterns, and can in turn induce abnormal motion and loading abnormalities (20). For instance, anterior cruciate ligament (ACL) reconstruction has been shown to induce abnormal joint mechanics (11, 21), which is believed to lead to OA (2, 4). Another example is the connection between abnormal patellar kinematics and patellofemoral pain (6). Techniques that facilitate quantification of joint kinematics, tissue deformation, and interactions between different (soft) tissue structures would enable measurement of normative values in the healthy population and diseased population and enable comparisons with pathological cases to accurately quantify the severity of the pathology relative to healthy conditions. Subsequently, the same technique can be

used to compare a post-surgical case to the normative data to assess whether intervention has normalized the pathology to the physiological level.

Furthermore, dynamic and stress MRI (MRI performed under load and/or in unusual patient positions) of the musculoskeletal system could provide information beyond conventional static imaging to understand the cause of pain. In fact, pain is often absent in static conditions and only presented during a specific movement or in loaded and weight bearing situations. The ability of performing this specific movement, or to apply a specific load inside the MRI scanner, could provide the radiologist with additional tools to understand the cause of pain and adapt treatment accordingly (8, 20).

Functional MRI suffers from many limitations, such as general low image resolution compared to the typical resolution that is usually achieved in conventional clinical MRI scans. As a consequence, small lesions or abnormalities are not easy to observe in typical functional MRI scans. Therefore, we do not expect functional protocols to replace conventional high-resolution static imaging. However, the addition of dynamic or loaded scan protocols to the existing static high-resolution clinical protocols may add important clinical information to aid in treatment decision.

## This thesis

Non-invasive *in vivo* functional techniques are of great importance in the field of orthopedics and biomechanics. *In vivo* measurements can be used to gather input data for biomechanical models, as well as to test the outcome of the models. Furthermore, functional imaging techniques can play an important role in radiology.

This thesis **aims** at developing new MRI-based techniques to obtain functional information of the human lower extremities. To this end, several novel strategies with regard to MRI measurements were developed. These included development of MRI sequences, loading devices and state-of-the-art image reconstruction techniques as well as image processing pipelines to extract the parameters of interest from the acquired data. Each tool implemented in this thesis was designed to measure a particular functional characteristic of the lower extremities. All the developed techniques were successfully tested in healthy volunteers.

## Thesis outline

The first part of my thesis provides a review of MRI-based methods that can be exploited to obtain functional information on the human lower extremities *in vivo* and in a non-invasive fashion. The current state-of-the-art technology for functional MRI of the lower extremities, including dynamic MRI, Diffusion Tensor MRI, and stress MRI, is provided in **Chapter 2**.

The other chapters of this thesis are divided in three sections, each one dealing with tools to visualize a particular functional aspect of the lower extremities: “skeletal muscle function and structure using Diffusion Tensor MRI”, “dynamic imaging of bone and soft tissues in the lower leg using MRI” and “stress MRI.”

The first section describes the use of Diffusion Tensor MRI (DT-MRI) as a tool to investigate the structural changes occurring in human skeletal muscles during passive contraction. In **Chapter 3**, a method was developed to (semi)automatically determine the length of muscle fibers in the lower leg from DT-MRI data. In **Chapter 4**, the changes in the amount of diffusion of water molecules within muscle tissue in the lower leg were measured at different foot flexion positions and the results were correlated with the changes in fiber length.

The second section of this thesis deals with MR imaging of the lower extremities during movement. In **Chapter 5**, we developed a method to obtain fat-suppressed single slice images of moving knees with high temporal resolution, using a Phase Sensitive Balanced SSFP (PS-bSSFP) approach. This allowed the visualization of soft tissue structures such as ligaments and cartilage that are usually difficult to visualize due to the hyperintense signal of the surrounding fat. In **Chapter 6**, a method was developed to obtain 4D (3D + time) images of the human knee during flexion extension, with high temporal and spatial resolution. For this purpose, a stack-of-stars k-space sampling in combination with Compressed Sensing reconstruction was implemented. Finally, **Chapter 7** deals with the development of an accelerated Phase Contrast MRI protocol to determine 4D velocity fields in skeletal muscles during active muscle contraction. Thanks to the use of state-of-the-art acceleration techniques, displacement fields and strain could be obtained in the full volume of the lower leg of healthy volunteers during dorsi/plantarflexion, in a clinically feasible scan time.

In the last section, we present experimental results in the field of stress MRI in the meniscus. In **Chapter 8**, the response of  $T_2$  and  $T_{1\rho}$  to compressive load in the *in vivo* human meniscus was investigated. For this purpose, two MRI compatible loading

devices were designed, built, and applied to a healthy subject cohort and to human cadaveric knees, respectively.

Finally, **Chapter 9** concludes this thesis with a summarizing discussion and future perspectives.

## References

1. **Arnold EM, Ward SR, Lieber RL, Delp SL.** A model of the lower limb for analysis of human movement. *Ann Biomed Eng* 38: 269–279, 2010.
2. **Barrance PJ, Williams GN, Snyder-Mackler L, Buchanan TS.** Altered knee kinematics in ACL-deficient non-copers: A comparison using dynamic MRI. *J Orthop Res* 24: 132–140, 2006.
3. **Blemker SS, Asakawa DS, Gold GE, Delp SL.** Image-based musculoskeletal modeling: Applications, advances, and future opportunities. *J Magn Reson Imaging* 25: 441–451, 2007.
4. **Butler RJ, Minick KI, Ferber R, Underwood F.** Gait mechanics after ACL reconstruction: implications for the early onset of knee osteoarthritis. *Br J Sports Med* 43: 366–370, 2009.
5. **Carbone V, Fluit R, Pellikaan P, van der Krogt MM, Janssen D, Damsgaard M, Vigneron L, Feilkas T, Koopman HFJM, Verdonschot N.** TLEM 2.0 - A comprehensive musculoskeletal geometry dataset for subject-specific modeling of lower extremity. *J Biomech* 48: 734–741, 2015.
6. **Carlson VR, Boden BP, Shen A, Jackson JN, Alter KE, Sheehan FT.** Patellar Maltracking Persists in Adolescent Females With Patellofemoral Pain. *Orthop J Sport Med* 5: 1–7, 2017.
7. **Delp SL, Anderson FC, Arnold AS, Loan P, Habib A, John CT, Guendelman E, Thelen DG.** OpenSim: Open source to create and analyze dynamic simulations of movement. *IEEE Trans Biomed Eng* 54: 1940–1950, 2007.
8. **Gold GE.** Dynamic and functional imaging of the musculoskeletal system. *Semin Musculoskelet Radiol* 7: 245–8, 2003.
9. **Guan S, Gray HA, Keynejad F, Pandy MG.** Mobile biplane X-Ray imaging system for measuring 3D dynamic joint motion during overground gait. *IEEE Trans Med Imaging* 35: 326–336, 2016.
10. **Hochberg MC.** Mortality in osteoarthritis. *Clin Exp Rheumatol* 26, 2008.
11. **Kaiser J, Vignos MF, Liu F, Kijowski R, Thelen DG.** American Society of Biomechanics Clinical Biomechanics Award 2015: MRI Assessments of Cartilage Mechanics, Morphology and Composition Following Reconstruction of the Anterior Cruciate Ligament. *Clin Biomech* 34: 38–44, 2016.
12. **Li G, Van de Velde SK, Bingham JT.** Validation of a non-invasive fluoroscopic imaging technique for the measurement of dynamic knee joint motion. *J Biomech* 41: 1616–1622, 2008.
13. **Malandrino A, Pozo JM, Castro-Mateos I, Frangi AF, van Rijsbergen MM, Ito K, Wilke H-J, Dao TT, Ho Ba Tho M-C, Noailly J.** On the Relative Relevance of Subject-Specific Geometries and Degeneration-Specific Mechanical Properties for the Study of Cell Death in Human Intervertebral Disk Models. *Front Bioeng Biotechnol* 3: 1–15, 2015.
14. **Marra MA, Strzelczak M, Heesterbeek PJC, van de Groes SAW, Janssen DW, Koopman BFJM, Wymenga AB, Verdonschot NJJ.** Anterior referencing of tibial slope in total knee arthroplasty considerably influences knee kinematics: a musculoskeletal simulation study. *Knee Surg. Sports Traumatol. Arthrosc.*

- (2017). doi: 10.1007/s00167-017-4561-3.
15. **Marra MA, Vanheule V, Rasmussen J, Verdonschot NJJ, Andersen MS, Fluit R, Koopman BHFJM, Rasmussen J, Verdonschot NJJ, Andersen MS.** A Subject-Specific Musculoskeletal Modeling Framework to Predict in Vivo Mechanics of Total Knee Arthroplasty. *J Biomech Eng* 137: 20904, 2014.
  16. **Natarajan RN, Williams JR, Andersson GBJ.** Recent Advances in Analytical Modeling of Lumbar Disc Degeneration. *Spine (Phila Pa 1976)* 29: 2733–2741, 2004.
  17. **Piazza SJ, Delp SL.** Three-Dimensional Dynamic Simulation of Total Knee Replacement Motion During a Step-Up Task. *J Biomech Eng* 123: 599, 2001.
  18. **Saveh AH, Katouzian HR, Chizari M.** Measurement of an intact knee kinematics using gait and fluoroscopic analysis. *Knee Surgery, Sport Traumatol Arthrosc* 19: 267–272, 2011.
  19. **Scifert CF, Brown TD, Pedersen DR, Heiner AD, Callaghan JJ.** Development and Physical Validation of a Finite Element Model of Total Hip Dislocation. *Comput Methods Biomech Biomed Engin* 2: 139–147, 1999.
  20. **Shapiro LM, Gold GE.** MRI of weight bearing and movement. *Osteoarthr Cartil* 20: 69–78, 2012.
  21. **Shefelbine SJ, Ma CB, Lee K-Y, Schrupf MA, Patel P, Safran MR, Slavinsky JP, Majumdar S.** MRI Analysis of In Vivo Meniscal and Tibiofemoral Kinematics in ACL-Deficient and Normal Knees. *J Orthop Res* 24: 1208–1217, 2006.
  22. **Ward SR, Eng CM, Smallwood LH, Lieber RL.** Are current measurements of lower extremity muscle architecture accurate? *Clin Orthop Relat Res* 467: 1074–1082, 2009.
  23. **Wolf AD, Pflieger B.** Burden of major musculoskeletal conditions. *Bull World Health Organ* 81: 646–656, 2003.

# Chapter



**Functional Magnetic Resonance  
Imaging of the lower extremities:  
imaging beyond anatomy**



## Abstract

Magnetic Resonance Imaging (MRI) has become a routine clinical imaging modality to gather information on pathological conditions in the lower extremities. Conventional MRI is usually performed while the subject lies motionless in the scanner, producing static anatomical images. While these static images are diagnostic for many conditions, they fail to depict problems that only reveal during the complex interaction of bone and soft tissue structures when joints and muscles move during normal functional activities. New advanced MRI tools for obtaining functional information of the lower extremities are rapidly developing. These methods will help to better reveal motion and deformation abnormalities, as well as provide input for patient-specific biomechanical models.

The purpose of this chapter is to review recent technical advances in the field of functional imaging of the human musculoskeletal system, with special emphasis on the lower extremities.

First, we will present the recent technical advances in the field of dynamic musculoskeletal imaging using several MRI-based techniques, including dynamic real time MRI, dynamic CINE MRI, phase contrast, MR tagging and displacement encoding (DENSE). Subsequently, we will discuss the functional information that can be obtained in human muscles by combining Diffusion tensor MRI (DT-MRI) and motion encoding techniques (i.e. MR tagging, phase contrast, DENSE). To conclude, we will describe the potential role of quantitative imaging for the assessment of the functional status of soft tissue structures such as cartilage and menisci.

We believe that functional imaging of the lower extremities will be a useful tool to improve our knowledge of the musculoskeletal system and could aid in radiological diagnosis. Further technical improvements are needed to translate functional MRI of the lower extremities into a routine clinical and research tool.

## Introduction

MRI provides excellent soft tissue contrast, thus enabling the assessment of soft tissue structures such as muscles, tendons, ligaments, and cartilage. These structures play a fundamental role in movement and load bearing, but currently imaging is mostly restricted to static and unloaded scans, which provide limited information on the biomechanical functioning of the lower extremities. This is an important shortcoming, since many musculoskeletal disorders, including osteoarthritis (OA) and patellofemoral pain (14, 15), are strongly linked to abnormal loading and abnormal motion patterns. Therefore, a single static scan in an unloaded situation may not be representative of the complex deformation and motion patterns occurring *in vivo* during daily activities. For instance, it has been shown that imaging during muscle contraction can modify patellar alignment (45) and that dynamic scans of the patella performed in an upright weight-bearing position can provide significantly different results in terms of bone kinematics as compared to conventional unloaded supine imaging (32).

Functional MRI of the musculoskeletal system refers to a broad collection of MRI techniques that allow measurements under physiological relevant loading conditions. However, clinical acceptance and broader routine application of functional imaging is still hampered by technical challenges and the lack of clinical validation studies in larger groups of patients. In this review, we highlight recent advances in the field, current limitations, and the open challenges that remain to be addressed in the future. We will mainly focus on topics of relevance to this thesis, in particular dynamic MRI, Diffusion Tensor MRI (DT-MRI) and stress MRI.

## Functional imaging of joints

### Dynamic MRI

Dynamic MRI of the lower extremities refers to a collection of fast imaging techniques that allow for acquisition of several images at different time points during a motion task. As opposed to conventional static imaging, which only provides a fixed snapshot while the patient is not moving, dynamic imaging allows to observe a joint during a realistic motion task and/or under a physiologically relevant loading condition. The principal acquisition strategies used in static and dynamic imaging of joints are summarized in **Figure 1**.

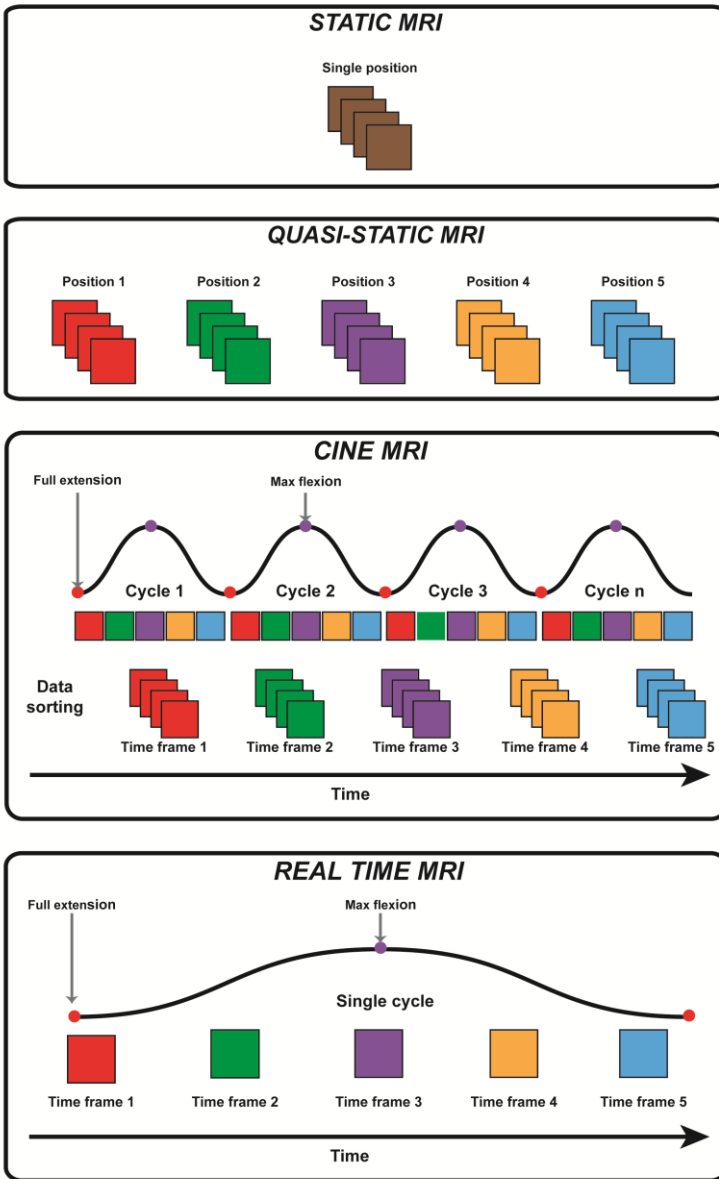


**Figure 1:** acquisition strategies in MRI of joints. In conventional **static MRI**, used in clinical practice, the subject is asked to keep the joint still while MR acquisition takes place. In **quasi-static MRI**, the subject is asked to lay still during image acquisition, but in between acquisitions, the joint is moved. The result is a series of fixed snapshots, where the joint is imaged at different static positions. In **CINE MRI**, different parts of k-space are acquired at different motion cycles. All the data corresponding to the same frame within the cycle are combined to create images of a single motion cycle. In **real-time MRI**, only a single motion cycle is needed to collect the k-space data. The results are several time frames over the motion cycle.

A number of studies (24, 76, 106) have obtained information about bone kinematics using a series of static postures. Images acquired at different joint positions are often played in a loop, suggesting the idea of joint motion. Therefore, quasi-static imaging is often considered a dynamic imaging technique, although it does not actually allow to image the joint during motion. While these quasi-static approaches present less technological challenges related to MRI acquisition and are therefore appealing for bigger studies, it has been shown that kinematic parameters are different during dynamic task as compared to a series of static positions, suggesting that static images are unable to capture the dynamic muscle and inertial effects that arise in active/voluntary motion and affect joint mechanics (25).

Dynamic MRI was originally developed for cardiac applications, but some peculiar differences between cardiovascular and musculoskeletal tissues prevented a straightforward translation of dynamic cardiac MRI protocols to study joint motion. In fact, the musculoskeletal system is characterized by very short transverse relaxation times of fibrous tissue, and this poses a number of challenges in MRI data acquisition. Furthermore, the anatomy of the musculoskeletal system is complex and contains several small structures, which require high-resolution 3D imaging techniques.

Another challenge in the field of dynamic imaging of the musculoskeletal system is synchronizing the data acquisition with the motion of the joint of interest. In fact, unlike electrocardiography (ECG) signal in a cardiac scans, the definition of a reliable signal to be used for triggering in musculoskeletal applications is not a trivial task. Moreover, while cardiac motion is involuntary, the acquisition of dynamic musculoskeletal MRI data requires the subject to actively and voluntarily perform a certain motion task inside the scanner, and often the task needs to be repeated several times. The difficulty for some subjects to perform a cyclic motion task consistently several times is one of the main challenges related to data acquisition.

Dynamic imaging can be performed following two main approaches: real time or in a segmented (triggered) fashion, often referred to as CINE (kinematic) MRI. Real-time imaging only requires a single repetition of the motion task and offers the ideal framework to study sudden or non-repetitive events (i.e. dislocation, (sub)luxation) and to evaluate subjects with poor coordination skills or suffering from conditions preventing them from repeating certain movements consistently. In general, real-time MRI offers great advantages in functional musculoskeletal MRI, as it makes subject fatigue less of a concern, and can also allow to test higher loads, which can be of interest to elucidate some abnormalities. Real-time imaging does not require any additional sensors or other hardware for triggering and it can be performed with a

temporal resolution as high as 20 ms (102). However, the acquisition speed of real-time MRI comes at the expenses of limited coverage and limited spatial resolution. In fact, the acquisition is usually performed in 2D in a single slice only (31) or in 3D with very coarse resolution (77). Real-time single slice imaging has been used, inter alia, to measure patellofemoral kinematics in subjects with patellofemoral pain (32, 33) and to measure femoral rotation (96). Although measurements were reported to have excellent intraobserver repeatability and relatively good tracking accuracy for the patella (2 mm accuracy for 6.25 s cycle duration) (34), much larger errors were reported for higher motion speeds, indicating that even higher temporal resolution may be required if one wants to investigate motion patterns occurring at the typical cycle durations involved in walking (~1.2 cycle/s). Another inherent limitation of real time approaches is the lack of accurate 3D information. In fact, since real time approaches are often limited to a single imaging slice, they can only provide 2D kinematic information (12, 32–34). 3D bone kinematics can be derived indirectly from a single slice real-time MRI data set through image registration to a 3D high-resolution volume, but this process is prone to error (43). Recent studies showed the feasibility of 3D real time MRI to assess 3D shoulder kinematics, although at low temporal and spatial resolution, especially in the slice direction (77, 100). However, while single slice and low-resolution 3D imaging techniques can allow for calculation of 3D kinematics when used in conjunction with appropriate image registration techniques, they offer limited value for radiological diagnosis, since the motion of most structures cannot be correctly depicted in a single plane. Moreover, movement and deformation of small structures such as ligaments, tendons, and cartilage cannot be appreciated if the voxel size exceeds a few mm due to partial volume effects with surrounding tissues.

As opposed to real-time imaging, where a single image can be acquired at once, in CINE MRI the image acquisition is gated or synchronized with the motion cycle. Using this approach only part of the k-space (the “raw” MRI data, which are subsequently Fourier-transformed to obtain the MR image) is acquired within each motion cycle, and k-space data acquired during multiple motion cycles are combined to create a single motion cycle dataset. CINE MRI offers higher bone tracking accuracy (0.5 mm error (50) as compared to 1.5 mm error for CINE MRI at 2 s cycle duration (34)).

CINE MRI approaches can be combined with Phase contrast (PC-CINE) to measure bone kinematic in the joints (14, 79, 82, 105). The PC technique relies on the application of motion sensitizing gradients, which result in the accumulation of the phase of moving spins proportional to their velocities and to the magnitude of velocity encoding magnetic field gradients (VENC). Gradients can be applied in three orthogonal directions, allowing for evaluation of tissue velocities in a time-resolved 3D

fashion. The velocity information obtained from PC data acquisition can then be integrated over time to obtain displacement information. PC acquisition aimed at determination of bone kinematics usually relies on the acquisitions of a high-resolution static scans and three single-slice dynamic scans, each with velocity encoding in three orthogonal directions. The typical processing pipeline used to obtain 3D kinematics from PC-CINE data is shown in **Figure 2**. The accuracy of PC-CINE in tracking bone kinematics has been reported to be 0.33 mm for translational degrees of freedom and  $0.97^\circ$  for rotational degrees of freedom (6).

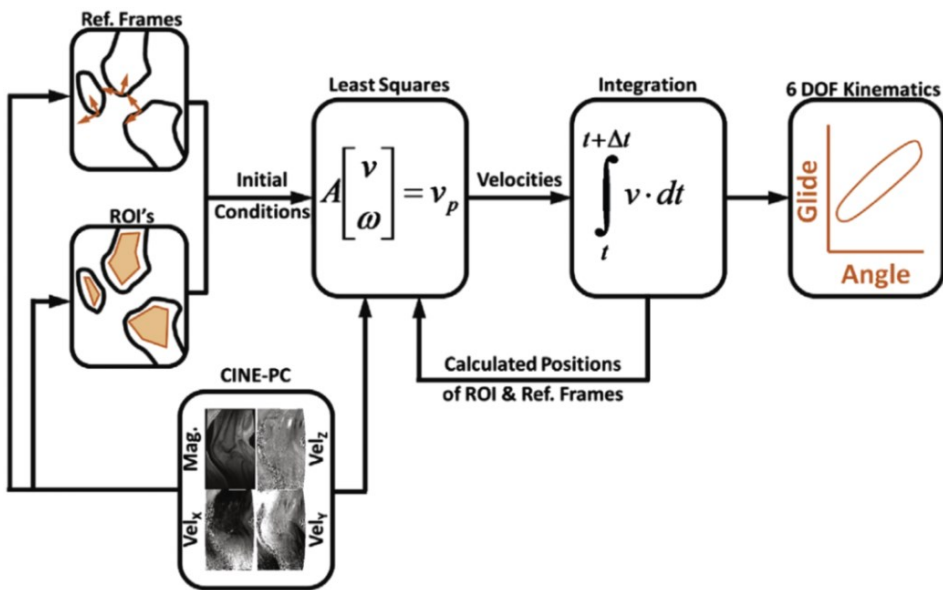


**Figure 2:** Schematic flowchart of the approach used to derive tibiofemoral kinematics from Phase Contrast (PC) MRI data. Regions of interest (ROIs) are initially defined in each bony segment. Subsequently, the segment translational ( $v$ ), and angular ( $\omega$ ) velocities that best agreed with measured pixel velocities ( $v_p$ ) are determined. Subsequently, the velocity data are numerically integrated to determine the subsequent position and angular orientation of the segments, and the location of the ROIs. This process was repeated across all frames, thereby producing the 6 degree-of-freedom (6 DOF) segment kinematic trajectories over the flexion/extension cycle. Taken from (105) with permission.

PC-CINE MRI has also been applied to measure patellofemoral contact mechanics (10, 11) and to measure patellar tendon strain by tracking the tendon insertion points on the bone (86) as well as patellar tendon moment arm (85). While bone kinematics can be accurately determined using this approach, it is intrinsically unsuitable for 3D visualization of soft tissue motion. Furthermore, since PC-CINE techniques encode velocity, they require integration to obtain displacement, which is a procedure prone to computational error.

Gated (CINE) approaches generally provide a higher spatial and temporal resolution (meant as number of frames that can be reconstructed during the motion cycle) as compared to real-time imaging. However, a drawback of all CINE MRI approaches, including PC-CINE, is that they heavily rely on the motion task being well repeatable and performed exactly in the same way during each repetition. Problems with reproducing the motion task consistently during data acquisition may result in image blurring, streaking, and ghosting, which obviously can hinder subsequent data analysis. Due to the strong dependence on the subject's ability to perform the given motion task in a repetitive way, CINE MRI studies are typically limited to "low-load" conditions and to healthy subjects having no pain or difficulties in performing the motion task.

One of the other major challenges in dynamic MRI of the lower extremities is related to difficulties in obtaining physiologically relevant ranges of motion within the bore of a typical MRI scanner (60 cm) due to geometrical constraints. Although the major vendors offer nowadays wide-bore scanners (70 cm), full range of motion is difficult to achieve for some joints, including the knee and the shoulder. When the knee joint is of interest, placing the subjects in a lateral position maximizes the range of motion, but may produce different results as compared to the more standard flexion/extension performed in a supine position. Some authors have investigated big ranges of motion of knee motion by limiting the analysis to small subjects. Fiorentino et al. (41) used real-time MRI to image a single sagittal slice of the knee joint while the subjects performed a loaded flexion extension task of the knee joint in lateral position and could achieve a flexion angle up to 120 degrees. This was made possible by the relatively low height of the subjects imaged (mean height=161 cm). Open-bore scanners, composed of two big flat magnets and open on three sides, are available in most hospitals and could be a viable option to increase the range of motion in dynamic MRI studies. However, the maximum field strength reached by these systems is typically 1T or lower, which leads to limited image resolution and higher errors in bone tracking for the determination of bone kinematics. In fact, it has been shown that measurement errors in bone kinematic are lower at higher field strengths (34).

Besides range of motion, also loading conditions during data acquisition play a fundamental role. A great challenge in dynamic MRI of the lower extremities is the difficulty in reproducing physiological postures and simulating a standing (loaded) position while the subject lays supine or in the lateral position. In order to overcome this limitation, dedicated MRI-compatible loading devices have been proposed (25, 90) to simulate typical upright activities while the subjects are supine inside the scanner bore. A more comprehensive description of loading devices will be provided in a separate section. However, while well-designed loading devices do increase the

physiological value of data obtained from dynamic MRI, they are still remote from mimicking the physiological conditions occurring in the lower extremities during daily activities. Additionally, when used in combination to the existing MR data acquisition approaches, these devices could potentially even worsen the repeatability of the motion task due to muscle fatigue, and this is a major concern with (prospectively gated) CINE MRI.

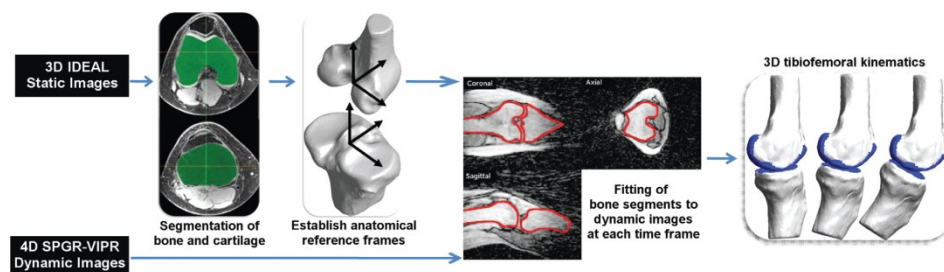


**Figure 3:** Schematic flowchart of the approach used to derive tibiofemoral kinematics from 3D dynamic MRI data. Static images are segmented to create volumetric bone and cartilage models. Subsequently, the volumetric models are registered to the dynamic 3D MRI dataset obtained from the same subjects. The final result is a 3D reconstruction of tibiofemoral kinematics. Reproduced from (49) with permission.

Recent advances in image acceleration techniques could potentially lead to faster data acquisition, that can decrease the number of motion repetitions needed in gated imaging, or ideally allow for real-time 3D imaging. One of the techniques used to accelerate data acquisition is parallel imaging. This technique can significantly reduce scan time, provided that a radiofrequency (RF) coil with sufficient receiver elements is available. Ideally a coil should have a large coverage and good signal reception, without restricting the range of motion (25, 73). Prospective trigger approaches in combination with acceleration techniques such as Compressed Sensing (CS) MRI (59) showed very promising results in cardiac and abdominal real time imaging, and could be translated in the musculoskeletal field to provide images with higher spatial and temporal resolution obtained with less repetitions of the motion task. Kaiser et al. (49, 50) developed a CS image acquisition and reconstruction pipeline, in combination with an external sensor for retrospective sorting of the data into different motion phases, to obtain high temporal (60 frames per cycle) and spatial (1.5 mm isotropic) resolution 3D images of the moving knee. The combination of 3D dynamic imaging with high-resolution static images can be used to measured 3D bone kinematics (**Figure 3**) and determine cartilage contact patterns in the tibiofemoral joint. However, a drawback of this approach is the need for an external optical sensor placed inside the MRI bore, which is not available in many hospitals.



## Functional imaging of Muscles

### 2

### Muscle structure (DT-MRI)

Diffusion Tensor MRI (DT-MRI or DTI) is an MRI-based technique that allows to measure the diffusion anisotropy of water molecules in biological tissues. In muscle DT-MRI acquisitions, the random motion of water molecules due to self-diffusion can be probed in several directions using diffusion encoding gradients, and these data can be used to reconstruct a diffusion tensor. The three eigenvectors obtained from the diffusion tensor indicate the principal directions of diffusion. The diffusion in biological tissues has a strongly anisotropic behavior: the direction of the first eigenvector corresponds to the direction of the muscle fibers, and can be used for fiber tractography as shown in **Figure 4**, while the second and third eigenvectors represent diffusion in the cross section of the fiber.



**Figure 4:** Fiber tractography reconstruction of the lower leg of a healthy volunteer, obtained from DT-MRI data. In the image the 3D reconstructions of the Tibialis Anterior (yellow), Gastrocnemius Lateralis (dark brown), and Gastrocnemius Medialis (light brown) muscles are shown.

DT-MRI can non-invasively provide *in vivo* information on tissue architecture, either normal or in a diseased state. For the interested readers, the technical aspects of DT-MRI acquisition and post processing, and its clinical applications are summarized in recent review articles (28, 74).

DT-MRI has been shown to be sensitive to transient changes in skeletal muscles such as contraction status and joint position (38, 81, 93). Furthermore, correlation has been shown between DT-MRI-derived parameters and maximum muscle power (80). DT-

MRI also allows to measure the pennation angle (27), the angle between the muscle fiber and the tendon it attaches to, which plays a fundamental role in determining muscle function and force production. Despite the relatively good performance of DT-MRI in quantifying biomechanically relevant parameters such as pennation angle and fiber length (28), the extraction of these parameters is still time consuming and poorly standardized. Furthermore, the physiological interpretation of some of the DT-MRI-derived parameters is unclear. Advances in image processing techniques, as well as basic research on the physiological origin of the DT-MRI data, are needed in order to obtain accurate geometrical information that can be readily used as input for biomechanical models of the lower extremities.

Despite the limitations, due to its ability to depict and characterize complex muscle architecture of deep and superficial muscles with a large field of view (FOV), DT-MRI is a very promising technique towards the implementation of patients specific muscle architecture into biomechanical models (7).

## **Muscle function (Phase contrast, MR tagging, DENSE)**

Besides accurate 3D representation of muscle architecture, MRI is also a promising tool to provide biomechanical information on muscle function. Dedicated MRI techniques have been developed to observe and quantify muscle deformation during contraction (78). Dynamic muscle imaging, similarly to dynamic imaging of the joints, could either be performed in a real time (3) or in a triggered fashion (23). Real-time imaging can be performed either in a 2D single slice approach, or in 3D fashion at lower resolution, but it is limited to displacement encoded in one single direction (3, 66). When the motion task can be consistently repeated, displacements (or velocities) can be encoded in three orthogonal directions, leading to the possibility to determine volumetric deformation patterns.

The MRI techniques used for dynamic muscle contraction imaging can be categorized in three main groups: MR tagging (SPAMM), Phase Contrast (PC), and displacement encoding with stimulated echoes (DENSE). In MR tagging, two preparatory RF pulses are usually applied, separated by a dephasing gradient (the so-called 1-1 module). As a result of the application of the MR tagging module, the acquired magnitude images result spatially modulated with a sinusoidal function. Following the distortion of these tag lines over time allows to measure soft tissue deformation. This technique has been used to monitor tissue displacement and deformation during active isometric contraction in humans (91, 94), as well as during muscle indentation both in rats (19) and in healthy humans (65, 66).

The PC technique, already introduced in the context of bone kinematics determination, allows to obtain 3D velocity information in each individual image voxel over time. This method has been used in the musculoskeletal field to quantify muscle inertial forces (104), as well as changes in muscle fascicle length (88) and strain rate (94). DENSE is conceptually similar to PC, as it encodes displacement on the phase of the signal, but it is based on the acquisition of stimulated echoes. One of the advantages of DENSE over PC is that it allows to encode motion over longer time intervals, which is especially beneficial for skeletal muscles, which are characterized by low velocities. DENSE has been successfully applied to the study of muscle contraction (107) and cartilage deformation under cyclic loading (21, 22, 69). One drawback of DENSE acquisition is the 50% reduction in SNR due to the use of stimulated echoes instead of primary echoes.

All the displacement and velocity techniques previously mentioned allow for quantification of tissue displacement and strain through post processing. However, techniques that directly encode displacement such as DENSE and MR tagging are more suitable if one wants to calculate strain. On the other hand, strain rate is often calculated from phase contrast data, since this does not involve integration in the time domain and does not require the definition of a reference frame, which is required for calculating strain.

MR tagging, PC and DENSE can be performed in a real-time fashion. However, since real time imaging only allows to study motion along one predefined direction, multiple repetitions of the motion are needed if a representation of displacement and strain is required in more than one direction. To that aim, several approaches have been implemented in order to perfectly synchronize the imaging sequence with the motion task. Sinha et al. (92) proposed a computer controlled foot pedal device, which is equipped with a force sensor that can be used to provide real time feedback to the subject performing the motion task. This allows for more consistent reproducibility of foot dorsi/plantarflexion (52, 94).

Another interesting approach for consistent muscle contraction is to induce passive contraction by using electrical stimulation (1). Deligianni et al. (30) developed a system with Electrical Muscle Stimulation (EMS) electrodes that can induce periodic muscle contraction synchronized with MRI acquisition, allowing for virtually artifact free scans. The idea of using electrical stimulation synchronized with MRI acquisition is appealing, but its value in assessing abnormalities in patients still has to be proven and the comparison with active muscle contraction should be investigated in more details.

Despite the technical advances in this field, muscle contraction imaging is still limited to a single slice, with velocity or displacement typically encoded along two orthogonal directions. In fact, 3D coverage of the full muscle volume with sufficient spatial and temporal resolution, in combination with 3D displacement or velocity encoding, can only be achieved by gated (CINE) acquisitions during many repetitions of a motion task, thus resulting in long scan times, which in turn can lead to muscle fatigue and poor repeatability in performing the task. For future widespread application of muscle contraction imaging, fast imaging techniques should ideally be employed, in order to reduce scan time and extend the imaging volume from a single slice to a full 3D volume.

Dynamic MRI techniques offer great opportunities in the field of musculoskeletal models of skeletal muscles. PC MRI in skeletal muscles showed non-uniform strain in the biceps brachii during elbow flexion (75). A later study (8) combined these results with Finite Element modeling and confirmed that a different fascicle length and curvature within the muscle are the main cause for non-uniform strain. Non-uniform strain was also reported in the tibialis anterior (35) and in the gastrocnemius muscle (61). In order to simplify calculations and decrease computational time, musculoskeletal geometry is often heavily simplified in musculoskeletal models. In fact, muscles are typically not described in a 3D fashion, but reduced to one or more line segments. (47). However, the complex muscle deformation highlighted in previous dynamic MRI studies, and the highly non uniform strain measured within individual muscles, motivate the development of more detailed and 3D muscle models.

When structural imaging is coupled with contraction imaging, the full complexity of muscle contraction mechanism can be studied in great details. Felton et al. (37) combined architectural information of muscles in the tongue with strain rate and strain derived from 2D PC MRI during swallowing.

Englund et al. (35) analyzed the spatial orientation of the main muscle fiber direction in a voxel-by-voxel basis. They compared it with the shortening direction derived using MR tagging and showed a significant angular discrepancy between the two ( $24.0 \pm 1.3^\circ$  and  $39.8 \pm 6.1^\circ$  in the deep and superficial compartments, respectively). Sinha et al. (94) found significant differences in strain rate derived from 2D PC between young and elderly subjects in the medial gastrocnemius, as well as smaller angles between the strain rate and the fiber direction in the older cohort. Since acquisition was limited to a single slice, the out-of-plane component of the strain rate could not be measured, and was estimated under the assumption of volume incompressibility (44, 99). The ability

of performing contraction imaging in a 3D fashion could shed more light on whether this assumption is justified.

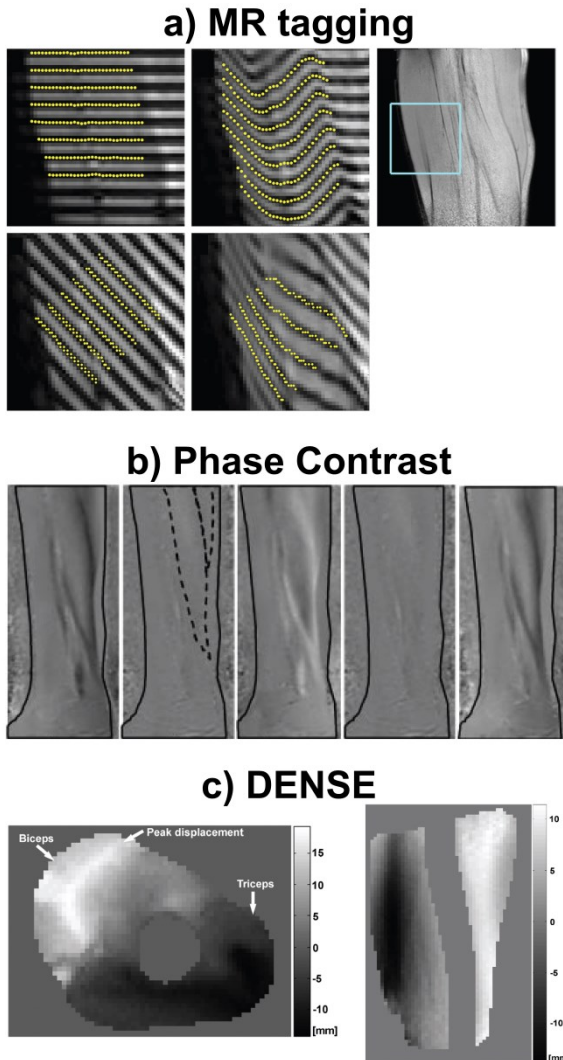


**Figure 5:** Overview of motion encoding techniques used in skeletal muscles. **a)** MR tagging images of part of the Tibialis Anterior muscle (indicated by the blue box), with displacement encoding in the z (first row) and yz (second row) direction, acquired in the contracted state (first column) and following relaxation (second column). Yellow points indicate the detected tag positions. Adapted from (35) with permission. **b)** PC-CINE images of the lower leg acquired during isometric plantarflexion contraction. The images show the time evolution of velocity values encoded in the foot-head direction over time. Black regions indicate tissue velocity in the foot direction, while white indicates tissue velocity in the head direction. Adapted from (39) with permission. **c)** DENSE-CINE MR imaging of the arm in the sagittal view (left) and axial (right) at maximal elbow flexion. The displacement was encoded in the vertical direction. The opposite signs of the biceps and the triceps muscles indicate the muscles working in opposite directions. Adapted from (107) with permission.

The non-collinearity of the strain directions and fiber directions and the non-uniform strain observed within a muscle are believed to be caused by architectural heterogeneity in terms of fiber lengths and pennation angles (35). Since DT-MRI acquisition, in combination with appropriate post-processing, allows for determination of fiber lengths (9, 46), fiber curvatures (29, 42) and pennation angles (46), this method could provide complementary information to dynamic muscle imaging.

The combination of the architectural parameters, obtained from DT-MRI, with local 3D strain measurement could lead in the future to a better understanding of mechanisms of muscle force production and lateral force transmission in healthy subjects, as well as in disease conditions such as dystrophy and aging. Additionally, the combination of the two imaging techniques could provide the basis for patient specific musculoskeletal models.

## Functional imaging of collagen-rich structures

### Cartilage

Osteoarthritis is a complex disease, originating from biological tissue modifications which are closely linked to cartilage loading (36). Quantification of cartilage thinning under load can be determined from anatomical high resolution scans acquired in the deformed and undeformed configuration (54) although the typical resolution achievable with the current MRI scanners limits the maximal achievable precision. Furthermore, the internal deformation of cartilage cannot be extrapolated from a simple thickness measurement performed on anatomical images. Combination with biomechanical calculations using, for example, Finite Element Modeling (FEM) can be used to infer internal tissue deformation given a deformed and an undeformed tissue state, but they are based on a series of assumptions and do not measure the actual deformation behavior of tissues. Therefore, current research is focusing on novel methods to directly estimate local mechanical behavior of cartilage *in vivo* and during physiologically relevant loading conditions.

Chan et al. (20) have developed a method based on DENSE MRI to quantify deformation and strain in human cartilage *in vivo* during cyclic loading with a precision of 0.3% (21). This was achieved by applying a single slice displacement encoding MRI technique based on DENSE, which was synchronized with the application of a cyclic externally applied load.

In addition to displacement encoding techniques to measure internal deformation and strain, MR relaxometry has also been proposed as a surrogate measurement of mechanical properties (70) and tissue response to load (68). MR relaxometry refers a number of quantitative MRI techniques such as  $T_1$ ,  $T_{1\rho}$ , and  $T_2$  that have been shown to provide information on cartilage beyond morphology and allow for prestructural cartilage assessment (57).  $T_2$  relaxation time is related to water content and collagen integrity, while  $T_{1\rho}$  is sensitive to proteoglycans content (2).

$T_2$  has been shown to correlate with Body Mass Index (BMI) in patellar cartilage (53) as well as in tibiofemoral cartilage (83) and was shown to return to normal values upon substantial weight loss (83). Furthermore significant decrease in cartilage  $T_2$  was reported after running (58) and following repeated knee bent exercise (56). These findings suggest the sensitivity of the parameters to different applied loads.

Although a unifying framework is still lacking, evidence has been provided that MR relaxometry is sensitive to (changes in) mechanical properties. Subburaj et al. found correlation between cartilage deformation patterns and relaxation times ( $T_2$  and  $T_{1\rho}$ ) in articular cartilage (98). Furthermore  $T_2$  was shown to correlate with Young's modulus and dynamic modulus in human patellar cartilage explants (72). In a more recent study, strong correlation was measured in patellar cartilage explants between the  $T_{1\rho}/T_2$  ratio and elastic modulus (51). Irrechukwu et al. (48) performed multiexponential analysis of  $T_2$  in cartilage explants following enzymatic degradation, and revealed the presence of four separate water compartments, with compartment fractions strongly correlating to material stiffness measured with mechanical testing. While additional experiments will be needed to understand the link between MR signal and mechanical properties of collagen-rich tissues, these preliminary results warrant further investigation.

Another technique that can potentially provide functional information on cartilage biomechanics is dGEMRIC ( $T_1$  mapping after injection of a gadolinium-based contrast agent). dGEMRIC has shown high correlation with proteoglycans content (101). Mayerhoefer et al. (64) have measured a significant decrease in cartilage dGEMRIC  $T_1$  values from the unloaded condition to loading with 50% body weight (63). This was interpreted as an increased concentration of gadolinium as a consequence of reduced cartilage thickness under compression. Interestingly, the load bearing areas of cartilage showed higher decrease in  $T_1$  as compared to non-weight bearing areas.

For an extensive description on functional imaging of cartilage, we refer the interested reader to the review paper by Neu (68).

## Meniscus

The meniscus is a fibrocartilaginous tissue pad with a semilunar shape. In humans, each knee contains two menisci, which are important for load transmission, shock absorption, stability, nutrition, joint lubrication, and proprioception in the knee joint.

Compared to articular cartilage, the meniscus is more difficult to image, due to its very short  $T_2$  and  $T_2^*$  relaxation times, which are reported to be 5-8 ms at 3T (5). Bae et al. (4) observed a correlation between mechanical properties (stiffness derived from indentation) of temporomandibular joint (TMJ) meniscus and UTE  $T_{1\rho}$ , suggesting a potential role of  $T_{1\rho}$  as a useful biomarker to detect softening due to degeneration. MacLeod et al. (60) measured meniscus deformation in healthy and OA subject (based on image registration) and found bigger displacements in OA subjects as compared to healthy controls. Calixto et al. (13) measured  $T_2$  and  $T_{1\rho}$  under compressive 50% body weight. Increases in both relaxation times were observed in healthy controls, while the changes were less consistent in OA. The regional dependent behavior was interpreted as a possible marker of load transmission. Son et al. (95) found significant correlation between relaxation times and mechanical properties of human menisci obtained from patients who underwent total knee arthroplasty (TKA).

Quantitative mechanical properties obtained from MRI, for cartilage, meniscus, other soft tissue structures such as ligaments, and tendons, will find an important application in the field of FEM for biomechanics application. Ideally material properties would be obtained in each node in the image, in a similar way as it is now currently done for CT-based FEM models (16). Although quantitative MRI correlated well with certain mechanical properties and provided a strong response under functionally loaded activities, the link between changes in quantitative MRI values and mechanical properties is still poorly understood. We foresee that experiments on cadaveric specimens or explants will be needed to increase our understanding and to lead to the use of quantitative MRI parameters in the computer modeling pipeline.

## Loading devices

The dynamic MRI techniques introduced in the previous sections can be coupled with the use of appropriate loading devices to increase the physiological value of the measurement.

Loading devices to be used in conjunction with MRI need to be made of MR compatible materials (26) and they should ideally provide no detectable signal, in order to avoid common artifacts such as foldover in the acquired images.



Several loading design for dynamic imaging have been designed. Silder et al. (90) designed a loading device that could be used to generate either elastic or inertial loads on the hamstring and quadriceps muscle during knee flexion/extension. The device was subsequently used for measurements of tibiofemoral and patellofemoral kinematics (40, 49, 55, 89, 105). D'entremont et al. (25) proposed a relatively simple loading rig that allowed free leg motion with a force of 8% body weight applied in the ankle hip direction.

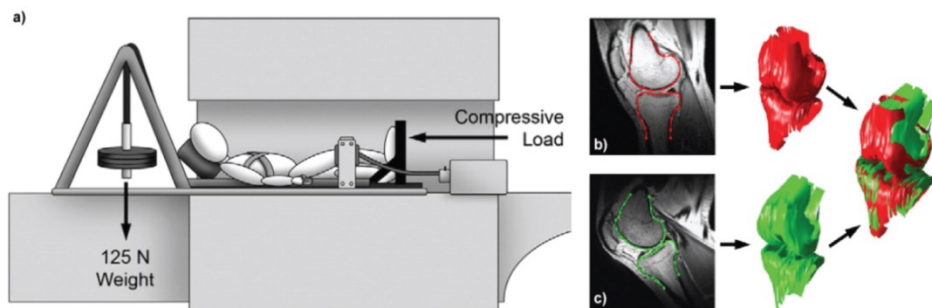


**Figure 6:** a) Static loading device. Weights are hung behind the patient in the MRI system, and a set of pulleys and a loading plate transfer the force into a compressive load at the foot. b) Static image of the knee in full extension c) static image of the knee at maximum flexion. After registration of the tibia models obtained at both positions, the femoral kinematics can be derived. Adapted from (17) with permission.

Besides providing assessment of the musculoskeletal system under conditions that can better represent daily tasks, MRI loading devices can also provide mechanical restriction of movement, which is beneficial to increase consistency during the repetitions of the motion task in dynamic imaging.

In addition to their use in dynamic imaging, loading devices are also of paramount importance in the field of loaded or stress MRI. Stress MRI has received growing interest in the last two decades, and has mostly been performed using an open MRI scanner (32, 62, 84), but this type of scanners usually has a very low main magnetic field strength and the images produced concomitantly suffer from very low signal-to-noise ratio (SNR). Therefore, efforts have been made to design an optimal joint loading set-up to simulate static upright stance in a typical close bore scanner (1.5T or 3T). Previously, several approaches have been reported, but only those devices designed for mechanical compressive loading of the knee joint are discussed. Nag et al. (67) designed a mechanical advantage pulley system which in essence was the precursor to later loading devices. In 2008, Nishii et al. (71) designed a set-up to measure cartilage thickness and  $T_2$  in response to loading. Shefelbine et al. (87) also made a device, which has been used extensively to investigate the effects of loading on the knee joint

in healthy volunteers and in patients (13, 17, 60, 87, 97, 98). The basic device was at a later stage coupled with a rotational device (18), in order to assess rotational stability of the knee. Several other groups have taken different approaches. These include load cells (103), pneumatic devices (20) and mechanical foot plates connected to a pulley for load application (54, 64).

For a more extensive description of loading devices used for dynamic and quasi-static studies, we refer to a review paper on this topic (26).

## Conclusions

In this work, we provided an overview of several MR-based techniques, which provide functional information of the musculoskeletal system, including bone kinematics, muscle structure and contraction, and tissue deformation under load. Functional imaging of the musculoskeletal system is a relatively new, yet fast growing, field of research. The techniques presented in this review have already shown potential in advancing our knowledge of the musculoskeletal system and in providing useful functional information for creating and validating biomechanical models. However, applications are yet confined to mostly healthy subjects and in a research setting. We believe that recent advances in MRI techniques, especially in the field of accelerated imaging, can facilitate a more widespread application of these methods.

## References

1. **Akbari A, Rockel CP, Kumbhare DA, Noseworthy MD.** Safe MRI-Compatible electrical muscle stimulation (EMS) system. *J Magn Reson Imaging* 44: 1530–1538, 2016.
2. **Akella S V, Regatte RR, Gougoutas a J, Borthakur a, Shapiro EM, Kneeland JB, Leigh JS, Reddy R.** Proteoglycan-induced changes in T1rho-relaxation of articular cartilage at 4T. *Magn Reson Med* 46: 419–423, 2001.
3. **Asakawa DS, Nayak KS, Blemker SS, Delp SL, Pauly JM, Nishimura DG, Gold GE.** Real-Time Imaging of Skeletal Muscle Velocity. *J Magn Reson Imaging* 18: 734–739, 2003.
4. **Bae WC, Biswas R, Statum S, Sah RL, Chung CB.** Sensitivity of quantitative UTE MRI to the biomechanical property of the temporomandibular joint disc. *Skeletal Radiol* 43: 1217–1223, 2014.
5. **Baum T, Joseph GB, Karampinos DC, Jungmann PM, Link TM, Bauer JS.** Cartilage and meniscal T2 relaxation time as non-invasive biomarker for knee osteoarthritis and cartilage repair procedures. *Osteoarthr Cartil* 21: 1474–1484, 2013.
6. **Behnam AJ, Herzka DA, Sheehan FT.** Assessing the accuracy and precision of musculoskeletal motion tracking using cine-PC MRI on a 3.0T platform. *J Biomech* 44: 193–197, 2011.
7. **Blemker SS, Asakawa DS, Gold GE, Delp SL.** Image-based musculoskeletal modeling: Applications, advances, and future opportunities. *J Magn Reson Imaging* 25: 441–451, 2007.
8. **Blemker SS, Pinsky PM, Delp SL.** A 3D model of muscle reveals the causes of nonuniform strains in the biceps brachii. *J Biomech* 38: 657–665, 2005.
9. **Bolsterlee B, Veeger HEJ, Van Der Helm FCT, Gandevia SC, Herbert RD.** Comparison of measurements of medial gastrocnemius architectural parameters from ultrasound and diffusion tensor images. *J Biomech* 48: 1133–1140, 2015.
10. **Borotikar BS, Sheehan FT.** In vivo patellofemoral contact mechanics during active extension using a novel dynamic MRI-based methodology. *Osteoarthr Cartil* 21: 1886–1894, 2013.
11. **Borotikar BS, Sipprell WH, Wible EE, Sheehan FT.** A methodology to accurately quantify patellofemoral cartilage contact kinematics by combining 3D image shape registration and cine-PC MRI velocity data. *J Biomech* 45: 1117–1122, 2012.
12. **Boutin RD, Buonocore MH, Immerman I, Ashwell Z, Sonico GJ, Szabo RM, Chaudhari AJ.** Real-time magnetic resonance imaging (MRI) during active wrist motion - Initial observations. *PLoS One* 8: 10–17, 2013.
13. **Calixto NE, Kumar D, Subburaj K, Singh J, Schooler J, Nardo L, Li X, Souza RB, Link TM, Majumdar S.** Zonal differences in meniscus MR relaxation times in response to in vivo static loading in knee osteoarthritis. *J Orthop Res* 34: 249–261, 2016.
14. **Carlson VR, Boden BP, Sheehan FT.** Patellofemoral Kinematics and Tibial

- Tuberosity–Trochlear Groove Distances in Female Adolescents With Patellofemoral Pain. *Am J Sports Med* 45: 1102–1109, 2017.
15. **Carlson VR, Boden BP, Shen A, Jackson JN, Alter KE, Sheehan FT.** Patellar Maltracking Persists in Adolescent Females With Patellofemoral Pain. *Orthop J Sport Med* 5: 1–7, 2017.
16. **Carpenter RD.** Finite element analysis of the hip and spine based on quantitative computed tomography. *Curr Osteoporos Rep* 11: 156–162, 2013.
17. **Carpenter RD, Majumdar S, Ma CB.** Magnetic Resonance Imaging of 3-Dimensional In Vivo Tibiofemoral Kinematics in Anterior Cruciate Ligament-Reconstructed Knees. *Arthrosc - J Arthrosc Relat Surg* 25: 760–766, 2009.
18. **Carpenter RD, Shefelbine SJ, Lozano J, Carballido-Gamio J, Majumdar S, Benjamin Ma C.** A New Device for Measuring Knee Rotational Kinematics Using Magnetic Resonance Imaging. *J Med Device* 2: 44501, 2008.
19. **Ceelen KK, Stekelenburg A, Mulders JLJ, Strijkers GJ, Baaijens FPT, Nicolay K, Oomens CWJ.** Validation of a numerical model of skeletal muscle compression with MR tagging: a contribution to pressure ulcer research. *J Biomech Eng* 130: 61015, 2008.
20. **Chan DD, Cai L, Butz KD, Trippel SB, Nauman EA, Neu CP.** In vivo articular cartilage deformation: noninvasive quantification of intratissue strain during joint contact in the human knee. *Sci Rep* 6: 19220, 2016.
21. **Chan DD, Neu CP.** Transient and microscale deformations and strains measured under exogenous loading by noninvasive magnetic resonance. *PLoS One* 7: e33463, 2012.
22. **Chan DD, Neu CP, Hull ML.** In situ deformation of cartilage in cyclically loaded tibiofemoral joints by displacement-encoded MRI. *Osteoarthr Cartil* 17: 1461–1468, 2009.
23. **Csapo R, Malis V, Sinha U, Sinha S.** Mapping of spatial and temporal heterogeneity of plantar flexor muscle activity during isometric contraction: correlation of velocity-encoded MRI with EMG. *J Appl Physiol* 119: 558–568, 2015.
24. **D’Entremont AG, McCormack RG, Horlick SGD, Stone TB, Manzary MM, Wilson DR.** Effect of opening-wedge high tibial osteotomy on the three-dimensional kinematics of the knee. *Bone Jt J* 96B: 1214–1221, 2014.
25. **D’Entremont AG, Nordmeyer-Massner JA, Bos C, Wilson DR, Pruessmann KP.** Do dynamic-based MR knee kinematics methods produce the same results as static methods? *Magn Reson Med* 69: 1634–1644, 2013.
26. **D’Entremont AG, Wilson DR.** Joint mechanics measurement using magnetic resonance imaging. *Top Magn Reson Imaging* 21: 325–334, 2010.
27. **Damon BM, Buck AKW, Ding Z.** Diffusion-Tensor MRI Based Skeletal Muscle Fiber Tracking. *Imaging Med* 3: 675–687, 2011.
28. **Damon BM, Froeling M, Buck AKW, Oudeman J, Ding Z, Nederveen AJ, Bush EC, Strijkers GJ.** Skeletal muscle diffusion tensor-MRI fiber tracking: rationale, data acquisition and analysis methods, applications and future directions. *NMR Biomed* 3: e3563, 2017.
29. **Damon BM, Heemskerk AM, Ding Z.** Polynomial fitting of DT-MRI fiber tracts allows accurate estimation of muscle architectural parameters. *Magn Reson*

- Imaging* 30: 589–600, 2012.
30. **Deligianni X, Pansini M, Garcia M, Hirschmann A, Schmidt-Trucksäss A, Bieri O, Santini F.** Synchronous MRI of muscle motion induced by electrical stimulation. *Magn Reson Med* 672: 664–672, 2016.
  31. **Dragoo JL, Phillips C, Schmidt JD, Scanlan SF, Blazek K, Steadman JR, Williams A.** Mechanics of the anterior interval of the knee using open dynamic MRI. *Clin Biomech* 25: 433–437, 2010.
  32. **Draper CE, Besier TF, Fredericson M, Santos JM, Beaupre GS, Delp SL, Gold GE.** Differences in patellofemoral kinematics between weight-bearing and non-weight-bearing conditions in patients with patellofemoral pain. *J Orthop Res* 29: 312–317, 2011.
  33. **Draper CE, Besier TF, Santos JM, Jennings F, Fredericson M, Gold GE, Beaupre GS, Delp SL.** Using real-time MRI to quantify altered joint kinematics in subjects with patellofemoral pain and to evaluate the effects of a patellar brace or sleeve on joint motion. *J Orthop Res* 27: 571–577, 2009.
  34. **Draper CE, Santos JM, Kourtis LC, Besier TF, Fredericson M, Beaupre GS, Gold GE, Delp SL.** Feasibility of using real-time MRI to measure joint kinematics in 1.5T and open-bore 0.5T systems. *J Magn Reson Imaging* 28: 158–166, 2008.
  35. **Englund EK, Elder CP, Xu Q, Ding Z, Damon BM.** Combined diffusion and strain tensor MRI reveals a heterogeneous, planar pattern of strain development during isometric muscle contraction. *Am J Physiol Regul Integr Comp Physiol* 300: R1079–R1090, 2011.
  36. **Felson DT.** Osteoarthritis as a disease of mechanics. *Osteoarthr Cartil* 21: 10–15, 2013.
  37. **Felton SM, Gaige TA, Benner T, Wang R, Reese TG, Wedeen VJ, Gilbert RJ.** Associating the mesoscale fiber organization of the tongue with local strain rate during swallowing. *J Biomech* 41: 1782–1789, 2008.
  38. **Filli L, Kenkel D, Wurnig MC, Boss A.** Diffusional kurtosis MRI of the lower leg: Changes caused by passive muscle elongation and shortening. *NMR Biomed* 29: 767–775, 2016.
  39. **Finni T, Hodgson J a, Lai AM, Edgerton VR, Sinha S.** Nonuniform strain of human soleus aponeurosis-tendon complex during submaximal voluntary contractions in vivo. *J Appl Physiol* 95: 829–37, 2003.
  40. **Fiorentino NM, Epstein FH, Blemker SS.** Activation and aponeurosis morphology affect in vivo muscle tissue strains near the myotendinous junction. *J Biomech* 45: 647–652, 2012.
  41. **Fiorentino NM, Lin JS, Ridder KB, Guttman MA, Mc Veigh ER, Blemker SS.** Rectus Femoris Knee Muscle Moment Arms Measured in Vivo During Dynamic Motion With Real-Time Magnetic Resonance Imaging. *J Biomech Eng* 135: 44501, 2013.
  42. **Froeling M, Nederveen AJ, Nicolay K, Strijkers GJ.** DTI of human skeletal muscle: The effects of diffusion encoding parameters, signal-to-noise ratio and T2 on tensor indices and fiber tracts. *NMR Biomed* 26: 1339–1352, 2013.
  43. **Gilles B, Perrin R, Magnenat-Thalmann N, Vallee JP.** Bone motion analysis from dynamic MRI: Acquisition and tracking. *Acad Radiol* 12: 1285–1292, 2005.
  44. **Gindre J, Takaza M, Moerman KM, Simms CK.** A structural model of passive

- skeletal muscle shows two reinforcement processes in resisting deformation. *J Mech Behav Biomed Mater* 22: 84–94, 2013.
45. **Guzzanti V, Gigante A, Di Lazzaro A, Fabbriani C.** Patellofemoral malalignment in adolescents. Computerized tomographic assessment with or without quadriceps contraction. *Am J Sports Med* 22: 55–60, 1994.
  46. **Heemskerk AM, Sinha TK, Wilson KJ, Ding Z, Damon BM.** Repeatability of DTI-based skeletal muscle fiber tracking. *NMR Biomed* 23: 294–303, 2010.
  47. **Hicks JL, Uchida TK, Seth A, Rajagopal A, Delp S.** Is my model good enough? Best practices for verification and validation of musculoskeletal models and simulations of human movement. *J Biomech Eng* 137: 20905, 2015.
  48. **Irrechukwu ON, Thae S Von, Frank EH, Lin PC, Reiter DA, Grodzinsky AJ, Spencer RG.** Prediction of cartilage compressive modulus using multiexponential analysis of T2 relaxation data and support vector regression. *NMR Biomed* 27: 468–477, 2014.
  49. **Kaiser J, Bradford R, Johnson K, Wieben O, Thelen DG.** Measurement of tibiofemoral kinematics using highly accelerated 3D radial sampling. *Magn Reson Med* 69: 1310–1316, 2013.
  50. **Kaiser J, Monawer A, Chaudhary R, Johnson KM, Wieben O, Kijowski R, Thelen DG.** Accuracy of model-based tracking of knee kinematics and cartilage contact measured by dynamic volumetric MRI. *Med Eng Phys* 38: 1131–1135, 2016.
  51. **Keenan KE, Besier TF, Pauly JM, Smith RL, Delp SL, Beaupre GS, Gold GE.** T1 $\rho$  Dispersion in Articular Cartilage: Relationship to Material Properties and Macromolecular Content. *Cartilage* 6: 113–22, 2015.
  52. **Kinugasa R, Hodgson J a, Edgerton VR, Sinha S.** Asymmetric deformation of contracting human gastrocnemius muscle. *J Appl Physiol* 112: 463–70, 2012.
  53. **Koff MF, Amrami KK, Kaufman KR.** Clinical evaluation of T2 values of patellar cartilage in patients with osteoarthritis. *Osteoarthr Cartil* 15: 198–204, 2007.
  54. **Lange T, Maclaren J, Herbst M, Lovell-Smith C, Izadpanah K, Zaitsev M.** Knee cartilage MRI with in situ mechanical loading using prospective motion correction. *Magn Reson Med* 71: 516–523, 2014.
  55. **Lenhart RL, Kaiser J, Smith CR, Thelen DG.** Prediction and Validation of Load-Dependent Behavior of the Tibiofemoral and Patellofemoral Joints During Movement. *Ann Biomed Eng* 43: 2675–2685, 2015.
  56. **Liess C, Lüsse S, Karger N, Heller M, Glüer CG.** Detection of changes in cartilage water content using MRI T2-mapping in vivo. *Osteoarthr Cartil* 10: 907–913, 2002.
  57. **Link TM, Neumann J, Li X.** Prestructural cartilage assessment using MRI. *J Magn Reson Imaging* 45: 949–965, 2017.
  58. **Luke AC, Stehling C, Stahl R, Li X, Kay T, Takamoto S, Ma B, Majumdar S, Link T.** High-Field Magnetic Resonance Imaging Assessment of Articular Cartilage Before and After Marathon Running. *Am J Sports Med* 38: 2273–2280, 2010.
  59. **Lustig M, Donoho D, Pauly JM.** Sparse MRI: The application of compressed sensing for rapid MR imaging. *Magn Reson Med* 58: 1182–1195, 2007.
  60. **MacLeod TD, Subburaj K, Wu S, Kumar D, Wyatt C, Souza RB.** Magnetic resonance analysis of loaded meniscus deformation: a novel technique

- comparing participants with and without radiographic knee osteoarthritis. *Skeletal Radiol* 44: 125–135, 2014.
61. **Malis V, Sinha U, Csapo R, Narici M, Sinha S.** Relationship of changes in strain rate indices estimated from velocity-encoded MR imaging to loss of muscle force following disuse atrophy. *Magn Reson Med* 0, 2017.
62. **Mariani S, La Marra A, Arrigoni F, Necozone S, Splendiani A, Di Cesare E, Barile A, Masciocchi C.** Dynamic measurement of patello-femoral joint alignment using weight-bearing magnetic resonance imaging (WB-MRI). *Eur J Radiol* 84: 2571–2578, 2015.
63. **Mayerhoefer ME, Riegler G, Welsch GH, Mamisch TC, Weber M, Trattnig S.** The in vivo effects of mechanical compression on T1 values of healthy articular knee cartilage and the menisci. In: *European Society of Radiology*. 2010, p. 1–5.
64. **Mayerhoefer ME, Welsch GH, Mamisch TC, Kainberger F, Weber M, Nemeč S, Friedrich KM, Dirisamer A, Trattnig S.** The in vivo effects of unloading and compression on T1-Gd (dGEMRIC) relaxation times in healthy articular knee cartilage at 3.0 Tesla. *Eur Radiol* 20: 443–449, 2010.
65. **Moerman KM, Sprengers AMJ, Simms CK, Lamerichs RM, Stoker J, Nederveen AJ.** Validation of SPAMM tagged MRI based measurement of 3D soft tissue deformation. *Med Phys* 38: 1248–1260, 2011.
66. **Moerman KM, Sprengers AMJ, Simms CK, Lamerichs RM, Stoker J, Nederveen AJ.** Validation of continuously tagged MRI for the measurement of dynamic 3D skeletal muscle tissue deformation. *Med Phys* 39: 1793–810, 2012.
67. **Nag D, Liney GP, Gillespie P, Sherman KP.** Quantification of T2 Relaxation Changes in Articular Cartilage with In Situ Mechanical Loading of the Knee. *J Magn Reson Imaging* 19: 317–322, 2004.
68. **Neu CP.** Functional imaging in OA: Role of imaging in the evaluation of tissue biomechanics. *Osteoarthr Cartil* 22: 1349–1359, 2014.
69. **Neu CP, Hull ML, Walton JH.** Error optimization of a three-dimensional magnetic resonance imaging tagging-based cartilage deformation technique. *Magn Reson Med* 54: 1290–1294, 2005.
70. **Nieminen MT, Töyräs J, Laasanen MS, Silvennoinen J, Helminen HJ, Jurvelin JS.** Prediction of biomechanical properties of articular cartilage with quantitative magnetic resonance imaging. *J Biomech* 37: 321–328, 2004.
71. **Nishii T, Kuroda K, Matsuoka Y, Sahara T, Yoshikawa H.** Change in knee cartilage T2 in response to mechanical loading. *J Magn Reson Imaging* 28: 175–180, 2008.
72. **Nissi MJ, Rieppo J, Töyräs J, Laasanen MS, Kiviranta I, Nieminen MT, Jurvelin JS.** Estimation of mechanical properties of articular cartilage with MRI - dGEMRIC, T2 and T1 imaging in different species with variable stages of maturation. *Osteoarthr Cartil* 15: 1141–1148, 2007.
73. **Nordmeyer-Massner JA, De Zanche N, Pruessmann KP.** Stretchable coil arrays: Application to knee imaging under varying flexion angles. *Magn Reson Med* 67: 872–879, 2012.
74. **Oudeman J, Nederveen AJ, Strijkers GJ, Maas M, Luijten PR, Froeling M.** Techniques and applications of skeletal muscle diffusion tensor imaging: A review. *J Magn Reson Imaging* 43: 773–788, 2016.

75. **Pappas GP, Asakawa DS, Delp SL, Zajac FE, Drace JE.** Nonuniform shortening in the biceps brachii during elbow flexion. *J Appl Physiol* 92: 2381–2389, 2002.
76. **Patel V V., Hall K, Ries M, Lotz J, Ozhinsky E, Lindsey C, Lu Y, Majumdar S.** A three-dimensional MRI analysis of knee kinematics. *J Orthop Res* 22: 283–292, 2004.
77. **Pierrart J, Lefevre-Colau MM, Skalli W, Vuillemin V, Masmajeun EH, Cuenod CA, Gregory TM.** New dynamic three-dimensional MRI technique for shoulder kinematic analysis. *J Magn Reson Imaging* 39: 729–734, 2014.
78. **Prompers JJ, Jeneson JAL, Drost MR, Oomens CCW, Strijkers GJ, Nicolay K.** Dynamic MRS and MRI of skeletal muscle function and biomechanics. *NMR Biomed* 19: 927–953, 2006.
79. **Rebmann AJ, Sheehan FT.** Precise 3D skeletal kinematics using fast phase contrast magnetic resonance imaging. *J Magn Reson Imaging* 17: 206–213, 2003.
80. **Scheel M, Prokscha T, von Roth P, Winkler T, Dietrich R, Bierbaum S, Arampatzis A, Diederichs G.** Diffusion Tensor Imaging of Skeletal Muscle—Correlation of Fractional Anisotropy to Muscle Power. *Fortschr Röntgenstr* 185: 857–861, 2013.
81. **Schwenzer NF, Steidle G, Martirosian P, Schraml C, Springer F, Claussen CD, Schick F.** Diffusion tensor imaging of the human calf muscle: Distinct changes in fractional anisotropy and mean diffusion due to passive muscle shortening and stretching. *NMR Biomed* 22: 1047–1053, 2009.
82. **Seisler AR, Sheehan FT.** Normative three-dimensional patellofemoral and tibiofemoral kinematics: A dynamic, in vivo study. *IEEE Trans Biomed Eng* 54: 1333–1341, 2007.
83. **Serebrakian AT, Poulos T, Liebl H, Joseph GB, Lai A, Nevitt MC, Lynch JA, McCulloch CE, Link TM.** Weight loss over 48 months is associated with reduced progression of cartilage T2 relaxation time values: Data from the osteoarthritis initiative. *J Magn Reson Imaging* 41: 1272–1280, 2015.
84. **Shapiro LM, Gold GE.** MRI of weight bearing and movement. *Osteoarthr Cartil* 20: 69–78, 2012.
85. **Sheehan FT.** The 3D patellar tendon moment arm: Quantified in vivo during volitional activity. *J Biomech* 40: 1968–1974, 2007.
86. **Sheehan FT, Drace JE.** Human Patellar Tendon Strain. *Clin Orthop Relat Res* : 201–207, 2000.
87. **Shefelbine SJ, Ma CB, Lee K-Y, Schrupf MA, Patel P, Safran MR, Slavinsky JP, Majumdar S.** MRI Analysis of In Vivo Meniscal and Tibiofemoral Kinematics in ACL-Deficient and Normal Knees. *J Orthop Res* 24: 1208–1217, 2006.
88. **Shin DD, Hodgson JA, Edgerton VR, Sinha S.** In vivo intramuscular fascicle-aponeuroses dynamics of the human medial gastrocnemius during plantarflexion and dorsiflexion of the foot. *J Appl Physiol* 107: 1276–1284, 2009.
89. **Silder A, Reeder SB, Thelen DG.** The influence of prior hamstring injury on lengthening muscle tissue mechanics. *J Biomech* 43: 2254–2260, 2010.
90. **Silder A, Westphal CJ, Thelen DG.** A Magnetic Resonance-Compatible Loading Device for Dynamically Imaging Shortening and Lengthening Muscle

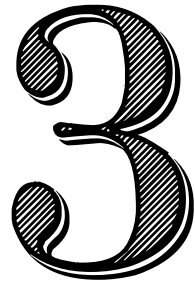


- Contraction Mechanics. *J Med Device* 3: 34504, 2009.
91. **Sinha S, Hodgson JA, Finni T, Lai AM, Grinstead J, Edgerton VR.** Muscle kinematics during isometric contraction: Development of phase contrast and spin tag techniques to study healthy and atrophied muscles. *J Magn Reson Imaging* 20: 1008–1019, 2004.
  92. **Sinha S, Shin DD, Hodgson JA, Kinugasa R, Edgerton VR.** Computer-controlled, MR-compatible foot-pedal device to study dynamics of the muscle tendon complex under isometric, concentric, and eccentric contractions. *J Magn Reson Imaging* 36: 498–504, 2012.
  93. **Sinha S, Sinha U.** Reproducibility analysis of diffusion tensor indices and fiber architecture of human calf muscles in vivo at 1.5 Tesla in neutral and plantarflexed ankle positions at rest. *J Magn Reson Imaging* 34: 107–119, 2011.
  94. **Sinha U, Malis V, Csapo R, Moghadasi A, Kinugasa R, Sinha S.** Age-related differences in strain rate tensor of the medial gastrocnemius muscle during passive plantarflexion and active isometric contraction using velocity encoded MR imaging: Potential index of lateral force transmission. *Magn Reson Med* 73: 1852–1863, 2015.
  95. **Son M, Goodman SB, Chen W, Hargreaves BA, Gold GE, Levenston ME.** Regional variation in T1rho and T2 times in osteoarthritic human menisci: Correlation with mechanical properties and matrix composition. *Osteoarthr Cartil* 21: 796–805, 2013.
  96. **Souza RB, Draper CE, Fredericson M, Powers CM.** Femur Rotation and Patellofemoral Joint Kinematics: A Weight-Bearing Magnetic Resonance Imaging Analysis. *J Orthop Sport Phys Ther* 40: 277–285, 2010.
  97. **Souza RB, Kumar D, Calixto N, Singh J, Schooler J, Subburaj K, Li X, Link TM, Majumdar S.** Response of knee cartilage T1rho and T2 relaxation times to in vivo mechanical loading in individuals with and without knee osteoarthritis. *Osteoarthritis Cartilage* 22: 1367–76, 2014.
  98. **Subburaj K, Souza RB, Stehling C, Wyman BT, Le Graverand-Gastineau MP, Link TM, Li X, Majumdar S.** Association of MR relaxation and cartilage deformation in knee osteoarthritis. *J Orthop Res* 30: 919–926, 2012.
  99. **Takaza M, Moerman KM, Gindre J, Lyons G, Simms CK.** The anisotropic mechanical behaviour of passive skeletal muscle tissue subjected to large tensile strain. *J Mech Behav Biomed Mater* 17: 209–220, 2012.
  100. **Tempelaere C, Pierrart J, Lefèvre-Colau MM, Vuillemin V, Cuénod CA, Hansen U, Mir O, Skalli W, Gregory T.** Dynamic three-dimensional shoulder MRI during active motion for investigation of rotator cuff diseases. *PLoS One* 11: 1–12, 2016.
  101. **van Tiel J, Kotek G, Reijman M, Bos PK, Bron EE, Klein S, Nasserinejad K, van Osch GJVM, Verhaar JAN, Krestin GP, Weinans H, Oei EHG.** Is T1p Mapping an Alternative to Delayed Gadolinium-enhanced MR Imaging of Cartilage in the Assessment of Sulphated Glycosaminoglycan Content in Human Osteoarthritic Knees? An In Vivo Validation Study. *Radiology* 279: 523–531, 2016.
  102. **Uecker M, Zhang S, Voit D, Karaus A, Merboldt KD, Frahm J.** Real-time MRI at a resolution of 20 ms. *NMR Biomed* 23: 986–994, 2010.
  103. **Wang H, Koff MF, Potter HG, Warren RF, Rodeo SA, Maher SA.** An MRI-

- compatible loading device to assess knee joint cartilage deformation: Effect of preloading and inter-test repeatability. *J Biomech* 48: 2934–2940, 2015.
104. **Wentland AL, McWalter EJ, Pal S, Delp SL, Gold GE.** Muscle velocity and inertial force from phase contrast MRI. *J Magn Reson Imaging* 42: 526–532, 2015.
105. **Westphal CJ, Schmitz A, Reeder SB, Thelen DG.** Load-dependent variations in knee kinematics measured with dynamic MRI. *J Biomech* 46: 2045–2052, 2013.
106. **Yao J, Yang B, Niu W, Zhou J, Wang Y, Gong H, Ma H, Tan R, Fan Y.** In vivo measurements of patellar tracking and finite helical axis using a static magnetic resonance based methodology. *Med Eng Phys* 36: 1611–1617, 2014.
107. **Zhong X, Epstein FH, Spottiswoode BS, Helm PA, Blemker SS.** Imaging two-dimensional displacements and strains in skeletal muscle during joint motion by cine DENSE MR. *J Biomech* 41: 532–540, 2008.



# Chapter



## A novel diffusion-tensor MRI approach for skeletal muscle fascicle length measurements

Jos Oudeman\*

**Valentina Mazzoli\***

Marco A. Marra

Klaas Nicolay

Mario Maas

Nico Verdonschot

Andre M. Sprengers

Aart J. Nederveen

Gustav J. Strijkers

Martijn Froeling

\* These authors contributed equally

**Physiol Rep. 2016 Dec;4(24). pii: e13012.**

**doi: 10.14814/phy2.13012**

## Abstract

**Introduction:** Musculoskeletal (dys-)function relies for a large part on muscle architecture, which can be obtained using Diffusion Tensor MRI (DT-MRI) and fiber tractography. However, reconstructed tracts often continue along the tendon or aponeurosis when using conventional methods, thus overestimating fascicle lengths. In this study, we propose a new method for semi-automatic segmentation of tendinous tissue using tract density (TD). We investigated the feasibility and repeatability of this method to quantify the mean fascicle length per muscle. Additionally, we examined whether the method facilitates measuring changes in fascicle length of lower leg muscles with different foot positions.

**Methods:** Five healthy subjects underwent two DT-MRI scans of the right lower leg, with the foot in 15° dorsiflexion, neutral, and 30° plantarflexion positions. Repeatability of fascicle length measurements was assessed using Bland-Altman analysis. Changes in fascicle lengths between the foot positions were tested using a repeated multivariate analysis of variance (MANOVA).

**Results:** Bland-Altman analysis showed good agreement between repeated measurements. The coefficients of variation in neutral position were 8.3%, 16.7%, 11.2% and 10.4% for Soleus (SOL), Fibularis Longus (FL), Extensor Digitorum Longus (EDL) and Tibialis Anterior (TA), respectively. The plantarflexors (SOL and FL) showed significant increase in fascicle length from plantarflexion to dorsiflexion whereas the dorsiflexors (EDL and TA) exhibited a significant decrease.

**Conclusions:** The use of a tract density for semi-automatic segmentation of tendinous structures provides more accurate estimates of the mean fascicle length than traditional fiber tractography methods. The method shows moderate to good repeatability and allows for quantification of changes in fascicle lengths due to passive stretch.

## Introduction

The architectural parameters of muscle-tendon units determine the function that these have within the musculoskeletal system. Among these parameters, we find most importantly: the optimal fiber length, the physiological cross-sectional area (PCSA) and the pennation angle. For instance, fascicles within long muscle-tendon units can sustain longer excursions during daily activities than short muscles having a large PCSA, which are instead optimized to produce high forces within a limited range of fascicle lengths (27).

It is well known that these architectural properties may change due to (patho-)physiological conditions such as aging, exercise, disease, or surgical intervention (23, 40), which has an influence on muscle function (23, 34). For example, it was shown that muscle fascicle length decreases due to inactivity and lengthens after exercise, but it has also been shown that fascicle length directly correlates with performance in athletes (23, 31, 34). Therefore obtaining architectural properties such as fascicle length in a reliable fashion is of vital importance to understand skeletal muscle function and alterations therein due to (patho-)physiological conditions.

Quantitative values for architectural parameters, are often estimated from available data obtained on dissected cadaveric specimens or from bright mode ultrasound (24, 25, 44). However, these methods have serious limitations. Cadaveric material does not provide patient-specific information. Ultrasound is limited to superficial muscles and offers mostly 2D measurements in a narrow field-of-view (FOV) (24). A few studies exploited conventional anatomical magnetic resonance imaging (MRI) to derive muscle architecture (1, 3). Anatomical  $T_1$ - and  $T_2$ -weighted scans provide sufficient contrast for quantification of muscle volume (1, 43), but fascicle orientations and pennation angles cannot be inferred from these scans.

Muscle fascicle architecture characterization by DT-MRI does not suffer from the above-mentioned shortcomings, as it can be applied to quantify subject specific *in vivo* 3D muscle architecture in a large FOV (18, 42). DT-MRI is a specialized MRI technique, capable of quantifying the self-diffusion of water molecules in tissue. Water diffusion in skeletal muscles is highest along the axis of the fascicles and lowest perpendicular to the axis of the fascicles. Although a definitive model underlying this diffusion anisotropy in skeletal muscle is lacking, it is generally accepted that diffusion perpendicular to the muscle fascicle axis is lower because water diffusion in this direction is hindered by intra- and extracellular tissue constituents (5, 33). Using the diffusion tensor, the muscle fascicle orientation can be quantified in each imaging

voxel. Tractography combines this information in 3D to obtain whole-muscle fascicle architecture (33). DT-MRI and tractography have been applied to visualize muscle architecture in various regions in the human body, including leg, forearm, heart, spine, pelvis, and tongue (8, 10, 11, 37, 46).

**3**

It has been shown that tractography provides a useful visual representation of muscle architecture in which pennation angles could be measured accurately (12, 36). However, measurements of fascicle length proved more challenging due to the presence of artificially long fascicles as tractography continued beyond the muscle origin and insertion due to partial volume effects with tendons and fascia (36, 39). Additionally, unrealistically short fascicles were observed near the borders of the segmented muscle volumes as a result of suboptimal segmentation and limited resolution (36).

Thus, accurate and automatic determination of fascicle lengths and pennation angles not only depends on accurate segmentations of the individual muscles, but also on the accurate segmentation of tendons, fasciae and (internal) aponeuroses (12, 39). However, due to their limited resolution, segmentation cannot be performed reliably on DT-MRI images (5, 33), therefore, segmentation has to be performed on high resolution co-registered anatomical scans. While this process is laborious and time consuming, it is also prone to errors due to difficulties in achieving a perfect registration between the anatomical and DT-MRI scans.

The purpose of this work is to introduce a novel method for semi-automatic segmentation of tendinous structures directly from the DT-MRI data, facilitating accurate and repeatable quantification of muscle fascicle lengths without the need for laborious segmentation and avoiding registration errors. We have explored this new method to quantify muscle fascicle lengths in several muscles of the human lower leg and we assessed changes in fascicle length due to passive ankle motion.

## Methods

### MRI

Five healthy male volunteers were scanned with a 3T Achieva MRI scanner (Philips) using a 6 channel torso coil. This study was approved by the local IRB and written informed consent was provided by all subjects prior to the study. A custom-built device was used to immobilize the foot in 3 different positions: 15° dorsiflexion, neutral position, and 30° plantarflexion. MRI measurements of the lower leg for all 3 foot

positions were performed in one examination. Each subject was measured twice on the same day in two separate MRI sessions, with at least 30 minutes in between. The MRI protocol consisted of an mDixon scan, for anatomical reference, and a DT-MRI scan. The following scan parameters were used for 3-point mDixon: sequence = FFE, FOV = 192x156 mm<sup>2</sup>, TR = 7.7 ms, TE1/ $\Delta$ TE = 2.1/1.7 ms, matrix size = 192x192, number of slices = 100, voxel size = 1x1x2.5 mm<sup>3</sup>. The following scan parameters were used in the DT-MRI scan: sequence = SE-EPI, FOV = 192x156 mm<sup>2</sup>; TR = 11191 ms, TE = 51.63 ms, matrix size = 64x52, number of slices = 50, voxel size = 3x3x5 mm<sup>3</sup>, SENSE acceleration factor = 1.5, number of gradient directions = 12, diffusion b-value = 400 s/mm<sup>2</sup>; Slice-selection gradient reversal (SSGR) was used for fat suppression, in combination with spectrally adiabatic inversion recovery (SPAIR) for aliphatic fat-suppression and spectrally selective suppression of the olefinic fat peak (15). The scan time for each foot position was 11 minutes, resulting in a total scan time of 33 minutes per session. Additionally, for each DT-MRI scan a noise scan was also performed in order to calculate SNR maps.

## Data processing

### Tensor calculation

DT-MRI data were processed using DTITools for Mathematica 10.3 (8). Data pre-processing comprised three steps: 1) Rician noise suppression (9), 2) affine registration of the diffusion weighted images to the non-weighted image to correct for motion and eddy current deformations (26), and 3) b-spline registration of the diffusion data to the mDixon water images to correct for susceptibility induced EPI deformations (16, 17, 45). In the last processing step, the resolution of the diffusion data was increased to a voxel size of 1.5x1.5x3.0 mm<sup>3</sup>. Directional diffusion data were fitted to a tensor model using a Weighted Least Linear Square (WLLS) algorithm, from which the principal direction of diffusion was determined. SNR (Signal to Noise Ratio) was defined as the ratio of the mean muscle signal in the DT-MRI images acquired with b=0 s/mm<sup>2</sup> and the standard deviation of noise, calculated from the noise scan.

### Muscle segmentation

Muscle segmentation was done by manual delineation of the 11 muscles in the lower leg (i.e. Tibialis Anterior, Tibialis Posterior, Extensor Digitorum Longus, Flexor Digitorum Longus, Flexor Hallucis Longus, Extensor Hallucis Longus, Gastrocnemius Medialis, Gastrocnemius Lateralis, Soleus, Fibularis Brevis and Fibularis Longus). The delineation was performed in the out-of-phase mDixon images of the first measurement session with the foot in neutral position. These mDixon images were



first down-sampled to a resolution of  $1 \times 1 \times 10 \text{ mm}^3$ , which resulted in only 25 slices for delineation. The segmentations were then transformed to all 6 datasets (3 positions, 2 measurements) by registering the down-sampled out of phase mDixon images to full resolution out-of-phase mDixon images using rigid registration followed by non-linear b-spline registration with Elastix (20).

## Tractography

Muscle tractography was performed using the vIST/e toolbox. Tractography was performed with an allowed FA range of 0.1 to 0.7, a maximal allowed angle change per step-size of  $20^\circ$  and a minimal fiber length of 0.2 cm. Seed points from which tracts continued bidirectionally were evenly spaced throughout the whole leg volume (seed distance = 1 mm) and a deterministic algorithm was used for tractography. This initial whole volume tractography was subsequently used to determine tract density maps, as explained in the next section.

## Tract density and fascicle length

### Tract density

The automatic segmentation of tendinous tissue is based on the notion that most muscle fibers have a well-defined origin and insertion and have a relatively constant density in the muscle body. As a consequence, the tract density (TD) of reconstructed muscle fascicles – from DT-MRI – should remain constant within the muscle volume (**Figure 1A**). However, muscle fascicle tracts reconstructed from DT-MRI data may artificially extend along tendons, aponeuroses, and fasciae, due to partial volume effects and diffusion anisotropy in these tendinous tissues (**Figure 1B**). As a consequence, the fascicle TD in voxels containing tendinous tissue is higher than those in the muscle belly (**Figure 1C**). Thus, voxels containing tendinous tissue can be segmented based on their higher TD value as compared to muscle tissue.

### Tractography based on tract density

TD maps were made by volume seeding of tracts in the whole leg with a seeding distance of  $1 \times 1 \times 1 \text{ mm}^3$ . TD was defined as the number of tracts crossing each voxel. The TD values were normalized to the mean TD of the entire volume, which contains mostly muscles, consequently  $\text{TD} \approx 1$  for muscle tissue. After the construction of the TD maps, a second tractography step is performed for each individual muscle, with step length = 0.2 max angle/step =  $10^\circ$ , and minimum fiber length = 20 mm, using the TD value as stopping criterion. If the TD value exceeds 1.5 tractography is halted, because this indicates the presence of a tendon, aponeurosis, fascia, or artifacts. Seed

points for tractography based on TD values were equally spaced within a volume obtained by eroding the segmented volume for each muscle to about 90% of its original size.

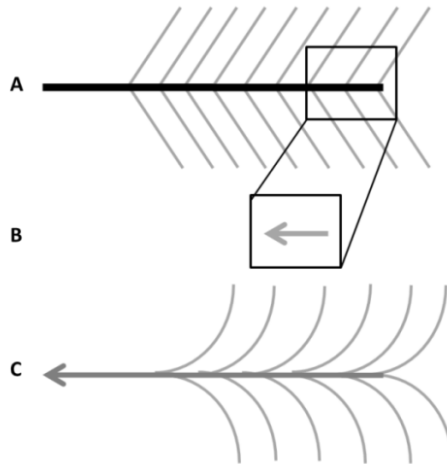


**Figure 1:** Schematic explanation of partial volume at muscle/tendon intersection. Schematic drawings of muscle and tendon in a pennate muscle with the artificial elongation. **A)** The *in vivo* situation in which the muscle fascicles (grey) attach to the tendon (black). **B)** When the voxel contains both tendon and muscle the average direction for tracking is along the tendon. **C)** Therefore tractography will continue along the tendon, leading to artificially long fascicles.

## Fascicle length measurements

The mean fascicle length for each muscle was derived from a fit of a skewed Gaussian distribution to the fascicle length distribution of all tracts of that muscle. Reconstructed fascicle tracts that terminated proximally or distally at the edges of the FOV were excluded from analysis, since these do not represent the full muscle fascicle length. As a comparison, our new method using TD maps was compared to two conventional tractography methods for determining fascicle lengths in the TA muscle. The first method used FA as a tracking stopping criterion with an allowed range of FA = 0.15 to 0.65 (32, 39, 41). The second one involved an accurate manual segmentation of the TA muscle and halting tractography at segmented boundaries of the TA muscle (13, 19, 36).

In-depth analysis of fascicle lengths and changes therein upon passive plantar- and dorsiflexion was restricted to the Soleus (SOL), Fibularis Longus (FL), Extensor Digitorum (EDL), and the Tibialis Anterior (TA).

## Statistical analysis

Repeatability of fascicle length measurements of the SOL, FL, EDL, and TA was investigated using Bland-Altman plots and reported as the coefficient of variation (CV). CV is defined as  $100\% \cdot \text{SD} / \text{Mean}$ , where SD is the standard deviation of the paired difference and Mean is the mean value calculated for the two repeated datasets. The CV is reported per muscle and position as well as for the 4 muscles combined. The minimal detectable difference (MDD) is calculated for each of the 4 muscles. The MDD is equal to 1.96 times the SD of the paired differences and represents the smallest difference in fascicle length that, with a 95% confidence interval, can be attributed to a true change in fascicle length rather than to a measurement error.

Significance ( $P < 0.05$ ) of changes in parameter values between the three ankle positions and repeated measurements were tested with a multivariate analysis of variance (MANOVA) (SPSS v. 22; IBM, Armonk, NY) with a Bonferroni post hoc test. For each variable, the assumption of sphericity was tested with the Mauchly test. If the sphericity assumption was violated, one of three corrections was used based on the Mauchly test output: the Greenhouse-Geisser, the Huynh-Feldt, or the lower-bound correction.

## Results

The five healthy males which were included in this study had a mean age of 27 years (range 24-29 years), a weight of 78 kg (range 62-89 kg), a length of 181 cm (range 171-189 cm), and a tibia length of 42 cm (range 37-47 cm). All DT-MRI scans were completed successfully (see **Figure 2A-D**) and were of sufficient quality to allow accurate tensor calculation.

For all scans, the average signal-to-noise (SNR) of muscle in the non-weighted images was at least 30 (range 30-70). For all subjects the muscle segmentation using the down-sampled out-of-phase mDixon images could be well aligned with the up-scaled diffusion data (see **Figure 2E-H**).

**Figure 3A** is a representative TD map of the lower leg in axial orientation. The image shows that muscle tissue has constant TD values (red;  $\text{TD} \approx 1$  by normalization). Boundaries between muscles are characterized by pixels with considerably higher TD values (white;  $\text{TD} > 1.5$ ). **Figure 3B** is the mDixon water image of the same slice, in which tendons and fasciae are hypo-intense. The overlay of TD on the mDixon water image (**Figure 3C**) shows that high TD pixels spatially correspond to mDixon water

hypointense pixels. High TD pixels can thus generally be ascribed to tendons and fasciae, with the exception of artifacts or low SNR regions.

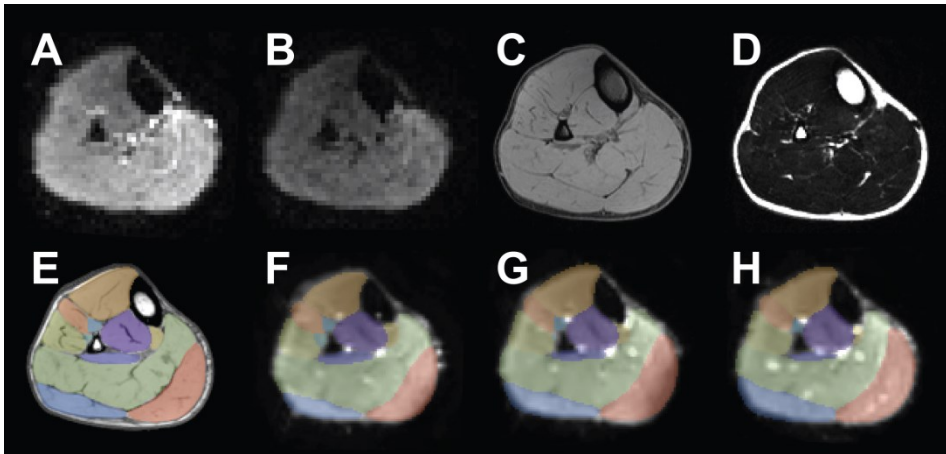


**Figure 2:** Transverse slice in a volunteer: raw MRI data and muscle segmentation. **A)** DT-MRI image obtained with  $b=0$  s/mm<sup>2</sup>; **B)** DT-MRI image obtained with  $b=400$  s/mm<sup>2</sup>; **C)** Water image from the mDixon scan; **D)** Fat image from the mDixon scan; **E)** Muscle segmentation overlaid to the out-of-phase mDixon image; **F, G, H)** Muscle segmentation obtained using the down-sampled out-of-phase mDixon images overlaid to the up-scaled diffusion data. **F)** 15° dorsiflexion; **G)** Neutral position; **H)** 30° plantarflexion.

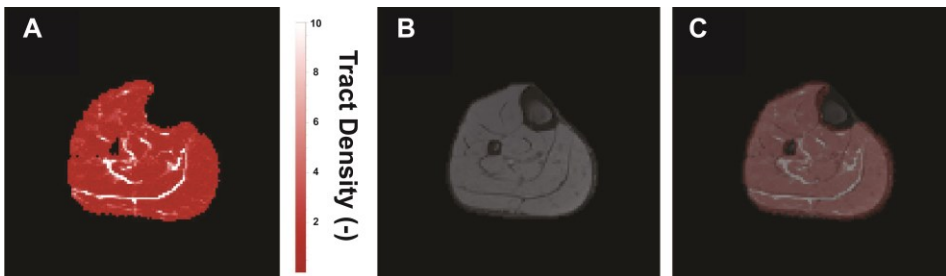


**Figure 3:** Tract density (TD) map and corresponding anatomical image. **A)** Axial tract density map of the lower leg of one subject in neutral position. High values of normalized tract density are represented in white and indicate tendons, while low values in red can be assigned to muscle tissue. **B)** Water image determined from the mDixon scan and **C)** the previous two images overlaid. There is good anatomical agreement for the tendons between the two images.

Comparisons of tractography methods with different stopping criteria, including TD, are shown in **Figure 4**. When comparing the conventional tractography methods, which are based on FA or using the muscle boundary as stopping criteria, it can be seen that non-Gaussian distributions of muscle fascicle lengths are obtained. When using FA as the sole stopping criteria, fascicles tend to extend into adjacent muscles and tendons (**Figure 4B**). As a consequence, the mean value of fascicle length is shifted towards artificially larger values (**Figure 4A**). When using muscle boundaries as a

cutoff, the reconstructed fascicle lengths near the muscle boundary terminate prematurely (**Figure 4F**), resulting in a skewed distribution towards short fascicle lengths (**Figure 4E**). Using the TD based method, both long and short fascicles are avoided (**Figure 4D**) and a normal distribution can be appreciated for all investigated muscles (**Figure 4C**).

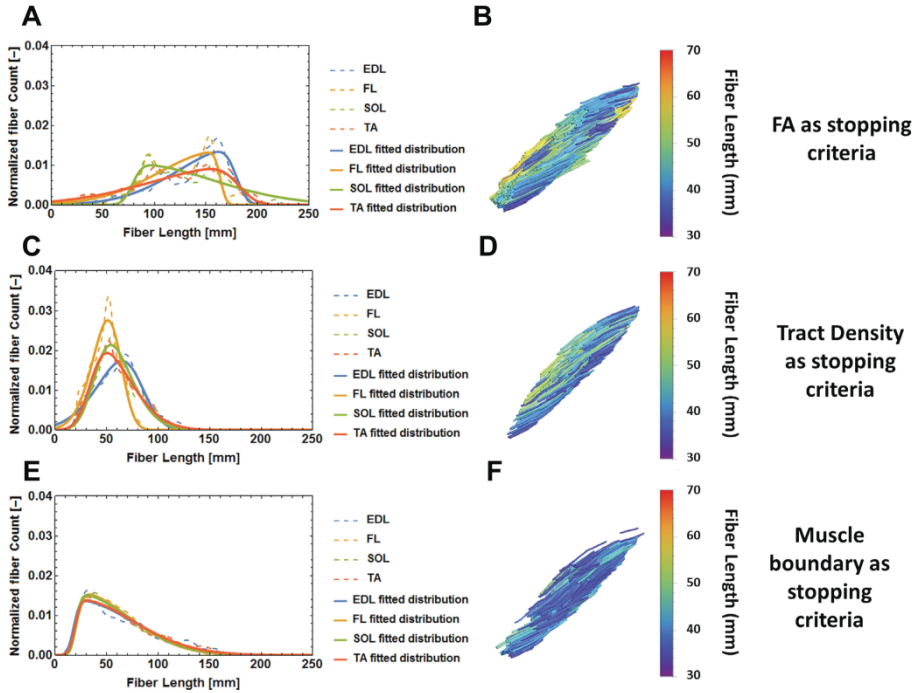


**Figure 4.** Comparison between tractography based on Tract Density, on FA and on muscle boundary. **A, C, E**) Histograms of fascicle length in 4 muscles (Extensor Digitorum Longus (EDL), Fibularis Longus (FL), Soleus (SOL) and Tibialis Anterior (TA)) in one volunteer with the foot in neutral position, using tracking stopping criteria based on FA, TD, and muscle segmentation volume respectively. The dotted lines represent the histogram of fascicle count, and the solid line indicates the fitted distribution. Values of fascicle count are normalized so that the total area under the curve is equal to 1. **B, D, F**) Tractography in the Tibialis Anterior colorcoded by fascicle length (in mm) in the same volunteer in neutral position.

Bland-Altman plots for fascicle length for SOL, FL, EDL, TA, and for all muscle together are shown in **Figure 5**. The graphs show that the differences between the two repeated measurements are distributed around a mean value of zero, indicating the absence of any systemic differences between sessions. Different limits of agreement were observed for different muscles, with the SOL showing overall the best reproducibility and TA showing the worst. The CVs were 8.3%, 16.7%, 11.2%, 10.43% in the neutral position, for the SOL, FL, EDL, and TA respectively (see **Table 1**). The CVs and MDDs per muscle and position are listed in **Table I**, showing a broad range for CVs (5.3 – 18.7%) with the repeatability being worst in dorsiflexion.

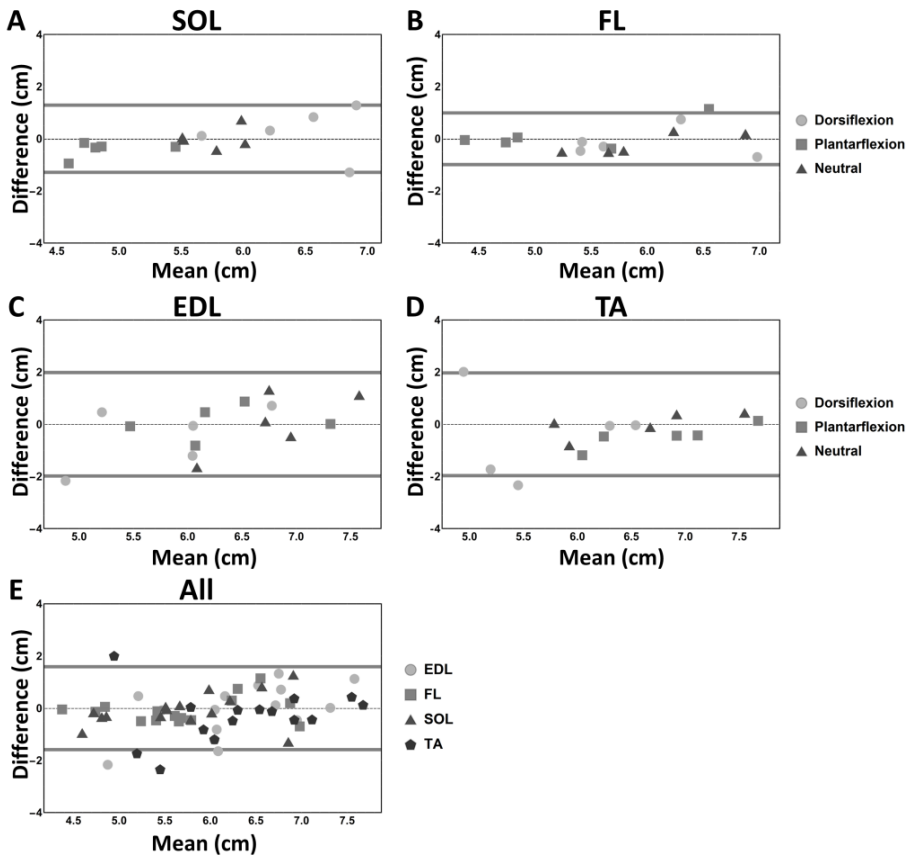


**Figure 5:** Bland-Altman of fascicle length measured in two different sessions. **A-D)** Bland-Altman plots for the Soleus (SOL), Fibularis Longus (FL), Extensor Digitorum Longus (EDL), and Tibialis Anterior (TA). **E)** Combined Bland-Altman plot for the four muscles. The dashed lines represent the mean difference, and the solid lines indicate 1.96 times the standard deviation.

**Figure 6** shows the fascicles of the SOL and TA color-coded for fascicle length in the three positions. In this figure, the fascicle length changes can be appreciated. Furthermore, none to very little artificially elongated or shortened fascicles are seen. The values of average fascicle lengths for SOL, FL, EDL, and TA and different positions are presented in **Table 1**. **Figure 7** shows the fascicle length as a function of ankle position for SOL, FL, EDL, and TA per subject; the black line indicates the mean calculated over the 10 measurement. Significant ( $P < 0.05$ ) change of the fascicle length was observed from dorsiflexion to neutral for SOL and EDL, from neutral to dorsiflexion for SOL, FL and EDL. From dorsiflexion to plantarflexion the change was significant for SOL, FL, EDL and TA (**Figure 7**).

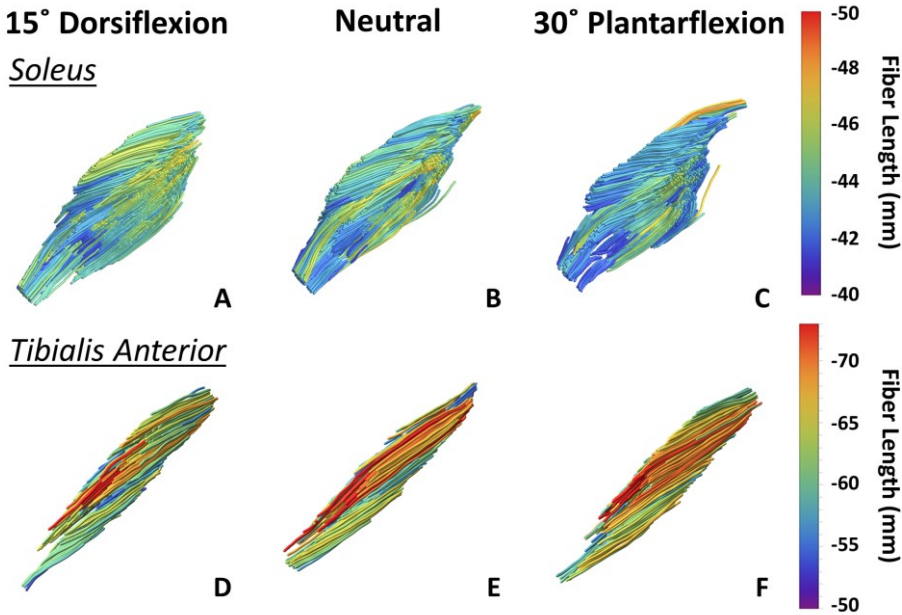


**Figure 6:** Fascicle tracts in Soleus and Tibialis Anterior muscle color-coded by fascicle length. Tractography in (A and D) dorsiflexion, (B and E) neutral, and (C and F) plantarflexion for the (A-C) Soleus and (D-F) for the Tibialis Anterior of one subject. No to very little artificially long and short fascicles were reconstructed. Differences in fascicle lengths are visible from the different color of the fascicles in the 3 positions.

		SOL	FL	EDL	TA
<b>Dorsiflexion</b>	<b>Mean±SD (cm)</b>	6.4±0.7	5.9±0.7	5.8±0.9	5.7±0.7
	<b>CV (%)</b>	10.6	10.5	16.3	18.7
	<b>MDD (cm)</b>	1.3	0.8	1.7	2.3
<b>Neutral</b>	<b>Mean±SD (cm)</b>	5.7±0.3	5.9±0.6	6.8±0.8	6.6±0.7
	<b>CV (%)</b>	8.3	16.7	11.2	10.4
	<b>MDD (cm)</b>	0.4	0.8	0.9	0.6
<b>Plantar flexion</b>	<b>Mean±SD (cm)</b>	4.9±0.4	5.2±0.9	6.3±0.7	6.8±0.6
	<b>CV (%)</b>	5.3	11.8	11.2	11.1
	<b>MDD (cm)</b>	0.6	0.6	1.7	0.7

**Table 1:** Mean values of fascicle length and intersession repeatability. Mean and standard deviation (SD) of the fascicle length, coefficient of variation (CV) and minimal detectable difference (MDD) per position indicated for 4 different muscles: Soleus (SOL), Fibularis Longus (FL), Extensor Digitorum Longus (EDL), and Tibialis Anterior (TA).

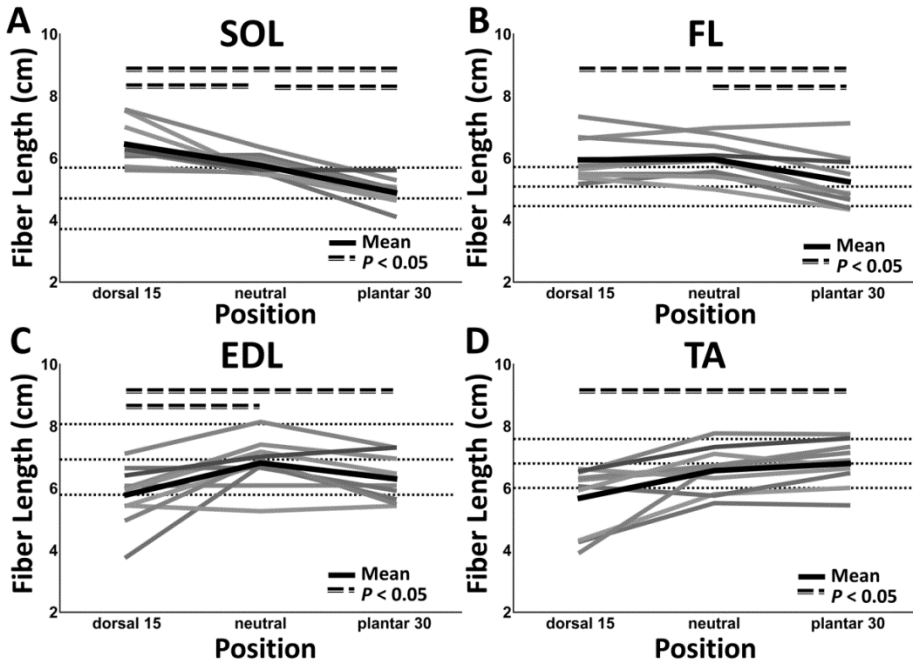


**Figure 7:** Mean muscle fascicle length in dorsiflexed, neutral, and plantarflexed foot position. Length (cm) plotted as a function of foot position for all separate scans for the Soleus (SOL), Fibularis Longus (FL), Extensor Digitorum Longus (EDL), and the Tibialis Anterior (TA). The mean value per muscle is indicated with the thick black line and the dotted lines indicate the mean and standard deviation found in literature (44). Furthermore, significance ( $p < 0.05$ ) is shown by the thick straight dotted lines above the data.

## Discussion

In this work, we introduced a novel method for automatic segmentation of tendinous structures directly from DT-MRI data, facilitating accurate and repeatable quantification of muscle fascicle lengths. The resulting fascicle lengths, obtained by excluding tendinous structures from tractography, are in agreement with previously reported muscle fascicle lengths in cadaveric specimens (44). Furthermore, fascicle length measurements showed good to moderate repeatability (CV of 5.3 – 18 %) and quantification of changes in fascicle length due to changes in ankle position proved possible.

The proposed method effectively avoids the reconstruction of artificially long and short fascicles, and the overall normalized counts of fascicle length within a muscle approached a Gaussian distribution, which is agreement with findings in cadaveric



material (36). The problem of artificially long fascicles along the aponeurosis and tendons, which bias the mean fascicle length towards higher values, was already addressed in a previous study by manual editing of fascicles (39). While manually editing results in correct fascicle lengths, it is a very time consuming process. Furthermore, it requires accurate tendon segmentation from high-resolution anatomical scans and/or careful visual inspection of all reconstructed fascicles. The strength of our method is that it facilitates automatic and user independent segmentation of tendons and estimations of muscle fascicle lengths.

The presented fascicle lengths are in agreement with literature (21, 24, 44). Ward et al. (44) reported fascicle length values for SOL, FL, EDL, and TA of cadaveric specimens in neutral position of  $4.7 \pm 1$  cm,  $5.1 \pm 0.6$  cm and  $7.0 \pm 1.1$  cm and  $6.8 \pm 0.8$  cm, respectively. We found average values of  $5.7 \pm 0.3$  cm,  $5.9 \pm 0.6$  cm,  $6.8 \pm 0.8$  cm and  $6.6 \pm 0.7$  cm, respectively, in neutral position. Our results are also in agreement with ultrasound values of TA fascicle length in neutral position, which range from 5.5 - 8 cm (2, 6, 22). However, most ultrasound studies have studied active contractions and small parts of the muscle only.

We found a wide range of reproducibility indices between muscles (see supplemental material) as well as between foot positions. In particular, an overall increased CV is observed for the dorsiflexed position, most likely caused by the fact that the position was not well tolerated by a few subjects resulting in some active involuntary muscle contraction. However, the repeatability of fascicle length measurements in our study is better compared to previous DT-MRI studies (4, 12) in which only the neutral position for a single muscle was measured.

The changes in fascicle length with respect to neutral foot position obtained in this study are in agreement with the known antagonistic function of muscles. In fact, the TA and the EDL, that play a role in dorsiflexing the foot, present a reduced fascicle length in the dorsiflexed foot position, when compared to the plantar flexed position, with the biggest change between dorsiflexion and the neutral position, being significant for the EDL. On the other hand, the SOL and the FL muscles, which are plantarflexor muscles, present the opposite behavior, with significant shorter fascicles in the plantarflexed position compared to the dorsiflexed position, with the biggest change between the plantarflexed and neutral position and which was significant for both SOL and FL.

With the new method we measure realistic fascicle lengths for all muscles (see supplemental material). For some muscles, specifically for GCM and GCL, fascicle

lengths changes from dorsi- to plantarflexion were small and not significant. We believe this is because for these muscles the change of length in the total muscle-tendon complex is partially attributed to stretch of the tendon during passive motion. As shown by Herbert et al. the contribution of tendon stretch in the total variation in length of the muscle-tendon complex is much larger for the GCM and GCL than for the TA (14). In individual cases, shortening of a muscle was observed where a lengthening was expected. We believe that this is in part due to tendon compliance, but most due to active contraction of these muscles in dorsiflexed position, which was perceived as uncomfortable by some of the volunteers.

Nevertheless, our study shows that the new method can be used to obtain reliable patient specific fascicle lengths, which ultimately might be used as geometrical input for biomechanical models (25, 29, 30, 38). More important, our study shows fascicle length measurements can be applied to monitor disease, therapy or training. As an example, previous studies reported that 90 days of bed rest caused a 10% decrease in fascicle length of the GCM and GCL (35), opposing to an 11% increase of the fascicle length of the Vastus Lateralis muscles (VL) of the upper leg in elderly people after training (34). Moreover, in competitive sprinting, fascicle length was found to be the main determinant of the performance (23). The reported changes of fascicle length observed in those studies were all in the range of the MDDs found in all of the muscles in our study, and therefore could also be determined using our new method.

Our method also opens the possibility to do longitudinal studies of the response in fascicle lengths to therapies or diseases. Furthermore, the automated tendon segmentation fascicle tractography could be extended with quantifications of pennation angles and muscle volumes. This should be possible in an automated fashion as we identified the voxels belonging to tendinous structures as well as the voxels which consist purely of muscle tissue.

## Limitations

This study has a few limitations. First of all, the number of subjects was limited to 5. However, for proof-of-concept and assessing repeatability of fascicle length quantification in various muscles in the lower leg, this proved sufficient. A second limitation was that the 15° dorsiflexion position was not always well tolerated and may have caused compensatory muscle contractions in some of the subjects. In general, complete passive stretch might be hard to achieve. Although our fascicle length estimates were in good agreement with cadaveric and ultrasound studies, we did not validate *in vivo* fascicle length measurement directly on the same muscles. This could

be done in animal studies, where after *in vivo* measurements the muscle could be dissected for *ex vivo* validation.

Another potential limitation is the positioning of the subject with the calf resting on the coil, rather than being suspended. While this set-up is favorable for maximizing SNR in the posterior compartment, it also leads to deformation and compression of the gastrocnemius muscles. If interested in these muscles, a set-up with the calf suspended would be preferable (7, 28).

## Conclusions

In conclusion, we presented a novel *in vivo* approach for skeletal muscle fascicle length measurement using DT-MRI. This method showed good to moderate repeatability and enabled quantification of changes in muscle fascicle lengths with passive stretch of lower leg muscles. Ultimately, validation of fascicle length estimations could be obtained by comparing post mortem DT-MRI with anatomical dissection.

## References

1. **Albracht K, Arampatzis A, Baltzopoulos V.** Assessment of muscle volume and physiological cross-sectional area of the human triceps surae muscle in vivo. *J Biomech* 41: 2211–2218, 2008.
2. **de Boer MD, Seynnes OR, di Prampero PE, Pišot R, Mekjavić IB, Biolo G, Narici M V.** Effect of 5 weeks horizontal bed rest on human muscle thickness and architecture of weight bearing and non-weight bearing muscles. *Eur J Appl Physiol* 104: 401–407, 2008.
3. **Böl M, Sturmat M, Weichert C, Kober C.** A new approach for the validation of skeletal muscle modelling using MRI data. *Comput Mech* 47: 591–601, 2011.
4. **Bolsterlee B, Veeger HEJ, Van Der Helm FCT, Gandevia SC, Herbert RD.** Comparison of measurements of medial gastrocnemius architectural parameters from ultrasound and diffusion tensor images. *J Biomech* 48: 1133–1140, 2015.
5. **Budzik J-F, Balbi V, Verclytte S, Pansini V, Le Thuc V, Cotten A.** Diffusion tensor imaging in musculoskeletal disorders. *Radiographics* 34: E56–72, 2014.
6. **Chleboun GS, Busic AB, Graham KK, Stuckey H a.** Fascicle length change of the human tibialis anterior and vastus lateralis during walking. *J Orthop Sports Phys Ther* 37: 372–379, 2007.
7. **Elzibak AH, Noseworthy MD.** Assessment of diffusion tensor imaging indices in calf muscles following postural change from standing to supine position. *MAGMA* ( December 2013). doi: 10.1007/s10334-013-0424-1.
8. **Froeling M, Nederveen AJ, Heijtel DFR, Lataster A, Bos C, Nicolay K, Maas M, Drost MR, Strijkers GJ.** Diffusion-tensor MRI reveals the complex muscle architecture of the human forearm. *J Magn Reson Imaging* 36: 237–248, 2012.
9. **Froeling M, Oudeman J, van den berg S, Vilanova A, Nicolay K, Maas M, Strijkers GJ, Nederveen AJ, Drost MR.** Muscle fiber tracking and segmentation in the human forearm. In: *Proc. Intl. Soc. Mag. Reson. Med. 17 (2009)*. 2009, p. 1929.
10. **Gilbert RJ, Napadow VJ.** Three-dimensional muscular architecture of the human tongue determined in vivo with diffusion tensor magnetic resonance imaging. *Dysphagia* 20: 1–7, 2005.
11. **Heemskerk AM, Sinha TK, Wilson KJ, Ding Z, Damon BM.** Quantitative assessment of DTI-based muscle fiber tracking and optimal tracking parameters. *Magn Reson Med* 61: 467–72, 2009.
12. **Heemskerk AM, Sinha TK, Wilson KJ, Ding Z, Damon BM.** Repeatability of DTI-based skeletal muscle fiber tracking. *NMR Biomed* 23: 294–303, 2010.
13. **Heemskerk AM, Strijkers GJ, Vilanova A, Drost MR, Nicolay K.** Determination of mouse skeletal muscle architecture using three-dimensional diffusion tensor imaging. *Magn Reson Med* 53: 1333–1340, 2005.
14. **Herbert RD, Moseley AM, Butler JE, Gandevia SC.** Change in length of relaxed muscle fascicles and tendons with knee and ankle movement in humans. *J Physiol* 539: 637–645, 2002.
15. **Hooijmans MT, Damon BM, Froeling M, Versluis MJ, Burakiewicz J,**

- Verschuuren JJGM, Niks EH, Webb AG, Kan HE.** Evaluation of skeletal muscle DTI in patients with duchenne muscular dystrophy. *NMR Biomed* 28: 1589–1597, 2015.
16. **Irfanoglu MO, Walker L, Sammet S, Pierpaoli C, Machiraju R.** Susceptibility distortion correction for echo planar images with non-uniform B-spline grid sampling: a diffusion tensor image study. *Med Image Comput Comput Assist Interv* 14: 174–81, 2011.
17. **Irfanoglu MO, Walker L, Sarlls J, Marengo S, Pierpaoli C.** Effects of image distortions originating from susceptibility variations and concomitant fields on diffusion MRI tractography results. *Neuroimage* 61: 275–288, 2012.
18. **Kermarrec E, Budzik J-F, Khalil C, Le Thuc V, Hancart-Destee C, Cotten A.** In vivo diffusion tensor imaging and tractography of human thigh muscles in healthy subjects. *AJR Am J Roentgenol* 195: W352-6, 2010.
19. **Khalil C, Budzik JF, Kermarrec E, Balbi V, Le Thuc V, Cotten A.** Tractography of peripheral nerves and skeletal muscles. *Eur J Radiol* 76: 391–397, 2010.
20. **Klein S, Staring M, Murphy K, Viergever MA, Pluim JPW.** Elastix: A toolbox for intensity-based medical image registration. *IEEE Trans Med Imaging* 29: 196–205, 2010.
21. **Klein Horsman MD, Koopman HFJM, van der Helm FCT, Prosé LP, Veeger HEJ.** Morphological muscle and joint parameters for musculoskeletal modelling of the lower extremity. *Clin Biomech* 22: 239–247, 2007.
22. **Klimstra M, Dowling J, Durkin JL, MacDonald M.** The effect of ultrasound probe orientation on muscle architecture measurement. *J Electromyogr Kinesiol* 17: 504–514, 2007.
23. **Kumagai K, Abe T, Brechue WF, Ryushi T, Takano S, Mizuno M.** Sprint performance is related to muscle fascicle length in male 100-m sprinters. *J Appl Physiol* 88: 811–816, 2000.
24. **Kwah LK, Pinto RZ, Diong J, Herbert RD.** Reliability and validity of ultrasound measurements of muscle fascicle length and pennation in humans: a systematic review. *J Appl Physiol* 114: 761–769, 2013.
25. **Lee D, Li Z, Sohail QZ, Jackson K, Fiume E, Agur A.** A three-dimensional approach to pennation angle estimation for human skeletal muscle. *Comput Methods Biomech Biomed Engin* 18: 1474–1484, 2015.
26. **Leemans A, Jones DK.** The B-matrix must be rotated when correcting for subject motion in DTI data. *Magn Reson Med* 61: 1336–1349, 2009.
27. **Li K, Dortch RD, Welch EB, Bryant ND, Buck AKW, Towse TF, Gochberg DF, Does MD, Damon BM, Park JH.** Multi-parametric MRI characterization of healthy human thigh muscles at 3.0 T - relaxation, magnetization transfer, fat/water, and diffusion tensor imaging. *NMR Biomed* 27: 1070–1084, 2014.
28. **Lorbergs AL, Noseworthy MD, MacIntyre NJ.** Age-related differences in the response of leg muscle cross-sectional area and water diffusivity measures to a period of supine rest. *Magn Reson Mater Physics, Biol Med* 28: 279–290, 2015.
29. **Mijailovich SM, Stojanovic B, Kojic M, Liang A, Wedeen VJ, Gilbert RJ.** Derivation of a finite-element model of lingual deformation during swallowing from the mechanics of mesoscale myofiber tracts obtained by MRI. *J Appl Physiol* 109: 1500–14, 2010.

30. **Napadow VJ, Kamm RD, Gilbert RJ.** A biomechanical model of sagittal tongue bending. *J Biomech Eng* 124: 547–56, 2002.
31. **Narici M V, Maganaris CN, Reeves ND, Capodaglio P.** Effect of aging on human muscle architecture. *J Appl Physiol* 95: 2229–34, 2003.
32. **Okamoto Y, Okamoto T, Yuka K, Hirano Y, Isobe T, Minami M.** Correlation between pennation angle and image quality of skeletal muscle fibre tractography using deterministic diffusion tensor imaging. *J Med Imaging Radiat Oncol* 56: 622–627, 2012.
33. **Oudeman J, Nederveen AJ, Strijkers GJ, Maas M, Luijten PR, Froeling M.** Techniques and applications of skeletal muscle diffusion tensor imaging: A review. *J Magn Reson Imaging* 43: 773–788, 2016.
34. **Reeves ND.** Effect of resistance training on skeletal muscle-specific force in elderly humans. *J Appl Physiol* 96: 885–892, 2003.
35. **Reeves NJ, Maganaris CN, Ferretti G, Narici M V.** Influence of simulated microgravity on human skeletal muscle architecture and function. *J Gravit Physiol* 9: P153-4, 2002.
36. **Schenk P, Siebert T, Hiepe P, Güllmar D, Reichenbach JR, Wick C, Blickhan R, Böhl M.** Determination of three-dimensional muscle architectures: Validation of the DTI-based fiber tractography method by manual digitization. *J Anat* 223: 61–68, 2013.
37. **Sieben JM, van Otten I, Lataster A, Froeling M, Nederveen AJ, Strijkers GJ, Drost MR.** In Vivo Reconstruction of Lumbar Erector Spinae Architecture Using Diffusion Tensor MRI. *J Spinal Disord Tech* 2013: 1, 2013.
38. **Siebert T, Leichsenring K, Rode C, Wick C, Stutzig N, Schubert H, Blickhan R, Böhl M.** Three-dimensional muscle architecture and comprehensive dynamic properties of rabbit gastrocnemius, plantaris and soleus: Input for simulation studies. *PLoS One* 10, 2015.
39. **Sinha U, Csapo R, Malis V, Xue Y, Sinha S.** Age-related differences in diffusion tensor indices and fiber architecture in the medial and lateral gastrocnemius. *J Magn Reson Imaging* 41: 941–953, 2015.
40. **Sinha U, Malis V, Csapo R, Moghadasi A, Kinugasa R, Sinha S.** Age-related differences in strain rate tensor of the medial gastrocnemius muscle during passive plantarflexion and active isometric contraction using velocity encoded MR imaging: Potential index of lateral force transmission. *Magn Reson Med* 73: 1852–1863, 2015.
41. **Sinha U, Sinha S, Hodgson JA, Edgerton R V.** Human soleus muscle architecture at different ankle joint angles from magnetic resonance diffusion tensor imaging. *J Appl Physiol* 110: 807–19, 2011.
42. **Sinha U, Yao L.** In vivo diffusion tensor imaging of human calf muscle. *J Magn Reson Imaging* 15: 87–95, 2002.
43. **Smeulders MJC, Van Den Berg S, Oudeman J, Nederveen AJ, Kreulen M, Maas M.** Reliability of in vivo determination of forearm muscle volume using 3.0 T magnetic resonance imaging. *J Magn Reson Imaging* 31: 1252–1255, 2010.
44. **Ward SR, Eng CM, Smallwood LH, Lieber RL.** Are current measurements of lower extremity muscle architecture accurate? *Clin Orthop Relat Res* 467: 1074–1082, 2009.

45. **Wu M, Chang LC, Walker L, Lemaitre H, Barnett AS, Marengo S, Pierpaoli C.** Comparison of EPI distortion correction methods in diffusion tensor MRI using a novel framework. *Med Image Comput Comput Assist Interv* 11: 321–9, 2008.
46. **Zijta FM, Lakeman MME, Froeling M, Van Der Paardt MP, Borstlap CS V, Bipat S, Montauban van Swijndregt a D, Strijkers GJ, Roovers JP, Nederveen AJ, Stoker J, van Swijndregt AD.** Evaluation of the female pelvic floor in pelvic organ prolapse using 3.0-Tesla diffusion tensor imaging and fibre tractography. *Eur Radiol* 22: 2806–13, 2012.

# Chapter

# 4

## Assessment of passive muscle elongation using Diffusion Tensor MRI: Correlation between fiber length and diffusion coefficients

Valentina Mazzoli\*

Jos Oudeman\*

Klaas Nicolay

Mario Maas

Nico Verdonschot

Andre M. Sprengers

Aart J. Nederveen

Martijn Froeling

Gustav J. Strijkers

\* These authors contributed equally

**NMR Biomed. 2016 Dec;29(12):1813-1824.**

**doi: 10.1002/nbm.3661**



## Abstract

**Introduction:** In this study we investigated the changes in fiber length and diffusion parameters as a consequence of passive lengthening and stretching of the calf muscles. We hypothesized that changes in Radial Diffusivity (RD) are caused by changes in the muscle fiber cross sectional area (CSA) as a consequence of lengthening and shortening of the muscle.

**Methods:** Diffusion tensor MRI (DT-MRI) measurements were performed twice in 5 healthy volunteers, with the foot in three different positions (30° plantarflexion, neutral position and 15° dorsiflexion). The muscles of the calf were manually segmented on co-registered high resolution anatomical scans, and maps of radial (RD) and axial diffusivities (AD) were reconstructed from the DT-MRI data. Fiber tractography was performed and mean fiber length was calculated for each muscle group.

**Results:** Significant negative correlations were found between the changes in RD and changes in fiber length in the dorsiflexed and plantarflexed positions, compared to the neutral foot position. Changes in AD did not correlate with changes in fiber length. Assuming a simple cylindrical model with constant volume for the muscle fiber, the changes in the muscle fiber CSA was calculated from the changes in fiber length. In line with our hypothesis, we observed a significant positive correlation of the CSA with the measured changes in radial diffusivity.

**Conclusions:** In conclusion, we showed that changes in diffusion coefficients induced by passive muscle stretching and lengthening can be explained by changes in muscle CSA, advancing the physiological interpretation of parameters derived from skeletal muscle DT-MRI.

## Introduction

DT-MRI (Diffusion Tensor MRI) is a MRI-based technique which allows measuring the diffusion anisotropy of water molecules in biological tissues. DT-MRI can non-invasively provide *in vivo* information on tissue architecture, either normal or in a diseased state. Using DT-MRI, the muscle fiber orientation can be quantified in each imaging voxel and used in combination with fiber tractography to reconstruct whole-muscle fiber architecture in 3D. In short, diffusion along multiple directions is probed with diffusion encoding gradients. The signal attenuation as a result of diffusion encoding can be geometrically described by a rank-2 tensor. When the tensor is diagonalized, its diagonal terms ( $\lambda_1, \lambda_2, \lambda_3$ , where  $\lambda_1 \geq \lambda_2 \geq \lambda_3$ ) represent the diffusion coefficients along the principal directions of diffusion. Diffusion in skeletal muscles is shown to be highest along the axis of the fibers (Axial Diffusivity (AD) or  $\lambda_1$ ) and lowest perpendicular to the axis of the fibers ( $\lambda_2, \lambda_3$  and Radial diffusivity (RD) =  $(\lambda_2 + \lambda_3)/2$ ).

Since the first measurements and applications of skeletal muscle DT-MRI, a number of papers have addressed the physiological interpretation of the diffusion tensor eigenvalues and eigenvectors. Although DT-MRI in skeletal muscles has found to be feasible and reproducible, the physiological correlation between muscle tissue properties and the derived parameters remain unclear (23). Generally it is agreed upon that diffusion perpendicular to the muscle fiber axis is lower since diffusion in this direction is hindered by cell membranes and intra- and extracellular tissue constituents. Simulation studies have shown that  $\lambda_2$  and  $\lambda_3$  in skeletal muscles are extremely sensitive to the SNR of the measurements and may be affected by sorting bias if the SNR is below a threshold value (2, 5). However previous studies performed at SNR > 100 (10) have shown that the difference in the secondary and third eigenvalues in skeletal muscles are maintained even at very high SNR, suggesting that the difference has a physiological origin rather than a methodological origin. This was also confirmed by studies demonstrating that the second and third eigenvectors can be tracked independently and consistently (13). Galban et al. (7) hypothesized that  $\lambda_2$  relates to the cross sectional area (CSA) of the endomysium, while  $\lambda_3$  correlates with CSA of the single fiber unit. This hypothesis has partly been confirmed by histological studies (11, 19). Furthermore, the relation of  $\lambda_2$  and  $\lambda_3$  with CSA is thought to be the basis for the sensitivity of DT-MRI to histo-pathological changes, but also to transient changes such as the relative stretch of the muscle fibers. It is known that passive stretch causes a decrease in diffusion in the muscle fiber (25) and several studies showed a dependency of the RD with stretch. Scheel et al. (18) measured maximal mechanical power in the soleus muscles during isokinetic plantarflexion and observed a positive correlation between RD and maximum muscle power, which was partially

explained with an increased ratio of type 2 fibers, which have a bigger diameter when compared to type 1 fibers. This would suggest that also *in vivo* the RD may (partially) reflect muscle fiber radius. Schwenger et al. (21) measured the lower leg of healthy volunteers with their foot in 40° plantarflexion, neutral position and 10° dorsiflexion. They observed a significant increase in  $\lambda_2$  and  $\lambda_3$  in the soleus and gastrocnemius muscles during plantarflexion, and a significant increase in the same parameters in the tibialis anterior (TA) muscle in the dorsiflexed position. Similar findings were reported by Sinha et al. (25). The observed increased RD in the shortened muscle groups was empirically explained with an increased CSA of the muscle fibers, while the decrease observed in the RD in the non-shortened muscle state would be explained with a decrease in CSA as a consequence of fiber lengthening. Although this effect was hypothesized by several authors, no further evidence has been provided.

To further explore the physiological framework presented by Schwenger et al. we utilize a recently described method for extracting fiber lengths from DT-MRI data (17). The aim of this work is to measure changes in fiber lengths for different foot positions using DT-MRI and correlate these with changes in diffusion parameters in the lower leg. We hypothesized that diffusion in the radial direction of the fibers would decrease with increasing fiber length, since it reflects a decrease in cell diameter or CSA. Furthermore, we interpret the changes in diffusivity using a cylindrical model of muscle fibers with constant volume, where the changes in radius caused by fiber stretching/lengthening can be inferred from the changes in RD.

## Methods

### Study population

Five healthy male subjects were included in the study. The subjects had a mean age of 27 years (range 24-29 years), a mean weight of 78 kg (range 62-89 kg) and a mean length of 181 cm (range 171-189 cm). None of the subject had any history of muscle diseases or injury. The study was approved by our local IRB and all subjects provided informed consent prior to the study.

### MRI protocol

All MRI scans were performed on a 3T Achieva MRI scanner (Philips) using a cardiac coil, composed of 3 posterior and 3 anterior elements. A custom device was used to immobilize the foot in 3 positions: 15° dorsiflexion, neutral (0°) position, and 30° plantarflexion (see **Figure 1**). MRI measurements of the calf were performed twice for

each position. Both measurement sessions were carried out on the same day, with at least 30 minutes in between the different sessions. The MRI protocol included an mDixon scan for anatomical reference and a DT-MRI protocol. For the 3-point mDixon scan the following parameters were used: sequence = FFE, FOV = 192x156 mm<sup>2</sup>, TR = 7.7 ms, TE1/ $\Delta$ TE = 2.1/1.7 ms, matrix size = 192x192, number of slices = 100, voxel size = 1x1x2.5 mm<sup>3</sup>. For the DT-MRI scan the scan parameters were: sequence = SE-EPI, FOV = 192x156 mm<sup>2</sup>; TR = 11191 ms, TE = 51.63 ms, matrix size = 64x52, number of slices = 50, voxel size = 3x3x5 mm<sup>3</sup>, Parallel imaging acceleration factor = 1.5, 12 gradient directions, diffusion b-value = 400 s/mm<sup>2</sup>; fat-suppression = spectrally adiabatic inversion recovery (SPAIR) and slice-selection gradient reversal (SSGR) for suppression on the aliphatic fat peak and spectrally selective suppression (SPIR) of the olefinic fat peak. The scan time was 8.5 minutes for DT-MRI, 1.5 minutes for mDixon and 1 minute for the noise scan. In addition to the DT-MRI scan and the Dixon scan, a noise scan was performed by repeating the DT-MRI scan with a single volume and setting the power of the RF to zero. The DT-MRI scan, the mDixon scan, and the noise scan were acquired with exactly the same FOV and orientation. The total scan time for each position (mDixon, DT-MRI and noise scan) was 11 minutes, resulting in a total scan time of 33 minutes per session.

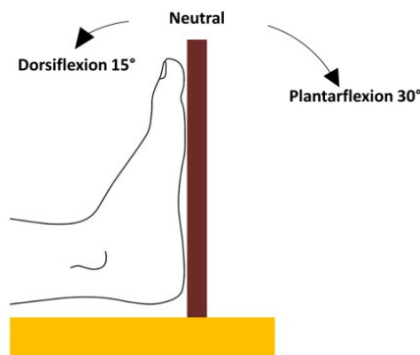


**Figure 1:** Schematic representation of the experimental setup. The right lower leg of the volunteers was scanned twice with the foot fixed in neutral, dorsiflexed, and plantar position.

## Data analysis

The DT-MRI data was analyzed using DTITools for Mathematica 10.3 (4). First, to assess data quality, SNR maps were calculated. SNR was defined as the ratio of the mean signal in the DT-MRI images acquired with  $b=0$  s/mm<sup>2</sup> and the standard deviation of noise corrected for the Rician distribution, calculated from the noise scan.

Prior to tensor fitting, the data was preprocessed using a Rician noise suppression algorithm and registered to the corresponding anatomical scan.

The registration pipeline consisted of three separate steps: first, all diffusion scans were registered to the corresponding non-weighted image using affine registration, in order to correct for eddy currents-induced deformations and motion. As a second step, we rescaled the mDixon data to a voxel size of  $1.5 \times 1.5 \times 3 \text{ mm}^3$ . Finally, we performed b-spline registration of all DT-MRI data to the water image obtained from the mDixon scan. This last step was performed in order to correct for deformations arising from the single-shot EPI acquisition. All registration steps have been performed using Elastix (16). For the b-spline registration we used the b-spline algorithm of Elastix with the metric `AdvancedMattesMutualInformation` and a b-spline interpolation order of 3. As an optimizer we have used an `AdaptiveStochasticGradientDescent` method. For more information, we would like to refer to the Elastix manual.

After image registration, the DT-MRI data was fitted to a tensor model using a Weighed Linear Least Square (WLLS) algorithm, from which  $\lambda_2$ ,  $\lambda_3$ , AD and RD were determined. These parameters were calculated for each muscle group individually, and indicated as mean over the full muscle volume. Subsequently, muscle fiber tractography was performed using the `vIST/e` toolbox.

All the muscle groups in the calf (*Extensor Digitorum Longus* (EDL), *Extensor Hallucis Longus* (EHL), *Flexor Digitorum Longus* (FDL), *Flexor Hallucis Longus* (FHL), *Gastrocnemius Medialis* (GCM), *Gastrocnemius Lateralis* (GCL), *Soleus* (SOL), *Tibialis Anterior* (TA), *Tibialis Posterior* (TP), *Fibularis Brevis* (FB) and *Fibularis Longus* (FL)) were manually segmented on the out-of-phase mDixon images using ITK-SNAP. Slice-wise segmentation of the entire muscle was performed for the dataset scanned with the foot in neutral position. First, the mDixon out-of-phase images were down-sampled to a resolution of  $1 \times 1 \times 10 \text{ mm}^3$ . Delineation of the muscles was done in the resulting 25 slices. The segmentations were then transformed to all six datasets (3 positions, 2 measurements) by registering the down-sampled mDixon images to full resolution out-of-phase mDixon images using rigid registration followed by non-linear b-spline registration.

Fiber length was calculated after automatic tendon segmentation, using a method previously described (17). In short, the method relies on the notion that due to partial volume effects, reconstructed fiber tracts are observed to continue along tendons, rather than stopping at the tendon insertion. This leads to an increased number of reconstructed tracts in voxels containing tendons, when compared to voxels

containing muscle fibers only. Consequently, the tract density (TD) allows segmentation of the non-muscle voxels and provides a stopping criterion for tractography. Fiber tractography was performed on the full leg volume in order to obtain tract density maps. Seed points were equally spaced within the leg volume, with a distance of 1 mm. Fiber tractography was performed in two steps. The first step consisted of whole-volume tractography to determine the tract density maps. For this initial step, the maximum allowed angle change per step was 20° and the minimum fiber length was set to 2 cm. Tract density was defined as the number of reconstructed tracts crossing each voxel, normalized to TD=1 for muscle tissue. Subsequently, tractography was performed a second time using TD>1.5 as the primary stopping criterion, with maximum angle step size 100, and minimum fiber length 2 cm. Seed points were placed equally spaced in the muscle belly. This second tractography step resulted in fibers that run the full distance from origin to insertion. For each muscle, a single value of fiber length was derived by performing a skewed Gaussian fit of the fiber length distribution of all tracts reconstructed in that muscle.

## Correlations between fiber length and diffusion parameters

Relative changes in fiber length were calculated for the dorsiflexed and plantarflexed position with respect to the neutral foot position according to:

$$\Delta l_{\text{dorsiflexion}} = l_{\text{dorsiflexion}} - l_{\text{neutral}}$$

$$\Delta l_{\text{plantarflexion}} = l_{\text{plantarflexio}} - l_{\text{neutral}}$$

where  $l$  represents the mean value of fiber length for a given muscle group.

RD was calculated as the average of  $\lambda_2$  and  $\lambda_3$ . The relative change in diffusion parameters from dorsiflexion and plantarflexion was calculated in the same way as for changes in fiber length:

$$\Delta X_{\text{dorsiflexion}} = X_{\text{dorsiflexion}} - X_{\text{neutral}}$$

$$\Delta X_{\text{plantarflexion}} = X_{\text{plantarflexio}} - X_{\text{neutral}}$$

where  $X$  represents RD or AD.

Pearson's correlation was used to determine the relation between changes in fiber length and changes in RD and AD respectively for each individual muscle. Post-hoc Bonferroni correction was used to correct for multiple comparisons. An adjusted  $p$ -value  $p < 0.05$  was considered statistically significant.

## Cylindrical model

Next, muscle fibers were modeled as cylinders with constant volume, hence a Poisson ratio of 0.5 was assumed (see **Figure 2**). In order to test this model, the relative changes in fiber length in the dorsiflexed and plantarflexed foot positions were calculated as:

$$\% \Delta l_{dorsiflexion} = \frac{l_{dorsiflexion} - l_{neutral}}{l_{neutral}} * 100$$

$$\% \Delta l_{plantarflexion} = \frac{l_{plantarflexion} - l_{neutral}}{l_{neutral}} * 100$$

The calculated percentage changes in fiber length were subsequently used to calculate the expected percentage change in  $r^2$  (square of the radius) assuming the muscles to be described by a cylinder with constant volume ( $V = \pi r^2 l = \text{constant}$ ).

According to Einstein's equation of diffusion:

$$\langle r^2 \rangle = 2Dt$$

where  $D$  is the diffusion coefficient,  $t$  the experimental diffusion time and  $\langle r^2 \rangle$  is the mean squared displacement of the water molecules. Although Einstein's equation is only strictly valid in the condition of free diffusion, we can assume that the lower diffusion coefficient measured experimentally in muscle tissue when compared to free diffusion of water in water would reflect the presence of membranes or barriers that hinder water displacement. Under this assumption, the mean squared displacement in the direction perpendicular to the axis of the fiber can be considered as a surrogate measure of the fiber radius. If the cylindrical model is suitable for describing muscle fibers, the calculated percentage changes in  $r^2$  are then expected to be linearly related to the changes in diffusion in the radial direction (% $\Delta RD$ ). This correlation was tested with Pearson's regression in each muscle individually. Post-hoc Bonferroni correction was used to correct for multiple comparisons. An adjusted p-value  $p < 0.05$  was considered statistically significant.

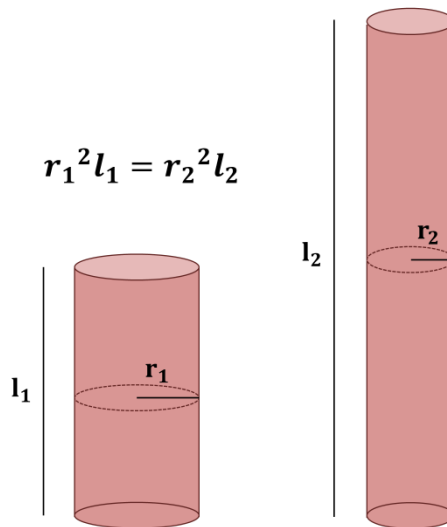


**Figure 2:** Schematic drawing of a muscle fiber. In the hypothesis that muscle fibers can be described as cylinders with constant volume, an increase in fiber length as a consequence of passive stretch would result in a decrease in radius ( $r$ ) and cross sectional area (CSA).

## Results

All DT-MRI scans were successfully completed, and visual inspection did not show the presence of artifacts in the raw DT-MRI data preventing data processing and analysis. All datasets were of sufficient quality to allow accurate tensor calculation.

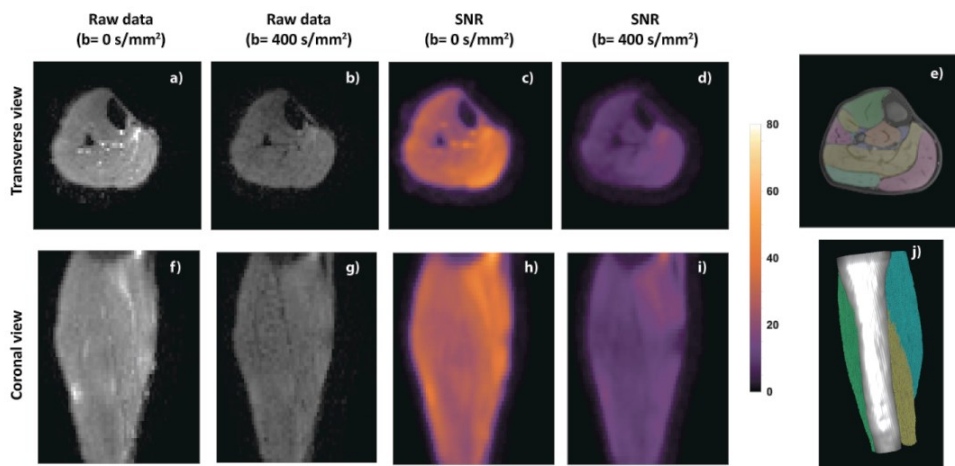
For all scans, average SNR of the non-weighted images was at least 30 (range 30-70). For all muscles in all subjects, automatic tendon segmentation based on TD threshold was successful. A typical transverse DT-MRI image of the lower leg with and without diffusion encoding is shown in **Figure 3**, together with muscle segmentation in the same slice, a typical SNR map, as well as fiber tractography of the Soleus, Tibialis Anterior and Gastrocnemius Lateralis. The coronal reconstruction (**Figure 3 h** and **i**) shows that the SNR was constant along the entire lower leg muscle volume.

Image registration could be successfully performed for all datasets. Typical registration results are presented in **Figure 4**. Almost perfect alignment between the anatomical mDixon scan and the DT-MRI dataset was observed after image registration, and little to none EPI distortion were present in the final images.



		EDL	EHL	FB	FDL	FHL	FL	GCL	GCM	SOL	TA	TP
<b>Dorsi flexion</b>	Fiber Length	5.78 (0.55)	5.70 (1.45)	5.35 (0.63)	5.48 (0.62)	5.87 (0.34)	5.81 (0.42)	6.62 (1.0)	6.13 (0.34)	6.31 (0.63)	6.00 (1.19)	4.58 (0.58)
	$\lambda_1$	2.61 (0.32)	2.60 (0.27)	2.34 (0.15)	2.38 (0.18)	2.21 (0.08)	2.52 (0.22)	2.55 (0.21)	2.55 (0.12)	2.29 (0.10)	2.64 (0.36)	2.33 (0.07)
	$\lambda_2$	1.67 (0.12)	1.83 (0.20)	1.54 (0.04)	1.60 (0.08)	1.56 (0.03)	1.54 (0.06)	1.48 (0.04)	1.51 (0.05)	1.55 (0.04)	1.75 (0.17)	1.61 (0.06)
	$\lambda_3$	1.42 (0.08)	1.59 (0.17)	1.37 (0.04)	1.38 (0.06)	1.35 (0.03)	1.34 (0.06)	1.28 (0.03)	1.29 (0.05)	1.38 (0.03)	1.49 (0.13)	1.39 (0.04)
	RD	1.54 (0.10)	1.71 (0.18)	1.45 (0.04)	1.49 (0.07)	1.46 (0.04)	1.44 (0.05)	1.38 (0.03)	1.40 (0.05)	1.46 (0.03)	1.62 (0.14)	1.50 (0.05)
	FA	0.31 (0.05)	0.26 (0.04)	0.28 (0.03)	0.28 (0.03)	0.26 (0.02)	0.33 (0.04)	0.36 (0.04)	0.35 (0.03)	0.27 (0.02)	0.29 (0.06)	0.28 (0.02)
	<b>Neutral</b>	Fiber Length	6.54 (0.48)	7.32 (1.31)	5.66 (0.67)	6.33 (1.17)	5.84 (0.37)	5.80 (0.45)	6.72 (1.06)	6.61 (0.08)	5.71 (0.25)	6.65 (0.67)
$\lambda_1$		2.59 (0.24)	2.66 (0.24)	2.39 (0.10)	2.50 (0.18)	2.36 (0.09)	2.49 (0.12)	2.48 (0.15)	2.65 (0.17)	2.32 (0.05)	2.64 (0.27)	2.40 (0.06)
$\lambda_2$		1.62 (0.09)	1.78 (0.19)	1.56 (0.05)	1.64 (0.08)	1.64 (0.05)	1.55 (0.08)	1.52 (0.09)	1.57 (0.05)	1.60 (0.04)	1.66 (0.07)	1.65 (0.05)
$\lambda_3$		1.42 (0.07)	1.56 (0.14)	1.40 (0.04)	1.41 (0.06)	1.41 (0.05)	1.37 (0.08)	1.31 (0.05)	1.32 (0.06)	1.42 (0.04)	1.44 (0.07)	1.43 (0.05)
RD		1.52 (0.07)	1.67 (0.16)	1.48 (0.04)	1.53 (0.07)	1.53 (0.05)	1.46 (0.08)	1.41 (0.06)	1.44 (0.05)	1.51 (0.04)	1.55 (0.06)	1.54 (0.05)
FA		0.31 (0.03)	0.28 (0.01)	0.29 (0.02)	0.30 (0.03)	0.27 (0.01)	0.31 (0.04)	0.33 (0.02)	0.35 (0.04)	0.26 (0.01)	0.31 (0.05)	0.27 (0.02)
<b>Plantar flexion</b>		Fiber Length	6.45 (0.49)	7.66 (0.71)	5.09 (1.56)	5.90 (0.70)	5.41 (0.50)	5.28 (0.71)	6.46 (1.10)	5.94 (0.46)	4.87 (0.37)	6.80 (0.61)
	$\lambda_1$	2.53 (0.15)	2.68 (0.28)	2.37 (0.11)	2.59 (0.33)	2.50 (0.17)	2.41 (0.08)	2.40 (0.12)	2.59 (0.22)	2.28 (0.09)	2.58 (0.19)	2.48 (0.08)
	$\lambda_2$	1.61 (0.09)	1.75 (0.23)	1.64 (0.14)	1.65 (0.10)	1.74 (0.09)	1.63 (0.10)	1.57 (0.04)	1.61 (0.07)	1.66 (0.07)	1.63 (0.08)	1.71 (0.05)
	$\lambda_3$	1.43 (0.06)	1.53 (0.17)	1.44 (0.09)	1.42 (0.08)	1.48 (0.06)	1.43 (0.08)	1.34 (0.01)	1.36 (0.05)	1.46 (0.05)	1.44 (0.06)	1.48 (0.05)
	RD	1.52 (0.07)	1.64 (0.20)	1.54 (0.12)	1.54 (0.09)	1.61 (0.07)	1.53 (0.09)	1.46 (0.02)	1.49 (0.06)	1.56 (0.06)	1.53 (0.07)	1.59 (0.05)
	FA	0.30 (0.02)	0.30 (0.02)	0.26 (0.05)	0.31 (0.05)	0.27 (0.02)	0.28 (0.03)	0.30 (0.02)	0.32 (0.04)	0.23 (0.01)	0.31 (0.03)	0.27 (0.01)

**Table 1:** Diffusion parameters ( $\lambda_1$ ,  $\lambda_2$ ,  $\lambda_3$ , radial diffusivity (RD) and fractional anisotropy (FA)) and fiber length for the 11 muscles in the lower leg in different foot positions. Results are expressed as mean (SD).



4

**Figure 3:** Raw (unregistered) data and SNR in a volunteer with his foot in dorsiflexed position. **a)** and **f)** Images acquired without diffusion encoding in transverse orientation and reformatted in coronal orientation, respectively. **b)** and **g)** Images acquired with diffusion encoding in transverse orientation and reformatted coronal orientation, respectively. **c)** and **h)** SNR map for images acquired without diffusion encoding. **d)** and **i)** SNR map for images acquired with diffusion encoding. **e)** Example of muscle segmentation overlaid to the mDixon anatomical scan. **j)** muscle fiber tracking for Soleus, Tibialis Anterior and Gastrocnemius Lateralis.

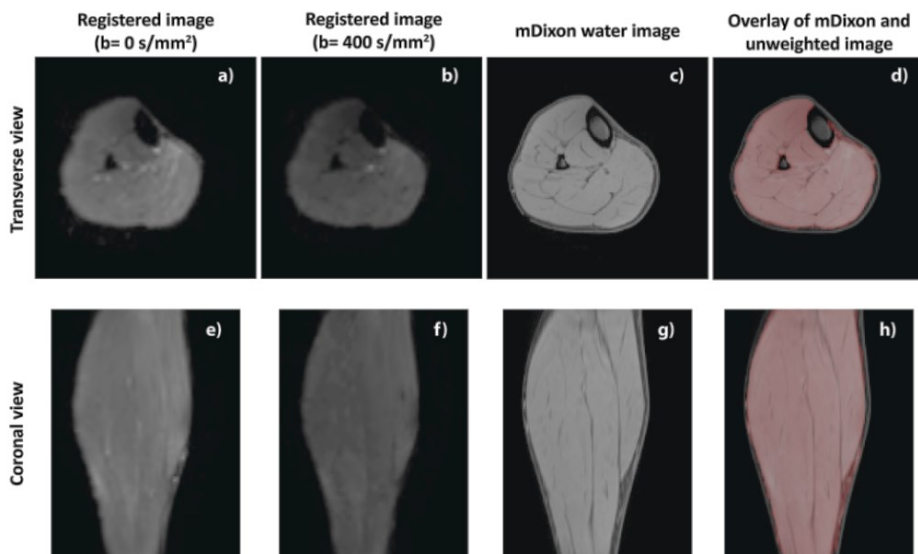


**Figure 4:** Registration results for a volunteer with his foot in dorsiflexed position. **a), b), c)** and **d)** transverse slice. **e), f), g)** and **h)** Reformatted coronal slice. **a)** and **e)** Non-weighted images, **b)** diffusion-weighted scans, **c)** and **g)** water image reconstructed from the mDixon scan, **d)** and **h)** overlay between the non-weighted scan, plotted in red, and the mDixon water image. The alignment between the two scans is almost perfect and no obvious residual EPI distortions are observed.

A representative RD map for the same volunteer with his foot in 3 different positions is shown in **Figure 5**. In general, an elevated RD value was observed in the anterior compartment in the dorsiflexed foot position, while lower RD values were present in the neutral and plantarflexed foot position.

**Figure 6** illustrates typical histograms of fiber tract length, used for determination of mean fiber length values, for the TA and SOL muscle. As can be observed, the peak of the distribution in the TA (**Figure 6a**) is shifted towards shorter values in the dorsiflexed position, while for the SOL (**Figure 6b**) a shift towards shorter fiber length is observed as the foot is moved from dorsiflexed to neutral and plantarflexed foot position. Dashed lines represent the data, while solid lines represent the fit with a skewed Gaussian distribution.

The mean fiber lengths and diffusion parameters ( $\lambda_1$ ,  $\lambda_2$ ,  $\lambda_3$ , RD and FA) for each muscle volume and position are reported in **Table 1**. Results are indicated as mean  $\pm$  standard deviation (SD).

## Correlations between fiber length and diffusion parameters

The mean  $\lambda_2$ ,  $\lambda_3$ , RDs, and fiber lengths averaged over all measurements are shown in **Figure 7**. For all investigated muscles an opposite behavior is observed for the parameters indicating radial diffusion ( $\lambda_2$ ,  $\lambda_3$ , and RD) and fiber length, suggesting an inverse correlation between changes in fiber length and changes in diffusion in the radial direction. In particular, in the EDL, EHL, and TA muscles an increase in  $\lambda_2$ ,  $\lambda_3$ , and RD and a decrease in fiber length were observed for the dorsiflexed foot position with respect to the plantarflexed position. On the other hand, for the FB, FHL, FL, GCL, GCM, SOL, and TP an opposite trend was seen, with an increase in RD and a decrease in fiber length in the plantarflexed foot position with respect to the dorsiflexed foot position. No clear trend was measured for the FDL muscle. **Figure 7** shows no remarkable differences in the trend of change in  $\lambda_2$  and  $\lambda_3$  with foot position. For the purpose of the current research, we therefore chose to analyze RD rather than  $\lambda_2$  and  $\lambda_3$  separately.

The correlations between fiber length and diffusion parameters (AD and RD) for each individual measurement are shown in **Figures 8** and **9**. **Figure 8** shows the relative changes in length and AD in dorsiflexion and plantarflexion position, with respect to neutral foot position and **Figure 9** shows the relative changes in length and RD. For both figures, the line that best fits the data is indicated in red. The Pearson's correlation coefficients  $r$  and the  $p$ -values for correlation with changes in AD and RD are presented in **Table 2** for all 11 muscle groups.

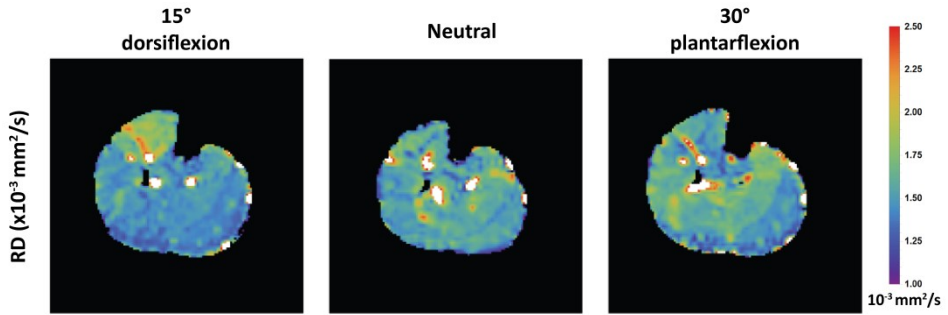


**Figure 5:** RD maps at different ankle joint positions (dorsiflexion, neutral position and plantarflexion). Increased RD is observed in the anterior compartment in the dorsiflexed foot position.

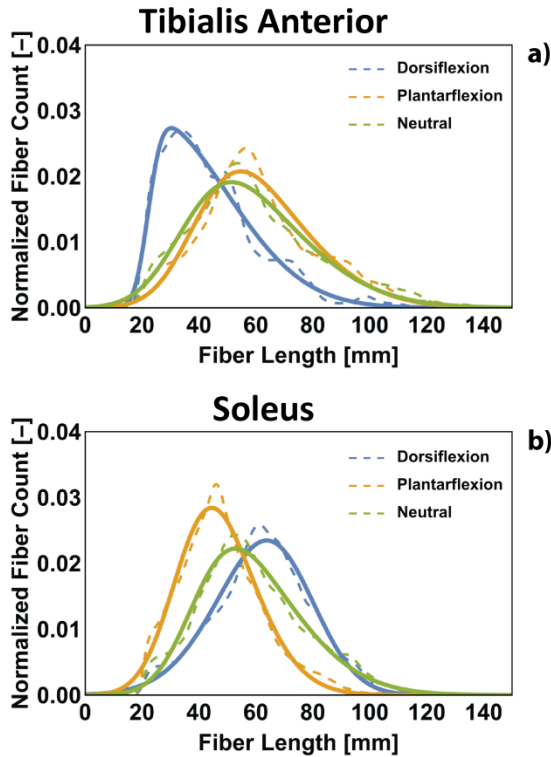


**Figure 6:** Distribution of fiber tract length as a function of foot position in Tibialis anterior (**a**) and Soleus (**b**) in the same volunteer. The dotted lines indicate the histogram of fiber length for each muscle in the different foot positions, while the solid lines indicate the fitted distribution. A clear shift of the distributions can be observed as a function of foot position.

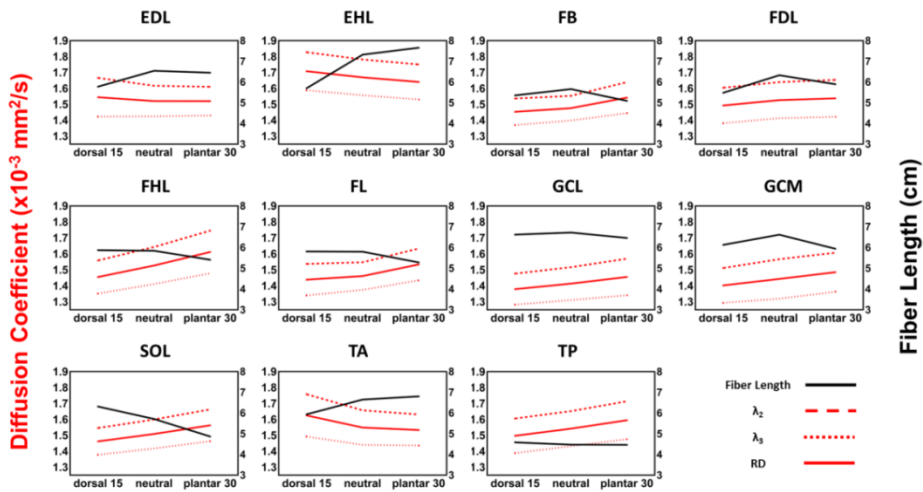


**Figure 7:** Diffusion parameters (red) and fiber length (black) for the 11 muscle groups of the lower leg as a function of foot position. Values are averaged across 10 measurements (5 subjects measured twice). Competing behavior is observed between radial diffusivity (RD) and fiber length. Dashed lines indicate  $\lambda_2$ , dotted lines indicate  $\lambda_3$ , and continuous lines indicate RD.

No significant correlation was observed between the changes in AD and the changes in fiber length in the different foot positions for all the investigated muscles (see **Table 2**). On the other hand, strong negative correlations between changes in RD and changes in fiber length were observed for EDL, FB, FL, SOL, and TA muscles. The opposite behavior in antagonist muscles can be appreciated in **Figure 8**. The EDL and the TA, which are dorsiflexor muscles, display a negative change in fiber length in the dorsiflexed position with respect to neutral position, which is associated with a positive change in RD. On the other hand, the FL and the SOL, which are involved in plantarflexion of the foot, present a decrease in fiber length associated with increased RD when the foot is in the plantarflexed position. The strongest correlation was observed for the TA muscle, accompanied with the biggest change in length.

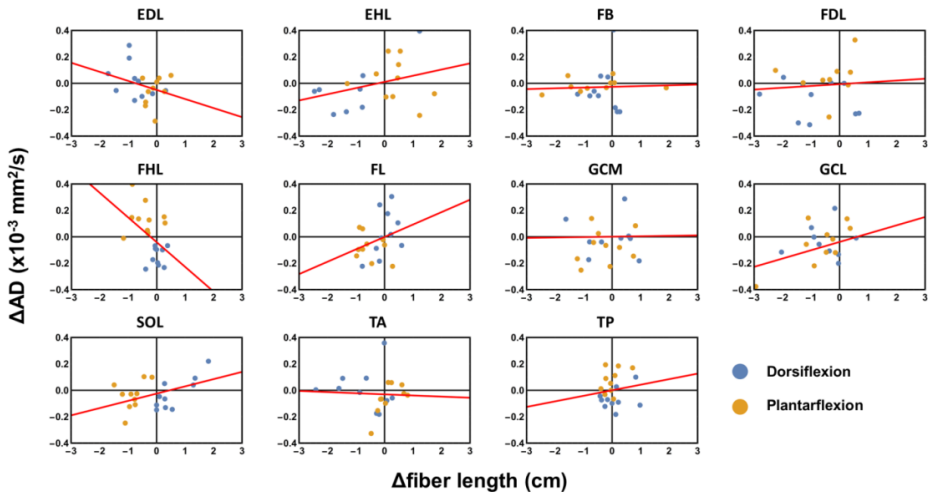


**Figure 8:** Relative changes in axial diffusivity (AD) plotted against relative change in fiber length. Differences are calculated with respect to the neutral foot position. The line that best fits the data is indicated in red. Correlations between the variables are summarized in **Table 2**.

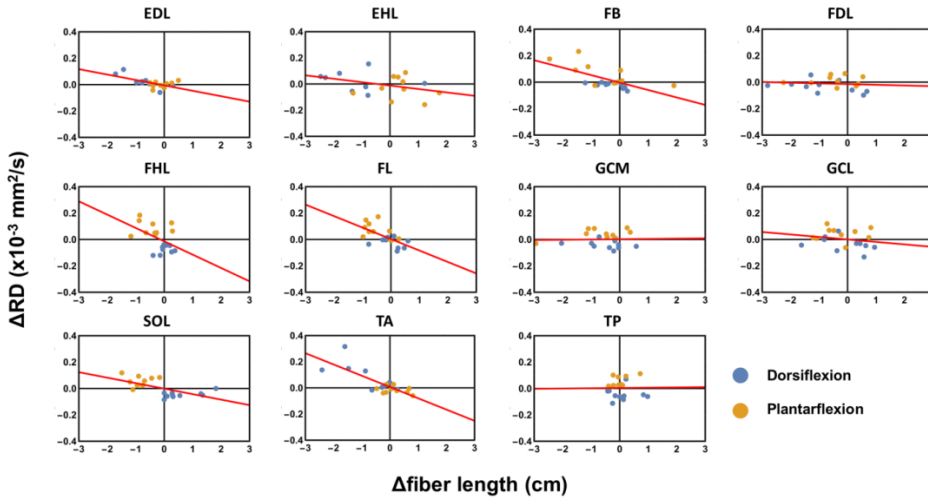


**Figure 9:** Relative changes in radial diffusivity (RD) plotted against relative change in fiber length. Differences are calculated with respect to the neutral foot position. The line that best fits the data is indicated in red. Correlations between the variables are summarized in **Table 2**.

Muscle	AD		RD	
	Pearson r	p value	Pearson r	p value
EDL	-0.31	0.8930	<u>-0.62</u>	<u>0.0398</u>
EHL	0.41	0.5457	-0.46	0.3488
FB	0.04	1	<u>-0.64</u>	<u>0.0219</u>
FDL	0.07	1	-0.11	0.9999
FHL	-0.45	0.3900	-0.47	0.3140
FL	0.31	0.8916	<u>-0.62</u>	<u>0.0386</u>
GCL	0.01	1	-0.22	0.9921
GCM	0.28	0.9498	0.03	1
SOL	0.44	0.8166	<u>-0.62</u>	<u>0.0364</u>
TA	-0.04	1	<u>-0.77</u>	<u>0.0006</u>
TP	0.15	0.9997	0.03	1

**Table 2:** Pearson correlation coefficient ( $r$ ) and  $p$ -value ( $p$ ) calculated between the relative change in fiber length and axial diffusivity (AD), and radial diffusivity (RD) respectively. All  $p$ -values are Bonferroni-corrected. Underlined values indicate a significant correlation ( $p < 0.05$ ) between the relative change in fiber length and the relative change in diffusion parameters.

## Cylindrical model

The relative changes in  $r^2$  derived from the cylindrical model to describe muscle fibers as a function of relative changes of muscle RD is shown **Figure 10**. The Pearson's correlation coefficients and the  $p$ -values are summarized in **Table 3**. Red lines indicate the best fit to the data. A significant and strong correlation was found for the changes in  $r^2$  (derived from the changes in fiber length assuming muscles fibers to be cylinders with constant volume) and changes in RD for the EDL, FB, FL, SOL and TA. Correlations of relative changes in RD vs. relative changes in  $r^2$  were stronger than the corresponding correlations between absolute changes in fiber length and absolute changes in RD.

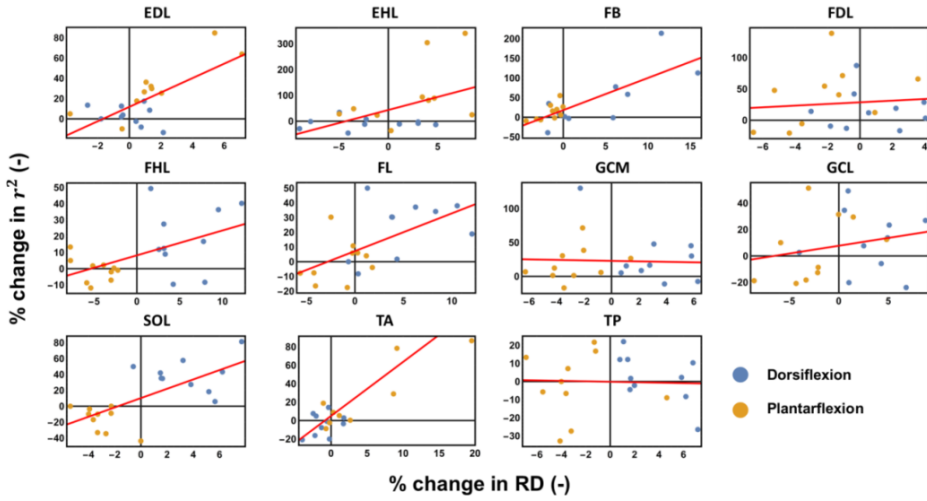


**Figure 10:** Relative percentage changes in radial diffusivity (RD) plotted against relative change in  $r^2$  in the different muscle groups. Changes in  $r^2$  are calculated from the measured changes in fiber length, assuming the muscle fibers to be cylinders with constant volume. The line that best fits the data is indicated in red. Correlations between the variables are summarized in **Table 3**.

%Radius <sup>2</sup> vs %RD		
Muscle	Pearson r	P value
EDL	<u>0.70</u>	<u>0.0057</u>
EHL	0.5	0.2708
FB	<u>0.78</u>	<u>0.0006</u>
FDL	0.10	0.9999
FHL	0.52	0.1887
FL	<u>0.60</u>	<u>0.0434</u>
GCL	0.22	0.9897
GCM	-0.04	1
SOL	<u>0.70</u>	<u>0.0078</u>
TA	<u>0.78</u>	<u>0.0006</u>
TP	-0.04	1

**Table 3:** Pearson correlation coefficient (r) and p-value (p) calculated between the relative changes in  $r^2$  (derived from the measured fiber length) and the measured relative changes in radial diffusivity (RD). All values are calculated with respect to the neutral foot position. Underlined values indicate a significant correlation ( $p < 0.05$ ). Significant correlation is observed for 5 of the 11 investigated muscles.



## Discussion

In this work, we showed that changes in fiber lengths have a negative correlation with changes in RD in the lower leg as a result of different foot positioning. We showed that changes in RD induced by passive stretching are connected to changes in cross sectional area derived from the fiber length changes using a cylindrical model with constant volume to describe the muscle fibers.

4

Previous studies have shown that fiber tractography may artificially continue at muscle origin, insertion, and along tendons and aponeurosis due to partial volume effects leading to over-estimations of fiber length (20). Manual editing of the reconstructed tracts in order to remove fibers that are too long has been suggested (26). However, this is time consuming and prone to errors. In this study we have therefore used the concept of TD as a stopping criterion, which has been shown to result in accurate fiber reconstructions with fibers running from origin to insertion (17). Furthermore, since TD is determined directly from the DT-MRI data, fiber length measurements do not critically rely on accurate registration to high-resolution anatomical scans, which makes the approach more robust to potential geometrical distortions and partial volume effects in low-resolution EPI data.

Shin et al. (22) used water saturated 2D images to detect changes in fascicle length of the gastrocnemius muscle during dorsiflexion/plantarflexion of the foot. Due to the high contrast between the saturated muscle tissue and the hyperintense fatty layers running parallel to muscle fascicles, tracking of fascicles endpoints proved to be possible. While this analysis was not in the scope of this study, it could be an interesting validation of the TD method for future studies. However, while 2D images are inherently less affected by distortions and provide higher resolution when compared to DT-MRI data, they are also only suitable for describing planar muscle motion and deformation, since they lack 3D information.

Previous studies have reported significant changes in diffusion parameters in the calf muscles as a function of the foot position. Sinha et al. (25) investigated the plantarflexed position (26° to 30°) with respect to the neutral foot position and found no significant difference in RD in the GCL and GCM and an average 8.3% decrease in RD from neutral position to dorsiflexion for the TA, which is in agreement with the change reported in this study (4.9%). The relative changes in RD reported by Schwenzer et al. (21) in the plantarflexed position compared to the dorsiflexed position are -11.4, +8.1%, +12.7 % and +10.8% for the TA, GCM, GCL and SOL respectively, which are in

agreement with the values of -5.2%, +5.9%, +5.7% and +6.9% presented in this study for the same muscles.

We found no significant changes in AD nor did we find a strong correlation with changes in fiber length. These findings indicate that diffusion along the axis of the fiber is mostly unaffected by lengthening or shortening. This is in agreement with the results previously reported by Schwenzer et al. (21) and can be explained by the fact that the fiber length and sarcomere length is too long to change the hindered diffusion of water molecules in the axial direction. On the other hand, Hatakenaka et al. (9) reported significant changes in AD in the TA muscle in different foot positions while no changes were observed in RD. This was interpreted as a change in sarcomere length due to contraction.

In our correlation analysis only the RD values of the muscles were investigated, rather than  $\lambda_2$  and  $\lambda_3$  separately. The first order approximation of cylindrical symmetry was assumed in order to simplify the model, and to avoid the risk of sorting bias between the two eigenvalues. Furthermore, in our preliminary study, although a slightly stronger correlation was observed for  $\lambda_3$  when compared to  $\lambda_2$ , we did not observe significant differences in the rate of change of  $\lambda_2$  and  $\lambda_3$  for different foot positions, and this could justify a joint analysis for the two eigenvalues. In a previous study Galban et al. (6) hypothesized that  $\lambda_2$  relates to the CSA of the endomysium, while  $\lambda_3$  correlates with the CSA of the single fiber unit. Karampinos et al. (12) used a cylindrical model with infinite length and elliptical cross sectional area to describe muscle fibers, thus taking into account differences between  $\lambda_2$  and  $\lambda_3$ . However, it is worth mentioning that in Karampinos' study a diffusion time of 40 ms was used, in comparison with 20 ms in our study. Since differences between the eigenvalues are expected to increase for increasing diffusion times, it could be of interest to assess  $\lambda_2$  and  $\lambda_3$  separately in future studies using longer diffusion times during data acquisition (23).

In general, our results support the hypothesis that diffusion along the radial direction in skeletal muscles relates to the CSA of the fibers. In particular, we observed that the changes in average CSA of fibers in a voxel might predict changes in the diffusion measured in the radial direction. These results are obtained under the assumption that muscle fiber volume would stay constant in conditions of passive stretch. Within the diffusion framework this would mean that cellular membranes and other structures that hinder water diffusion in the radial direction can be modeled as impermeable or in slow exchange with the extracellular space. In previous studies (7, 13) muscle fibers were modeled using a bi-compartment model, in which intracellular diffusion was considered as anisotropic and the diffusion in the extracellular space was modeled as

isotropic, similarly to the ball-and-stick model used in brain DT-MRI (1). A single-compartment model was used for interpretation of changes in RD upon muscle stretching, thus neglecting the extracellular space and the exchange of magnetization between intracellular and extracellular space. We believe this is justified since in muscle the extracellular volume fraction is small, typically around 5-10% (28). Such a small contribution would be hard to detect with our DT-MRI experiment with a single short mixing time. Nevertheless, previous histological studies have shown that the volume of extracellular space decreases with increasing axial strain (27). It would therefore be interesting to study the role of the extracellular space using DT-MRI sequences with multiple mixing-times and b-values.

The diffusion time used in our study was 20 ms, which would result in a displacement of water molecules in the order of 10  $\mu\text{m}$ . Considering that this size is much smaller than the typical cellular size ( $\sim 60 \mu\text{m}$ ), we can infer that the changes in RD are not determined by the cellular membrane alone, but are also affected by intra- and extracellular structures, as already suggested in previous *ex vivo* studies (15). A regime of restricted diffusion, which can be probed at long diffusion times, has been shown to be beneficial for quantitative and modeling of structural properties in *ex vivo* experiments on tongue and cardiac muscles (14). Sigmund et al. (23) showed that *in vivo* RD of skeletal muscles is strongly time dependent, with a reduced RD measured for prolonged diffusion times, for both control subjects and compartment syndrome patients. In a follow-up study (24) significant differences were observed in terms of RD pre and post exercise when comparing long (1.02 s) and short (30 ms) diffusion times, suggesting the increased ability of longer diffusion times to probe transient effects such as exercise and muscle contraction. We believe that increasing the diffusion time in DT-MRI of skeletal muscles at different contraction status could provide a better understanding of changes in diffusion properties and geometrical characteristics and could potentially highlight the role of cellular membrane in the measured changes in RD (24).

In our study, we observed small changes in  $\lambda_2, \lambda_3$  in the gastrocnemius group (GCL and GCM) which resulted in low or no correlation between changes in fiber length and changes in diffusion parameters, while previous studies have shown significant changes in these muscles as a function of different foot positions. However, unlike in the previously mentioned studies, in our experimental setup the lower leg was not suspended, but rather compressed between the anterior and posterior element of the cardiac coil. We believe this compression might have caused deformation of muscle, especially in the most posteriorly located muscle groups, as suggested by Hata et al.

(8), who reported significant changes in RD and fractional anisotropy (FA) in the lower leg between different externally applied pressure forces.

Accurate DT-MRI tensor fitting and tractography requires an SNR of the non-weighted image of at least 25. In fact lower SNR could lead to more tortuous paths of tracked fibers, thus artificially increasing fiber length, or could cause an overestimation of FA and underestimation of  $\lambda_2$  and  $\lambda_3$ . However, for SNR values above 25, the measured  $\lambda_2$  and  $\lambda_3$  have been seen to deviate from the real value by only 5%, while the fiber length was only overestimated by 1% (5). Since our reported changes in RD and fiber length in different foot positions exceed these values, we believe that our results and conclusions unlikely to be biased by SNR effects.

The repeated measures for all muscles were analyzed as independent measurements. This enabled a repeatability analysis of diffusion coefficients and fiber length (data not shown) in which a moderate repeatability was observed for both. The errors in calculation of diffusion coefficients and the errors in the calculation of fiber length can be assumed to be independent, therefore the strong correlations we found between fiber length and diffusion coefficients suggests that poor repeatability reflects a difference in contraction status being measured, rather than a measurement error. This might be explained by the fact that some subjects experienced slight discomfort during the scan session -especially in the dorsiflexed position- and might have compensatively contracted their muscles in one of the repeated measures.

We therefore would like to emphasize the importance of consistent patient positioning for DT-MRI studies of the lower leg, in terms of foot angulation and active contraction needed to keep the position, especially when differences in diffusion parameters will be used as a diagnostic tool or in longitudinal studies.

This study has a number of limitations. First of all, the number of subjects was small (n=5). A bigger number of subjects in future studies could increase the statistical value of the correlation. However, for the purpose of this merely explorative study, we believe the number of experiments is sufficient.

Another limitation is the fact that perfusion effects were not taken into account. Previous studies showed that diffusion-based methods as IVIM are sensitive enough to show differences in skeletal muscle with exercise (3) . However, in our study, movement was passive and therefore the effect of perfusion on RD would likely be negligible.

Despite the limitations of this study, we have shown that RD is sensitive to small changes in cellular geometry. This suggests that in a controlled experiment, such as the one we performed, changes in RD can be used to infer changes in fiber length. Furthermore, RD could potentially be a useful biomarker for cellular size, in longitudinal studies of muscle disease progression or healing.

## 4

### Conclusions

In conclusion, we showed that changes in fiber length induced in skeletal muscles by passive stretching significantly negatively correlated with changes in RD. The rate of change in diffusivity perpendicular to the fiber is in agreement with expected changes in the square of the radius, indicating that in first approximation muscle fibers can be adequately described by a simple cylindrical model. Taken together, our data show that changes in RD induced by passive muscle stretching/lengthening can be explained with a change in muscle CSA, therefore advancing the physiological interpretation of parameters derived using a diffusion tensor model.

## References

1. **Behrens TEJ, Woolrich MW, Jenkinson M, Johansen-Berg H, Nunes RG, Clare S, Matthews PM, Brady JM, Smith SM.** Characterization and Propagation of Uncertainty in Diffusion-Weighted MR Imaging. *Magn Reson Med* 50: 1077–1088, 2003.
2. **Damon BM.** Effects of image noise in muscle diffusion tensor (DT)-MRI assessed using numerical simulations. *Magn Reson Med* 60: 934–944, 2008.
3. **Filli L, Boss A, Wurnig MC, Kenkel D, Andreisek G, Guggenberger R.** Dynamic intravoxel incoherent motion imaging of skeletal muscle at rest and after exercise. *NMR Biomed* 28: 240–246, 2015.
4. **Froeling M, Nederveen AJ, Heijtel DFR, Lataster A, Bos C, Nicolay K, Maas M, Drost MR, Strijkers GJ.** Diffusion-tensor MRI reveals the complex muscle architecture of the human forearm. *J Magn Reson Imaging* 36: 237–248, 2012.
5. **Froeling M, Nederveen AJ, Nicolay K, Strijkers GJ.** DTI of human skeletal muscle: The effects of diffusion encoding parameters, signal-to-noise ratio and T2 on tensor indices and fiber tracts. *NMR Biomed* 26: 1339–1352, 2013.
6. **Galban CJ, Maderwald S, Uffmann K, de Greiff A, Ladd ME.** Diffusive sensitivity to muscle architecture: A magnetic resonance diffusion tensor imaging study of the human calf. *Eur J Appl Physiol* 93: 253–262, 2004.
7. **Galban CJ, Maderwald S, Uffmann K, Ladd ME.** A diffusion tensor imaging analysis of gender differences in water diffusivity within human skeletal muscle. *NMR Biomed* 18: 489–498, 2005.
8. **Hata J, Yagi K, Hikishima K, Komaki Y, Goto M, Yano K, Si SIS.** Diffusion fractional anisotropy-based transformation in skeletal muscle caused by pressure. *Magn Reson Med Sci* 11: 179–84, 2012.
9. **Hatakenaka M, Matsuo Y, Setoguchi T, Yabuuchi H, Okafuji T, Kamitani T, Nishikawa K, Honda H.** Alteration of proton diffusivity associated with passive muscle extension and contraction. *J Magn Reson Imaging* 27: 932–937, 2008.
10. **Heemskerk AM, Sinha TK, Wilson KJ, Ding Z, Damon BM.** Repeatability of DTI-based skeletal muscle fiber tracking. *NMR Biomed* 23: 294–303, 2010.
11. **Heemskerk AM, Strijkers GJ, Drost MR, van Bochove GS, Nicolay K.** Skeletal muscle degeneration and regeneration after femoral artery ligation in mice: monitoring with diffusion MR imaging. *Radiology* 243: 413–21, 2007.
12. **Karampinos DC, King KF, Sutton BP, Georgiadis JG.** In vivo study of cross-sectional skeletal muscle fiber asymmetry with diffusion-weighted MRI. *Annu. Int. Conf. IEEE Eng. Med. Biol. - Proc.* (2007). doi: 10.1109/IEMBS.2007.4352290.
13. **Karampinos DC, King KF, Sutton BP, Georgiadis JG.** Myofiber ellipticity as an explanation for transverse asymmetry of skeletal muscle diffusion MRI in vivo signal. *Ann Biomed Eng* 37: 2532–2546, 2009.
14. **Kim S, Chi-Fishman G, Barnett AS, Pierpaoli C.** Dependence on diffusion time of apparent diffusion tensor of ex vivo calf tongue and heart. *Magn Reson Med* 54: 1387–1396, 2005.
15. **Kinsey ST, Locke BR, Penke B, Moerland TS.** Diffusional anisotropy is induced

- by subcellular barriers in skeletal muscle. *NMR Biomed* 12: 1–7, 1999.
16. **Klein S, Staring M, Murphy K, Viergever MA, Pluim JPW.** Elastix: A toolbox for intensity-based medical image registration. *IEEE Trans Med Imaging* 29: 196–205, 2010.
  17. **Oudeman J, Mazzoli V, Marra MA, Nicolay K, Maas M, Verdonschot N, Sprengers AM, Nederveen AJ, Strijkers GJ, Froeling M.** A novel diffusion-tensor MRI approach for skeletal muscle fascicle length measurements. 4: 1–12, 2016.
  18. **Scheel M, Prokscha T, von Roth P, Winkler T, Dietrich R, Bierbaum S, Arampatzis A, Diederichs G.** Diffusion Tensor Imaging of Skeletal Muscle—Correlation of Fractional Anisotropy to Muscle Power. *Fortschr Röntgenstr* 185: 857–861, 2013.
  19. **Scheel M, von Roth P, Winkler T, Arampatzis A, Prokscha T, Hamm B, Diederichs G.** Fiber type characterization in skeletal muscle by diffusion tensor imaging. *NMR Biomed* 26: 1220–1224, 2013.
  20. **Schenk P, Siebert T, Hiepe P, Güllmar D, Reichenbach JR, Wick C, Blickhan R, Böl M.** Determination of three-dimensional muscle architectures: Validation of the DTI-based fiber tractography method by manual digitization. *J Anat* 223: 61–68, 2013.
  21. **Schwenzer NF, Steidle G, Martirosian P, Schraml C, Springer F, Claussen CD, Schick F.** Diffusion tensor imaging of the human calf muscle: Distinct changes in fractional anisotropy and mean diffusion due to passive muscle shortening and stretching. *NMR Biomed* 22: 1047–1053, 2009.
  22. **Shin DD, Hodgson JA, Edgerton VR, Sinha S.** In vivo intramuscular fascicle-aponeuroses dynamics of the human medial gastrocnemius during plantarflexion and dorsiflexion of the foot. *J Appl Physiol* 107: 1276–1284, 2009.
  23. **Sigmund EE, Novikov DS, Sui D, Ukpebor O, Baete S, Babb JS, Liu K, Feiweier T, Kwon J, McGorty K, Bencardino J, Fieremans E.** Time-dependent diffusion in skeletal muscle with the random permeable barrier model (RPBM): Application to normal controls and chronic exertional compartment syndrome patients. *NMR Biomed* 27: 519–528, 2014.
  24. **Sigmund EE, Sui D, Ukpebor O, Baete S, Fieremans E, Babb JS, Mechlin M, Liu K, Kwon J, McGorty K, Hodnett PA, Bencardino J.** Stimulated echo diffusion tensor imaging and SPAIR T2-weighted imaging in chronic exertional compartment syndrome of the lower leg muscles. *J Magn Reson Imaging* 38: 1073–1082, 2013.
  25. **Sinha S, Sinha U.** Reproducibility analysis of diffusion tensor indices and fiber architecture of human calf muscles in vivo at 1.5 Tesla in neutral and plantarflexed ankle positions at rest. *J Magn Reson Imaging* 34: 107–119, 2011.
  26. **Sinha U, Csapo R, Malis V, Xue Y, Sinha S.** Age-related differences in diffusion tensor indices and fiber architecture in the medial and lateral gastrocnemius. *J Magn Reson Imaging* 41: 941–953, 2015.
  27. **Smith LR, Gerace-Fowler L, Lieber RL.** Muscle extracellular matrix applies a transverse stress on fibers with axial strain. *J Biomech* 44: 1618–1620, 2011.
  28. **Vincensini D, Dedieu V, Renou JP, Otal P, Joffre F.** Measurements of

extracellular volume fraction and capillary permeability in tissues using dynamic spin-lattice relaxometry: Studies in rabbit muscles. *Magn Reson Imaging* 21: 85–93, 2003.





# Chapter

# 5

## Water and fat separation in real-time MRI of joint movement with Phase Sensitive bSSFP

**Valentina Mazzoli**

Aart J. Nederveen

Jos Oudeman

Andre Sprengers

Klaas Nicolay

Gustav J. Strijkers

Nico Verdonshot

**Magn Reson Med. 2017 Jul;78(1):58-68.**

**doi: 10.1002/mrm.26341**

## Abstract

**Introduction:** The aim of this work is to introduce a method for obtaining fat-suppressed images in real time MRI of moving joints at 3T using a bSSFP sequence with phase detection to enhance visualization of soft tissue structures during motion.

**Methods:** The wrist and knee of 9 volunteers were imaged with a real-time bSSFP sequence while performing dynamic tasks. For appropriate choice of sequence timing parameters, water and fat pixels showed an out-of-phase behavior, which was exploited to reconstruct water and fat images. Additionally, a 2-point Dixon sequence was used for dynamic imaging of the joints, and resulting water and fat images were compared with our proposed method.

**Results:** The joints could be visualized with good water fat separation and SNR, while maintaining a relatively high temporal resolution (5 fps in knee imaging and 10 fps in wrist imaging). The proposed method produced images of moving joints with higher SNR and higher image quality when compared to the Dixon method.

**Conclusions:** Water-fat separation is feasible in real time MRI of moving knee and wrist at 3T. PS-bSSFP offers movies with higher SNR and higher diagnostic quality when compared to Dixon scans.

## Introduction

Dynamic imaging of joints in the musculoskeletal system allows observation of the joint while in motion and to appreciate the relative displacement and interactions of the different bony and soft tissue structures. The evaluation of a joint during movement can add information over standard static images or series of static images (6). Therefore, it could provide important diagnostic information for detailed assessment of malformations and misalignment or better elucidate the cause of pain that is only reported while performing dynamic tasks.

Magnetic Resonance Imaging of joints during dynamic tasks can be performed in two different ways, namely with Cine MRI or using real-time techniques. In Cine, or kinematic MRI, several repetitions of the same motion are needed in order to completely fill the k-space for a given image frame. Cine MRI has been widely exploited in literature to study patellofemoral contact mechanics (2), and to analyze alterations in kinematics in pathological circumstances, such as ACL deficiency (1). Several approaches have been reported for synchronizing the acquisition to the movement. While the most common approach is prospective triggering, with the patient instructed to move at a constant rate with the help of a metronome, retrospective triggering based on the measurement of the knee flexion angle has also been used (18). Although triggered acquisition may potentially provide advantages in terms of spatial and temporal resolution and contrast manipulation, it is limited in its clinical applicability due to the need for precise and reproducible repetition of the movement. In order to overcome these limitations, real-time MRI has been proposed as a more robust method to image joints in motion, especially in uncooperative subjects or patients that experience pain during the motion tasks.

Real-time MRI was previously applied to image joint motion for the study of bone kinematics (7–9) and muscle deformation in several joints such as knee (11) and wrist (3). However, it has found so far limited applicability in the dynamic study of other soft tissue structures such as ligaments and tendons, due to the difficulty in effectively suppressing all signals from fat tissue surrounding these structures during movement. Fibrous structures such as ligaments, menisci and tendons are hypointense in conventional  $T_2$ - and  $T_1$ -weighted MRI due to the presence of collagen with short  $T_2/T_2^*$ . Several imaging strategies have been employed to obtain positive contrast from fibrous tissue (22) since it is believed that this may help in early detection of degenerative changes and may increase the structural information of the MRI scan. Due to the high signal intensity of fat in bones and other anatomical areas around

ligaments, tendons and cartilage, fat suppression is a main requirement in order to achieve positive contrast.

Balanced SSFP (bSSFP, TrueFISP or bFFE) is a rapid and SNR efficient sequence already widely used in static (12) and dynamic imaging (3, 24) of the musculoskeletal system. However, due to the characteristic  $T_2/T_1$  signal dependence, fat appears as hyperintense, preventing positive contrast of tissue structures with short  $T_2$  such as ligaments and tendons and obscuring clinically relevant features, thus enforcing the need for robust fat suppression. Conventional fat suppression prepulses such as SPIR and SPAIR are not suitable for bSSFP sequences since they interrupt the steady state and cause changes in image contrast. Several methods have been proposed in literature for suppressing the fat signal in bSSFP sequences without interrupting the steady state, which mainly rely on repeated acquisitions, such as LAMA (25), Linear Combination bSSFP (31) and Fluctuating Equilibrium bSSFP (30), or on modification of the Frequency Response Function (FRF) to broaden the stopband that can be used for fat suppression, such as the Alternating Repetition Time approach (14, 20, 27). While a repeated acquisition approach is unfeasible in real-time imaging, the FRF manipulation inherently involves lengthening of the TR. This is not desirable because it will degrade temporal resolution and will also increase the sensitivity to  $B_0$  inhomogeneities, making it unsuitable for imaging large joint motion when an optimal shim for every joint position is hard to achieve.

Hargreaves et al. (15) proposed a method for water fat/separation based on a standard bSSFP sequence at 1.5 T exploiting the phase difference between the water and the fat peaks. This Phase Sensitive bSSFP (PS-bSSFP) technique, which does not require any repeated acquisition and does not lead to increased sensitivity to off-resonance effects, has been applied as a fast fat suppression method in the musculoskeletal system (29) and in CINE imaging of the heart (13) at 1.5 T.

The main purpose of this study is to show the feasibility of using the bSSFP sequences with phase sensitive reconstruction for doing fat-suppressed real-time MRI of moving joints at 3 T and to obtain visualization of ligaments and cartilage during motion with positive contrast. The performance of this sequence is compared to 2-point Dixon water/fat separation in a phantom and in *in vivo* imaging of the knee. In order to provide an additional application, the feasibility of the PS-bSSFP approach is also shown in the moving wrist.

# Methods

## Theory

The fat-suppression method used in this work is based on a standard bSSFP sequence with  $TE = TR/2$ . In this condition, the phase of the signal is largely independent of the local resonance frequency and of the flip angle of the excitation pulse (**Figure 1**) within each passband. On the other hand, the signal intensity displays a periodic behavior as a function of the resonance frequency with a period of  $1/TR$ . Since at 3 T water and fat peaks have resonance frequencies that are about 440 Hz apart, it is possible to choose TR such that the water and the fat peaks will be in two different passbands of the frequency response function. In this situation, the water and fat signals will be out-of-phase and this can be exploited to separate the complex signal into water-only and fat-only images.

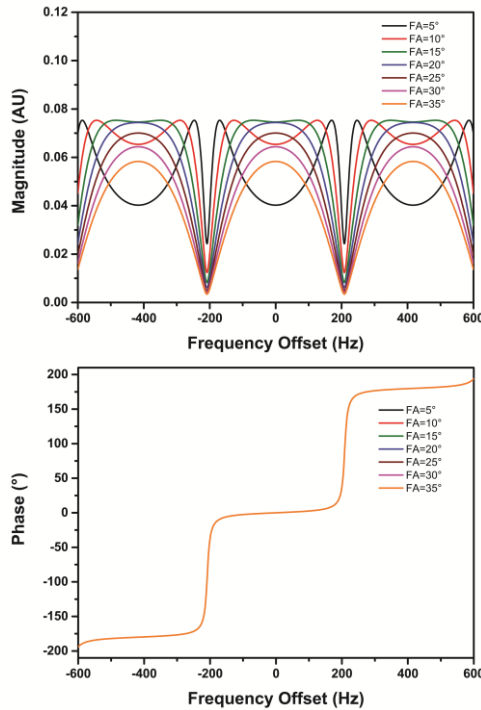


**Figure 1:** Frequency response function of a bSSFP sequence. Parameters used for the simulation were  $TR = 2TE = 2.4$  ms,  $T_1 = 1100$  ms and  $T_2 = 25$  ms. Magnitude and phase of the signal are shown as a function of the resonance frequency. The phase of the signal is independent of the flip angle of the excitation pulse and all curves therefore overlap.

The optimal condition for robust water-fat separation and reduced sensitivity to off-resonance effects is obtained when each passband has a maximum width. This is obtained when  $TR=1/\sigma$  with  $\sigma$  the chemical shift difference between water and fat in Hz. At 3 T this condition is achieved when  $TR = 2.4$  ms.

## Phantom MR experiment

All images were acquired using an Ingenia 3 T scanner (Philips Healthcare, Best, The Netherlands) with a 70 cm bore and a Torso coil for signal reception.

For absolute comparison of PS-bSSFP and the 2-point Dixon method in terms of SNR, phantom validation was performed. The phantom consisted of a set of 14 Falcon gel tubes with longitudinal relaxation time  $T_1$  ranging from 150 ms to 1700 ms and transverse relaxation time  $T_2$  ranging from 16 ms to 120 ms and one tube filled with peanut oil.  $T_1$  and  $T_2$  of the Falcon tubes were adjusted by adding  $GdCl_3$  and agarose (16) and measured using a single slice Look-Locker sequence ( $TR/TE = 10/3.7$  ms,  $\Delta TI = 80$  ms,  $\alpha = 8^\circ$ , cycle repetition time = 10 s) and a multislice CPMG sequence ( $TR = 2$  s,  $\Delta TE = 6$  ms), respectively (5).

Acquisition parameters common to all acquisitions in the phantom were: 2D single slice acquisition,  $FOV = 400 \times 400$  mm<sup>2</sup>, slice thickness = 5 mm, acquired pixel size =  $2 \times 2$  mm<sup>2</sup>, reconstructed pixel size =  $1 \times 1$  mm<sup>2</sup>. For the PS-bSSFP scan,  $TR$  was 2.4 ms and  $TE$  was 1.2 ms. Parallel imaging acceleration (SENSE factor 2.4) was used, resulting in a total scan time of 200 ms (5 fps). In order to optimize the protocol for the PS-bSSFP sequence, 7 different flip angles ( $FA = 5^\circ, 10^\circ, 15^\circ, 20^\circ, 25^\circ, 30^\circ$  and  $35^\circ$ ) were used.

For the shortest 2-point Dixon protocol (Dixon Short), the spatial resolution was kept the same as in the PS-bSSFP scan. Other relevant imaging parameters were:  $TR = 3.4$  ms,  $TE_1 = 1$  ms,  $TE_2 = 1.8$  ms. The effect of flip angle was investigated by performing 7 different scans with  $FA = 5^\circ, 8^\circ, 10^\circ, 12^\circ, 15^\circ, 17^\circ$  and  $20^\circ$ , respectively. In order to achieve the same temporal resolution as the PS-bSSFP scan (200 ms), scan time was reduced using partial Fourier encoding. The maximum investigated flip angle for the Dixon scan was lower than for the corresponding PS-bSSFP scan because the Dixon scan was based on an RF-spoiled sequence, for which the Ernst angle was expected to occur at small excitation angles in the short  $TR$  regime. On the other hand, a broader range of flip angles was investigated for the PS-bSSFP sequence because in this case the excitation angle at which the maximum signal occurs does not depend on the  $TR$  of the sequence, but only on  $T_1$  and  $T_2$ .

Two additional sets of Dixon scans were acquired in order to investigate the effects of acceleration on the quality of water/fat separation and the resulting SNR. The Dixon Long scan was the same as the Dixon Short scan, but without the use of Partial Fourier, and resulted in a temporal resolution of 280 ms.

The effect of using in-phase and out-of-phase echoes in the resulting SNR of the water image was also investigated. For these scans (Dixon IP) the relevant imaging parameters were TR = 3.6 ms, TE<sub>1</sub> = 1.15 ms, TE<sub>2</sub> = 2.3 ms. Two different flip angles were investigated: FA = 5° and FA = 10°.

All the relevant imaging parameters are summarized in **Table 1**. For each sequence, twenty consecutive scans of the phantom were acquired for SNR calculation.

Scan Type	TR (ms)	TE <sub>1</sub> (ms)	TE <sub>2</sub> (ms)	Partial Fourier	Temporal resolution	Total scan time
Dixon Short	3.4	1.00	1.8	71 %	200 ms	4 s
Dixon Long	3.4	1.00	1.8	0 %	283 ms	5.7 s
Dixon IP	3.6	1.15	2.3	71 %	213 ms	4.3 s

**Table 1:** Summary of scan parameters used for the 2-point Dixon scans.

## Static *in vivo* MR experiment

Nine (n = 9) healthy volunteers were scanned in compliance with regulations of our local institution. For the study of the knee (n = 5), the subjects were positioned laterally with one of their knees on the coils embedded in the scanner table. For signal reception a 16-channel torso coil was placed above the knee on top of a plastic support. Subjects were positioned to maximize the achievable range of flexion/extension. A single slice was planned with the knee in approximately 15 degrees flexion, which enabled visualization of both tibial and femoral attachment point of the PCL.

Acquisition parameters for the PS-bSSFP acquisition in the knee were the same as used in the phantom experiment: 2D single slice acquisition, FOV = 400x400 mm<sup>2</sup>, slice thickness = 5 mm, acquired pixel size = 2x2 mm<sup>2</sup>, reconstructed pixel size = 1x1 mm<sup>2</sup>, temporal resolution = 200 ms, TR = 2.4 ms, TE = 1.2 ms. For sequence optimization, the flip angle was varied from 5° to 35°, in steps of 5°.



To compare sequence performance, the following sequences were also used: Dixon Short 5, Dixon Short 10, Dixon Short 15, Dixon Long 5, Dixon Long 10, Dixon IP 5 and Dixon IP10. The scan parameters for these scans were the same as those used for the phantom. Sequence optimization, already performed in the phantoms, was repeated *in vivo* due to the fact that the relaxation times  $T_1$  and  $T_2$  of the phantom used did not match exactly the expected relaxation times in the *in vivo* situation.

For the imaging of the wrist the subjects were positioned prone in the “superman position”, with the arm extended in front of their head and the wrist inside a 16 channel head coil. A single slice was planned in the coronal plane. For imaging of the wrist we used a smaller FOV = 200x200 mm<sup>2</sup> which allowed a higher temporal resolution (100 ms). All other imaging parameters were identical to the protocols used for the phantom and the imaging of the knee.

For SNR quantification, twenty identical sets of images were acquired for each imaging protocol.

Significance ( $p < 0.05$ ) of changes in SNR values between the Dixon and the PS-bSSFP scans were tested using one-way ANOVA with a Bonferroni post hoc test.

### **Dynamic *in vivo* MR experiment**

For dynamic imaging of the knee, a foam cushion was placed below the subject’s lateral epicondyle to provide a pivot point for motion in the sagittal plane. The maximum achievable knee flexion angle was dependent on the size of the subject and ranged from 45 to 80 degrees. In order to minimize occurrence of bSSFP banding artifacts in the patella area during motion, a pillow filled with pineapple juice was placed on the anterior side of the lower leg.

For dynamic imaging of the wrist, the subjects were asked to perform a radial/ulnar deviation manoeuvre.

A first order volume shim routine was executed before each dynamic scan, with the joint approximately in the middle of the range of motion. For the dynamic *in vivo* scan the PS-bSSFP sequence was used, with a flip angle of 25°, while for the Short-Dixon scan a flip angle of 10° was used.

### **Image processing**

For the bSSFP acquisitions, both on phantom and volunteers, magnitude and phase images were exported and water and fat images were reconstructed using the

algorithm proposed in (19) implemented in Matlab. Using a region-growing algorithm on the complex image data, the phase information was corrected for a slowly varying background phase component. After this, the water and fat components could be separated by taking positive and negative real values of the resulting complex data.

The water and fat images from the 2-point Dixon method were reconstructed on-line by the scanner software. For SNR calculation the twenty identically acquired water-only images were combined following the “subtraction method” (26). In the knee images, regions of interest (ROIs) in the SNR maps were drawn in the quadriceps muscles, posterior cruciate ligament, and patellofemoral cartilage. In the wrist, images SNR was calculated in two ROIs placed in articular cartilage and muscles respectively.

## Image scoring

One radiologist (MM) with over 20 years of experience in MSK MRI and a radiologist in training (RH) were blinded and scored the *in vivo* movies of the knee. The following categories were scored: overall visibility of cartilage, overall visibility of PCL, overall sharpness, overall contrast, and fat suppression in the area of interest. All categories were scored on an ordinal 5-point scale. The following scoring was used: for overall visibility of PCL and cartilage: 1 = the structure cannot be identified, 2 = poor visibility of the structure, 3 = acceptable visibility, 4 = good visibility in most of the dynamic frames, 5 = good visibility in all dynamic frames. For overall sharpness: 1 = no edges can be detected, 2 = edges are mainly blurry, 3 = acceptable sharpness, 4 = good sharpness in most of the dynamic frames, 5 = good sharpness in all dynamic frames. For overall contrast: 1 = no contrast between structures, 2 = low contrast, 3 = acceptable contrast for identification of structures, 4 = soft tissue is visible in some of the dynamic frames and can be partially followed, 5 = soft tissue is visible in all of the dynamic frames and can be fully followed. For fat suppression (in the area of interest): 1 = no fat suppression, 2 = some areas with fat suppression are present, 3 = fat is mostly suppressed but still visible in some areas of interest, 4 = fat is mostly suppressed in all area of interest and dynamic frames, 5 = excellent fat suppression.

Statistics analysis on image scoring was performed using IBM SPSS Statistics v.21. A Wilcoxon Signed Rank Test was used to test for significance. A p value  $p < 0.05$  was considered to be significant.

# Results

## Phantom MR experiment

The water and fat images of the phantom are shown in **Figure 2**. The signal evolution as a function of time showed that for all the dynamic frames a steady state condition was reached (data not shown). For all the scans, correct separation of water and fat components was obtained (**Figure 2a-d**). Residual signal from fat was observed in the water images obtained with the Dixon method.

The resulting SNR of the water-only imaged showed a clear dependence on flip angle, for both PS-bSSFP and Dixon sequences.

The optimal flip angle for the bSSFP was observed to be dependent on the  $T_2/T_1$  ratio. The resulting SNR for the PS-bSSFP and Dixon sequences is shown in **Figure 3a-c** for three different  $T_2/T_1$  ratios. In agreement with the simulation performed for the same relaxation times measured in the phantom (**Figure 2e**), the optimal flip angle for the lower  $T_2/T_1$  ratios in PS-bSSFP sequences is lower than for the high  $T_2/T_1$  ratios. However, for all the investigated ratios, the PS-bSSFP showed higher SNR when compared to the all Dixon scans. As expected, higher SNR was observed in all the tubes in the long Dixon scan when compared to the short Dixon scan. The IP-OP Dixon only showed a minor improvement in SNR when compared to the short Dixon scans. Even the IP-OP Dixon showed lower SNR than the PS-bSSFP. The difference in SNR between the Dixon and the PS-bSSFP scans was more pronounced for the higher  $T_2/T_1$  ratios.

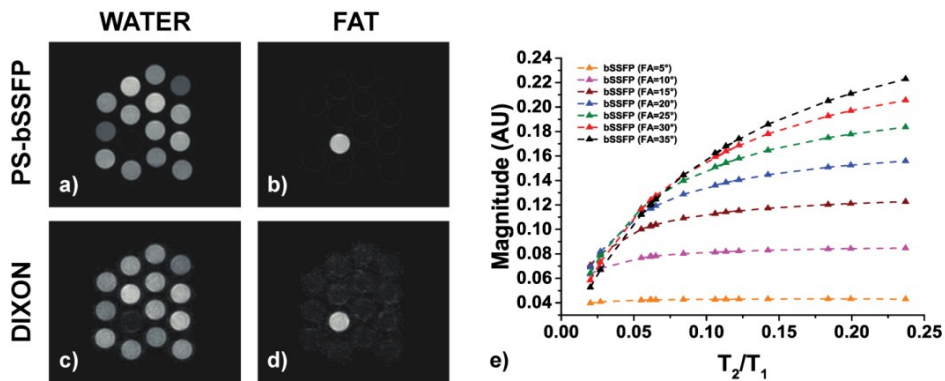


**Figure 2:** MRI images of the phantom. **a, b**) water and fat images obtained with PS-bSSFP sequence (FA = 25°). **c, d**) water and fat images obtained with Dixon sequence. **e**) Simulations showing the maximum signal obtained for the  $T_2/T_1$  ratios of the phantoms measured experimentally. Data are plotted for a bSSFP sequence with TR = 2TE = 2.4 ms.

## Static *in vivo* MR experiment

The SNR values calculated *in vivo* from the series of 20 static images are shown in **Figure 4**. For the knee, three regions of interest were selected: quadriceps muscle, PCL and patellofemoral cartilage (**Figure 4a-c**). The results are indicated as average over 5 subjects  $\pm$  standard deviation.

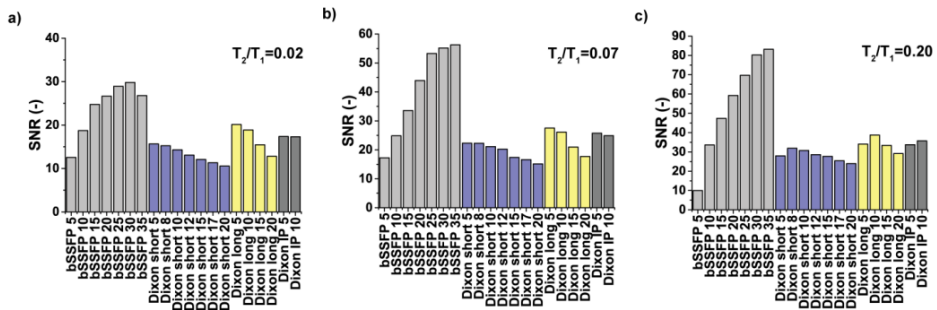


**Figure 3:** a, b, c) Bar plots showing the SNR for tubes with different T<sub>2</sub>/T<sub>1</sub> ratios, calculated from water images obtained with different sequences. Light gray color indicated images obtained for PS-bSSFP sequences, purple indicates the SNR for the Dixon Short sequence, yellow indicates the SNR for the Dixon Long sequence and dark grey the Dixon sequence with in-phase and out-of-phase echoes.

Images of the knee obtained with the proposed method showed higher SNR of posterior cruciate ligament, cartilage and muscles in the water-only image when compared to the water-only image obtained from the Dixon reconstructions. For all the investigated structures, slightly higher SNR was observed for IP-OP Dixon and the long Dixon when compared to the short Dixon scan, although even in these cases the SNR of the PS-bSSFP with the optimal flip angle was higher. The PCL showed lower optimal flip angle for the PS-bSSFP sequence when compared to the cartilage and muscle.

Similar results were obtained for the wrist (**Figure 4d and e**). The results are indicated as average over 4 subjects  $\pm$  standard deviation. The overall SNR for the structures of the wrist were lower than in the knee, and the PS-bSSFP sequences were shown to perform better than the Dixon scans.

The difference in SNR between the PS-bSSFP scan (FA=25°) and the Short Dixon with (FA=10°) was statistically different for all the investigated structures in the knee:  $p=0.0451$  for the PCL,  $p=0.0006$  for the muscle and  $p=0.0411$  for the cartilage. On the other hand, for the wrist scans, statistically significant differences in SNR were only observed in the muscle ( $p=0.0003$ ), while no significance difference was observed in cartilage.

## Dynamic *in vivo* MR experiment

Good image quality of moving knees in real time was obtained using the proposed method. The temporal resolution achieved (5 fps) allowed for good depiction of the different anatomical structures without apparent motion artifacts.

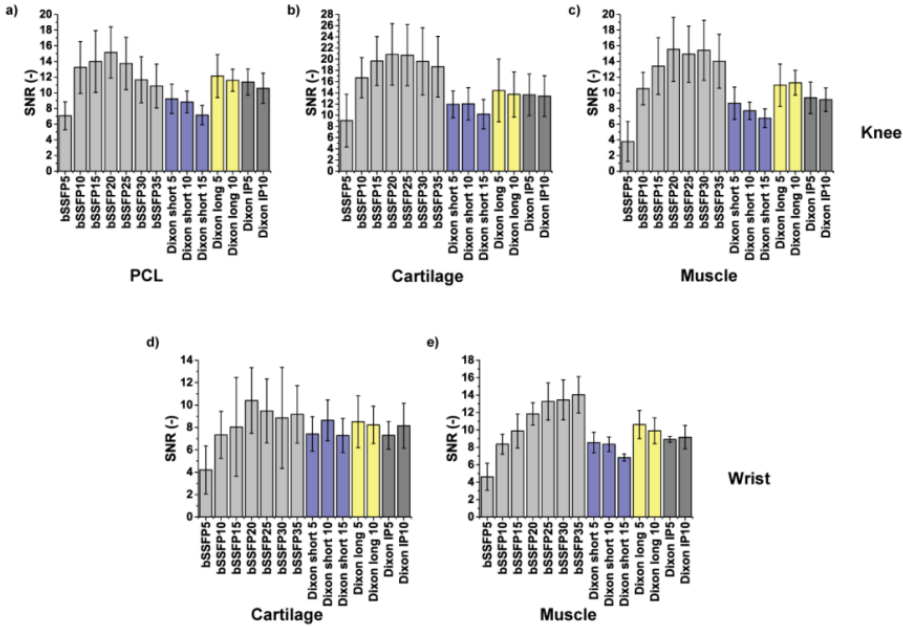


**Figure 4:** a, b, c) Bar plots of SNR calculated in the knee of the 5 volunteers in the PCL, patellar cartilage and quadriceps muscles respectively. d, e) Bar plots of SNR calculated in the wrist of the 4 volunteers in the articular cartilage and muscles respectively. Results are expressed as mean  $\pm$  standard deviation. Light gray color indicates the SNR for the PS-bSSFP sequences, purple indicates the SNR for the Dixon Short sequence, yellow indicates the SNR for the Dixon Long sequence and dark grey the Dixon sequence with in-phase and out-of-phase echoes.

Movies of a moving knee obtained using the PS-bSSFP technique are presented in **Supporting Video S1** and **S2**. The separation of water and fat components in the images allowed visualization of water structures with positive contrast. Water images obtained with the PS-bSSFP method are shown in **Figure 5a** and **e** for two different flexion positions of the knee. In the Dixon images presented for the same positions (**Figure 5c** and **g**), residual signal from fat components around the PCL reduced its contrast.

Water and fat tissues were occasionally misclassified in the PS-bSSFP images at the locations in which banding artifacts were present in the original magnitude images. These banding artifacts occur when the resonance frequency shift of water exceeds

$\pm 220$  Hz. However, these artifacts were mostly present at the edges of the field of view and in the susceptibility-matching pillow, and did not hinder image analysis of the relevant anatomical features of the knee. The presence of the pillow filled with pineapple juice placed on the anterior side of the tibia was effective in reducing artifacts in the leg and misclassification appeared to be mostly confined to the pillow (**Figure 5a** and **e**).

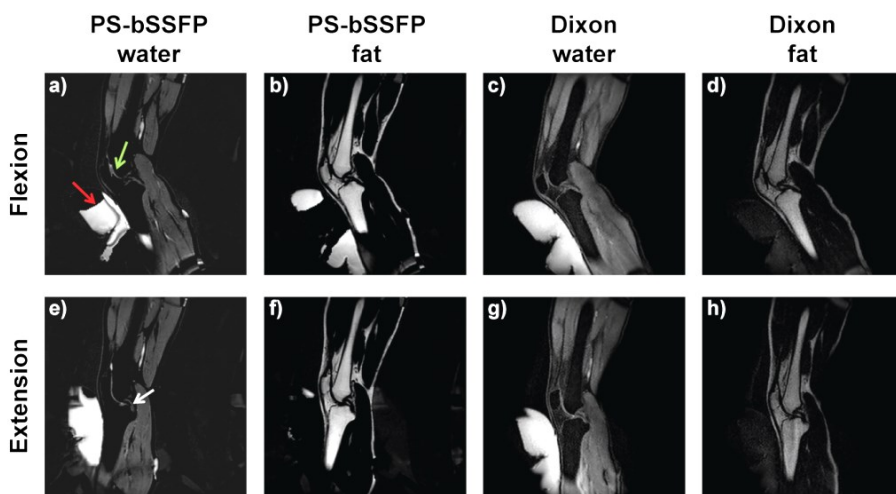


**Figure 5:** Snapshots of the knee of a male healthy volunteer during flexion/extension. **a, e**) Water images obtained with the PS-bSSFP approach. **b, f**) Fat images obtained with the PS-bSSFP approach. **c, g**) Water images obtained with the Dixon method. **d, h**) Fat images obtained with the Dixon method. The bright signal in front of the leg originates from a pillow filled with pineapple juice, used for susceptibility matching. The Posterior Cruciate ligament (PCL) and patellofemoral cartilage are indicated by the white and green arrows, respectively. In the PS-bSSFP images, incorrect water or fat assignment occasionally occurs outside the most relevant areas in the knee, as indicated by the red arrow.

Dixon images also showed occasional water fat misclassification, which was mostly obvious as the presence of signal from the susceptibility-matching pillow in the fat images (**Figure 5d** and **h**) at all knee positions. However, as in the case of the PS-bSSFP scans, with the water/fat swap outside the region of interest, the resulting overall image quality was not compromised.

Tissue with short  $T_2$  components such as PCL and patellofemoral cartilage could be visualized with positive contrast. Subtle details such as the movement pattern of the PCL during motion could be appreciated, with high curvature at relaxed extension (**Figure 6l**) and decreasing curvature for increasing flexion angle (**Figure 6a**), in agreement with the hypothesis that the PCL is slack at full flexion and is increasingly loaded for increasing flexion angles of the knee.

The proposed method for fat suppression in real time MRI of moving joints is also suitable for dynamic wrist imaging. The articular cartilage of the metacarpal bones could be visualized in great detail during active wrist motion due to the suppression of fat components in the bones in the PS-bSSFP scan (**Figure 7a, b, e and f**). On the other hand, the Dixon sequence (**Figure 7c, d, g and h**) shows reduced SNR and overall image quality, which does not allow for a good delineation of the cartilage.

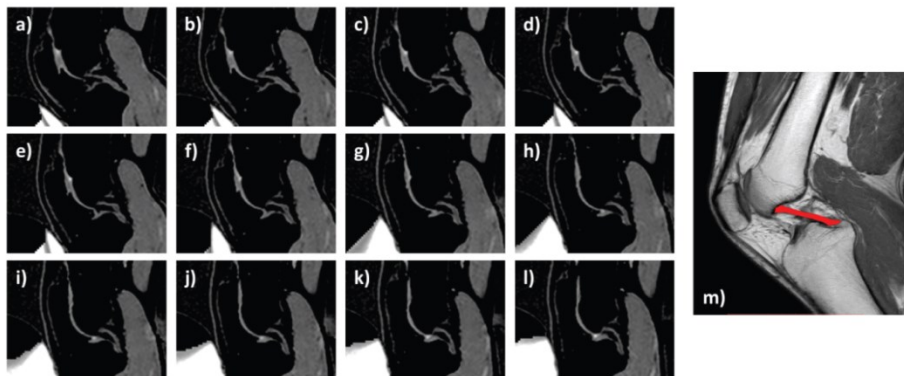


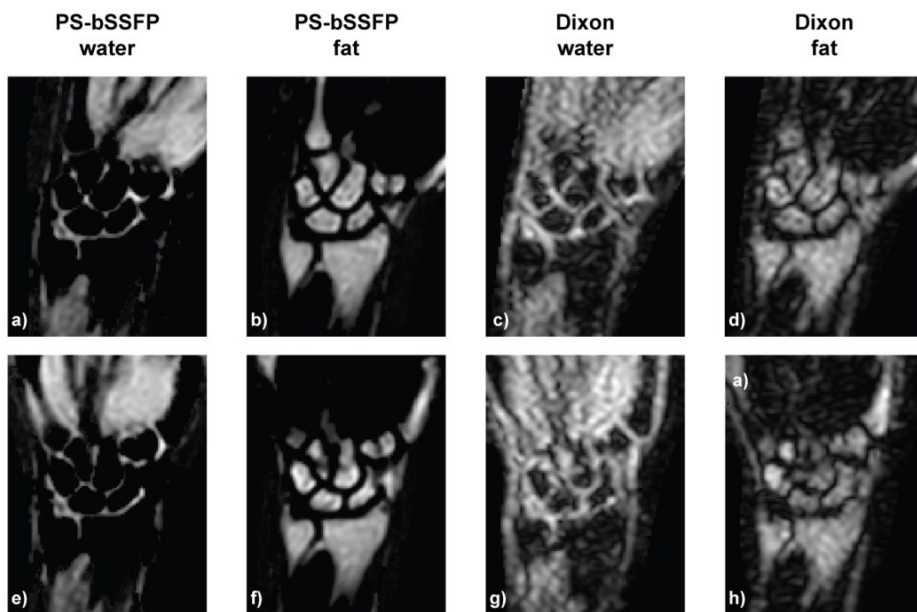
**Figure 6:** a-l) Dynamic water images representing a flexion/extension movement. Images were obtained using the PS-bSSFP method for water fat separation. The volunteer performed the flexion/extension movement in 9.6 seconds. With the achieved temporal resolution (5 fps) the motion was captured in 48 frames. Here every fourth dynamic scan is depicted. m) Anatomical PD weighted scan (not from the same subject). The PCL is indicated in red.

## Image scoring

The results of the scoring by two musculoskeletal radiologists for the dynamic knee scans are presented in **Figure 8**. The movies of water images obtained from the PS-bSSFP sequence obtained higher scores than the corresponding movies obtained with Dixon, although only the differences in overall visibility of PCL, overall sharpness and overall contrast proved to be significant ( $p < 0.05$ ).

## Discussion

With the proposed method, dynamic images with fat suppression were obtained that allowed to observe the knee and wrist joints during motion. Tissues with short  $T_2$  such as cartilage and ligaments could be observed dynamically with positive contrast. Thanks to the suppression of fat tissue surrounding the PCL, its pattern of motion and stretching could be appreciated.



5

**Figure 7:** Snapshots of the wrist of a female healthy volunteer during pronation/supination. **a, e)** Water images obtained with the PS-bSSFP approach. **b, f)** Fat images obtained with the PS-bSSFP approach. **c, g)** Water images obtained with the Dixon method. **d, h)** Fat images obtained with the Dixon method.

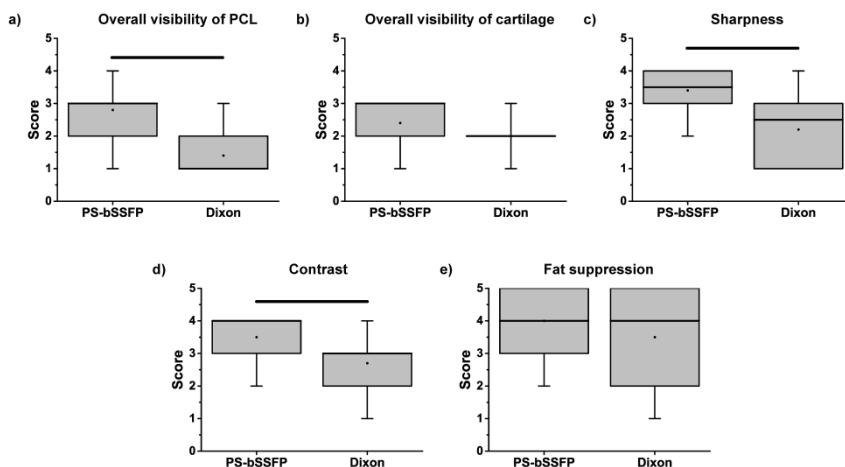


**Figure 8:** Boxplots for scores of **a)** overall visibility of PCL, **b)** overall visibility of cartilage, **c)** overall sharpness, **d)** overall contrast and **e)** fat suppression in area of interest. Whiskers indicate the 95% CI and the black line indicates the median value. Brackets mark significant differences ( $P < 0.05$ ).



Previous studies also aimed at characterizing the PCL behavior as a function of the flexion angle of the knee. King et al. (19) used a series of 7 static datasets acquired at different flexion angles of the knee and observed a change in shape and length of the PCL between extension and flexion positions. However, the requirement of static positions may provide a limited view relative to the true biomechanical function and subsequent deformation of the PCL (e.g. due to inertia and visco-elastic effects within the knee joint). Therefore, it is important to create technologies to assess the deformation of tissues like the PCL under *in vivo*, dynamic conditions.

Although the main focus of the present study was the visualization of fibrous soft tissue structures with positive contrast, the present technique could provide advantages also for studies involving bone kinematics. Single slice real time MRI of moving joints has already been employed in a number of studies to measure bone kinematics. Draper et al. (8) measured patellar kinematics in subjects with patellofemoral maltracking using a standing MRI. Patellar bone kinematics was here quantified by manual identification of bony landmarks. The ability of separating fat and water signal during real time MRI could potentially provide facilitated (semi)automatic segmentation of bones, thus minimizing the user input in future dynamic MRI studies using real time techniques.

To the best of our knowledge, the only attempt to increase tissue contrast through fat suppression in real time MRI of moving joints was described by Uecker et al. (28). They proposed the use of a FLASH-based sequence with Dixon water/fat separation. However, the present study shows that, when compared to Dixon acquisition, images obtained with PS-bSSFP show an increased SNR for the same scan time, both *in vivo* and in the phantom experiments and an increased image quality, as assessed by musculoskeletal radiologists.

One of the main advantages of using bSSFP sequences for real time imaging is that the signal intensity in the steady state is largely independent on the TR of the sequence, and this can allow the use of short TRs without compromising the SNR efficiency. On the other hand, the SNR performance of standard RF spoiled gradient echo sequences, as the ones used for the Dixon approach, is strongly dependent on the TR used. In this case, a short TR, although beneficial for speed, results in suboptimal image quality.

Due to need to accommodate at least two echoes within each TR for obtaining water/fat separation in the Dixon sequence, the minimum achievable TR is longer in all the Dixon sequences when compared to bSSFP sequences. In order to compare scans with the same temporal resolution, the scan time was reduced for the Dixon sequence

by using partial Fourier encoding. As expected, this led to a reduction in SNR when compared to the fully sampled k-space. Furthermore, in order to minimize TR, the shortest possible TEs were used (1.0 ms and 1.8 ms), which were not corresponding to either spins being in-phase or out-of-phase. Although the original Dixon method and most related algorithms for water/fat separation (21) require the use of perfectly in-phase or out-of-phase echoes, our reconstruction algorithm was based on the use of asymmetric echoes (10). It was shown that using this algorithm, the choice of “suboptimal echoes” would only cause a decrease in SNR (~35%) without compromising the image quality and the reliability of water and fat separation, which is in agreement with our phantom and *in vivo* data. Furthermore, we emphasize that even for the scans performed using no partial Fourier and exactly in-phase and out-of-phase echoes, the resulting SNR remains lower than in the PS-bSSFP sequence. This suggests that for dynamic imaging of joint movement in real time, where temporal resolution is a major constraint, a PS-bSSFP approach is advisable for water/fat separation since it makes it possible to maintain a relatively high SNR and image quality even at reduced scan time.

The PS-bSSFP approach is in general more sensitive to field inhomogeneities than the Dixon method, since the Dixon algorithm for water/fat separation estimates  $B_0$ , while the water/fat separation based on the phase of a bSSFP image assumes homogeneous  $B_0$ . For our application in knee and wrist motion, thanks to careful shimming, this did not seem to create a major problem. However, for imaging other anatomical areas of the body, that may present higher susceptibility-induced inhomogeneities, water and fat could be misclassified using a PS-bSSFP approach. In these circumstances, a Dixon approach would then be preferable, although it will result in a lower SNR.

Furthermore, while multi-echo approaches such as Dixon are able to differentiate water and fat contributions to the signal within a voxel, the PS-bSSFP approach can only identify water and fat based on their predominance in each voxel. Therefore, voxels that contain predominantly fat will be classified as being fat-only voxels. While some abnormalities such as bone marrow edema, tumors and fatty infiltrations in muscles may produce mixing of water and fat, other situations in which water and fat are mixed in a single voxel are relatively uncommon in the musculoskeletal system and have not been previously reported in ligaments, tendons and cartilage. We therefore do not foresee that this partial volume limitation may hinder visualization and analysis of these structures.

It should be pointed out that both the PS-bSSFP and the Dixon method used in this study assume a single peak model for fat, thus neglecting spectral complexity. While

this assumption could potentially affect the accuracy of water/fat quantification, we believe it will have negligible effect for the purpose of improved visibility of water structures through fat suppression.

It was observed that the SNR obtained for the *in vivo* knee images is in general reduced when compared to the phantom experiments. The determination of the correct  $T_2/T_1$  ratios for some of the investigated structures (ligaments and cartilage) is not straightforward due to the different effect of dipolar interactions on  $T_1$  and  $T_2$ . It is assumed in fact that while the change in orientation with respect to  $B_0$  has a strong influence on  $T_2$  relaxation time, the effect on  $T_1$  is less evident (4). Nonetheless, we expect that in the knee the  $T_2/T_1$  ratio would typically be below 0.05 (17) and our phantom and simulation experiments showed worse SNR in these conditions. For  $T_2/T_1 = 0.02$  the phantom experiments showed that the ratio between SNR for the PS-bSSFP water image and for Dixon was 2, which was reduced to 1.5 for the ligaments in the *in vivo* knee scans. It has to be noticed in general that the SNR gain in the PS-bSSFP scans when compared to the Dixon scans was seen to depend on the  $T_2/T_1$  ratio, with lower gain observed for lower ratios. In the ligaments the  $T_2/T_1$  ratio could be smaller than 0.02, and this could explain the difference in SNR ratio between the phantom and the *in vivo* scans. The generally lower SNR of the *in vivo* experiments when compared to the phantom experiments can partially be explained by the fact that, while for the dynamic imaging of the knee the Torso coil used for signal reception was not in contact with the knee itself in order not to hinder the motion of the joint, for the phantom experiments the coil was placed on top of the phantom, therefore higher SNR is to be expected for the latter case. Future studies will focus on the use of a flexible coil with multiple elements, as the one proposed by Nordmeyer-Massner et al. (23) to improve SNR performance while not reducing the range of motion.

One possible limitation of the current approach is the limited spatial resolution. In fact, due to the need of maintaining the repetition time constant at a value of 2.4 ms, the in plane resolution and the slice thickness are consequently compromised. Although water-fat separation based on phase detection would be possible even for longer TRs, which would allow higher resolution, placing the water and the fat peaks in the center of two adjacent passbands ( $TR = 2.4$  ms) will ensure the greatest robustness against spatial and temporal variation in resonance frequency ( $\pm 220$  Hz at 3 T). Robust methods for dynamic shimming update could be a viable option if one wants to obtain higher spatial resolution images, since it could allow for a longer minimum TR. However, this will consequently lengthen the dynamic time for a single frame. In order to maintain adequate temporal and spatial resolution in combination to high

robustness against  $B_0$  inhomogeneities, a TR of 2.4 ms is the optimal choice for fat suppression in dynamic imaging of moving joints at 3 T.

For SNR calculation in the *in vivo* images, a subtraction method based on twenty identically acquired static images was used. A different approach would have been to determine the SNR in the dynamic images, by calculating the ratio of the signal in a ROI in the tissue and the standard deviation of noise from the background. However, collagen-rich structures, such as ligaments, tendons and cartilage, are known to show different signal intensity as a function of their orientation to the static magnetic field as a result of different strength of dipolar interactions (“magic angle” effect) (4). Since this effect is to be expected as the structures move during the dynamic task, SNR is more reliable when calculated in the static images, although it may not take into account possible changes over time as a function of local differences in  $B_0$  and  $B_1$  as the tissues move through the scanner bore. It is worth mentioning that misregistration of the individual images used for SNR calculation would negatively affect the SNR quantification. Although registration of the individual images was not performed in this study, the difference between subsequent scans showed to be “noise-like” and did not present any structure, indicating a negligible effect of subject movement in the presented results.

Due to the speed and simplicity of the PS-bSSFP method for water-fat separation, this could be useful in the future as a simple addition to clinical routine MRI protocols for joints evaluation, in which currently the joints are only evaluated in a single static position. This could provide additional tools to better understand the cause of pain or impaired function in musculoskeletal diseases.

## Conclusion

The proposed approach for fat suppression of moving joints in real time MRI using a clinically available bSSFP sequence provided detailed information on wrist and knee motion and superior results in terms of image quality and SNR compared to a Dixon method. Ligaments and cartilage could be evaluated with positive contrast due to the suppression of the surrounding fat. Further research on a larger number of subjects and orthopedic patients is still needed to further assess the clinical potential of this technique.

## References

1. **Barrance PJ, Williams GN, Snyder-Mackler L, Buchanan TS.** Altered knee kinematics in ACL-deficient non-copers: A comparison using dynamic MRI. *J Orthop Res* 24: 132–140, 2006.
2. **Borotikar BS, Sheehan FT.** In vivo patellofemoral contact mechanics during active extension using a novel dynamic MRI-based methodology. *Osteoarthr Cartil* 21: 1886–1894, 2013.
3. **Boutin RD, Buonocore MH, Immerman I, Ashwell Z, Sonico GJ, Szabo RM, Chaudhari AJ.** Real-time magnetic resonance imaging (MRI) during active wrist motion - Initial observations. *PLoS One* 8: 10–17, 2013.
4. **Bydder M, Rahal A, Fullerton GD, Bydder GM.** The magic angle effect: A source of artifact, determinant of image contrast, and technique for imaging. *J Magn Reson Imaging* 25: 290–300, 2007.
5. **Coolen BF, Poot DHJ, Liem MI, Smits LP, Gao S, Kotek G, Klein S, Nederveen AJ.** Three-dimensional quantitative T1 and T2 mapping of the carotid artery: Sequence design and in vivo feasibility. *Magn Reson Med* 0: 1–10, 2015.
6. **D'Entremont AG, Nordmeyer-Massner JA, Bos C, Wilson DR, Pruessmann KP.** Do dynamic-based MR knee kinematics methods produce the same results as static methods? *Magn Reson Med* 69: 1634–1644, 2013.
7. **Draper CE, Besier TF, Fredericson M, Santos JM, Beaupre GS, Delp SL, Gold GE.** Differences in patellofemoral kinematics between weight-bearing and non-weight-bearing conditions in patients with patellofemoral pain. *J Orthop Res* 29: 312–317, 2011.
8. **Draper CE, Besier TF, Santos JM, Jennings F, Fredericson M, Gold GE, Beaupre GS, Delp SL.** Using real-time MRI to quantify altered joint kinematics in subjects with patellofemoral pain and to evaluate the effects of a patellar brace or sleeve on joint motion. *J Orthop Res* 27: 571–577, 2009.
9. **Draper CE, Santos JM, Kourtis LC, Besier TF, Fredericson M, Beaupre GS, Gold GE, Delp SL.** Feasibility of using real-time MRI to measure joint kinematics in 1.5T and open-bore 0.5T systems. *J Magn Reson Imaging* 28: 158–166, 2008.
10. **Eggers H, Brendel B, Duijndam A, Herigault G.** Dual-echo Dixon imaging with flexible choice of echo times. *Magn Reson Med* 65: 96–107, 2011.
11. **Fiorentino NM, Lin JS, Ridder KB, Guttman MA, Mc Veigh ER, Blemker SS.** Rectus Femoris Knee Muscle Moment Arms Measured in Vivo During Dynamic Motion With Real-Time Magnetic Resonance Imaging. *J Biomech Eng* 135: 44501, 2013.
12. **Gold GE, Hargreaves BA, Reeder SB, Block WF, Kijowski R, Vasanawala SS, Kornaat PR, Bammer R, Newbould R, Bangerter NK, Beaulieu CF.** Balanced SSFP imaging of the musculoskeletal system. *J Magn Reson Imaging* 25: 270–278, 2007.
13. **Goldfarb JW, Arnold-Anteraper S.** Water-fat separation imaging of the heart with standard magnetic resonance bSSFP CINE imaging. *Magn Reson Med* 71: 2096–2104, 2014.
14. **Gonçalves SI, Ziech MLW, Lamerichs R, Stoker J, Nederveen AJ.** Optimization

- of alternating TR-SSFP for fat-suppression in abdominal images at 3T. *Magn Reson Med* 67: 595–600, 2012.
15. **Hargreaves BA, Vasanawala SS, Nayak KS, Hu BS, Nishimura DG.** Fat-suppressed steady-state free precession imaging using phase detection. *Magn Reson Med* 50: 210–213, 2003.
  16. **Ikemoto Y, Takao W, Yoshitomi K, Ohno S, Harimoto T, Kanazawa S, Shibuya K, Kuroda M, Kato H.** Development of a human-tissue-like phantom for 3.0-T MRI. *Med Phys* 38: 6336–42, 2011.
  17. **Jordan CD, Saranathan M, Bangerter NK, Hargreaves BA, Gold GE.** Musculoskeletal MRI at 3.0 T and 7.0 T: A comparison of relaxation times and image contrast. *Eur J Radiol* 82: 734–739, 2013.
  18. **Kaiser J, Bradford R, Johnson K, Wieben O, Thelen DG.** Measurement of tibiofemoral kinematics using highly accelerated 3D radial sampling. *Magn Reson Med* 69: 1310–1316, 2013.
  19. **King AJ, Deng Q, Tyson R, Sharp JC, Matwiy J, Tomanek B, Dunn JF.** In Vivo Open-Bore MRI Reveals Region- and Sub-Arc-Specific Lengthening of the Unloaded Human Posterior Cruciate Ligament. *PLoS One* 7: 1–10, 2012.
  20. **Leupold J, Hennig J, Scheffler K.** Alternating repetition time balanced steady state free precession. *Magn Reson Med* 55: 557–565, 2006.
  21. **Ma J.** Dixon techniques for water and fat imaging. *J Magn Reson Imaging* 28: 543–558, 2008.
  22. **Martirosian P, Schraml C, Springer F, Schwenzer NF, Würslin C, Schick F, Deimling M.** Positive contrast MR imaging of tendons, ligaments, and menisci by subtraction of signals from a double echo steady state sequence (Sub-DESS). *Magn Reson Med* 71: 294–301, 2014.
  23. **Nordmeyer-Massner JA, De Zanche N, Pruessmann KP.** Stretchable coil arrays: Application to knee imaging under varying flexion angles. *Magn Reson Med* 67: 872–879, 2012.
  24. **Quick HH, Ladd ME, Hoevel M, Bosk S, Debatin JF, Laub G, Schroeder T.** Real-time MRI of joint movement with TrueFISP. *J Magn Reson Imaging* 15: 710–715, 2002.
  25. **Quist B, Hargreaves BA, Cukur T, Morrell GR, Gold GE, Bangerter NK.** Simultaneous fat suppression and band reduction with large-angle multiple-acquisition balanced steady-state free precession. *Magn Reson Med* 67: 1004–1012, 2012.
  26. **Reeder SB, Wintersperger BJ, Dietrich O, Lanz T, Greiser A, Reiser MF, Glazer GM, Schoenberg SO.** Practical approaches to the evaluation of signal-to-noise ratio performance with parallel imaging: Application with cardiac imaging and a 32-channel cardiac coil. *Magn Reson Med* 54: 748–754, 2005.
  27. **Al Saleh H, Hernandez L, Lee KS, Rosas HG, Block WF, Kijowski R.** Rapid isotropic resolution cartilage assessment using radial alternating repetition time balanced steady-state free-precession imaging. *J Magn Reson Imaging* 40: 796–803, 2013.
  28. **Uecker M, Zhang S, Voit D, Merboldt K-D, Frahm J.** Real-time MRI: recent advances using radial FLASH. *Imaging Med* 4: 461–476, 2012.
  29. **Vasanawala SS, Hargreaves BA, Pauly JM, Nishimura DG, Beaulieu CF, Gold**

- GE.** Rapid Musculoskeletal MRI with Phase-Sensitive Steady-State Free Precession: Comparison with Routine Knee MRI. : 1450–1455, 2005.
30. **Vasanawala SS, Pauly JM, Nishimura DG.** Fluctuating equilibrium MRI. *Magn Reson Med* 42: 876–883, 1999.
31. **Vasanawala SS, Pauly JM, Nishimura DG.** Linear combination steady-state free precession MRI. *Magn Reson Med* 43: 82–90, 2000.

## Supplemental Material

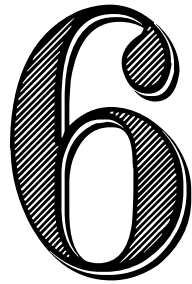
Supplemental material can be found online (doi: [10.1002/mrm.26341](https://doi.org/10.1002/mrm.26341)).

**Supporting Video S1:** Knee of a healthy volunteer during flexion/extension task. Water images are obtained using the PS-bSSFP techniques.

**Supporting Video S2:** Knee of a healthy volunteer during flexion/extension task. Fat images are obtained using the PS-bSSFP techniques.



# Chapter



## Accelerated 4D self-gated MRI of tibiofemoral kinematics

**Valentina Mazzoli\***

Jasper Schoormans\*

Martijn Froeling

Andre M. Sprengers

Bram F. Coolen

Nico Verdonshot

Gustav J. Strijkers

Aart J. Nederveen

\* These authors contributed equally

**NMR in Biomed. 2017;e3791. doi: 10.1002/nbm.3791**



## Abstract

**Introduction:** Anatomical (static) MRI is the most useful imaging technique for evaluation and assessment of internal derangement of the knee, but it does not provide dynamic information and does not allow to study the interaction of the different tissues during motion. Since knee pain is often only experienced during dynamic tasks, the ability to obtain four-dimensional (4D) images of the knee during motion could improve diagnosis and provide a deeper understanding of the knee joint. In this work, we present a novel approach for dynamic, high-resolution 4D imaging of the freely moving knee without a need for external triggering.

6

**Methods:** The dominant knee of 5 healthy volunteers was scanned during a flexion/extension task. To evaluate the effects of non-uniform motion and poor coordination skills on the quality of the reconstructed images, we performed a comparison between fully free movement and movement instructed by a visual cue. The trigger signal for self-gating was extracted using Principal Component Analysis (PCA), and the images were reconstructed using a parallel imaging and compressed sensing reconstruction pipeline. The reconstructed 4D movies were scored for image quality and used to derive bone kinematics through image registration.

**Results:** Using our method, we were able to obtain 4D high-resolution movies of the knee without the need for external triggering hardware. The movies obtained with and without instructions did not significantly differ in terms of image scoring and quantitative values for tibiofemoral kinematics.

**Conclusions:** Our method showed to be robust to extract self-gating signal even for uninstructed motion. This can make the technique suitable for patients that due to pain may find difficult to exactly comply with instructions. Furthermore, bone kinematics can be derived from accelerated MRI without the need for additional hardware for triggering.

## Introduction

Although anatomical magnetic resonance imaging (MRI) is the most commonly used imaging technique for evaluation and assessment of the knee joint, it does not provide dynamic information and therefore does not allow to study the interaction of the different tissues during motion tasks.

The normal mechanism of motion in the tibiofemoral joint depends on both static and dynamic factors. Dynamic interaction between the different tissues during motion plays a fundamental role in the stability of the knee joint. For instance, one of the main dynamic stabilizers of the patella is the quadriceps muscle group. Due to the fundamental role of the musculature in the biomechanical behavior of the patella, active quadriceps contraction is required to get a realistic assessment. This implies that a series of static images is not appropriate for describing the real kinematic behavior. The added value of dynamic imaging has been shown by d'Entremont et al. (7), who compared dynamically acquired MRI datasets with a series of static scans at different knee positions, and found significant differences in kinematic parameters. Furthermore, dynamic MRI of the musculoskeletal system could provide information beyond static imaging to understand the cause of pain. Pain is often absent in static conditions and only present during a specific movement, as it is often the case with impingements for example. The ability to perform this specific movement inside the MRI scanner could provide the radiologist with additional tools to understand the cause of pain and adapt treatment accordingly (14, 28).

Fluoroscopy (1) has been proposed as a powerful method to study bone kinematics. Unlike MRI, it can provide bone kinematics under physiologically relevant loading conditions and during daily motion tasks. However, since it requires ionizing radiation, it is not an ideal candidate for longitudinal studies. Furthermore, fluoroscopy provides very limited soft tissue contrast, thus preventing the study of the interaction of the different soft tissue structures during motion.

MRI has been proposed as an alternative technique to assess tibiofemoral kinematic. Unlike fluoroscopy, it does not make use of ionizing radiation and allows for visualization of soft tissues such as cartilage and muscles. Draper et al. (9, 10) have assessed patellar tilt in patellofemoral dislocation using single slice real-time MRI. While a real-time approach is desirable, it does not allow for volumetric imaging and thus does not provide 3-dimensional information. Joint motion can also be visualized by Phase Contrast (PC)-CINE (synchronized) techniques (26, 27, 31). These methods rely on the acquisitions of a high-resolution static scans and 3 single-slice dynamic

scans. While bone kinematics can be accurately determined using this approach, it is intrinsically unsuitable for 3D visualization of soft tissue motion. Furthermore, since PC techniques encode velocity, they require integration to obtain displacement, which is a procedure prone to error.

Kaiser et al. have developed a 4D MRI imaging technique to study tibiofemoral kinematic in healthy subjects (17) and patients after Anterior Cruciate Ligaments reconstruction (ACL reconstruction) (18). After ACL reconstruction altered kinematic parameters were measured in comparison to the contralateral healthy knee. Abnormal kinematic parameters are believed to induce abnormal cartilage loading patterns, which could be a primary cause of osteoarthritis. Therefore, there is great clinical interest in tools to quantify knee kinematic parameter. Kaiser et al. acquired data using a 3D radial k-space encoding scheme. During data acquisition, the knee flexion angle was constantly externally monitored and this information was used for retrospective sorting of the k-space spokes into a desired number of 3D frames (17).

3D radial methods offer highly incoherent sampling of k-space, which is highly beneficial for compressed sensing reconstruction, and are inherently insensitive to motion artifacts within a given 3D time frame. However, eddy current related artifacts pose a challenge and the image reconstruction is a computationally expensive process.

Stack-of-stars is an alternative 3D MRI acquisition scheme that consists of a radial sampling pattern in the  $k_x - k_y$  plane, and a Cartesian encoding in the  $k_z$  direction. Like 3D radial sampling, it is robust to motion artifacts (13) and appropriate for undersampling and compressed sensing reconstruction. The stack-of-stars has some added benefits compared to 3D radial sampling: a reduced sampling time ( $\pi/2$  times fewer sampling points are required for a fully sampled image), and easier correction strategies for eddy currents effects (4). Furthermore, the Cartesian encoding in the stack direction enables different slices to be reconstructed in parallel, therefore greatly reducing computation times. An advantage of stack-of-stars over Cartesian imaging is that each readout for the central slice encode passes through the center of k-space, thus facilitating retrospective self-gating (11) and eliminating the need for external sensors and/or navigators.

Radial trajectories can be acquired following a golden angle ordering scheme (32), where the angle between two consecutive radial spokes is increased by  $111.246^\circ$ . This approach allows to obtain an almost uniform coverage of k-space for each given number of consecutive spokes, which has the advantage of allowing continuous data acquisition and retrospective sorting of the spokes into several motion frames. The

uniform distribution of the spokes using a golden angle ordering scheme allows for reconstruction of an almost arbitrary number of time frames, thus offering high flexibility in terms of temporal resolution.

For dynamic MRI studies, the knee motion can either be externally imposed, making it less suitable to assess contributions from active muscle contraction in the kinematics (7), or be based on visual/audio instructions, synchronized with an external TTL (transistor-transistor logic) trigger. The latter approach heavily relies on the perfect execution of the motion task, which becomes problematic if the subject is not able to comply with instructions due to poor coordination skills or pain. An alternative approach is the use of an external sensor to continuously monitor the position of the leg in the scanner (17). However this requires additional hardware which is not standard available with clinical MRI scanners.

In this study, we have developed a self-gated 4D stack-of-stars protocol to facilitate 4D imaging of the knee during uninstructed motion. We have performed measurements in healthy volunteers during synchronized as well as free uninstructed movement of the knee, compared image quality, and quantified the derived tibiofemoral kinematics. In addition to dynamic bone imaging, we show feasibility for dynamic visualization of soft tissue structures in the knee.

## Methods

### Subjects

We collected images of the dominant knee of five healthy female volunteers (age  $28 \pm 1$  y/o, weight  $61 \pm 6$  kg, BMI  $22 \pm 3$  kg/m<sup>2</sup>). None of the subjects had a history of knee injury or knee pain. We received informed consent from all the subjects prior to the study, according to our institution's regulations.

### Knee motion

The subjects were placed supine on the scanner table, with a triangular-shaped support underneath their knee, and were asked to perform a knee flexion/extension task. Two sand bags were placed laterally on each side of the knee, in order to prevent sliding and rotation of the knee during the motion task. Three different experiments were performed for each subject: in the first two experiments, the subjects were asked to flex and extend their knee for about 5 minutes at a frequency of 0.67 Hz. In order to improve the repeatability and consistency of the motion task, the subjects were shown a video of a ball bouncing up and down with the required frequency while inside the

scanner, and asked to follow the movement of the ball (“*with instructions*”). Prior to the start of the experiments, subjects were instructed to always touch the support when in the mostly flexed position, and to extend their knees until the edge of the bore would be reached. Consequently, the amount of knee flexion was dependent on the size of the subject, but was kept relatively constant between different repetitions of the motion task for each subject. In order to simulate the effect of poor motor coordination skills, a third experiment was performed without constraints on the frequency of the motion. For this experiment, no instruction was shown and the subjects were asked to move at their preferred pace (“*without instructions*”). For all experiments, the subjects flexed and extended their knees without any external weight.

## Image acquisition

MRI image acquisition was performed with a 3T Philips Ingenia scanner (Philips, Best, The Netherlands). All acquisitions were performed using a custom-built 15 channel flexible coil array (MR Coils BV, Zaltbommel, The Netherlands). The coil array (3x5) was placed around the knee with Velcro straps and centered around the patella. The scan protocol consisted of five different datasets: two high-resolution anatomical datasets to be used for segmentation, and three dynamic scans during the knee-movement tasks previously described.

The first high-resolution anatomical scan was a Turbo Spin Echo (TSE) scan with proton density contrast (TR=1000 ms and TE=29.9 ms, scan time=8 minutes). The second anatomical scan was a Fast Field Echo (FFE) with ProSet fat suppression (TR=10 ms, TE=4.5 ms, scan time 6 minutes). Both scans had a reconstructed matrix size of 352x352x230, and 0.68x0.68x0.7 mm<sup>3</sup> image resolution.

The dynamic scans were obtained using a golden angle stack-of-stars sequence. A spoiled gradient echo sequence was used for data acquisition. Sequence parameters were: matrix size = 160x160x47, voxel size=1.5x1.5x3 mm<sup>3</sup>, FOV=240x240x141 mm<sup>3</sup>, TE/TR=1.3/3.9 ms. For Experiment 1 a flip angle of 20° was used, to obtain high SNR from the bones. For Experiment 2 the same imaging sequence was used, with a flip angle of 5° to enhance signal from collagen-rich structures such as ligaments and cartilage. For Experiment 3 (movement “*without instructions*”) a flip angle of 20° was used. The acquisition was performed with 47 radial stacks with 1.3x slice oversampling. A zy ordering approach was used for the spoke acquisition, meaning that for each radial angle, spokes from all stacks were acquired before advancing to the next radial angle. A total of 1410 spokes was acquired for each stack, with a tiny golden angle increment of 20.89°. A tiny golden angle increment was used instead of 111.246° in

order to reduce eddy current effects, which could lead to artifacts in the reconstructed images (33). Data were continuously acquired during 5min20s of knee flexion/extension. All static and dynamic scans were acquired with readout in the sagittal orientation.

## Image reconstruction

The main steps used in the reconstruction process are summarized in **Figure 1**. Raw scan data was exported and post-processed with MRecon (Gyrotools, Zürich, Switzerland) and Matlab (The Mathworks Inc., Natick, MA). We applied a coil channel compression routine, reducing the number of channels from 24 (15 ch flexible coil + 8 ch embedded in the scanner table + body coil) to 10 virtual channels (3). Eddy current correction was performed offline (4, 24). An inverse fast Fourier transform (FFT) was applied along the fully sampled z-dimension, resulting in a set of 2D k-spaces which could be reconstructed in parallel (11).

The synchronization signal required for self-gating was derived from the center of k-space after FFT in the z-dimension. A principal component analysis (PCA) was calculated on the data matrix from the k-space center of the middle three slices of 10 channels and 1410 spokes. The matrix on which PCA was performed had size 30\*1410, corresponding to 3 slices in 10 channels (rows) and 1410 radial spokes (columns). All principal components were analyzed. We selected the principal components with the highest signal power in the frequency bands [0.6-0.75] Hz, and [0.45-0.9] Hz for the instructed and non-instructed motion respectively (11). Next, the self-gating signal was filtered with a band-pass filter to suppress additional periodic signals not of interest (such as the rotational frequency in k-space). The cutoff frequencies for the band-pass filter were the upper and lower values of the corresponding frequency bands. Subsequently, a peak-finding algorithm was applied to the filtered self-gating signal to define a fixed time-point in each motion cycle. This was used to sort the measured spokes into 20 motion states, each with an equal number of k-space spokes. This resulted in 20 k-space frames containing 70 randomly angled spokes each, which corresponds to an undersampling factor of 3.59 (with respect to a fully sampled radial acquisition).

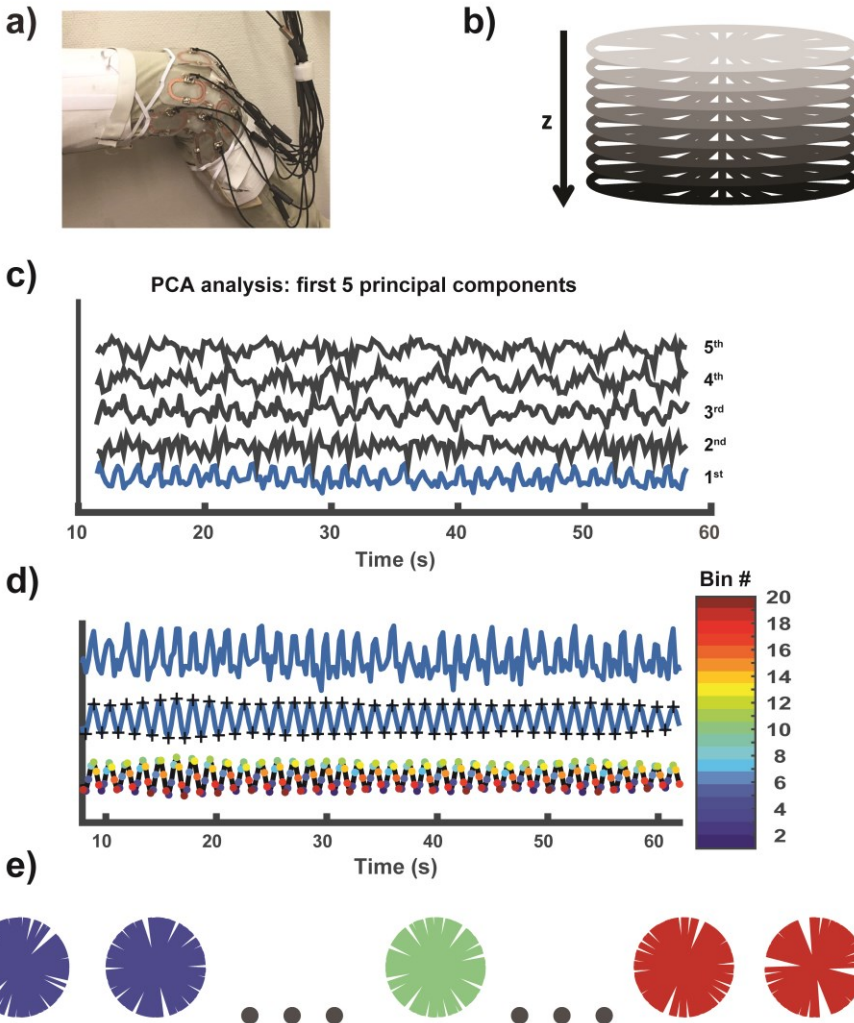


**Figure 1:** Schematic overview of the image acquisition and reconstruction pipeline. All images were acquired using a 15ch custom-built coil that could be wrapped around the subject's knee, offering high signal-to-noise ratio (SNR) without hindering the flexion/extension range of motion (**Figure a**). A stack-of-stars sampling scheme was used (**Figure b**). The 3 center stacks were used to determine the gating signal, based on Principal Component Analysis. The five first principal components are shown in **Figure c**, from bottom to top. The first component, depicted in blue, represents the knee motion frequency. This component is filtered (**Figure d**, middle row) and, after detection of minima and maxima, it is used to correctly assign each radial spoke to a given time bin (**Figure d**, bottom row). The 20 sorted k-spaces, which will be used to reconstruct 20 time frames, have an equal number of uniformly distributed spokes (**Figure e**).

A parallel-imaging compressed-sensing reconstruction was performed using the BART toolbox [DOI: <https://github.com/mrirecon/bart/releases/tag/v0.3.01>]. Relevant parameters were: total-variation L1-regularization (regularization parameters=0.01, in the temporal and three spatial dimensions) and 100 iterations. Reconstructions were performed in parallel for all slices. Dynamic sensitivity maps used for the reconstruction were estimated using the ESPIRiT method (30). Sensitivity map estimation was performed for each dynamic frame independently, based on a sliding windows approach, in which the sensitivity map of frame  $m$  was constructed using  $k$ -lines from frame  $m-1$ ,  $m$ , and  $m+1$ . The average reconstruction time for a dataset was 3 hours on a server with two Intel Xeon E5-2690 processors and 256GB RAM. The reconstruction resulted in a set of 20 3D images for each single flexion extension cycle.

## Image scoring

The movies obtained with and without instructions (Experiment 1 and Experiment 3) were scored in a blinded fashion by two independent musculoskeletal MR imaging experts for sharpness, contrast, bone visibility, fluency of motion, and presence of artifacts. The scores were assigned on a scale from 0 to 3, where 0 was insufficient and 3 was of diagnostic quality. One-way analysis of covariance (ANCOVA) was used to compare the scoring obtained for the movies with instructions and without instructions. The reviewer was set as a covariate and  $p < 0.05$  was considered to be significant

## Image segmentation

The femur and the tibia of the 5 volunteers were segmented from the high resolution FFE scan using a semiautomatic algorithm based on region growing (ITK-snap (34)). The contours were manually adjusted where necessary using the high-resolution proton density weighted scan as an additional reference.

## Determination of bone kinematics

After image reconstruction, a 3D registration pipeline was applied on the datasets obtained from Experiment 1 and Experiment 3 to determine the bone kinematics. The main registration steps are summarized in **Figure 2**. We used a rigid registration pipeline implemented in Elastix (20), with 500 iteration steps and 2 levels of resolution. First, the segmented bone masks were convolved with a Gaussian kernel, and then dilated by a 3x3x3 cubic voxel to increase their volume. The dilation of the masks was needed in order to include the interface between the bone and the adjacent tissues into the registration target, which is the primary feature that drives the registration of



the dynamic datasets. Subsequently, the dynamic datasets were reformatted to an isotropic resolution of  $1.5 \times 1.5 \times 1.5 \text{ mm}^3$ . The femur in the first dynamic frame was registered to the femur in the proton density weighted scans. The registered frame was used as a registration target for the subsequent 19 dynamic frames over the motion cycle. The results of this registration steps were 20 time frames with a static femur, and a moving tibia. An automated selection routine based on minimum detection of the femur translation curve was applied on this dataset to define the first time frame in a consistent way across the volunteers. This corresponded to the knee in full flexion. After femur registration, the same pipeline was repeated for the tibia, using the images with the registered femur as target.

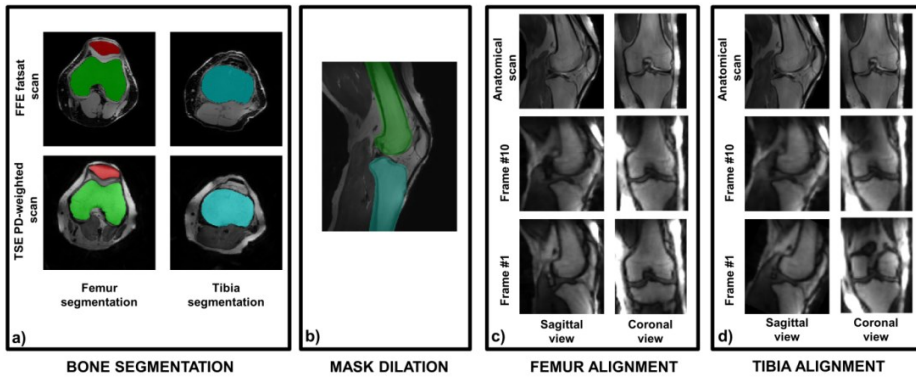


**Figure 2:** Image registration pipeline used to derive tibiofemoral kinematics from the reconstructed 4D images. **a)** 3D bone masks are segmented from the high-resolution anatomical scans. **b)** Bone masks are slightly dilated, in order to contain the interface between bones and other tissues (muscle and fat). **c)** A rigid registration is performed with constraints on the femur, using the anatomical proton density weighted scan as target. The result is a series of dynamic scans in which the femur is fixed. **d)** A second rigid registration step is performed with constraints on the tibia. The first time frame of the previously determined dataset with fixed femur was used as registration target. The result is a series of dynamic scans in which the tibia is fixed. The registration parameters of the last registration steps represent the tibiofemoral kinematics (three rotations and three translations).

The final result was a set of rigid-body trajectories (three rotations and three translations) of the tibia with respect to the femur over the full motion cycle (20 dynamic frames). For each volunteer, the center of rotation was defined in the center of mass of the high-resolution anatomical scan used for segmentation and the axis parallel to the axis of the image. The angles presented refer to the roll pitch and yaw convention, with rotations performed in the order roll, yaw and pitch. All kinematic trajectories were subsequently smoothed using a Gaussian filter with a smoothing factor of 2. Differences between the peak kinematics values measured at time frame #10 (where peak flexion occurred in all the subjects), with and without instructions,

were statistically evaluated using a paired t-test, where  $p < 0.05$  was considered to be significant.

## Results

All volunteers were able to perform the motion task very consistently when instructed via a visual cue, which is illustrated by a narrow peak in the frequency spectrum of the self-gating signal (**Figure 3a** and **4a**). The typical spectra derived from the first principal component for instructed motion are shown in **Figure 3a** (before filtering) and **Figure 3b** (after the application of a band pass filter) for one of the volunteers. On the other hand, for uninstructed motion a worse repeatability of the motion task is observed in the same volunteer, as indicated by the broadening of the motion peak in **Figure 3c** (before filtering) and **Figure 3d** (after the application of a band pass filter).

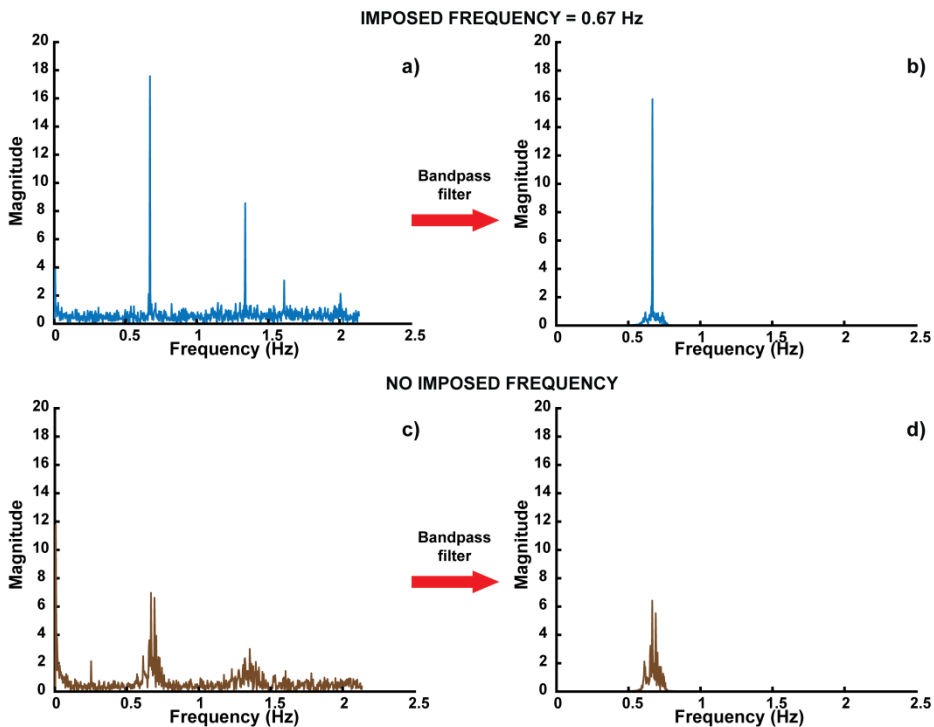


**Figure 3:** First principal component for one volunteer before (figure **a**) and after filtering with a bandpass filter (figure **b**). The main peak corresponds to the frequency of the visual cue (0.67 Hz). When no visual cue is provided, a typical broadening of the motion peak is observed (Figure **c** and **d**, before and after filtering respectively). The Fourier transform of the filtered spectra, shown in Figure **b** and **d**, are used as self-gating signal.

**Figure 4a** and **Figure 4b** show the mean self-gating signal averaged over the 5 volunteers. The agreement between the visual cue frequency and the self-gating frequency spectra of all volunteers (**Figure 4a**) indicates a credible self-gating signal. Without visual cue the peak of the motion frequency was different for the different volunteers (**Figure 4b**) and the peak broadened indicating a larger variability in motion during the ~5 min acquisition (**Figure 4b** and **Figure 4c**).

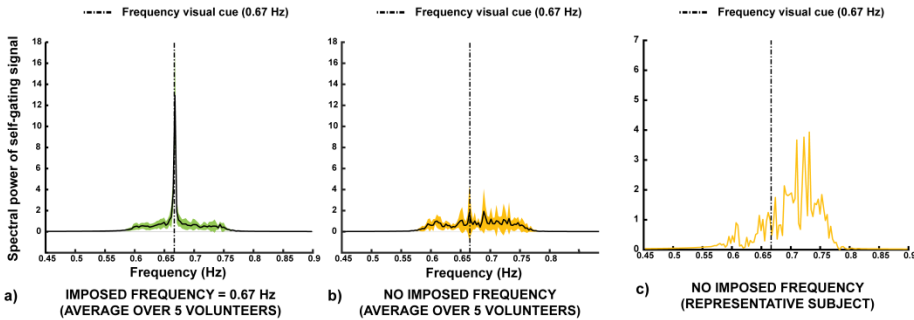


**Figure 4:** Mean self-gating signal, averaged over the 5 volunteers when instructions were given using a visual cue (Figure a) and when the motion task was performed without instructions (**Figure b**). The frequency of the visual cue, corresponding to 0.67 Hz, is indicated as dotted line for reference in **Figure a, b** and **c**, although the visual cue was only used to acquire the data in **Figure a**. **Figure c** shows the representative motion spectrum for one of the volunteers. In this case the frequency peak appears to be broader and at average higher frequency, suggesting that the motion task performed without instruction could be a good way to simulate the motion task performed by an orthopedic patient.

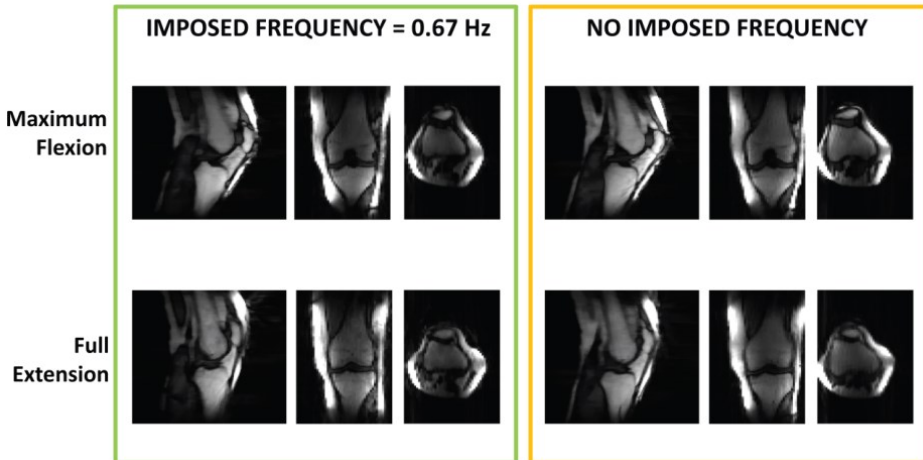


**Figure 5:** Two reconstructed dynamic frames (out of 20) representing the maximum achieved flexion and the full extension for a volunteer. Sagittal, coronal, and transverse views are presented. The left images were acquired when the subject was instructed to move at 0.67 Hz, while during the acquisition of the right images the subject was free to move at his own preferred pace. For both datasets the flip angle used was 20°.

However, in both cases, the self-gating approach based on PCA analysis allowed for a correct assignment of the motion states resulting in 3D movie frames of high quality without significant motion-related blurring and artifacts (**Figure 5**). There was no significant difference in the expert image scores for the movies reconstructed from the instructed and uninstructed acquisitions (**Table 1**).

The range of knee flexion achieved in the scanner by the subjects was  $16.2^{\circ} \pm 1.7^{\circ}$  (motion *with instructions*) and  $14.5^{\circ} \pm 3.0^{\circ}$  (motion *without instructions*) averaged over the 5 subjects. The kinematic parameters representing tibiofemoral motion are presented in **Figure 6**.

Criteria	With instructions	Without instructions	p
<b>Sharpness</b>	2.2	2.1	0.721
<b>Contrast</b>	2.3	2.2	0.692
<b>Bone visibility</b>	2.2	2.3	0.703
<b>Fluency of motion</b>	3.0	2.9	0.331
<b>Artifacts</b>	2.0	1.9	0.668

**Table 1:** Results of scoring of the 4D movies by two musculoskeletal imaging experts. Scores are indicated on a scale from 0 to 3. No statistical difference ( $p > 0.05$ ) was observed in terms of sharpness, contrast, bone visibility, fluency of motion and presence of artifacts when the instructed frequency was 0.67 Hz ("*with instructions*") as compared to free movement ("*without instructions*").

A small tibial external/internal rotation was measured for all subjects with increasing flexion angle. The peak tibial internal rotation across subjects was  $3.4^{\circ} \pm 1.9^{\circ}$  (motion *with instructions*) and  $2.8^{\circ} \pm 2.6^{\circ}$  (motion *without instructions*). Bigger inter-subject variation was detected for the translation degrees of freedom, as compared to rotations.

Taken together, the three rotational and three translational values and their variability, which describe the full range of possible tibiofemoral motions during knee flexion and extension, were similar for instructed and uninstructed tasks.

The mean values for each kinematic parameter was calculated at frame #10, which corresponds to the knee in maximum flexion. The results are presented in **Figure 7**. A paired t-test revealed no differences between the results obtained with and without instructions ( $p > 0.17$ ).

The use of a low flip angle resulted in higher signal from collagen-rich structures such as ligaments and cartilage. In **Figure 8**, two time frames with the knee in maximum

flexion and full extension respectively are shown. The posterior cruciate ligament (PCL) presents high curvature in the extended position, and becomes progressively more stretched as a function of increasing knee flexion angle.

Representative 4D movies obtained for a volunteer moving with and without instruction are presented as supplementary material (see **Video 1** and **2** respectively), together with the movie obtained with instructions and the low flip angle (**Video 3**).

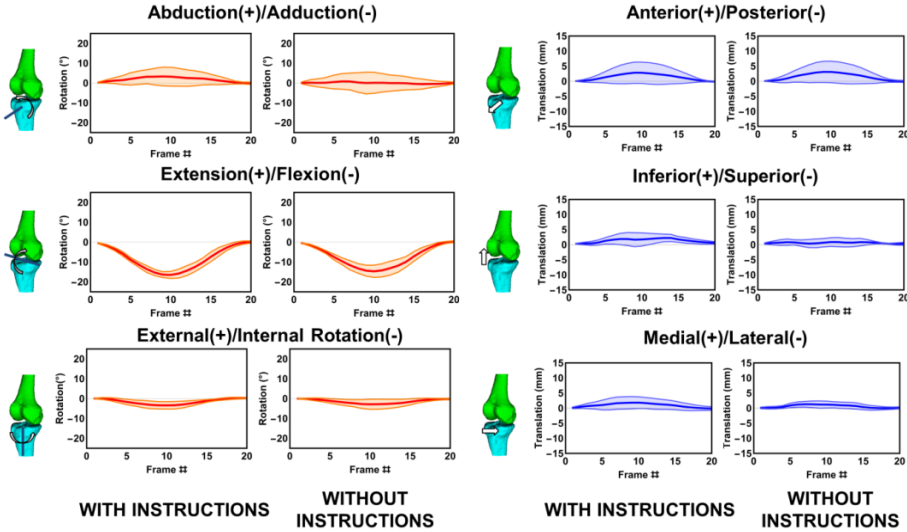


**Figure 6:** Tibiofemoral kinematics averaged over five healthy volunteers (shaded curves represent mean  $\pm$  standard deviation) as a function of frame number. The three rotational degrees of freedom (abduction/adduction, extension/flexion and external/internal rotation) are indicated in red. The three translational degrees of freedom (posterior/anterior, superior/inferior and medial/lateral translation) are indicated in blue. Similar curves are observed when the instructed frequency was 0.67 Hz (“with instructions”) as compared to free movement (“without instructions”).

## Discussion

The proposed golden angle radial sequence enabled acquisition of self-gating signals, which were successfully used for binning the data in 20 time frames over the flexion/extension cycle of the knee. We tested the sequence in 5 female volunteers, which were instructed to keep a constant frequency of 0.67 Hz during motion. Additionally, the volunteers were also asked to perform flexion extension without any visual instruction. We found no statistically significant differences in image quality scores between the two methods. Furthermore, we obtained similar results in terms of tibiofemoral kinematics extracted from the movies with and without instructions.

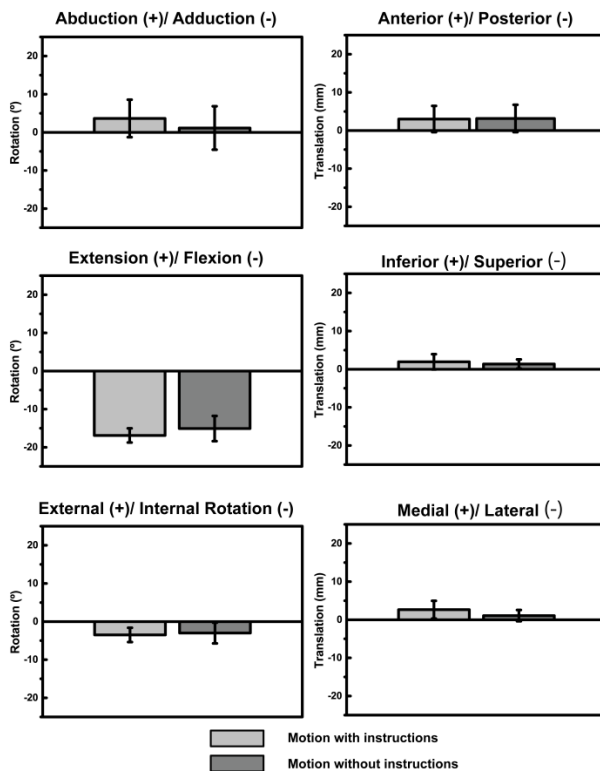


**Figure 7:** Bar graphs representing the tibiofemoral kinematics in the middle time frame (#10). Results are averaged over the five volunteers and the bars indicate standard deviation. No statistical significant differences observed between the peak kinematics parameters obtained with (light gray) and without instructions (dark gray).

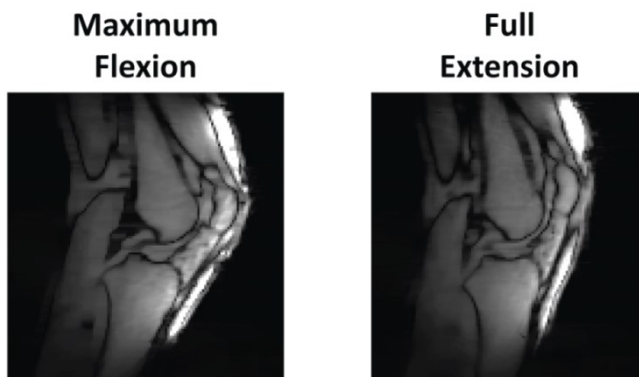


**Figure 8:** Two different reconstructed dynamic frames (out of 20) representing the maximum achieved flexion and the full extension for a volunteer during instructed motion at a frequency of 0.67 Hz. The flip angle used in the acquisition was 5°. The increasing stretching pattern of the PCL for increasing flexion angle of the knee can be observed.

Self-gated MRI is gaining popularity for cardiac imaging (23, 25) as well as in abdominal imaging (6, 8) to estimate motion in relation to radiotherapy treatment planning. The self-gating approach is very attractive since it allows binning of the data in several motion states based on the k-space itself without relying on external triggering devices. Since the binning is done retrospectively, the number of movie frames and the data undersampling factor can be chosen after data acquisition.

A higher number of movie frames with increased data undersampling generally leads to lower SNR and more image artifacts, such as streaking. However, these artifacts can be reduced by compressed sensing image reconstruction (2, 11). In practice, a compromise has to be reached between temporal resolution and presence of image reconstruction artifacts, since a low number of movies frames will result in motion blurring, and a high number of movie frames will lead to undersampling artifacts even with compressed sensing reconstruction. We heuristically found that 20 frames over the flexion/extension cycle was the optimal trade off.

It should be understood that with our technique the motion is not depicted in real time, but rather averaged over several motion cycles. This is not a limitation specific to our particular approach, but rather inherently related to the fact that 3D MRI with sufficient spatial resolution is too slow for real-time imaging even with state-of-the-art acceleration techniques. For the practical application of dynamic knee imaging, this implies that sudden movements such as dislocations cannot be visualized using a gated method. A real-time method (21) would then be required, but this is currently limited to single slice imaging.

Using our imaging method, in combination with novel image registration techniques, we were able to quantify the displacement of the tibia relative to the femur. The current gold standard for determination of bone kinematics is biplane fluoroscopy. This technique allows to acquire functional information during physiologically relevant task such as stair rising (1) and gait (15), with very high temporal and spatial resolution. However, fluoroscopy involves the use of ionizing radiation, which makes its use unpractical for longitudinal studies, and requires highly specialized machines, which are not largely available in clinical settings. On the other hand, MRI scanners are present in virtually every hospital and routinely used for evaluation of the knee joint.

Since we used a closed-bore scanner, we had to deal with a limited range of motion of the knee joint due to geometrical constrains. This limitation could be solved with the use of an open-bore (19) or a vertical MRI system(10), although at the expense of

temporal and spatial resolution related to the typically lower field strength of these systems.

Previous studies focused on determination of normative patellofemoral and tibiofemoral kinematics using Phase Contrast (PC) MRI (26, 27). PC-MRI relies on velocity measurements over time, which can be integrated to provide displacement measurements. The technique proposed by Rebmann et al. (26) is based on an unloaded flexion/extension task that is synchronized with an external trigger. Due to the need for acquiring velocity information along 3 orthogonal directions and the compliance of the subjects, the measurements are limited to 3 single slice acquisition of 2min48s each (through patella, through femur and through tibia). This technique heavily relies on the ability of the subject to keep a constant motion frequency, and small imperfections in the execution of the task can result in spatial and temporal blurring of the velocity values, that may lead to errors in the quantification of bone kinematics and even make the images unusable.

While bone motion can also be evaluated precisely and with higher frame rate using dynamic CT(5), the ability to simultaneously observe soft tissue and bone during motion makes our MRI-based approach unique. We were able to obtain images of the moving knee with relatively high resolution and sufficient soft tissue contrast, as indicated by the image scoring.

In this study, image scoring by experts was used instead of more conventional SNR and CNR measurements due to the use of compressed sensing reconstruction. In fact, when compressed sensing is used, high SNR can be obtained by simply increasing the regularization parameter, without any corresponding increase in image quality or diagnostic information(12).

The images obtained with a low flip angle show high signal from ligaments and cartilage, potentially allowing the evaluation of these tissues during motion. The added values of dynamic imaging for soft tissue assessment in diagnosis still has to be systematically evaluated, and spatial resolution will likely have to be improved in order to increase the usefulness of these images. Nonetheless, the preliminary results presented in this study are a first step towards assessment of soft tissue motion in 3D.

In general, the lack of motion instructions resulted in a poorer repeatability of the task, as indicated by the lack of a well-defined frequency peak in this condition. Although this could lead to an incorrect sorting of the k-space spokes in bins, the expert quality scoring of the movies from the instructed and uninstructed tasks were similar, suggesting that sorting was robust to non-repetitive motion. Although we believe that



visual (or auditory) guidance to motion should always be provided for dynamic MRI studies, conventional acquisition strategies based on prospective gating do not offer robustness against deviation from the given instructions. Many repetitions of the motion, especially under load, can lead to error in the executions of the task. Similarly, execution errors can be expected in orthopedic patients or subjects that due to pain may find it difficult to comply with instructions. Therefore our self-gating method based on PCA and phase binning could be a useful tool for evaluation of those subjects, especially during long and/or loaded acquisitions.

All our acquisitions were obtained using a custom flexible knee coil, consisting of a 3x5 ch coil array. While the coil did add benefits in terms of SNR and image quality, our imaging pipeline is not hardware dependent and can be easily generalized to other anatomies (such as wrist and ankle) and to other coil configurations.

Our self-gating signal was extracted from the three center slices of  $k$ -space. Other methods exist (i.e.  $z$  intensity-weighted projections, ZIP (29)). However, for our application and slice orientation, they proved unreliable. We performed phase binning, instead of magnitude binning often used in respiratory motion (16) because in our experiments the volunteers were instructed to maintain a fixed start and end points for the flexion extension task. In this situation, an almost fixed magnitude of the motion was expected, but significant variation in the frequency could occur. Therefore, phase binning could be used more robustly than magnitude binning.

A general limitation of self-gating methods is that there is no absolute time stamp that indicates beginning and end of the flexion and extension cycle. For image scoring by the experts this was no problem, since movies were visualized in an infinite loop. However, quantification of the bone kinematics analysis requires knowledge about the time frame of maximum flexion and extension. Here we determined these time points by automatic detection of the minimum in the translation curve after the registration of femur, and this represented the maximum achievable extension. The starting point was chosen to be the full extension position, since the bone position was relatively constant for all volunteers in full extensions, while the maximum flexion position was largely dependent on the size of the subjects.

An additional limitation of our self-gating method is that it fails to determine the motion frequency when too much net translation of the knee occurs in the mediolateral direction. In our study, the problem was mitigated by placing sand bags on each side of the knee. In order to completely avoid this problem, a motion device should be designed that restricts the range of motion in the mediolateral direction,

while allowing full range of motion in the sagittal plane. Furthermore, a loading device could also increase the physiological values of the kinematic measurements, as compared to the “no-load” condition applied in this study.

We did not define an anatomical frame of reference based on the tibia and the femur at this point. Therefore our kinematic results cannot be directly compared previous studies (26, 27). The determination of an anatomical frame of reference based on bony landmarks could introduce additional inter-subject variation(22). Therefore, for the purpose of this study, we preferred a direct comparison of the derived motions from the datasets obtained with and without instructions.

## Conclusions

In conclusion, we have implemented a method to obtain self-gated 4D images of the moving knee using a golden angle radial sampling of k-space. Using a stack-of-stars sampling scheme we were able to derive the trigger signal directly from the data itself, without the need of any external monitoring device. Compressed sensing allowed for high undersampling factor (3.59-fold), and the achieved scan time allows application of the technique as an addition to standard clinical protocols. Furthermore, we showed that high-resolution anatomical scans could be co-registered with the dynamic images to provide measurements of bone kinematics. Due to its simplicity, the method shows potential in evaluation of knee structures during motion and to track *in vivo* skeletal kinematics non-invasively in a clinical setting.

## References

1. **Akbarshahi M, Fernandez JW, Schache AG, Pandy MG.** Subject-specific evaluation of patellofemoral joint biomechanics during functional activity. *Med Eng Phys* 36: 1122–1133, 2014.
2. **Benkert T, Feng L, Sodickson DK, Chandarana H, Block KT.** Free-Breathing Volumetric Fat/Water Separation by Combining Radial Sampling, Compressed Sensing, and Parallel Imaging. *Magn Reson Med* 576: 565–576, 2016.
3. **Buehrer M, Pruessmann KP, Boesiger P, Kozerke S.** Array compression for MRI with large coil arrays. *Magn Reson Med* 57: 1131–1139, 2007.
4. **Buonincontri G, Methner C, Krieg T, Carpenter TA, Sawiak SJ.** Trajectory correction for free-breathing radial cine MRI. *Magn Reson Imaging* 32: 961–964, 2014.
5. **Carelsen B, Jonges R, Strackee SD, Maas M, Van Kemenade P, Grimbergen CA, Van Herk M, Streekstra GJ.** Detection of in vivo dynamic 3-D motion patterns in the wrist joint. *IEEE Trans Biomed Eng* 56: 1236–1244, 2009.
6. **Cruz G, Atkinson D, Buerger C, Schaeffter T, Prieto C.** Accelerated motion corrected three-dimensional abdominal MRI using total variation regularized SENSE reconstruction. *Magn Reson Med* 1498: 1484–1498, 2015.
7. **D’Entremont AG, Nordmeyer-Massner JA, Bos C, Wilson DR, Pruessmann KP.** Do dynamic-based MR knee kinematics methods produce the same results as static methods? *Magn Reson Med* 69: 1634–1644, 2013.
8. **Deng Z, Pang J, Yang W, Yue Y, Sharif B, Tuli R, Li D, Fraass B, Fan Z.** Four-dimensional MRI using three-dimensional radial sampling with respiratory self-gating to characterize temporal phase-resolved respiratory motion in the abdomen. *Magn Reson Med* 75: 1574–1585, 2016.
9. **Draper CE, Besier TF, Fredericson M, Santos JM, Beaupre GS, Delp SL, Gold GE.** Differences in patellofemoral kinematics between weight-bearing and non-weight-bearing conditions in patients with patellofemoral pain. *J Orthop Res* 29: 312–317, 2011.
10. **Draper CE, Besier TF, Santos JM, Jennings F, Fredericson M, Gold GE, Beaupre GS, Delp SL.** Using real-time MRI to quantify altered joint kinematics in subjects with patellofemoral pain and to evaluate the effects of a patellar brace or sleeve on joint motion. *J Orthop Res* 27: 571–577, 2009.
11. **Feng L, Axel L, Chandarana H, Block KT, Sodickson DK, Otazo R.** XD-GRASP: Golden-angle radial MRI with reconstruction of extra motion-state dimensions using compressed sensing. *Magn Reson Med* 75: 775–788, 2016.
12. **Feng L, Benkert T, Block KT, Sodickson DK, Otazo R, Chandarana H.** Compressed sensing for body MRI. *J Magn Reson Imaging* 45: 966–987, 2017.
13. **Glover GH, Pauly JM.** Projection Reconstruction Techniques for Reduction of Motion Effects in MRI. *Magn Reson Med* 28: 275–289, 1992.
14. **Gold GE.** Dynamic and functional imaging of the musculoskeletal system. *Semin Musculoskelet Radiol* 7: 245–8, 2003.
15. **Guan S, Gray HA, Keynejad F, Pandy MG.** Mobile biplane X-Ray imaging system for measuring 3D dynamic joint motion during overground gait. *IEEE Trans*

- Med Imaging* 35: 326–336, 2016.
16. **Han F, Zhou Z, Cao M, Yang Y, Sheng K, Hu P.** Respiratory motion-resolved, self-gated 4D-MRI using rotating cartesian k-space (ROCK). *Med Phys* 44: 1359–1368, 2017.
  17. **Kaiser J, Bradford R, Johnson K, Wieben O, Thelen DG.** Measurement of tibiofemoral kinematics using highly accelerated 3D radial sampling. *Magn Reson Med* 69: 1310–1316, 2013.
  18. **Kaiser J, Vignos MF, Liu F, Kijowski R, Thelen DG.** American Society of Biomechanics Clinical Biomechanics Award 2015: MRI Assessments of Cartilage Mechanics, Morphology and Composition Following Reconstruction of the Anterior Cruciate Ligament. *Clin Biomech* 34: 38–44, 2016.
  19. **King AJ, Deng Q, Tyson R, Sharp JC, Matwiy J, Tomanek B, Dunn JF.** In Vivo Open-Bore MRI Reveals Region- and Sub-Arc-Specific Lengthening of the Unloaded Human Posterior Cruciate Ligament. *PLoS One* 7: 1–10, 2012.
  20. **Klein S, Staring M, Murphy K, Viergever MA, Pluim JPW.** Elastix: A toolbox for intensity-based medical image registration. *IEEE Trans Med Imaging* 29: 196–205, 2010.
  21. **Mazzoli V, Nederveen AJ, Oudeman J, Sprengers A, Nicolay K, Strijkers GJ, Verdonchot N.** Water and fat separation in real-time MRI of joint movement with phase-sensitive bSSFP. *Magn Reson Med* 78: 58–68, 2017.
  22. **Morton NA, Maletsky LP, Pal S, Laz PJ.** Effect of Variability in Anatomical Landmark Location on Knee Kinematic Description. *J Orthop Res* 9: 1221–1230, 2007.
  23. **Motaal AG, Coolen BF, Abdurrachim D, Castro RM, Prompers JJ, Florack LMJ, Nicolay K, Strijkers GJ.** Accelerated high-frame-rate mouse heart cine-MRI using compressed sensing reconstruction. *NMR Biomed* 26: 451–457, 2013.
  24. **Moussavi A, Untenberger M, Uecker M, Frahm J.** Correction of gradient-induced phase errors in radial MRI. *Magn Reson Med* 71: 308–312, 2014.
  25. **Paul J, Divkovic E, Wundrak S, Bernhardt P, Rottbauer W, Neumann H, Rasche V.** High-resolution respiratory self-gated golden angle cardiac MRI: Comparison of self-gating Methods in combination with k-T SPARSE SENSE. *Magn Reson Med* 73: 292–298, 2015.
  26. **Rebmann AJ, Sheehan FT.** Precise 3D skeletal kinematics using fast phase contrast magnetic resonance imaging. *J Magn Reson Imaging* 17: 206–213, 2003.
  27. **Seisler AR, Sheehan FT.** Normative three-dimensional patellofemoral and tibiofemoral kinematics: A dynamic, in vivo study. *IEEE Trans Biomed Eng* 54: 1333–1341, 2007.
  28. **Shapiro LM, Gold GE.** MRI of weight bearing and movement. *Osteoarthr Cartil* 20: 69–78, 2012.
  29. **Spincemaille P, Liu J, Nguyen T, Prince MR, Wang Y.** Z intensity-weighted position self-respiratory gating method for free-breathing 3D cardiac CINE imaging. *Magn Reson Imaging* 29: 861–868, 2011.
  30. **Uecker M, Lai P, Murphy MJ, Virtue P, Elad M, Pauly JM, Vasanawala SS, Lustig M.** ESPIRiT - An eigenvalue approach to autocalibrating parallel MRI: Where SENSE meets GRAPPA. *Magn Reson Med* 71: 990–1001, 2014.

31. **Westphal CJ, Schmitz A, Reeder SB, Thelen DG.** Load-dependent variations in knee kinematics measured with dynamic MRI. *J Biomech* 46: 2045–2052, 2013.
32. **Winkelmann S, Schaeffter T, Koehler T, Eggers H, Doessel O.** An optimal radial profile order based on the golden ratio for time-resolved MRI. *IEEE Trans Med Imaging* 26: 68–76, 2007.
33. **Wundrak S, Paul J, Ulrici J, Hell E, Rasche V.** A small surrogate for the golden angle in time-resolved radial MRI based on generalized fibonacci sequences. *IEEE Trans Med Imaging* 34: 1262–1269, 2015.
34. **Yushkevich PA, Piven J, Hazlett HC, Smith RG, Ho S, Gee JC, Gerig G.** User-guided 3D active contour segmentation of anatomical structures: Significantly improved efficiency and reliability. *Neuroimage* 31: 1116–1128, 2006.

6

## Supplemental material

**Video 1:** Sagittal slice for a volunteer moving with instructions (frequency of motion = 0.67 Hz, flip angle = 20°).

**Video 2:** Sagittal slice for a volunteer moving without instructions (flip angle = 20°).

**Video 3:** Sagittal slice for a volunteer moving with instructions (frequency of motion = 0.67 Hz, flip angle = 5°).



# Chapter

# 7

## Accelerated 4D phase contrast MRI in skeletal muscles contraction

**Valentina Mazzoli**

Lukas M. Gottwald

Eva Peper

Martijn Froeling

Bram F. Coolen

Nico Verdonshot

Andre M. Sprengers

Pim van Ooij

Gustav J. Strijkers

Aart J. Nederveen

**Submitted**

## Abstract

**Introduction:** 3D time-resolved (4D) Phase Contrast MRI can be used to study muscle contraction. However, 3D coverage with sufficient spatiotemporal resolution can only be achieved by interleaved acquisitions during many repetitions of the motion task, resulting in long scan times. The aim of this study was to develop a Compressed Sensing accelerated time-resolved 3D Phase Contrast MRI technique for quantification of velocities and strain rate of the muscles in the lower leg during active plantar- and dorsiflexion.

**Methods:** Nine healthy volunteers were scanned during active dorsiflexion/plantarflexion task. For each volunteer we acquired a reference scan, as well as four different accelerated scans (k-space undersampling factors: 3.14X, 4.09X, 4.89X, and 6.41X) obtained using Cartesian Poisson disks undersampling schemes. The data was reconstructed using a Compressed Sensing pipeline. For each scan, velocity and strain rate values were quantified in the Gastrocnemius Lateralis, Gastrocnemius Medialis, Tibialis Anterior and Soleus.

**Results:** No significant differences in velocity values were observed as a function acceleration factor in the four investigated muscles. The strain tensor calculation resulted in one positive ( $s_+$ ) and one negative ( $s_-$ ) eigenvalue, while the third eigenvalue ( $s_3$ ) was consistently zero for all the acquisitions. No significant differences were observed for the eigenvalues of the strain rate tensor as a function of acceleration factor.

**Conclusions:** Data undersampling combined with Compressed Sensing reconstruction allowed to obtain time-resolved Phase Contrast acquisitions with 3D coverage and quantitative information comparable to the reference scan. The 3D sensitivity of the method can help in understanding the connection between muscle architecture and muscle function in future studies.

## Introduction

Mathematical models of skeletal muscles have been shown to contribute to our understanding of the musculoskeletal system and to optimize surgical treatment (2, 4, 5). However, due to lack of input information, these models often need to rely on considerable simplifications. For instance, it is often assumed that muscles shorten uniformly along their longitudinal axis, while evidence has been provided for more complex contraction patterns and that the direction of shortening is not aligned with the muscle fiber (9, 31). Furthermore, differences in deformation patterns were observed between deep and superficial muscles (9) and between proximal and distal locations (12, 31). Due to the highly complex pattern in muscle contraction and deformation, 3D visualization of contracting muscles would be extremely valuable.

The quantification of muscle deformation occurring during contraction is also a very valuable clinical tool to discriminate between healthy and diseased muscles. Deformation is typically quantified in terms of strain, which is a local property of a tissue that indicates the amount of shortening and lengthening of an object along a given direction, or in terms of strain rate, which is the rate at which the deformation occurs in time. Strain has the same direction as strain rate, and can be calculate by integrating strain rate over time.

Phase Contrast (PC) is an MRI-based technique widely used in the cardiovascular field to measure velocity of blood flowing inside arteries and veins. PC relies on the application of motion sensitizing gradients, which result in phase accumulation of moving spins proportional to their velocities and to the magnitude of velocity encoding magnetic field gradients, the so-called VENC. Gradients are usually applied in three orthogonal directions, allowing for evaluation of tissue velocities in a 3D fashion.

In the field of muscle MRI, PC sequences have been applied to quantify inter alia changes in fascicle length (26), strain rates (21, 31), muscle inertial forces (35) and to gather insight into the complex muscle interaction in tongue movement (11). PC in skeletal muscles can either be performed in a real-time approach or in a CINE (triggered) fashion. Real-time PC has the advantage that measured velocity are not averaged over several motion cycles, thus reducing the need for exact repetition of the task and making the measurement more independent from muscle fatigue (3). On the other hand, real-time PC imaging only allows for imaging of a single slice with velocity encoded in one direction. Encoding of velocity over three directions requires interleaved/synchronized acquisition.



Even when Interleaved (CINE) techniques are used, PC acquisition is usually performed in a single slice fashion. In fact, 3D coverage with sufficient spatiotemporal resolution ( $\sim 3 \times 3 \times 5 \text{ mm}^3$ , 160 ms) can only be achieved by interleaved acquisitions during many repetitions of a motion task, resulting in long scan times ( $>10 \text{ min}$ ). Many repetitions of the motion task can lead to muscle fatigue, which can result in poor reproducibility and can hamper applications in diseased or injured subjects. In general, PC in skeletal muscle requires low VENC, due to the relatively low typical velocity of muscles as compared to flowing blood in veins and arteries. This usually results in lengthened Echo Time (TE) and Repetition Time (TR), which lead to even longer scan times. Therefore, PC in skeletal muscle would greatly benefit from acceleration techniques to reduce the total acquisition time, which would also allow to decrease muscle fatigue, as a reduced number of motion repetitions would be required.

**7**

The aim of this study was therefore to develop a Compressed Sensing (CS) (20) accelerated 4D PC MRI technique for quantifying velocities and strain rates of skeletal muscles in the lower leg during active foot plantar- and dorsiflexion in a clinically feasible scan time.

## Methods

### Subjects

We collected images of the right lower leg of 9 healthy volunteers (4 males, 5 females) with no abnormalities in the lower leg. We received informed consent from all the subjects prior to the study, according to our institution's regulations.

### Data acquisition

MR imaging was performed with an Ingenia 3T MRI scanner (Philips Healthcare, Best, Netherlands) using a 16-channel Torso and 8-channel posterior coil. Subjects were placed supine, feet first in the scanner. The scan protocol consisted of a high-resolution mDixon scan, performed with the leg at rest, and a series of 4D (3D time-resolved) PC scans during active muscle contraction. In order to minimize gross motion of the leg during dynamic data acquisitions, and to minimize displacement over different acquisitions, sand bags were placed on either side of the imaged leg. The scan parameters for the mDixon scan were: RF-spoiled FFE with flip angle  $10^\circ$ , TR=10 ms, 3 echoes with TE<sub>1</sub>=1.96 ms,  $\Delta\text{TE}$ =1.3 ms, matrix size=  $400 \times 160 \times 150 \text{ mm}^3$ , voxel size= $1 \times 1 \times 1 \text{ mm}^3$ . After the anatomical mDIXON scan at rest, the volunteers were instructed to make continuous smooth movements with the right foot between

approximately 30° plantarflexion to 10° dorsiflexion. Each volunteer was instructed to start the motion in the maximum achievable plantarflexed position, move the foot towards a dorsiflexed position and then return to the starting plantarflexed position. During the dynamic task, the volunteers received a visual cue from a bouncing ball displayed on a screen in the scanner room, with cycle duration of 2000 ms to guide their motion task. The MRI scan was motion-triggered at the same pace. Five time-resolved 3D turbo field echo (TFE) PC acquisitions were executed during the motion task: one reference scan and four accelerated acquisitions. In order to take into account the potential effect of muscle fatigue as a function of the scan number, the order in which the dynamic scans were performed was randomized. Scan parameters for the reference 3D TFE scan were: TFE-factor=3, half scan in phase-encoding direction=0.6, matrix size=153x53x30, voxel size=3x3x5 mm<sup>3</sup>, TE/TR=4.5/6.4 ms, VENC=12 cm/s in three orthogonal directions (FH, AP, LR), and a temporal resolution of 160 ms. Accelerated acquisitions were performed with the same parameters, but without half scan and with different k-space undersampling schemes (k-space undersampling factors: 3.14X, 4.09X, 4.89X, and 6.41X) as shown in **Figure 1**. For the undersampled scans, the scanner software was modified to acquire a predefined number of sampling profiles (AMC CSENSE patch, version 5.1.8). The sampling profiles ( $k_y$ ,  $k_z$ ) were generated in MATLAB (The MathWorks Inc., Natick, MA, USA) using the Berkeley Advanced Reconstruction Toolbox (BART) (33) and were designed according to a Poisson-disk pattern with variable density (14). Total acquisition times for the five scans were 10:52 (reference scan), 5:38, 4:20, 3:38, and 2:46 min, corresponding to 326, 169, 130, 109, and 83 executions of the motion task, respectively.

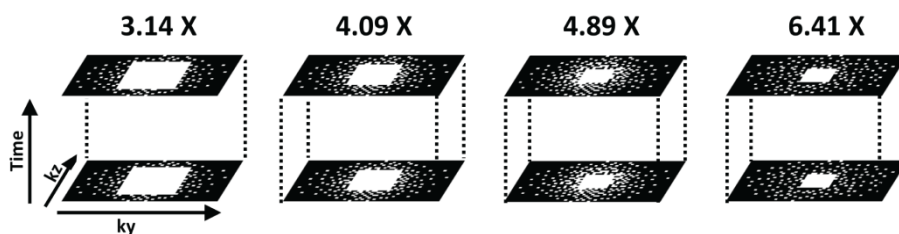


**Figure 1:** Undersampling patterns in ( $k_y$ ,  $k_z$ )-space for the different acceleration factors (k-space undersampling factors: 3.14X, 4.09X, 4.89X, and 6.41X). For all undersampling factors, the center of k-space was fully sampled. The outer points followed a Poisson disk distribution with variable density.

## Image reconstruction

Raw data was imported in MATLAB using ReconFrame (Gyrotools, Zurich, CH) and CS reconstruction was performed using the BART toolbox, with a wavelet transform in space ( $x$ ,  $y$ ,  $z$ ) and an additional sparsifying total variation (TV) transform in space ( $x$ ,  $y$ ,

z) and time. The L1-regularization was performed with a regularization parameter of  $r=0.01$  for both wavelet and TV transform, and 50 iteration steps.

## Data processing

Four muscle groups in the lower leg (Tibialis Anterior, TA; Soleus, SOL; Gastrocnemius Lateralis, GCL; and Gastrocnemius Medialis, GCM) were manually segmented on water mDixon scans. Segmentation was performed using ITK-snap (36). In order to take into account the change in shape of the different muscle groups during the motion task, image registration was performed. For this purpose, the mDixon scan was downsampled to the same resolution of the PC data and registered to each motion phase of the magnitude scan. The registration pipeline was repeated for each of the five acquired datasets (reference scan and five accelerated scans), and it consisted of a b-spline registration approach, with two levels of resolution. All the registration steps were performed using Elastix (17). Subsequently the transformation used to register the downsampled high-resolution scan was applied to the masks of each muscle group. This resulted in a set of muscle segmentations for each one of the 12 time points. These masks were subsequently used to extract the values of velocity and strain rate over the whole muscle groups.

## Strain rate calculation

As a first preprocessing step, the phase images were corrected by subtracting from each time frame the average phase over all the 12 time frames. This is based on the assumption that the net velocity over the full dorsiflexion/plantarflexion cycle is zero (28). Since strain calculation involves the spatial gradients, which are extremely sensitive to noise, each 3D velocity image was filtered prior to further calculation. A Savitzky-Golay filter (25) was used for this purpose because of its generally good performance in denoising data, while keeping peak values preserved.

Calculation of strain rate started from the measured 3D velocity vector  $\mathbf{v}(x,y,z)=v_x(x,y,z)\mathbf{x}+v_y(x,y,z)\mathbf{y}+v_z(x,y,z)\mathbf{z}$  and the 3D spatial gradient of this velocity vector:

$$\mathbf{L} = \begin{pmatrix} \frac{\partial v_x}{\partial x} & \frac{\partial v_x}{\partial y} & \frac{\partial v_x}{\partial z} \\ \frac{\partial v_y}{\partial x} & \frac{\partial v_y}{\partial y} & \frac{\partial v_y}{\partial z} \\ \frac{\partial v_z}{\partial x} & \frac{\partial v_z}{\partial y} & \frac{\partial v_z}{\partial z} \end{pmatrix}$$

The symmetric part of the strain rate tensor was then calculated according to:

$$\mathbf{S} = \frac{1}{2}(\mathbf{L} + \mathbf{L}^T) = \frac{1}{2} \begin{pmatrix} 2 \frac{\partial v_x}{\partial x} & \frac{\partial v_x}{\partial y} + \frac{\partial v_y}{\partial x} & \frac{\partial v_x}{\partial z} + \frac{\partial v_z}{\partial x} \\ \frac{\partial v_x}{\partial y} + \frac{\partial v_y}{\partial x} & 2 \frac{\partial v_y}{\partial y} & \frac{\partial v_y}{\partial z} + \frac{\partial v_z}{\partial y} \\ \frac{\partial v_x}{\partial z} + \frac{\partial v_z}{\partial x} & \frac{\partial v_y}{\partial z} + \frac{\partial v_z}{\partial y} & 2 \frac{\partial v_z}{\partial z} \end{pmatrix}$$

The tensor  $\mathbf{S}$  was subsequently diagonalized to obtain the three eigenvalues. The eigenvalues were then sorted on a pixel-by-pixel basis in the following order: maximum negative eigenvalue ( $s_-$ ), maximum positive eigenvalue ( $s_+$ ), remaining eigenvalue ( $s_3$ ). The principal direction of strain can be considered in first approximation to be aligned with the axis of the muscles fibers within a given voxel. Therefore, the strain will be associated with negative eigenvalues ( $s_-$ ) during muscle contraction and positive values ( $s_+$ ) during muscle relaxation. A schematic drawing of principal strain directions is presented in **Figure 2**.

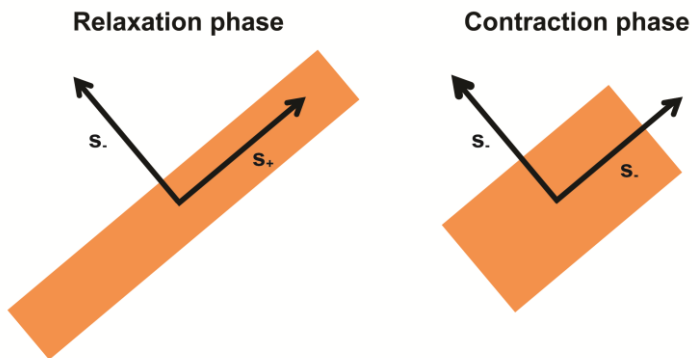


**Figure 2:** Schematic drawing of a muscle fiber during relaxation and contraction.

## Statistical Analysis

One way ANOVA was used to compare the mean FH velocities, the mean magnitude velocities and the mean strain rates as a function of acceleration factors for the different muscle groups (GCL, GCM, SOL, and TA) for frame #3 and frame #9 (peak negative and peak positive velocity). Statistical analysis was performed in SPSS.  $p < 0.05$  was considered to be significant.

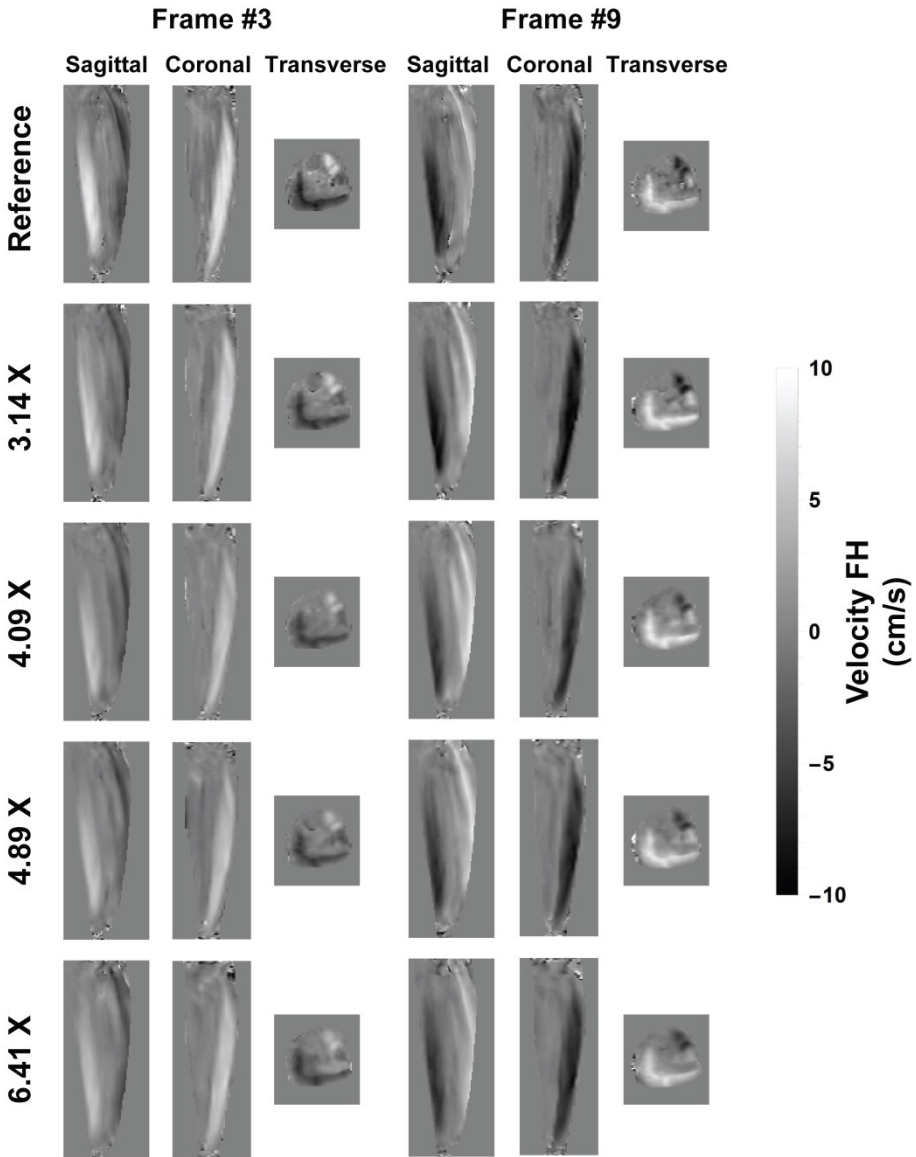


**Figure 3:** Representative FH velocity for a volunteer in three orthogonal planes (sagittal, coronal and transverse) for the reference scan and for the 4 accelerated scans. The antagonist function of the muscles in the posterior and anterior compartment can be observed for all accelerated scans, as indicated by the opposite sign of the velocity.

## Results

The data acquisition was successful for all volunteers. All results were visually inspected and judged to be of sufficient quality to continue with further analysis.

**Figure 3** shows velocity images reconstructed from undersampled data in comparison to the reference scan for a male volunteer. Phase images clearly show consistency with the muscle function. In fact, antagonist muscles (posterior and anterior compartments) show opposite velocity in both visualized frames (#3 and #9). The average velocities for the four muscle groups are shown in **Figure 4** (mean  $\pm$  standard deviation).

The mean peak velocities averaged over all 9 subjects, together with their standard deviations, are shown in **Table 1** (FH velocity) and **Table 2** (magnitude velocity) for the four investigated muscle groups (GCL, GCM, SOL, and TA).

No significant differences were observed for the velocity values in the two peak frames (#3 and #9) as function of undersampling factor for either FH velocity or velocity magnitude. Smaller peak velocity values were observed in the soleus muscle as compared to the other muscle groups.

The strain rate tensor was calculated for all the volunteers. For all the subjects, the first two principal eigenvalues of the strain tensor were one high positive ( $s_+$ ) and one high negative ( $s_-$ ) value. The third eigenvalue ( $s_3$ ) was near zero for all investigated muscle groups and for all volunteers. **Figure 5** and **Figure 6** show the complex geometrical pattern of the principal positive and negative strain rate eigenvector across the gastrocnemius muscle group and the posterior aponeurosis.

In **Figure 5** the principal strain rate eigenvector in the gastrocnemius during plantarflexion is oriented in a similar way to the known fiber direction (as indicated by the anatomy drawing), indicating that during active muscle activation the principal direction of contraction was roughly oriented along the fiber direction, while local expansion occurred along the cross-sectional area of the fibers. In frame #3, representing the dorsiflexion phase, the principal direction of contraction was oriented perpendicular to the principal eigenvector observed during contraction, indicating fascicle axial elongation and compression along the perpendicular direction. The same behavior is observed in **Figure 6** for the posterior compartment, with muscle shortening during contraction in the plantarflexion task (frame #9) and muscle elongation during dorsiflexion (frame #3).

	GCL		GCM		SOL		TA	
	Velocity FH (cm/s)							
Frame #	3	9	3	9	3	9	3	9
<b>Ref. scan</b>	-2.42 (0.92)	1.75 (0.59)	-2.23 (1.15)	2.04 (0.96)	-1.27 (0.80)	1.40 (0.74)	2.25 (1.03)	-2.75 (1.06)
<b>3.14X</b>	-2.37 (0.89)	2.07 (0.97)	-2.18 (0.70)	2.37 (1.38)	-1.36 (0.87)	1.56 (0.87)	2.45 (1.11)	-2.83 (1.22)
<b>4.09X</b>	-2.27 (1.06)	1.93 (1.19)	-2.20 (1.00)	2.12 (1.23)	-1.23 (0.80)	1.49 (0.94)	2.17 (0.87)	-2.80 (0.82)
<b>4.89X</b>	-2.33 (0.74)	1.90 (0.81)	-2.30 (0.78)	2.15 (1.36)	-1.09 (0.90)	1.24 (0.83)	2.21 (0.82)	-2.33 (0.82)
<b>6.41X</b>	-2.15 (1.16)	1.85 (1.13)	-1.92 (0.74)	2.04 (1.20)	-1.30 (1.13)	1.24 (1.00)	2.37 (0.90)	-2.58 (0.80)

**Table 1:** FH velocities in the GCL, GCM, SOL, and TA, averaged over the muscle groups and over the 9 volunteers. Velocities are presented for two time frames, i.e. frame #3 and frame #9. No significant differences in velocity were observed as a function of the k-space undersampling factor ( $p > 0.05$ ).

	GCL		GCM		SOL		TA	
	Magnitude velocity (cm/s)							
Frame #	3	9	3	9	3	9	3	9
<b>Ref. scan</b>	2.91 (1.00)	2.81 (0.80)	2.69 (1.14)	2.68 (0.68)	2.06 (0.81)	2.20 (0.71)	2.55 (1.05)	3.00 (1.07)
<b>3.14X</b>	2.84 (0.91)	2.96 (1.04)	2.63 (0.73)	2.90 (1.36)	2.16 (0.80)	2.15 (0.87)	2.72 (1.02)	3.10 (1.24)
<b>4.09X</b>	2.75 (1.00)	2.77 (1.13)	2.61 (0.93)	2.67 (1.11)	1.98 (0.74)	2.06 (0.91)	2.50 (0.76)	2.97 (0.86)
<b>4.89X</b>	2.90 (0.79)	2.75 (1.13)	2.74 (0.72)	2.64 (1.31)	2.09 (0.63)	1.78 (0.68)	2.57 (0.70)	2.43 (0.84)
<b>6.41X</b>	2.94 (0.83)	2.68 (0.97)	2.45 (0.72)	2.52 (1.15)	2.16 (0.82)	1.90 (0.79)	2.75 (0.81)	2.67 (0.78)

**Table 2:** Velocities magnitudes (modulus of the 3D velocity vector) in the GCL, GCM, SOL, and TA, averaged over the whole muscle volumes and over the 9 volunteers. Velocities are presented for two time frames, i.e. frame #3 and frame #9. No significant differences in velocity were observed as a function of the k-space undersampling factor ( $p > 0.05$ ).

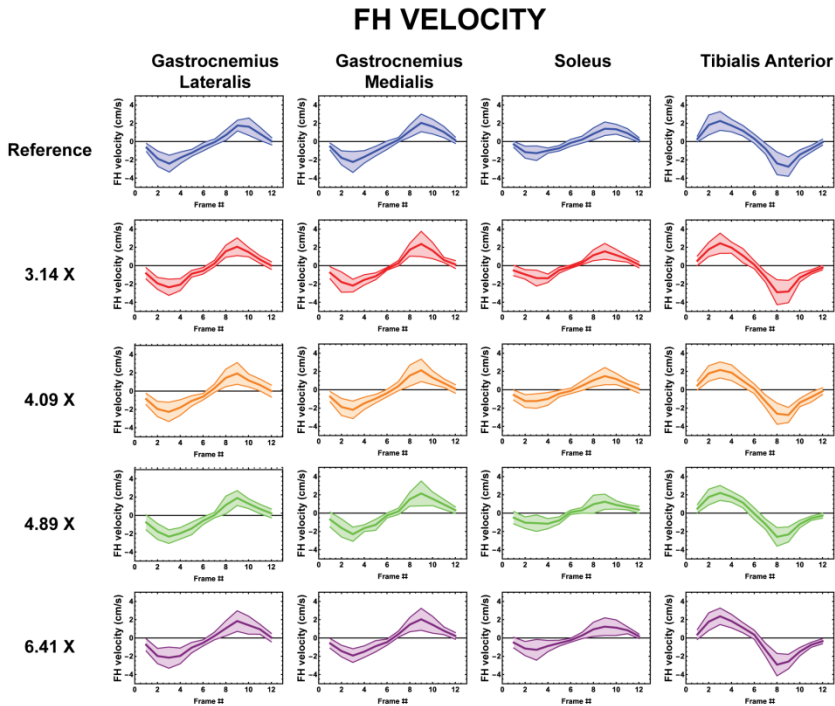


**Figure 4:** FH velocity averaged over all subjects (mean=thick line and standard deviation=shaded area). No significant differences were observed as a function of k-space undersampling factor (Blue: reference scan, red: 3.14X, orange: 4.09X, green: 4.89 and purple: 6.41X). All results are presented for four different muscles in the lower leg (GCL, GCM, SOL, and TA). The opposite signs of the muscles in the posterior compartment and the tibialis anterior are consistent with the muscles working in opposite directions.

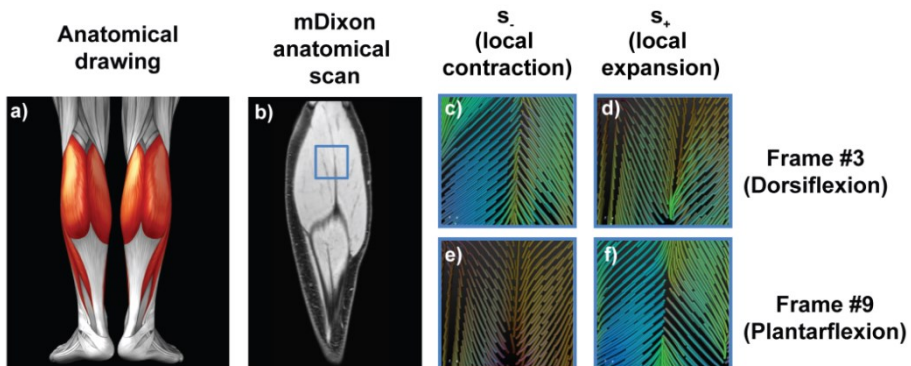


**Figure 5:** Color-coded strain rate images in a ROI in the gastrocnemius muscle for one volunteer. **a)** Anatomical drawing of the lower leg. **b)** mDixon anatomical scan. **c-f)** Color-coded strain rate images obtained in the ROI indicated in **b)**. This dataset was acquired with a k-space undersampling factor of 6.41X. The strain rate is color coded according to the standard convention: green: FH, red: AP, blue: LR. The tracts represent the principal direction of contraction ( $s_c$ ) (**c** and **e**) and the principal direction of expansion ( $s_e$ ) (**d** and **f**).



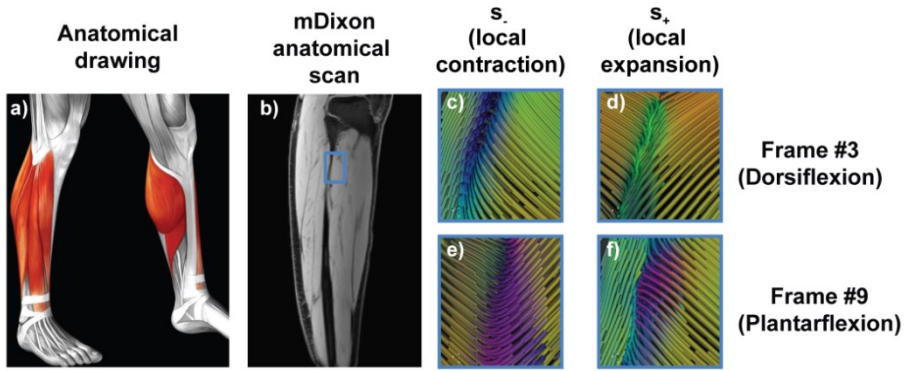


**Figure 6:** Color-coded strain rate images in a ROI in the posterior aponeurosis for one volunteer. **a)** Anatomical drawing of the lower leg. **b)** mDixon anatomical scan. **c-f)** Color-coded strain rate images obtained in the ROI indicated in **b)**. This dataset was acquired with a k-space undersampling factor of 6.41X. The strain rate is color coded according to the standard convention: green: FH, red: AP, blue: LR. The tracts represent the principal direction of contraction ( $s^-$ ) (**c** and **e**) and the principal direction of expansion ( $s^+$ ) (**d** and **f**).

The three peak eigenvalues ( $s^-$ ,  $s^+$ , and  $s_3$ ) of the strain rate tensor, averaged over all the volunteers, are visualized in **Figure 7**. These values were calculated on the whole muscle volumes. No significant differences were observed in the three eigenvalues as a function of the acceleration factor for any of the investigated muscles ( $p > 0.8$ ). The sum of the three eigenvalues over the full muscle volume was nearly zero for all volunteers. The third eigenvalue was not significantly different from zero for any muscle or acceleration factor. The time evolution of the three eigenvalues is shown in the supplemental material (**Figure S1: SOL**, **Figure S2: TA**, **Figure S3: GCL**, **Figure S4: GCM**).

## Discussion

The purpose of this study was to apply 4D Phase Contrast MRI to characterize muscle velocity and strain rate in the full lower leg during foot dorsiflexion/plantarflexion and to explore the feasibility of accelerating the data acquisition by using data undersampling and Compressed Sensing reconstruction.

The comparison of undersampled 4D PC-MRI data to the data obtained with the reference scan showed no significant differences in velocity values, even up to a k-space undersampling factor of 6.41X. Although deviations in the velocity curves in each single frame may exist, on average, reference and highly undersampled data provide the same results in terms of velocity and strain rate, thus facilitating a significant decrease in scan time from 10:52min for the reference scan down to 2:46min with the highest k-space undersampling.

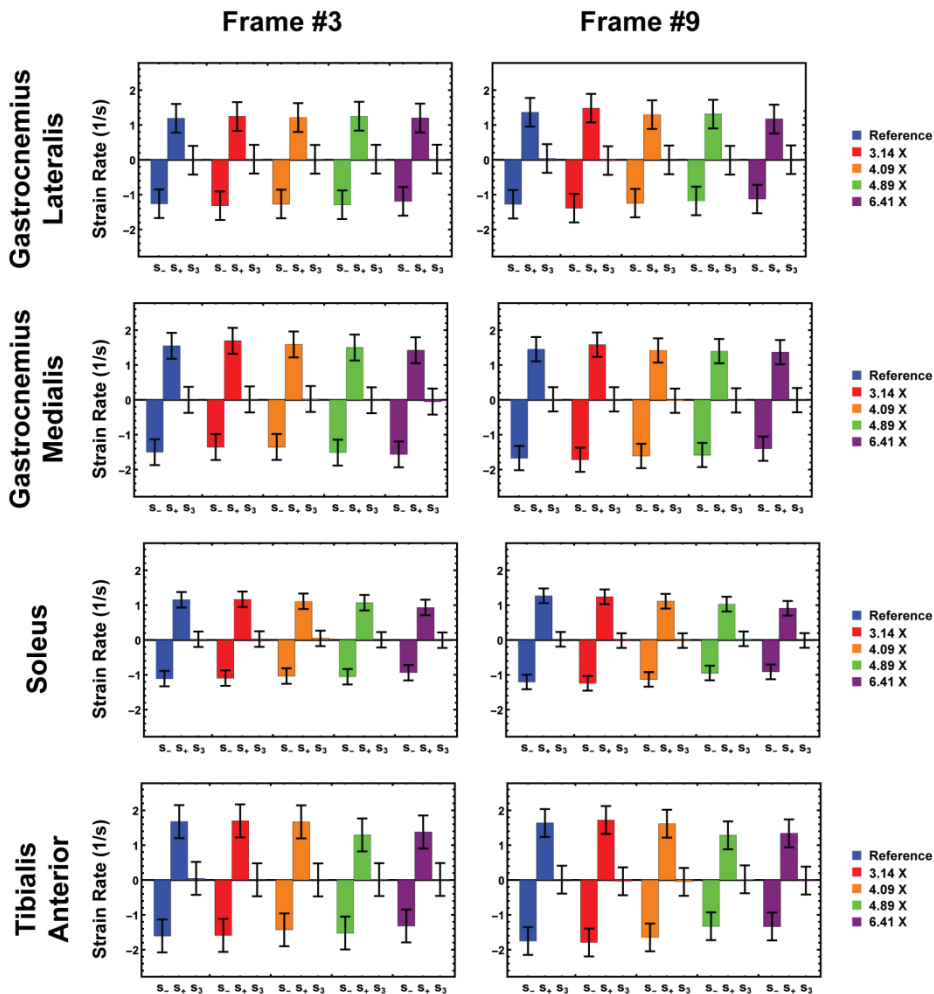


**Figure 7:** Strain rate eigenvalues ( $s_1$ ,  $s_2$ , and  $s_3$ ). The results are averaged over all the subjects. Third principal strain rate was not significantly different from zero. No significant differences were observed as a function of the k-space undersampling factor (blue: reference scan, red: 3.14X, orange: 4.09X, green: 4.89X and purple: 6.41X).

For some of the volunteers, which could achieve a very high level of consistency during the execution of the motion task, the peak velocity values in the lower leg showed a small reduction as a function of acceleration, which is related to the known temporal smoothing involved in Compressed Sensing reconstruction (16). However, significant temporal smoothing and consequent reduction of peak velocity values is to be expected also in case of problems with repeating the motion task consistently over time. This effect could be especially dramatic in case of long scan times, and it is expected to decrease with a decreasing number of motion repetitions needed. As a consequence, the effects of small reduction in the peak velocity values is compensated by the increased likelihood of successful repetition of the motion task, as indicated by the fact that no significant differences were observed in mean velocity as a function of increasing acceleration factor. Our data show that with the use of Compressed Sensing we could recover highly undersampled data, thus highly reducing the scan duration and the number of repetitions of the task that the subjects has to perform.

Our experimental setup does not allow for the definition of gold standard measurements, due to the possible variability in the execution of the motion task within a single subject, and the quality of the repeatability depending on the scan time. Furthermore, our reference scan was not a fully sampled scan, but used halfscan encoding. This was done because a fully sampled scan would have required an excessively long scan time (>15 minutes). Pilot experiments for the purpose of protocol optimization showed that it was impossible for the volunteers to perform the motion task consistently during such a long scan time.

The peak velocity values in our study were in agreement with previously published results performed under similar low-load conditions (28, 29, 35). Furthermore, the velocity data obtained were suitable for calculation of strain rate for all the volunteers. The 3D strain tensor showed consistent patterns across volunteers. In particular, the first two eigenvalues were always one big positive and one big negative value, while the third eigenvalue was consistently nearly zero. This is consistent with the presence of one shortening and one lengthening direction of muscle fibers, and the Poisson ratio of skeletal muscle being close to 0.5. This finding of near incompressibility of skeletal muscle tissue is in agreement with previous studies (9, 13, 19, 32).

Detailed information on muscle contraction can be obtained using ultrasonography techniques (13, 19, 27), with high temporal and spatial resolution. However, these measurements usually provide a small field of view (FOV). Besides ultrasounds, other MRI techniques, including MR tagging and DENSE, are available that allow *in vivo* measurements of strain characteristics with a large FOV. In MR tagging, a prepulse

applied prior to image readout creates a spatial modulation of the magnetization with a periodic function. This results in a line or in a grid of low signal intensity superimposed on the anatomical images. The tag lines can be manually or automatically tracked, and directly provide information on tissue displacement. Following the distortion of these tag lines over times allows to measure soft tissue deformation. MR tagging techniques have been used to monitor tissue displacement during active isometric contraction in humans (28), as well as during muscle indentation both in rats (6) and in healthy humans (22, 23). The main drawbacks of tagging are that it is commonly a 2D technique with limited spatial resolution, and that tag lines fade due to  $T_1$  relaxation, which limits the duration of the motion cycle that can be assessed. Furthermore, MR tagging often requires manual or semi-automated tracking of tag lines, which is a laborious and time-consuming task.

To decrease user interaction for quantification of displacement and strain in MR tagging data, techniques such as HARP have been proposed (18, 34), where strain can be directly computed from the local spatial frequency of tag lines. While this approach does not require the tracking of tag lines and may facilitate strain analysis, it still does not provide advantages over MR tagging in terms of spatial resolution of strain.

On the other hand, PC MRI approaches allow for the acquisition of velocity information encoded in each pixel of the image, thereby providing intrinsically higher resolution as compared to MR tagging and HARP. Another MR-based displacement encoding technique with that can provide strain values on a pixel-by-pixel basis is DENSE (1). DENSE is conceptually similar to PC, as it encodes displacement on the phase of the signal, but it is based on the acquisition of stimulated echoes rather than primary echoes. DENSE has been successfully applied to the study of muscle contraction (37) and cartilage deformation under cyclic loading (7, 8, 24). One of the advantages of DENSE is that it allows for encoding displacements over long time intervals, which is especially beneficial for the study of skeletal muscles contraction, characterized by low velocities. However, the use of a stimulated approach leads to a reduction in SNR by a factor two, which is usually compensated for by decreasing the spatial resolution or by increasing the number of acquisitions (10), thus leading to much longer scan time.

A great advantage of our method compared to previous works is the fully 3D nature of the acquisition. To the best of our knowledge, this is the first study that measured muscle deformation in the entire lower leg with a full 4D sensitivity (full 3D volume with velocity encoding over 3 orthogonal directions), and this enables a full 3D analysis of strain and velocity. This is especially important because many muscles present a curved geometry, which may be difficult to correctly depict using a single plane.

Additionally, muscle groups undergo rotation during motion, which may be erroneously interpreted as contraction when imaging only in a single plane. Furthermore, the ability of imaging a 3D volume implies that no assumptions were needed on the planar nature of the motion, or on local volume conservation (30), as these parameters could be measured directly from the data. Additionally, our acquisition scheme allows for a pixel-by-pixel based analysis, instead of the more common ROI-based analysis. The ability to perform a pixel-by-pixel analysis allows for the 3D visualization of the principal strain rate directions, as was demonstrated in this work.

7 Previous studies have correlated the anatomical fiber direction with the principal direction of strain. Englund et al. (9) measured the Tibialis Anterior muscle during isometric dorsiflexion contraction using MR tagging and combined these data with fiber direction obtained from Diffusion Tensor MRI (DT-MRI) for the same subjects. They found an average difference of  $40^\circ$  between the principal direction of strain and the fiber direction in the superficial compartment and a difference of  $20^\circ$  in the deep compartment. At first, this shows a complex and non-uniform pattern of contraction, probably due to fibers with different lengths and different connective tissue arrangements across the muscle. Similar findings were reported by Sinha et al. (31) and Malis et al. (21) who observed a location dependent difference in fiber angle (about  $45^\circ$  for the proximal gastrocnemius and around  $25^\circ$  for the distal gastrocnemius). However, these previously reported data were based on small ROI analysis. Due to the 3D nature of the acquisition in our study, our data can potentially be combined with DT-MRI measurements at a local level, which could help elucidate the complex geometrical patterns of muscle fiber strain and its connection with the underlying anatomy.

This study has a number of limitations. First of all, due to the very long reference acquisition we used, which required a high number of repetitions of the motion task, we were limited to low load conditions. However, considering that even with high undersampling factors we can obtain consistent patterns for velocity and strain rate, higher loads could be investigated in the future using our method. An additional limitation of our scan method is that the measurements are still partially dependent on the ability of the subjects to perform the dorsiflexion/plantarflexion task in very a repeatable way. While reducing the number of repetitions needed increases the likelihood of successful motion repetition, the dependency on the subject's motion skills is not completely eliminated.

Advances in MRI acceleration techniques may further decrease the scan time for the acquisition of a full datasets in the future. In our study, we used a constant undersampling scheme over time. However, other undersampling strategies exist that can create unique sampling patterns for each time frame, which in turns allow for higher acceleration factors by exploiting additional sparsifying transform over time (15). Therefore, time-varying undersampling patterns may improve the results in future studies. Ideally, a real time PC acquisition is required for subjects who find it difficult to consistently comply with the motion task. However, real-time approaches are currently limited to single slice acquisition with a single velocity encoded direction (3).

## Conclusions

In conclusion, this study demonstrated that it is possible to reconstruct highly undersampled 4D PC MRI data of the muscles in the lower leg during active plantar- and dorsiflexion using a CS acquisition and reconstruction scheme. This strategy facilitates a significant decrease in scan time while keeping comparable velocity values. Furthermore, the data was suitable for strain rate calculation. Further research will focus on combining motion with structural data, and to apply these methods in subjects with muscle pathologies, such as sarcopenic subjects. These results, coupled to accurate structural information, may lead to a deeper understanding of movement abnormalities and optimization of treatment/intervention strategies.

## References

1. **Aletras AH, Ding S, Balaban RS, Wen H.** DENSE: displacement encoding with stimulated echoes in cardiac functional MRI. *J Magn Reson* 137: 247–52, 1999.
2. **Asakawa DS, Blemker SS, Gold GE, Delp SL, Asakawa DS.** In vivo motion of the rectus femoris muscle after tendon transfer surgery. *J Biomech* 35: 1029–1037, 2002.
3. **Asakawa DS, Nayak KS, Blemker SS, Delp SL, Pauly JM, Nishimura DG, Gold GE.** Real-Time Imaging of Skeletal Muscle Velocity. *J Magn Reson Imaging* 18: 734–739, 2003.
4. **Blemker SS, Asakawa DS, Gold GE, Delp SL.** Image-based musculoskeletal modeling: Applications, advances, and future opportunities. *J Magn Reson Imaging* 25: 441–451, 2007.
5. **Blemker SS, Pinsky PM, Delp SL.** A 3D model of muscle reveals the causes of nonuniform strains in the biceps brachii. *J Biomech* 38: 657–665, 2005.
6. **Ceelen KK, Stekelenburg A, Mulders JIJ, Strijkers GJ, Baaijens FPT, Nicolay K, Oomens CWJ.** Validation of a numerical model of skeletal muscle compression with MR tagging: a contribution to pressure ulcer research. *J Biomech Eng* 130: 61015, 2008.
7. **Chan DD, Neu CP.** Transient and microscale deformations and strains measured under exogenous loading by noninvasive magnetic resonance. *PLoS One* 7, 2012.
8. **Chan DD, Neu CP, Hull ML.** In situ deformation of cartilage in cyclically loaded tibiofemoral joints by displacement-encoded MRI. *Osteoarthr Cartil* 17: 1461–1468, 2009.
9. **Englund EK, Elder CP, Xu Q, Ding Z, Damon BM.** Combined diffusion and strain tensor MRI reveals a heterogeneous, planar pattern of strain development during isometric muscle contraction. *Am J Physiol Regul Integr Comp Physiol* 300: R1079–R1090, 2011.
10. **Epstein FH, Gilson WD.** Displacement-encoded cardiac MRI using cosine and sine modulation to eliminate (CANSEL) artifact-generating echoes. *Magn Reson Med* 52: 774–781, 2004.
11. **Felton SM, Gage TA, Reese TG, Wedeen VJ, Gilbert RJ.** Mechanical basis for lingual deformation during the propulsive phase of swallowing as determined by phase-contrast magnetic resonance imaging. *J Appl Physiol* 103: 255–65, 2007.
12. **Finni T, Hodgson J a, Lai AM, Edgerton VR, Sinha S.** Nonuniform strain of human soleus aponeurosis-tendon complex during submaximal voluntary contractions in vivo. *J Appl Physiol* 95: 829–37, 2003.
13. **Gijsbertse K, Sprengers AMJ, Nillesen MM, Hansen HHG, Lopata RGP, Verdonschot N, de Korte CL.** Three-dimensional ultrasound strain imaging of skeletal muscles. *Phys Med Biol* 62: 596–611, 2017.
14. **Hollingsworth KG.** Reducing acquisition time in clinical MRI by data undersampling and compressed sensing reconstruction. *Phys Med Biol* 60: R297–R322, 2015.

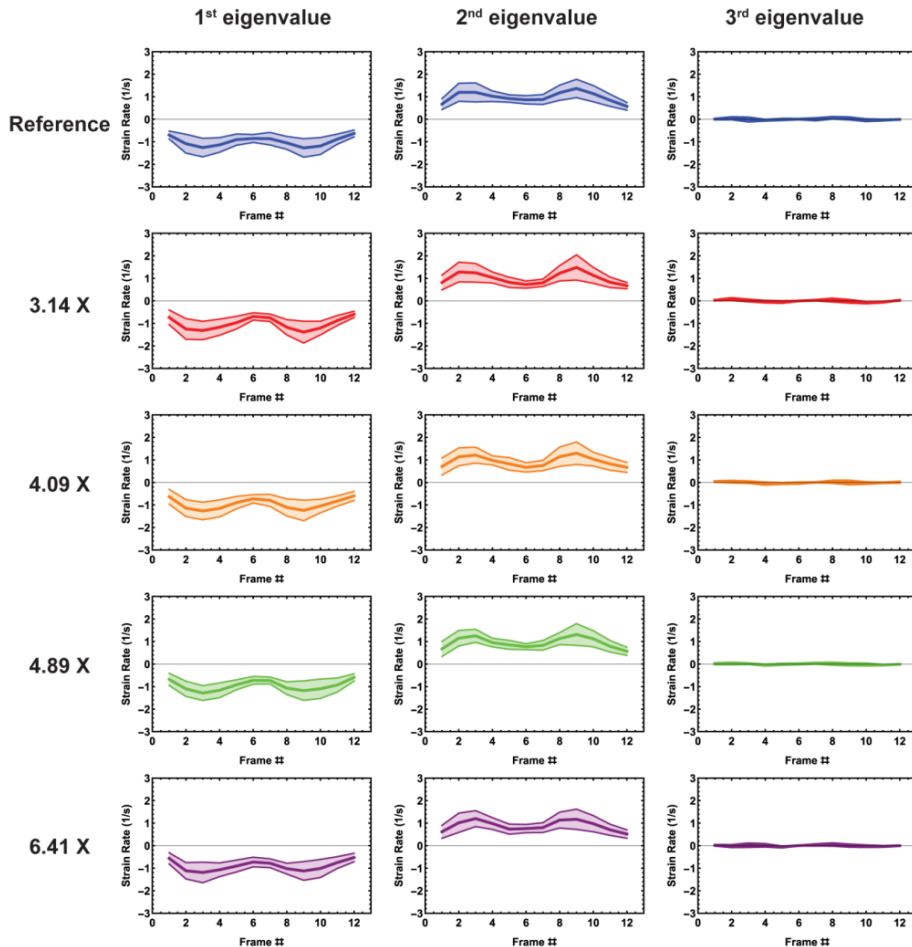
15. **Hutter J, Grimm R, Forman C, Greiser A, Hornegger J, Schmitt P.** Multi-dimensional flow-adapted compressed sensing (MDFCS) for time-resolved velocity-encoded Phase Contrast MRA. *Proc - Int Symp Biomed Imaging* 2: 13–16, 2013.
16. **Kim D, Dyvorne HA, Otazo R, Feng L, Sodickson DK, Lee VS.** Accelerated Phase-Contrast Cine MRI using k-t SPARSE-SENSE. *Magn Reson Med* 67: 1054–1064, 2012.
17. **Klein S, Staring M, Murphy K, Viergever MA, Pluim JPW.** Elastix: A toolbox for intensity-based medical image registration. *IEEE Trans Med Imaging* 29: 196–205, 2010.
18. **Kuijjer JPA, Hofman MBM, Zwanenburg JJM, Marcus JT, Van Rossum AC, Heethaar RM.** DENSE and HARP: Two views on the same technique of phase-based strain imaging. *J Magn Reson Imaging* 24: 1432–1438, 2006.
19. **Lopata RGP, van Dijk JP, Pillen S, Nillesen MM, Maas H, Thijssen JM, Stegeman DF, de Korte CL.** Dynamic imaging of skeletal muscle contraction in three orthogonal directions. *J Appl Physiol* 109: 906–915, 2010.
20. **Lustig M, Donoho D, Pauly JM.** Sparse MRI: The application of compressed sensing for rapid MR imaging. *Magn Reson Med* 58: 1182–1195, 2007.
21. **Malis V, Sinha U, Csapo R, Narici M, Sinha S.** Relationship of changes in strain rate indices estimated from velocity-encoded MR imaging to loss of muscle force following disuse atrophy. *Magn Reson Med* 0, 2017.
22. **Moerman KM, Sprengers AMJ, Simms CK, Lamerichs RM, Stoker J, Nederveen AJ.** Validation of SPAMM tagged MRI based measurement of 3D soft tissue deformation. *Med Phys* 38: 1248–1260, 2011.
23. **Moerman KM, Sprengers AMJ, Simms CK, Lamerichs RM, Stoker J, Nederveen AJ.** Validation of continuously tagged MRI for the measurement of dynamic 3D skeletal muscle tissue deformation. *Med Phys* 39: 1793–810, 2012.
24. **Neu CP, Hull ML, Walton JH.** Error optimization of a three-dimensional magnetic resonance imaging tagging-based cartilage deformation technique. *Magn Reson Med* 54: 1290–1294, 2005.
25. **Savitzky A, Golay MJE.** Smoothing and differentiation of data by simplified least squares procedures. *Anal Chem* 36: 1627–1639, 1964.
26. **Shin DD, Hodgson JA, Edgerton VR, Sinha S.** In vivo intramuscular fascicle-aponeuroses dynamics of the human medial gastrocnemius during plantarflexion and dorsiflexion of the foot. *J Appl Physiol* 107: 1276–1284, 2009.
27. **Sikdar S, Wei Q, Cortes N.** Dynamic ultrasound imaging applications to quantify musculoskeletal function. *Exerc Sport Sci Rev* 42: 126–135, 2014.
28. **Sinha S, Hodgson JA, Finni T, Lai AM, Grinstead J, Edgerton VR.** Muscle kinematics during isometric contraction: Development of phase contrast and spin tag techniques to study healthy and atrophied muscles. *J Magn Reson Imaging* 20: 1008–1019, 2004.
29. **Sinha S, Shin DD, Hodgson JA, Kinugasa R, Edgerton VR.** Computer-controlled, MR-compatible foot-pedal device to study dynamics of the muscle tendon complex under isometric, concentric, and eccentric contractions. *J Magn Reson Imaging* 36: 498–504, 2012.



30. **Sinha U, Csapo R, Malis V, Xue Y, Sinha S.** Age-related differences in diffusion tensor indices and fiber architecture in the medial and lateral gastrocnemius. *J Magn Reson Imaging* 41: 941–953, 2015.
31. **Sinha U, Malis V, Csapo R, Moghadasi A, Kinugasa R, Sinha S.** Age-related differences in strain rate tensor of the medial gastrocnemius muscle during passive plantarflexion and active isometric contraction using velocity encoded MR imaging: Potential index of lateral force transmission. *Magn Reson Med* 73: 1852–1863, 2015.
32. **Takaza M, Moerman KM, Gindre J, Lyons G, Simms CK.** The anisotropic mechanical behaviour of passive skeletal muscle tissue subjected to large tensile strain. *J Mech Behav Biomed Mater* 17: 209–220, 2012.
33. **Uecker M, Ong F, Tamir JI, Bahri D, Virtue P, Cheng JY, Zhang T, Lustig M.** Berkeley Advanced Reconstruction Toolbox. *Proc Intl Soc Mag Reson Med* : 2486, 2015.
34. **Venkatesh BA, Gupta H, Lloyd SG, Dell'Italia L, Denney TS.** 3D left ventricular strain from unwrapped harmonic phase measurements. *J Magn Reson Imaging* 31: 854–862, 2010.
35. **Wentland AL, McWalter EJ, Pal S, Delp SL, Gold GE.** Muscle velocity and inertial force from phase contrast MRI. *J Magn Reson Imaging* 42: 526–532, 2015.
36. **Yushkevich PA, Piven J, Hazlett HC, Smith RG, Ho S, Gee JC, Gerig G.** User-guided 3D active contour segmentation of anatomical structures: Significantly improved efficiency and reliability. *Neuroimage* 31: 1116–1128, 2006.
37. **Zhong X, Epstein FH, Spottiswoode BS, Helm PA, Blemker SS.** Imaging two-dimensional displacements and strains in skeletal muscle during joint motion by cine DENSE MR. *J Biomech* 41: 532–540, 2008.

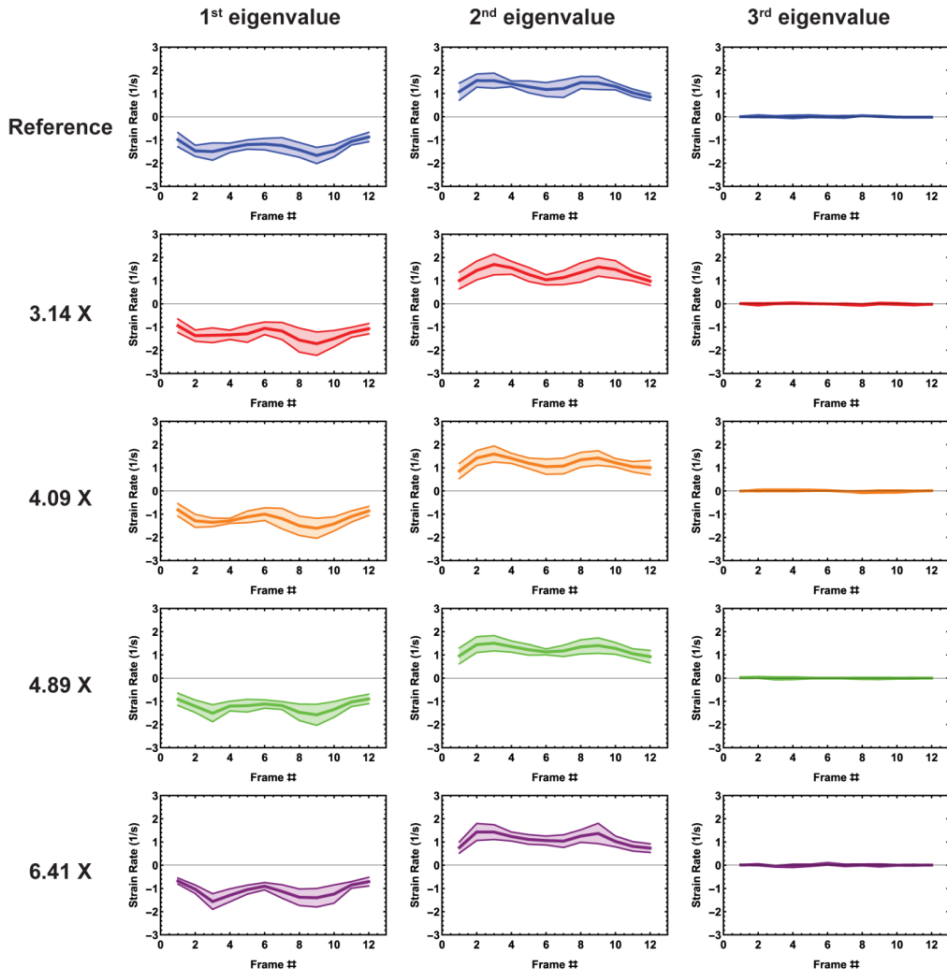
## Supplemental Material

## Gastrocnemius Lateralis

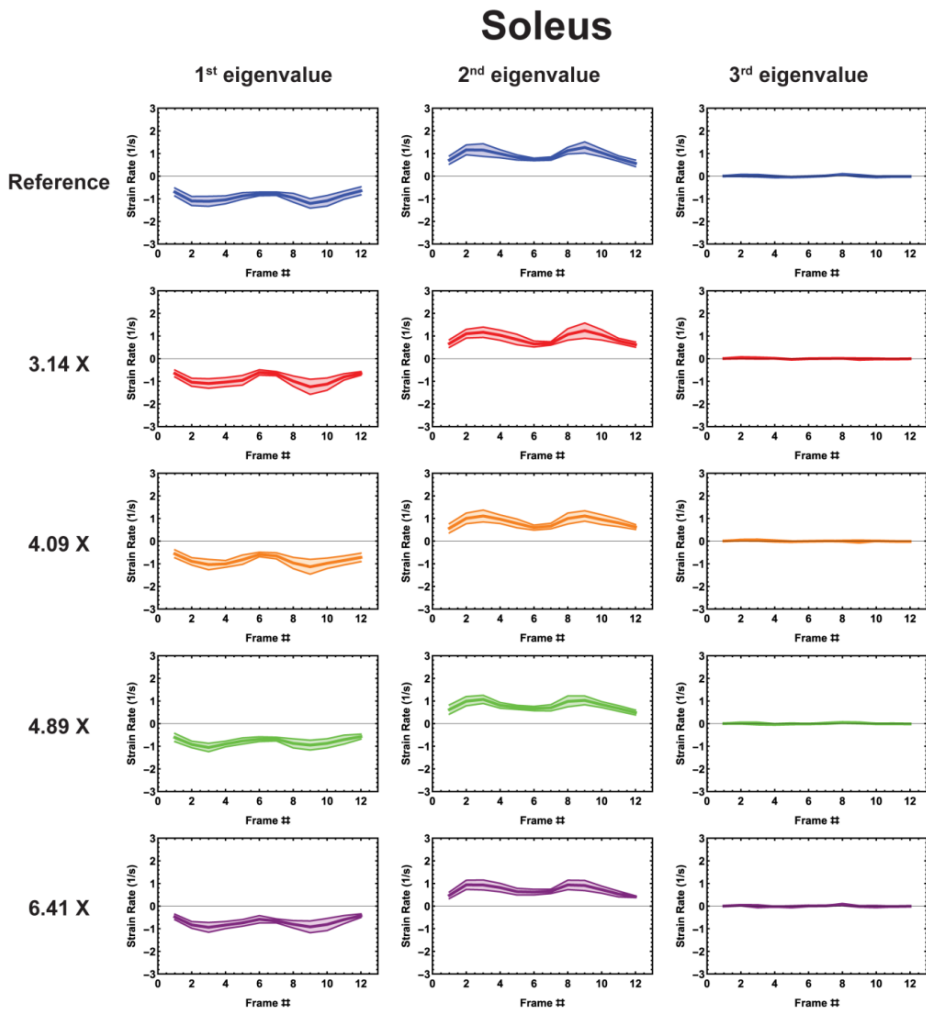


**Supplemental figure 1:** Time evolution of the three strain rate eigenvalues ( $s_1$ ,  $s_2$  and  $s_3$ ) for the Gastrocnemius Lateralis muscle (GCL). The results are averaged over all the subjects (mean, thick line and standard deviation, thin lines). No significant differences are observed as a function of the acceleration factor (blue: reference scan, red: 3.14X, orange: 4.09X, green: 4.89X and purple: 6.41X) for the peak strain rates during contraction (frame #9) and during relaxation (frame #3).

## Gastrocnemius Medialis

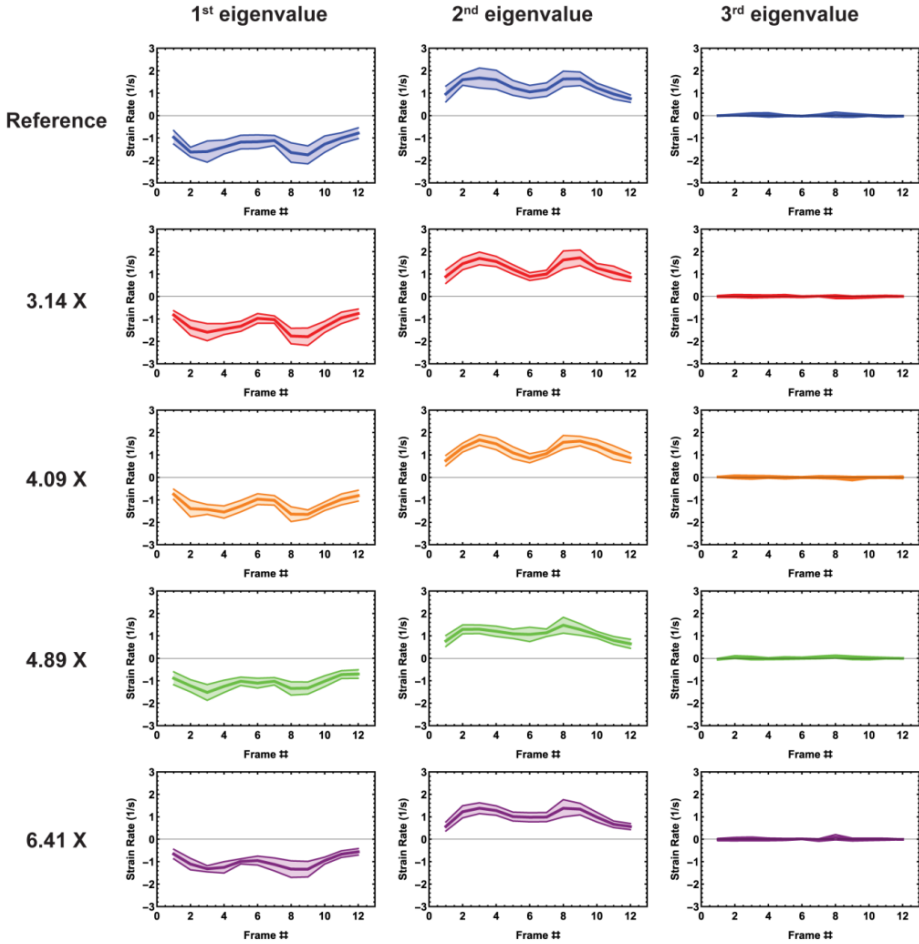


**Supplemental figure 2:** time evolution of the three strain rate eigenvalues ( $s_1$ ,  $s_2$  and  $s_3$ ) for the Gastrocnemius Medialis muscle (GCM). The results are averaged over all the subjects (mean, thick line and standard deviation, thin lines). No significant differences are observed as a function of the acceleration factor (blue: reference scan, red: 3.14X, orange: 4.09X, green: 4.89X and purple: 6.41X) for the peak strain rates during contraction (frame #9) and during relaxation (frame #3).



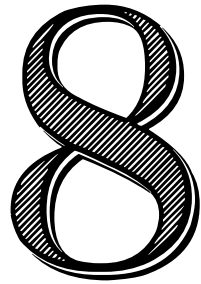
**Supplemental figure 3:** time evolution of the three strain rate eigenvalues ( $s_1$ ,  $s_2$ , and  $s_3$ ) for the Soleus muscle (SOL). The results are averaged over all the subjects (mean, thick line and standard deviation, thin lines). No significant differences are observed as a function of the acceleration factor (blue: reference scan, red: 3.14X, orange: 4.09X, green: 4.89X and purple: 6.41X) for the peak strain rates during contraction (frame #9) and during relaxation (frame #3).

## Tibialis Anterior



**Supplemental figure 4:** time evolution of the three strain rate eigenvalues ( $s_1$ ,  $s_2$ , and  $s_3$ ) for the Tibialis Anterior muscle (TA). The results are averaged over all the subjects (mean, thick line and standard deviation, thin lines). No significant differences are observed as a function of the acceleration factor (blue: reference scan, red: 3.14X, orange: 4.09X, green: 4.89X and purple: 6.41X) for the peak strain rates during contraction (frame #3) and during relaxation (frame #9).

# Chapter



## On the origin of changes in $T_2$ and $T_{1\rho}$ in the meniscus under loading conditions

**Valentina Mazzoli**

Danny Tsui

Larry de Graaf

Hamid Naghibi

Dennis Janssen

Andre M. Sprengers

Nico Verdonschot

Aart J. Nederveen

Gustav J. Strijkers

**Submitted**

## Abstract

**Introduction:** Knee injury can be cause and consequence of abnormal biomechanical loading patterns in the menisci. Techniques to obtain quantitative information on in vivo loading patterns are therefore in high demand for prevention and therapy. MRI studies showed that meniscal  $T_2$  and  $T_{1\rho}$  values increased upon application of load. These parameters were introduced as surrogate markers of knee load, although the mechanisms leading to changes in the relaxation values remained unclear. In this study, we investigated the origin of changes in meniscal  $T_2$  and  $T_{1\rho}$  under compressive load.

**Methods:**  $T_2$  and  $T_{1\rho}$  were measured in healthy volunteers ( $n=17$ ) before and after application of a static compressive load of 25% bodyweight. To test the hypothesis that the magic angle effect could cause the increase in relaxation times observed in vivo, human cadaveric intact knees ( $n=4$ ) were scanned with and without load in 4 different orientations with respect to  $B_0$ .

**Results:** In the volunteers, loading had a significant effect on  $T_2$  ( $p<0.028$ ) except for the medial anterior and central meniscus, while it affected  $T_{1\rho}$  only in the global, lateral whole, posterior and outer meniscus and the medial anterior horn ( $p<0.04$ ). In the *ex vivo* experiment, increases during loading were also present, with larger changes at larger angles to  $B_0$ . Smaller effects with loading were observed in the meniscus body than in the horns.

**Conclusions:** Our data support the hypothesis that compression-induced internal fiber reorganization and the magic angle effect lead to load-induced changes in  $T_2$  and to a lesser extent in  $T_{1\rho}$ .

## Introduction

The menisci in the knee joint are two C-shaped fibrocartilage structures that consist of water (74% by wet weight) and a solid phase (26% by wet weight) (1), of which the main components are type-I collagen (75% by dry weight (2)) and proteoglycans (PGs, 1-5% by wet weight, 17% by dry weight (3–5)). The menisci are entrapped in a dense and complex fiber network of collagen fibers, consisting of four (6) to six (7) fiber groups. The main fiber group runs along the circumferential direction while so-called tie-fibers course and arborize radially. Through Donnan osmosis, the high negative fixed-charge density attracts water. The water influx increases the volume of the meniscus and, in turn, creates tensile stresses in the collagen fibers, thereby providing compressive stiffness to the tissue. Due to the meniscal insertions into the tibia, the compressive femoral-tibial loads acting on the menisci are redistributed as tensile hoop stresses. The interplay between the matrix components provides the menisci with their biomechanical characteristics and facilitates compressive load transmission. Hence, it improves joint congruency, distributing the load and reducing friction and aiding in an overall stabilization of the knee joint.

Knee injury and disorders are often a cause but may also be a consequence of abnormal biomechanical loading patterns in the knee joint menisci. Therefore, imaging techniques to obtain quantitative information on in vivo loading patterns are in high demand for early diagnosis, therapy evaluation, and prevention of further damage. Due to the major role of meniscus in dispersing load and reducing friction in the articular cartilage, an abnormal loading pattern and deformation of the meniscus could provide an early sign of progressive osteoarthritis (OA) or indicate an increased risk of OA. Therefore, imaging of the deformation patterns of meniscus in vivo can potentially increase our understanding of the mechanisms involved in OA development.

The biomechanical behavior of the meniscus in response to load has been studied extensively in the past using various techniques ranging from controlled compression to finite element modeling simulations (8,9). In MRI studies,  $T_2$  and  $T_{1\rho}$  ( $T1$ -rho) have been introduced as surrogate markers of biochemical content as well as tools to quantify the loading in articular cartilage (10–12). Meniscal  $T_2$  and  $T_{1\rho}$  values have been correlated to the PG and collagen content, as well as to the tissue architecture, and were shown to increase upon application of load (13,14). However, the underlying mechanisms leading to changes in the relaxation values with load remain unclear.

In tissues with highly structured collagen compartments, like meniscus, tendon, ligament and articular cartilage, but also in certain peripheral nerves (8), the well-



known magic angle effect is a complicating factor in the interpretation of image contrast and relaxation time values. This effect manifests as a variation in signal intensity as a function of collagen fiber orientation with respect to the  $B_0$  field, and it is caused by the modulation of dipolar interactions by a  $3 \cos^2(\theta) - 1$ , with  $\theta$  the fiber orientation with respect to  $B_0$  (9). For  $\theta = 54.7^\circ$  (the magic angle), the dipolar interactions are 0 and since  $T_2$  is directly influenced by the strength of the dipolar interaction,  $T_2$  experiences a maximum value at the magic angle (29, 32), whereas  $T_{1\rho}$  is less affected by dipole-dipole interactions (1, 30).

The aim of this study was to reproduce previously reported increases in relaxation times under loading and to investigate the origin of changes in meniscal  $T_2$  and  $T_{1\rho}$  under compressive load. We hypothesize that these changes are caused by changes in the proton dipolar interactions when the internal fiber structure reorients upon compressive loading.

## 8

## Materials and methods

### *In vivo* experiments

Seventeen young healthy volunteers (8 males, 9 females) aged  $27.0 \pm 2.7$  years were recruited and provided informed consent to participate in the study. All experiments started after one hour of rest (i.e. no weight bearing). For all volunteers the left knee was scanned. All images were acquired using a Philips Achieva 3T MRI scanner (Best, the Netherlands).

An 8-channel knee coil was employed for all scans. A 3D water-selective single-shot TFE anatomical scan (water excitation using a binomial 1331 RF pulse, voxel size =  $0.49 \times 0.49 \times 1 \text{ mm}^3$ , matrix =  $512 \times 512 \times 91$ , flip angle =  $10^\circ$ , TR/TE = 8.8/4.5 ms, scan duration = 5:28 min) was acquired at the beginning of the scan protocol for segmentation purposes. Subsequently,  $T_2$  and  $T_{1\rho}$  scans were measured using a  $B_0$  and  $B_1$ -compensated  $T_{1\rho}$ -prepared 3D gradient echo sequence (31).

Each spin lock pulse consisted of 2 continuous RF pulses with opposite phase to compensate for  $B_1$  variations, and a  $180^\circ$  refocusing pulse was inserted between 2 continuous RF pulses to compensate for  $B_0$  errors (14, 21, 22). The spin lock frequency was set to 0 Hz and 300 Hz for  $T_{1\rho}$  and  $T_2$  respectively. Other imaging parameters were: spin-lock times (TSL) = 0/10/20/35 ms for  $T_{1\rho}$ , echo times = 0/10/20/35 ms for  $T_2$ , FOV =  $150 \times 150 \times 91 \text{ mm}^3$ , acquired voxel size =  $0.6 \times 0.6 \times 3 \text{ mm}^3$ , reconstructed voxel size =  $0.3 \times 0.3 \times 1.5 \text{ mm}^3$ , TR/TE = 7.5/3.3 ms, flip angle =  $10^\circ$ , scan duration = 5:10 min for each scan).

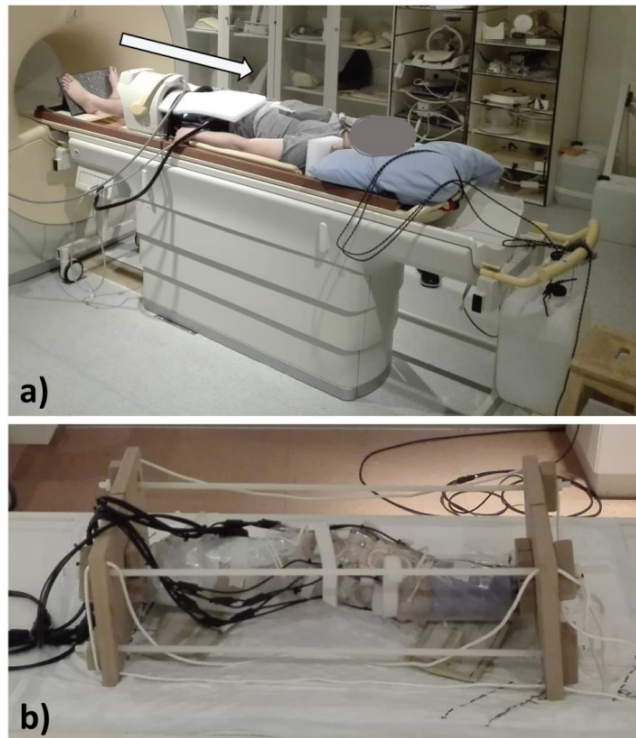


**Figure 1:** Photographs of loading devices used to apply compressive load on the menisci. **a)** *In vivo* loading device. 50% of the subject's body weight was applied to both feet using MRI water and a pulley system. This resulted in about 25% body weight applied on each knee. **b)** Loading device used for applying the compressive load on the cadaveric knees.

Subsequently, the compressive load was applied and the  $T_2$  and  $T_{1\rho}$  scans were repeated after 30 min of loading. A pulley system with a water weight was employed to generate a compressive load of 50% body weight (BW) to the knee joint (25% per knee) while the subjects were lying horizontally in the scanner, as indicated in **Figure 1a**. The load weight was applied to the foot through a foot plate in order to simulate the static standing position. The timeline of the *in vivo* experiment is schematically illustrated in **Figure 2**.

The  $T_2$  and  $T_{1\rho}$  scans were non-rigidly registered to the higher resolution anatomical scan using Elastix (17). Manual segmentation of the meniscus was performed using ITK-SNAP 3.4.0 to yield four different groups of regions of interest (ROIs): global, individual, horn/body, and circumferential. The different groups of ROIs are schematically shown in **Figure 3**. The latter two subdivisions along the circumferential and the radial directions were done to enable analysis of the horns and the body of the meniscus, as well as the vascularized and avascular portions of the meniscus. The

horn/body division was made by roughly dividing the meniscus into three equal radial sections in the axial view, while the circumferential division was made by superimposing two ellipses on the outer and inner margins of the meniscus in an axial slice close to the tibial plateau and by defining the mean ellipse as the boundary between the inner and outer region. The global ROI resulted from pooling the two individual meniscus ROIs.

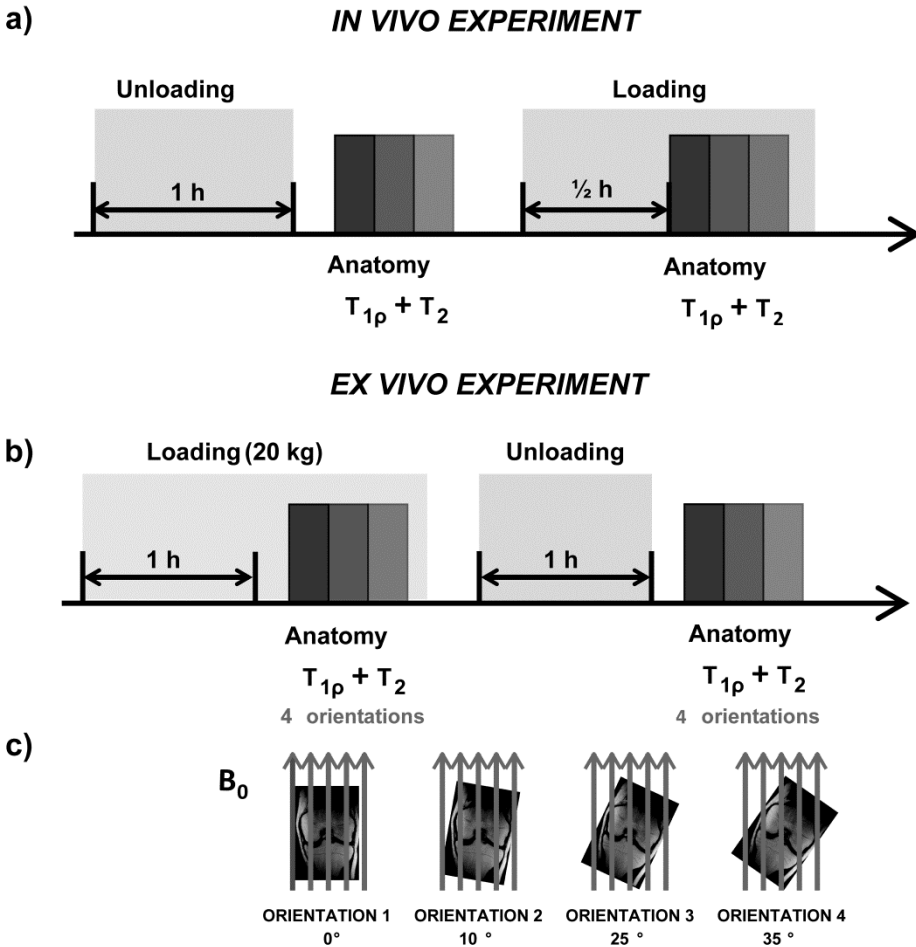


**Figure 2:** timeline of the *in vivo* and *ex vivo* experiments. **a)** The anatomical,  $T_{1p}$  and  $T_2$  are acquired at baseline as well as after 30 minutes from load application. **b)** For the *ex vivo* scan the knees were loaded for 1 hour and the scans were while the load was applied. The scans were repeated one hour after the load was removed. **c)** Schematic explanations of the *ex vivo* experiment. The knee was rotated at 4 different orientations with respect to the static magnetic field  $B_0$  (indicated by the gray arrows).

To quantify the decay of  $T_2$  or  $T_{1p}$ , a pixel-wise mono-exponential curve fit was performed in Wolfram Mathematica 10.4 (Wolfram Research, Champaign, IL, USA)

using the model:  $SI(TSL) = A e^{-TSL/\tau} + B$ , with SI the signal intensity and  $\tau$  either  $T_2$  or  $T_{1\rho}$ . Mean  $\pm$  SD over the volunteers was determined for the mean  $T_2$  and  $T_{1\rho}$  per ROI.

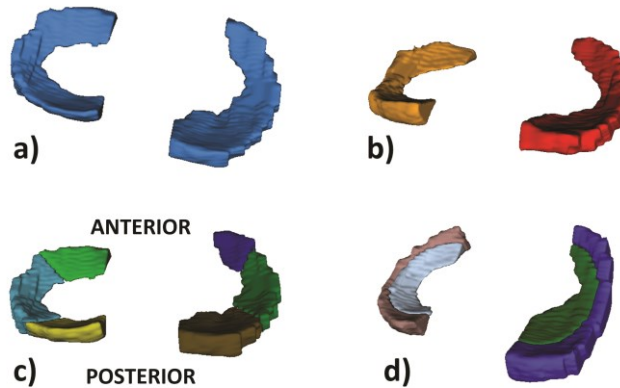


**Figure 3:** Schematic drawing of the regions of interest (ROIs) used for the *in vivo* experiment. **a)** Global division (both menisci are considered together). **b)** Individual division (red: medial meniscus, orange: lateral meniscus). **c)** Horn/body division (anterior horn, posterior horn and meniscus body) and **d)** Circumferential division (inner/outer meniscus).

### Ex vivo experiments

Four fresh-frozen ( $-80^{\circ}\text{C}$ ) cadaveric right legs from male donors were scanned in 4 different orientations (circa  $0^{\circ}/10^{\circ}/25^{\circ}/35^{\circ}$  with respect to  $B_0$ ) in an unloaded and loaded configuration using a Philips Ingenia 3.0T scanner (Best, the Netherlands). A schematic explanation of the rotations is presented in **Figure 2c**. The cadavers were first scanned in the loaded configuration, for all orientations. The load was applied on the knees one hour before the start of the first scan. Subsequently, the compressive load was removed and, after waiting one hour, the quantitative scans were repeated for all orientations. The applied load was 20 kg (representing approximately 25% BW as used in the *in vivo* study). The loading device consisted of wooden plates, threaded rods, and bolts (**Figure 1b**). The applied load was monitored outside the scanner room using a dynamometer.

A proton density-weighted anatomical scan (multishot TSE with TSE factor = 60, FOV =  $150 \times 150 \times 120 \text{ mm}^3$ , voxel size =  $0.49 \times 0.49 \times 0.7 \text{ mm}^3$ , matrix =  $432 \times 432 \times 171$ , TR/TE =  $1000/40$  (or 38) ms, scan duration = 6:47 min) was followed by  $T_2$  and  $T_{1\rho}$  measurements similar to those performed *in vivo*, but with TSL =  $1/10/20/35 \text{ ms}$ , FOV =  $150 \times 150 \times 120 \text{ mm}^3$ , parallel imaging acceleration factor (SENSE)=1.7 (AP and RL), resulting in scan duration = 4:30 min. A flexible 15-channel knee coil was employed (MR Coils, Zaltbommel, The Netherlands) for signal reception. Both  $T_2$  and  $T_{1\rho}$  images

were rigidly registered in Elastix to the scan where the leg was parallel to  $B_0$ . Pixel-wise fits were applied and mean values were determined in ROIs drawn along the circumference of the menisci.

## Statistical analysis

Motion artifacts complicated quantitative analysis for the *in vivo* loading scans. For this reason, three datasets were discarded for  $T_2$  and two for  $T_{1\rho}$ . Hence, statistical evaluation was performed for 14  $T_2$  datasets and 15  $T_{1\rho}$  datasets. To investigate the effect of loading in each ROI, a repeated-measures analysis of variance with additional simple effects analysis was applied using SPSS 23.0 (IBM Corp., Armonk, NY, USA). The repeated measure was loading and the between-subjects factor was ROI. A significance level of 0.05 was employed.

## Results

### *In vivo* experiments

All quantitative scans were successfully completed. Due to severe motion artifacts, only 14  $T_2$  datasets and 15  $T_{1\rho}$  datasets were processed and included in statistical analysis. Visual inspection of these datasets did not show the presence of artifacts.

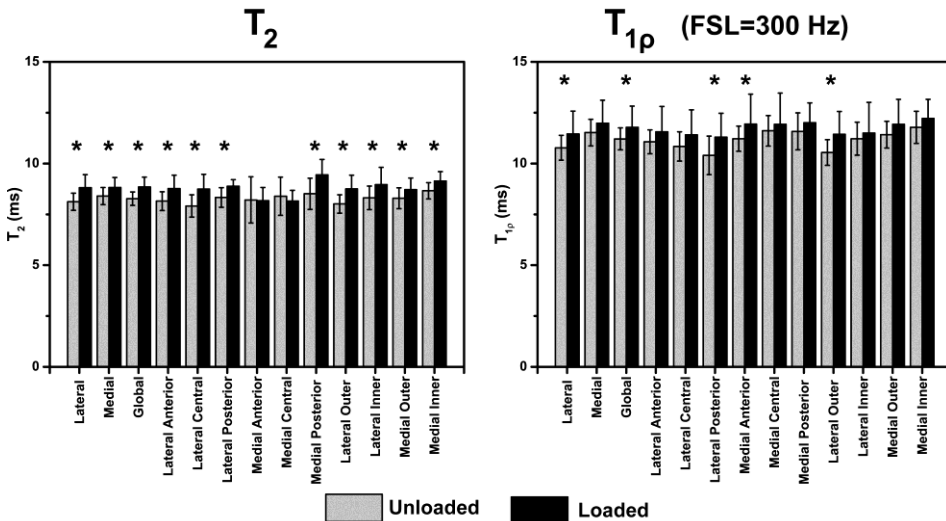


**Figure 4:** Mean  $\pm$  SD  $T_2$  (left) and  $T_{1\rho}$  (right) in the unloaded and loaded state for each ROI. Visualizations of the ROIs are provided in the bottom row. \* indicates a significant effect of loading in a specific ROI ( $\alpha=0.05$ ). A general increase in  $T_2$  is observed upon load for all ROIs except medial anterior and medial central meniscus. More significant increases are observed in  $T_2$  as compared to  $T_{1\rho}$ .

**Figure 4** shows the mean  $T_2$  and  $T_{1\rho}$  for each of the ROIs depicted in **Figure 3**. Loading led to a significant increase in the mean  $T_2$  in each ROI ( $p < 0.028$ ) except for the medial anterior and medial central meniscus, while it significantly increased  $T_{1\rho}$  only globally (containing both whole menisci), in the whole lateral meniscus, in the posterior and outer meniscus, and the medial anterior horn ( $p < 0.04$ ). The  $p$ -values for the simple effects of loading are summarized in **Table 1**.

ROI	$T_2$	$T_{1\rho}$
Lateral	<0.001	0.025
Medial	0.013	0.119
Global	<0.001	0.039
Lateral Anterior	0.010	0.153
Lateral Central	0.001	0.098
Lateral Posterior	0.024	0.010
Medial Anterior	0.835	0.036
Medial Central	0.321	0.344
Medial Posterior	<0.001	0.217
Lateral Outer	<0.001	0.005
Lateral Inner	0.001	0.359
Medial Outer	0.027	0.106
Medial Inner	0.013	0.155

**Table 1:**  $p$ -values of simple effects analysis (*in vivo*, unloaded versus loaded).

## Ex vivo experiments

**Figure 5** displays representative  $T_2$  maps for both loading situations and for different orientations to  $B_0$  for one representative example. The histograms of the  $T_2$  values in the posterior horn of the medial meniscus for one cadaver are shown in **Figure 6**. An increase as a function of orientation as well as of load is visible. **Figure 7** shows the mean relaxation value as a function of orientation in several ROIs placed along the circumference of the meniscus, averaged over the 4 cadavers. Generally, a small increase as a function of orientation number, and thus amount of coronal rotation, was seen for both  $T_2$  and  $T_{1\rho}$ .

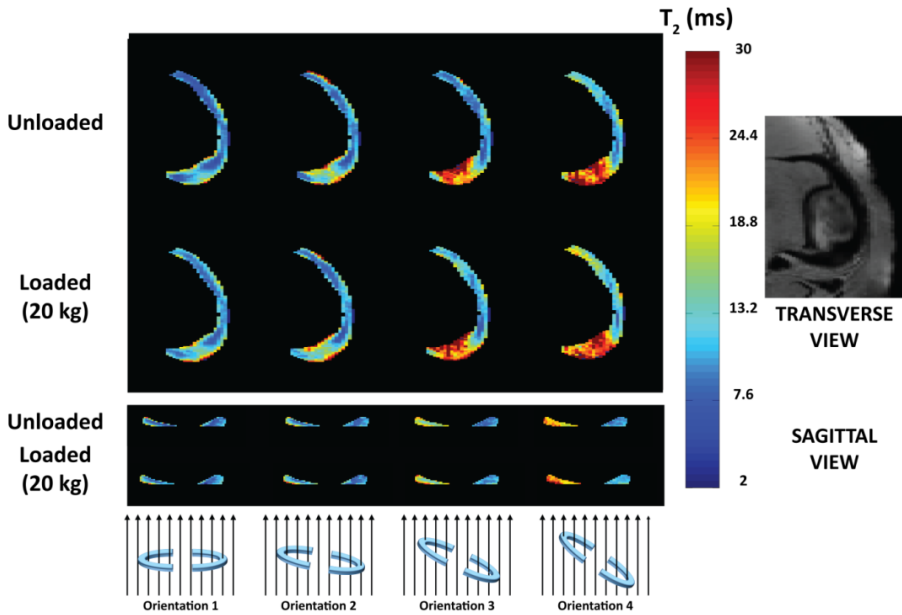


**Figure 5:**  $T_2$  maps of the medial meniscus of the cadaver leg in different orientations with respect to the  $B_0$  field (indicated in the bottom row). Transverse and sagittal coregistered images are presented. A general increase in  $T_2$  upon load was observed, as well as changes as a function of orientation.

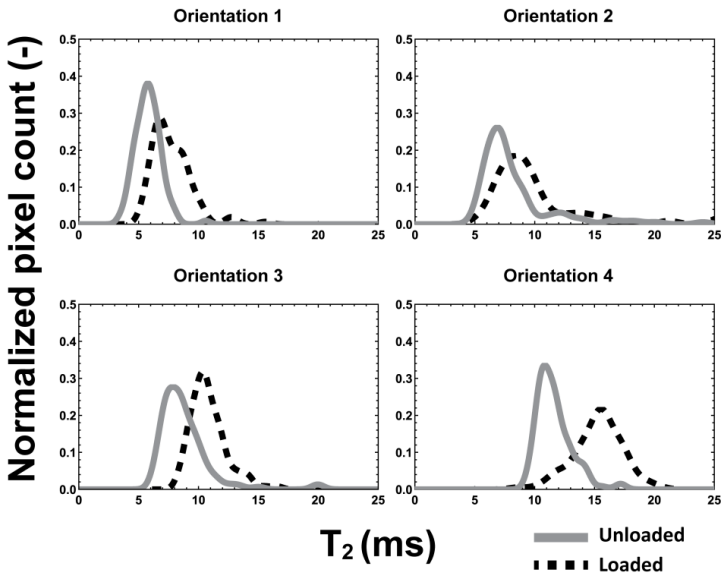


**Figure 6:** Histograms of  $T_2$  values within an ROI in the medial posterior meniscus of the cadaver leg in different orientations with respect to the  $B_0$  field. A general increase in  $T_2$  upon load was observed, as well as changes as a function of orientation.

In the lateral meniscus, an increase of both  $T_2$  and  $T_{1\rho}$  with loading was seen with increasing coronal rotation, except for the ROI located in the central part of the meniscal body (blue). Upon loading, relaxation times mostly increased, and larger changes were measured in more rotated positions (orientation 4). In the medial meniscus, increasing values with increasing rotation were observed as well, except for the ROI located in the center of the meniscal body (blue). Similarly to what observed for the lateral meniscus, upon loading of the medial meniscus, the average relaxation times increased. The absolute difference in relaxation times between loaded and unloaded configuration was in general relatively small, as already observed in the *in vivo* results.

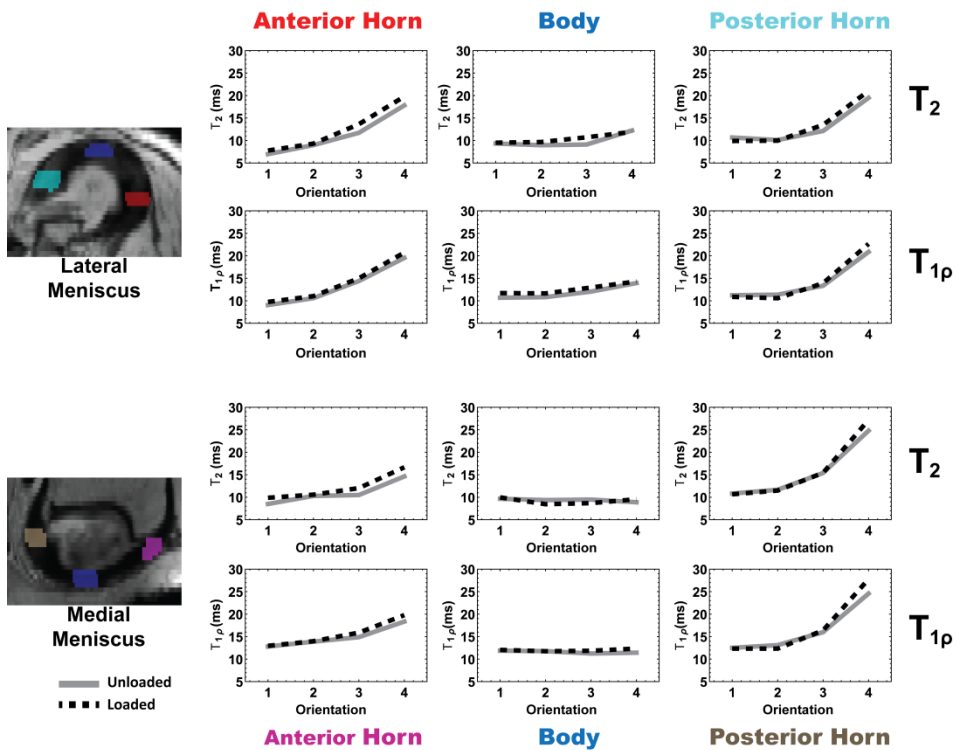


**Figure 7:** Mean relaxation value ( $T_{1\rho}$  and  $T_2$ ) as a function of orientation in several ROIs (shown on the left) placed along the circumference of the meniscus, averaged over the 4 cadavers. Generally, an increase as a function of orientation, and thus amount of coronal rotation, was seen for both  $T_{1\rho}$  and  $T_2$ . For the ROIs located in the meniscus body, small effect of orientation is seen, indicating that the mean orientation of the collagen fibers in the meniscus undergoes little rotation with respect to the  $B_0$  field when the legs are rotated in the coronal plane. The solid and dotted lines represent the meniscus in the unloaded and loaded configuration respectively.



## Discussion

In this study, meniscal  $T_2$  and  $T_{1\rho}$  were evaluated in human knee joints that underwent compressive loading. A significant increase in relaxation times was observed in healthy volunteers upon load. The *ex vivo* data, obtained by varying both the load and the orientation with respect to the static magnetic field, support our hypothesis that the changes in relaxation times observed *in vivo* are caused by changes in the proton dipolar interactions when the internal fiber structure reorients upon compressive loading. Obviously, the magnitude of change of the fiber-orientation due to load will be rather small, which explains the relatively small, yet significant, changes reported in this study.

The average  $T_2$  values measured in this study in healthy volunteers were in agreement with previously reported values (7, 24, 33). On the other hand, our  $T_{1\rho}$  values are slightly lower than reported literature values, but this is likely a consequence of the different spin lock frequency used for data acquisition (typically 500 Hz, vs 300 Hz in this study).

The load-induced increases observed *in vivo* were in agreement with the increases found in previous studies of meniscal  $T_2$  and  $T_{1\rho}$  upon loading of the knee joint (7, 28), which confirms that in the meniscus  $T_2$  seems more sensitive to changes in load than  $T_{1\rho}$ . The magnitude of load-induced changes seen in healthy volunteers in these studies was generally small (usually within 2 ms), as was the case in the current study, where similar loading conditions were applied. However, regarding  $T_{1\rho}$  measurements, in our study the spin-lock frequency was 300 Hz, as compared to 500 Hz (7, 28). Although this likely has some effects on the results, we believe a similar trend in changes due to load application can still be expected.

In the *ex vivo* experiments, a general increase in  $T_2$  and  $T_{1\rho}$  with orientation was measured, as already observed by Peterfy et al. (23).  $T_2$  and  $T_{1\rho}$  values were mostly higher in the loaded configuration when the leg was placed parallel to  $B_0$  (orientation 1), in agreement with the *in vivo* results obtained at the same orientation. The larger dynamic range seen *ex vivo* for increasing rotation angle is most likely a result of the higher sensitivity of  $T_2$  to changes in fiber-to- $B_0$  angle resulting from the dipolar interactions. In addition, higher differences were observed for increasing angle of rotation in the ROIs located at the horns. On the other hand, in the ROIs located in the central part of meniscus body, both in the medial and lateral meniscus, no distinct change with rotation in the coronal plane was seen. The absence of changes in relaxation times in these regions as a function of orientation, both at baseline and

under load, can be explained by the theoretical anteroposterior fiber orientation in that region. With coronal sample rotation, the majority of the fibers in these ROIs are expected to remain perpendicular to the main magnetic field and therefore they do not undergo a significant change in relaxation time. Lai *et al.* (23) reported that meniscal deformation starts internally and then propagates outward, attributed to buckling of secondary fibers, shearing, and reorganization of the circumferential fibers, which would allow for optimized accommodation of the compressive stress. Such buckling may have reoriented some fibers closer to the magic angle, causing the increase in relaxation times that we observed in this study.

Our findings are in agreement with previous *ex vivo* studies performed on cartilage explants, that observed an orientation-dependent behavior in  $T_2$  anisotropy, which suggested a modification in the organization of the collagen matrix upon load (3).

The influence of loading on the relaxation times has been investigated more frequently in cartilage than in meniscus. Significant local increases in  $T_2$  and  $T_{1\rho}$  were observed in articular cartilage upon load (20, 26). Those changes were attributed to water displacement within the tissue as well as to in- and efflux of water. The opposite behavior observed in the meniscus as compared to cartilage was proposed to be related to differences in the composition of the two tissues as well as fluid dynamics (28). An alternative explanation therefore might be that fluid influx upon loading was responsible for the observed relaxation time changes in the menisci (7) 27). However, the orientation-dependent behavior of load response in the menisci observed in our *ex vivo* experiment shows that fluid influx cannot be the only source of changes in relaxation times. Moreover, relaxation time changes in the meniscus body were smaller than the changes observed in the horns, which shows that fiber reorientation plays a bigger role than effects of fluid dynamics.

Tendons contain crimp fibers, which have a wavy appearance as they make an angle of about  $20^\circ$  to the collagen fibril axis and are responsible for the banding patterns seen in polarized light microscopy as well as high resolution MRI (19). Fiber crimp has also been reported to exist in the meniscus (5). In tendons, tensile loading, and thereby straightening of the crimp fibers, was observed to increase  $T_2$  in different orientations with respect to  $B_0$  (19). As tendon and meniscus both contain almost exclusively type-I collagen in an orderly fashion, it could be that compression-induced tensile strains of the circumferential fiber group cause crimp extinction which leads to a similar pattern of  $T_2$  increases observed in tendons. This explanation would also be compatible with our experimental results. In the study by Mountain *et al.* (19) load-induced release of collagen-bound water was proposed as a mechanism to explain the

increase in  $T_2$ . Based on our *ex vivo* results, we cannot exclude this hypothesis, but we can infer that this mechanism alone would not explain the observed change in relaxation times. In order to decouple the two effects (fiber rearrangement and net change in the ratio between free water and bound water) diffusion experiments would be of interest. However, due to the relatively short  $T_2$  and  $T_2^*$  components of meniscus tissue, conventional EPI-based DWI is not an appropriate tool. Spectroscopic diffusion imaging can achieve much lower echo times compared to imaging, potentially enabling the investigation of changes in free water content in meniscus upon load. Furthermore, since dipolar interactions are progressively decreasing for increasing spin-lock power at any angle with respect to  $B_0$  (1), it could be of interest to compare the load-induced response for a range of spin-lock frequencies. If fiber rearrangement were the biggest contributor to the changes in relaxation times, we would expect the load-induced response to decrease with increasing spin-lock frequency.

## 8

The present study has some limitations. First, it is known that application of a phase-cycled train of refocusing pulses improves  $T_2$  quantification, but to keep  $T_2$  and  $T_{1\rho}$  mutually comparable,  $T_2$  was measured as  $T_{1\rho}$  at a spin-lock frequency of 0 Hz. Furthermore, different ways of segmenting the meniscus in the *in vivo* images were used since the meniscus has spatially heterogeneous material properties which are related to the complex biomechanical environment, biochemical constitution and microarchitectural features and which generally result in a concomitant spatial variation of relaxation times (25). The inner portion experiences more compression and has a higher PG content, while the outer region experiences more hoop stresses and has a lower PG content. Additionally, the horns and the body display different biomechanical behavior (10). However, anatomical landmarks were not readily seen on the MR images. Even with specialized sequences using ultrashort echo times (UTE), it is difficult, if not impossible, to distinguish for instance between the meniscal horns and the body, or between the vascularized and non-vascularized portions of the meniscus. Hence, such divisions are generally subject to interpretation, and may have influenced the results. However, since our study focus was the effect of loading, rather than intrameniscal differences in relaxation time, we believe this uncertainty in region classification would not change the interpretation of the results. Another limitation is that while the volunteers were young, the cadaver legs were harvested from donors of high age, which increases the likelihood of the presence of meniscal damage, although none of the cadavers presented joint narrowing or meniscal lesions on the high-resolution anatomical scan.

Despite these limitations, our study shows that relaxation times are sensitive to load application in the meniscus, and this is likely caused by internal reorientation of fibers.

Information on the actual fiber orientation and architecture obtained from histology or dissection and changes therein upon loading might provide further evidence to support our findings.

## **Conclusion**

The presented data showed that in the meniscus  $T_2$  is more sensitive to load-induced changes than  $T_{1\rho}$  and that these load-induced changes are dependent on the sample-to- $B_0$  orientation. This supports the hypothesis that compression-induced internal fiber reorganization and the magic angle effect lead to load-induced changes in  $T_2$  and to a lesser extent in  $T_1$ .

## References

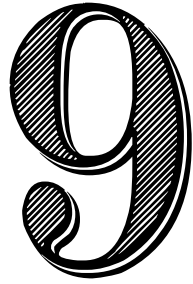
1. **Akella SVS, Regatte RR, Wheaton AJ, Borthakur A, Reddy R.** Reduction of residual dipolar interaction in cartilage by spin-lock technique. *Magn Reson Med* 52: 1103–1109, 2004.
2. **Ala-Myllymäki J, Honkanen JT, Töyräs J, Afara IO.** Optical spectroscopic determination of human meniscus composition. *J Orthop Res* 34: 270–8, 2016.
3. **Alhadlaq HA, Xia Y.** Modifications of orientational dependence of microscopic magnetic resonance imaging T2 anisotropy in compressed articular cartilage. *J Magn Reson Imaging* 22: 665–673, 2005.
4. **Allen AA, Caldwell GL, Fu FH.** Anatomy and biomechanics of the meniscus. *Oper Tech Orthop* 5: 2–9, 1995.
5. **Aspden RM, Yarker YE, Hukins DW.** Collagen orientations in the meniscus of the knee joint. *J Anat* 140: 371–80, 1985.
6. **Bae W, Du J, Bydder G, Chung C.** Conventional and Ultrashort MRI of Articular Cartilage, Meniscus and intervertebral disc. *Top Magn Reson Imaging* 21: 275–289, 2010.
7. **Calixto NE, Kumar D, Subburaj K, Singh J, Schooler J, Nardo L, Li X, Souza RB, Link TM, Majumdar S.** Zonal differences in meniscus MR relaxation times in response to in vivo static loading in knee osteoarthritis. *J Orthop Res* 34: 249–261, 2016.
8. **Chappell KE, Robson MD, Stonebridge-Foster A, Glover A, Allsop JM, Williams AD, Herlihy AH, Moss J, Gishen P, Bydder GM.** Magic Angle Effects in MR Neurography. *Am J Neuroradiol* 25: 431–440, 2004.
9. **Erickson SJ, Prost RW, Timins ME.** The “Magic Angle” Effect: Background Physics and Clinical Relevance. *Radiology* 188: 23–25, 1993.
10. **Fithian DC, Kelly MA, Mow VC.** Material properties and structure-function relationships in the menisci. *Clin. Orthop. Relat. Res.* (1990). doi: 10.2144/000113917.
11. **Fox AJS, Bedi A, Rodeo S a.** The basic science of human knee menisci: structure, composition, and function. *Sports Health* 4: 340–51, 2012.
12. **Freutel M, Galbusera F, Ignatius A, Dürselen L.** Material properties of individual menisci and their attachments obtained through inverse FE-analysis. *J Biomech* 48: 1343–1349, 2015.
13. **Hamada H, Nishii T, Tamura S, Tanaka H, Wakayama T, Sugano N.** Comparison of load responsiveness of cartilage T1rho and T2 in porcine knee joints: An experimental loading MRI study. *Osteoarthr Cartil* 23: 1776–1779, 2015.
14. **Hectors SJCG, Jacobs I, Strijkers GJ, Nicolay K.** Multiparametric MRI analysis for the identification of high intensity focused ultrasound-treated tumor tissue. *PLoS One* 9, 2014.
15. **Herwig J, Egner E, Buddecke E.** Chemical changes of human knee joint menisci in various stages of degeneration. *Ann Rheum Dis* 43: 635–40, 1984.
16. **Khoshgoftar M, Vrancken ACT, van Tienen TG, Buma P, Janssen D, Verdonschot N.** The sensitivity of cartilage contact pressures in the knee joint to the size and shape of an anatomically shaped meniscal implant. *J Biomech*

- 48: 1427–1435, 2015.
17. **Klein S, Staring M, Murphy K, Viergever M a., Pluim J.** elastix: A Toolbox for Intensity-Based Medical Image Registration. *IEEE Trans Med Imaging* 29: 196–205, 2010.
  18. **McNicol D, Roughley PJ.** Extraction and characterization of proteoglycan from human meniscus. *Biochem J* 185: 705–713, 1980.
  19. **Mountain KM, Bjarnason TA, Dunn JF, Matyas JR.** The functional microstructure of tendon collagen revealed by high-field MRI. *Magn Reson Med* 66: 520–527, 2011.
  20. **Nishii T, Kuroda K, Matsuoka Y, Sahara T, Yoshikawa H.** Change in knee cartilage T2 in response to mechanical loading. *J Magn Reson Imaging* 28: 175–180, 2008.
  21. **van Oorschot JW, El Aidi H, Jansen Of Lorkeers SJ, Gho JM, Froeling M, Visser F, Chamuleau SA, Doevendans P a, Luijten PR, Leiner T, Zwanenburg JJ.** Endogenous assessment of chronic myocardial infarction with T1 $\rho$ -mapping in patients. *J Cardiovasc Magn Reson* 16: 104, 2014.
  22. **van Oorschot JWM, Güçlü F, de Jong S, Chamuleau SAJ, Luijten PR, Leiner T, Zwanenburg JJM.** Endogenous assessment of diffuse myocardial fibrosis in patients with T<sub>1 $\rho$</sub> -mapping. *J. Magn. Reson. Imaging* (2016). doi: 10.1002/jmri.25340.
  23. **Peterfy CG, Janzen DL, Tirman PFJ, Van Dijke CF, Pollack M, Genant HK.** “Magic-angle” phenomenon: A cause of increased signal in the normal lateral meniscus on short-TE MR images of the knee. *Am J Roentgenol* 163: 149–154, 1994.
  24. **Rauscher I, Stahl R, Cheng J, Li X, Huber MB, Luke A, Majumdar S, Link TM.** Meniscal Measurements of T1 $\rho$  and T2 at MR Imaging in Healthy Subjects and Patients with Osteoarthritis. *Radiology* 249: 591–600, 2008.
  25. **Son M, Goodman SB, Chen W, Hargreaves BA, Gold GE, Levenston ME.** Regional variation in T1 $\rho$  and T2 times in osteoarthritic human menisci: Correlation with mechanical properties and matrix composition. *Osteoarthr Cartil* 21: 796–805, 2013.
  26. **Souza RB, Kumar D, Calixto N, Singh J, Schooler J, Subburaj K, Li X, Link TM, Majumdar S.** Response of knee cartilage T1 $\rho$  and T2 relaxation times to in vivo mechanical loading in individuals with and without knee osteoarthritis. *Osteoarthritis Cartilage* 22: 1367–76, 2014.
  27. **Subburaj K, Souza RB, Stehling C, Wyman BT, Le Graverand-Gastineau MP, Link TM, Li X, Majumdar S.** Association of MR relaxation and cartilage deformation in knee osteoarthritis. *J Orthop Res* 30: 919–926, 2012.
  28. **Subburaj K, Souza RB, Wyman BT, Le Graverand-Gastineau MPH, Li X, Link TM, Majumdar S.** Changes in MR relaxation times of the meniscus with acute loading: An in vivo pilot study in knee osteoarthritis. *J Magn Reson Imaging* 41: 536–543, 2015.
  29. **Szeverenyi NM, Bydder GM.** Dipolar anisotropy fiber imaging in a goat knee meniscus. *Magn Reson Med* 65: 463–470, 2011.
  30. **Wang N, Xia Y.** Anisotropic analysis of multi-component T2 and T1 $\rho$  relaxations in achilles tendon by NMR spectroscopy and microscopic MRI. *J*

- Magn Reson Imaging* 38: 625–633, 2013.
31. **Witschey WRT, Borthakur A, Elliott MA, Mellon E, Niyogi S, Wallman DJ, Wang C, Reddy R.** Artifacts in T1rho-weighted imaging: Compensation for B1 and B0 field imperfections. *J Magn Reson* 186: 75–85, 2007.
  32. **Wright AC, Yoder JH, Vresilovic EJ, Elliott DM.** Theory of MRI contrast in the annulus fibrosus of the intervertebral disc. *Magn Reson Mater Physics, Biol Med* 29: 711–722, 2016.
  33. **Zarins ZA, Bolbos RI, Pialat JB, Link TM, Li X, Souza RB, Majumdar S.** Cartilage and meniscus assessment using T1rho and T2 measurements in healthy subjects and patients with osteoarthritis. *Osteoarthr Cartil* 18: 1408–1416, 2010.

# Chapter

Summary and general discussion





# Functional MRI of the lower extremities

## Summary

The overall goal of this thesis was to develop a set of MRI-based tools to assess the functional status of the human lower extremities. In this final chapter, the main findings of the studies are summarized and discussed, and some ideas for future research are presented.

In **Chapter 2**, the MRI methods currently used in the field of functional imaging of the musculoskeletal system were reviewed, with special emphasis on the lower extremities. In particular, we discussed recent advances in the field of Diffusion Tensor MRI (DT-MRI), dynamic imaging of moving joints, dynamic imaging of skeletal muscles, and stress MRI. Although the field has advanced considerably over the last two decades, our review highlights that technical improvements are still needed to translate functional MRI of the lower extremities into a routine clinical and research tool.

Despite the great improvement in DT-MRI data acquisition over the last years, the bottleneck remains robust quantification and automated extraction of the parameters of interest. For instance, the extraction of fiber length from DT-MRI tractography data typically involves manual editing, which makes the process time consuming and increases the variability of the outcome parameters. Automatic or semiautomatic methods for extraction of functional parameters are therefore needed. In **Chapter 3**, we developed a novel DT-based approach to measure muscle fiber length in the muscles of the lower extremities. The concept of Tract Density (TD) was introduced and we showed the feasibility of segmenting tendinous structures (tendons and aponeuroses) based on TD. Our method was applied in five volunteers, scanned in three different foot positions (dorsiflexion, neutral, and plantarflexion). The (semi)automatic segmentation of tendinous structures based on TD allowed to obtain a reliable stopping criterion for fiber tractography, therefore allowing for automatic fiber length estimation. We were able to obtain reproducible results and we measured fascicle lengthening/shortening patterns according to the known muscle function.

Another aspect of DT-MRI that needs further investigation is the physiological interpretation of DT-derived parameters. In **Chapter 4**, we tested the hypothesis that Radial Diffusivity (RD, diffusion occurring in the plane perpendicular to the fiber axis) would provide information about the cross sectional area (CSA) of the muscle fibers. Using the methods developed in chapter 3, we measured fiber length changes occurring in dorsiflexed and plantarflexed positions, and we correlated those with the corresponding changes occurring in diffusion scalars estimated from the DT-MRI model. Our findings suggest that changes in fiber length induced in skeletal muscles by passive stretching negatively correlates with changes in RD, indicating that passive muscle stretching induces lengthening of muscle fibers and decrease in diffusion perpendicular to their axis. The observed rate of change in RD and fiber length suggests that, in first approximation, a simple cylindrical model with constant volume can adequately describe muscle fibers. Using a cylindrical model with constant volume to describe the muscle fibers, we showed that changes in RD induced by passive stretching are connected to changes in cross sectional area derived from the fiber length changes. Our results support the hypothesis that diffusion along the radial direction in skeletal muscles relates to the cross sectional area of the fibers. Taken together, our data show that changes in RD induced by passive muscle stretching/lengthening can be explained with a change in muscle cross sectional area, therefore advancing the physiological interpretation of parameters derived using a diffusion tensor model.

The following part of the thesis presented some technical advances in the field of dynamic musculoskeletal imaging. In **Chapter 5**, we proposed a method to obtain fat-suppressed images of the moving knee and the moving wrist. Our method, based on a Phase Sensitive bSSFP (PS-bSSFP) approach was compared with a more conventional Dixon method in terms of SNR and image quality. Our data, in combination with appropriate post-processing, allowed us to obtain fat suppressed 2D images of the knee and wrist joints during motion. The PS-bSSFP used in our study could provide real time imaging of moving joints and detailed information on wrist and knee motion. The results obtained with the PS-bSSFP sequence were superior in terms of SNR and image quality compared to a Dixon method. Ligaments and cartilage could be evaluated with positive contrast due to the suppression of the surrounding fat. This study is a promising small step towards the use of dynamic imaging with tissue specific contrast. Further research on a larger number of subjects and orthopedic patients is still needed to assess the clinical potential of this technique and to expand the method to 3D acquisition.

While MRI data acquisition can be performed with relatively high temporal resolution in a single slice fashion, as shown in chapter 5, fully volumetric (3D) visualization of a moving joint is difficult to achieve due to unrealistically long scan times needed, and the difficulty of keeping a consistent motion rate over time. In fact, current technology is based on synchronized acquisition and the subject is required to perform a given motion task several times in a very repeatable fashion. Synchronized techniques, widely used in healthy volunteers, may therefore find limited value in studying patients who experience pain during motion task and cannot maintain a high level of consistency. We addressed this main limitation in **Chapter 6**, where we proposed an accelerated self-gated MRI approach to image the moving knee during a flexion/extension task. We tested our imaging method in volunteers who received visual instruction on how to move, and compared the results with fully free uninstructed movement. The similarity in image quality and MRI-derived bone kinematic demonstrates the robustness of the method against imperfections in the execution of the motion task.

Similarly to dynamic imaging of joints, also dynamic imaging of skeletal muscle contraction heavily relies on the perfect repeatability of the motion task. Phase Contrast is one of the most commonly used methods to measure muscle velocity, displacement, and deformation. However, only a single 2D slice is usually imaged, and the difficulties in performing a given motion task over extended acquisition times had so far precluded the possibility of using Phase Contrast MRI in a 3D fashion. In **Chapter 7**, we presented the first fully 3D Phase Contrast protocol. Using highly undersampled data, in combination with Compressed Sensing reconstruction, we obtained 3D time-resolved (4D) quantification of muscle velocity during a foot dorsiflexion/plantarflexion task. Furthermore, we also quantified the 3D strain rate tensor and we found good agreement between the fully sampled scan and the accelerated scans. The ability of obtaining time-resolved Phase Contrast information with a 3D sensitivity may open up new possibilities in understanding the connection between muscle architecture and muscle contraction mechanisms.

Finally, in **Chapter 8**, we developed a device that could apply axial compressive load on the subject's knee inside the MRI scanner.  $T_2$  and  $T_{1\rho}$  relaxation time constants were measured in the menisci before and after the load was applied. A significant increase in both relaxation times was observed in the volunteers. We hypothesized that this change could be caused by the effect of dipolar interaction ("magic angle effect") as the meniscal fiber architecture is rearranged due to the application of the load. This hypothesis was tested using cadaveric knees, which were scanned in different orientation in the scanner, as well as in different loading conditions. Our preliminary

results partially confirm our hypothesis. This study is a small step towards a better understanding of the processes occurring *in vivo* under loading conditions and their connection with the MRI properties of the tissues.

## DT-MRI-based functional MRI

Diffusion Tensor MRI (DT-MRI or DTI) is an established technique for the evaluation of skeletal muscle function. Furthermore, diffusion parameters that can be obtained from this technique, such as Mean Diffusivity (MD) and Fractional Anisotropy (FA) are becoming useful tools in clinical practice to evaluate muscle injury and recovery, as well as to follow the progression of neuromuscular diseases (48). The following part of this section will address opportunities for DT-MRI in the field of biomechanics, as well as future perspectives in the field.

### DT-MRI and fiber length

Models of muscle mechanics are very useful tools to improve our understanding of tissue function and to provide a platform to simulate treatments and interventions. In order to obtain accurate predictions, validated models are needed. However, the development of highly accurate models of the musculoskeletal system is challenging because of its high level of complexity (6). The force that a muscle can generate depends on many factors, including geometrical characteristics. For instance, the physiological cross sectional areas (PCSA) correlates with the maximum force that a muscle can generate. Accurate estimation of PCSA requires the knowledge of geometrical parameters such as optimal fiber length and pennation angle. DT-MRI could be a suitable candidate for the *in vivo* and noninvasive determination of these parameters, considering its convincing results in determination of pennation angle (20), and absolute fiber length (8). Other aspects that favor DT-MRI over other methods to measure fiber length *in vivo* are the large coverage, the inherent 3D sensitivity and the use of a fixed frame of reference (18).

The key variables in muscle architecture from a biomechanics standpoint are fiber length, which is normalized to internal sarcomere length, and PCSA, which uses this normalized fiber length value. Normalized fiber length predicts muscle shortening and lengthening capacity as well as velocity of contraction, while PCSA predicts maximum isometric force production. An inherent limitation of all of the non-invasive tools to measure fiber length is the lack of information on sarcomere length. Minimally invasive methods to measure sarcomere length and changes in sarcomere length based on microendoscopy exist (12, 13, 39), but they only provide very localized

information. Due to this limitation, combining sarcomere length from these methods with DT-MRI-derived fiber length may be challenging, especially considering the wide range in sarcomere length values at different muscle locations (44).

Normalized fiber length is also connected to optimal fiber length, which is important in computational biomechanical models (30). In order to understand muscle function during functional activities in terms of the force-length and force-velocity properties, it is necessary to characterize the lengths of muscle fibers relative to their optimal length, and subject specific musculoskeletal models have shown high sensitivity to optimal fiber length (10). However, while DT-MRI studies, including chapter 3 and chapter 4 of this thesis, have shown promising results in the determination of absolute fiber length (9, 43, 47), the measurement of optimal fiber length remain challenging. In fact it is difficult to measure the operating length of muscle fibers (i.e. the lengths of muscle fibers relative to optimal fiber length) during functional activities (3).

As muscles passively stretch due to different ankle orientations, sarcomeres are expected to change their length. However, our results in chapter 4 show little to no changes in axial diffusivity with increasing fiber length. This is probably caused by our experimental parameters (especially diffusion time) not being sensitive enough to the small diffusion restriction effects within sarcomeres. Conventional Diffusion MRI experiments, including our own experiments illustrated in chapter 3 and 4, are performed using Pulsed Gradients. Conventional Pulsed Gradients methods are adequate to estimate cellular cross sectional area (25), but they have limited ability in reaching low diffusion times and they are therefore not adequate to measure the small typical size of sarcomeres (in the order of few  $\mu\text{m}$ ). On the other hand, Oscillating Gradients methods, in combination with suitable tissue modeling, have shown better performance in estimating small sized restriction effects (52, 55). These methods could be promising tools to determine of sarcomere length *in vivo*, with a large coverage. These measurements, coupled with absolute fiber length derived from the DT-MRI tractography, could lead to *in vivo* measurement of optimal/normalized fiber length. The ability of determining the optimal fiber length *in vivo* with a large FOV using MRI could open new perspectives in the field of biomechanics and lead to greatly improved models of skeletal muscles function. In turn, achievement of accurate models of skeletal muscles could have important implications in multiple fields, including biomechanics, orthopedics, and rehabilitation sciences.

## **DT-MRI and strain imaging**

Additionally, the field of muscle modeling could benefit from the combination of imaging during contraction (i.e. MR tagging, Phase Contrast or DENSE) and DT-MRI. It is

commonly assumed that muscles shorten along their longitudinal axis, and that shortening occurs uniformly along the muscle length. However, studies of skeletal muscle contraction have shown non-uniform strain within muscle groups (23, 26, 57, 62). Musculoskeletal models often assume that all the fibers within a given muscle have the same length (41). Blemker et al. (7) used a 3D finite element model to show that heterogeneity of fiber length and fiber curvature within a muscle was the primary cause of the experimentally measured non-uniform strain. Since DT-MRI is a suitable technique to measure absolute fiber length and curvature, the combination with MR imaging of muscle contraction can help elucidating the connection between muscle architecture and function. Furthermore, accurate definition of strain directions with respect to the underlying fiber architecture, rather than with respect to the long axis of the muscle, could lead to a better understanding of lateral force transmission in healthy and diseased conditions (57).

### **DT-MRI data post-processing**

In order to couple MRI data with functional information (bone kinematic, displacement, force measurement etc.) 3D models of the anatomical structures of interest are needed. To this aim, accurate segmentation of individual muscle groups is needed in order to extract relevant parameters (6). This is usually achieved through manual segmentation, which is a very time consuming and tedious process. Automated approaches exist to allow for fully automatic bone (2), meniscus (49), and cartilage segmentation. For the interested readers, we refer to a comprehensive review on segmentation of musculoskeletal structures from MRI data (51). On the other hand, muscle segmentation is much more challenging, since the boundaries between different muscles are not well defined and a lot of previous anatomical knowledge is needed. Current semiautomatic approaches are atlas-based (35) or based on random walks segmentation (4). Pulse sequences that highlight fat (56, 58) (or that completely suppress it) could facilitate automatic muscle segmentation by increasing the contrast between neighboring muscles. However, some subjects and some particular anatomical areas present very little amount of intramuscular fat, making the approach difficult to generalize.

Besides image segmentation, a number of complicated image processing steps are needed in order to extract relevant parameters such as fiber length and pennation angle (19). These often require heavy user interaction and are in general poorly standardized, making comparison between different studies difficult.

We believe that advances in automatic segmentation and standardization of post processing steps could facilitate the diffusion of DT-MRI techniques outside few specialized centers and allow for bigger studies to be performed.

## Dynamic imaging

Dynamic MRI of the musculoskeletal system is a fast developing field in the recent years (54). In this thesis, we developed novel MRI sequences, in combination with advanced image reconstruction techniques and image processing pipelines, to evaluate bones and soft tissues in the lower extremities during motion. However, a number of technical challenges still exist, and they preclude the spread and expansions of dynamic imaging outside a small number of highly specialized centers. In this section, we will highlight some future perspectives in the field, together with possible applications of dynamic imaging of the musculoskeletal system.

## CINE and Real-Time imaging

A number of studies have reported normative values for soft tissue deformation and bone kinematics parameters in healthy, young and physically active subjects (14, 32, 61). However dynamic MRI has found so far limited applicability in patients and less complying subjects populations (33). In our opinion, this is related to a number of pitfalls in data collection. In fact, as already outlined in chapter 6 and chapter 7 of this thesis, one of the main challenges related to dynamic imaging when performed in CINE or triggered fashion, is the high level of repeatability of the motion task required. Prospective gating techniques, based on external monitoring of the motion cycle with a sensor (32) or on self-gating approaches (chapter 6 of this thesis) could be promising to make perfect repeatability of the motion task less of a concern, and to facilitate the application of dynamic MRI in patient studies. However at the current stage prospective gating techniques for these applications are limited to research, as image reconstruction is still a challenging and computationally expensive problem.

In general, in order to make repeatability and motion consistency less of a concern, faster acquisition schemes are required. In particular, Compressed Sensing (CS) is a very interesting technique to this aim (40). The full range of possibilities that CS has to offer have not been explored yet in the musculoskeletal field, and potentially new developments could also enable real time 3D imaging of moving joints, as preliminarily shown in recent studies focusing on the pharyngeal airway (34) and in the vocal tract (63). Recent attempts have also been made in incorporating Deep Learning (38) approaches into the conventional image reconstruction pipeline (31, 60) in order to

solve some of the shortcomings of conventional CS image reconstructions (restrictions on the MRI sequence design and long computation time required to reconstruct the images). Advances in this field are likely to improve the quality of dynamic MRI of joints, and to make its application possible outside a research setting in the near future.

We should point out that even if faster acquisition speed will be achieved, CINE imaging will not be suitable to assess sudden events such as subluxations, since CINE acquisition itself is based on the assumption of repeatable motion. If sudden events are of interest, a real time approach is favorable. However one of the main current limitations of real time dynamic MRI is the limited temporal (and spatial) resolution, which may be needed to identify subtle motion patterns. Real time MRI at its current stage only allows for acquisition in a multislice fashion for unrealistically slow motion (13), while motion speeds that are similar to the typical motion speeds in daily tasks are requested in order to obtain representative motion information. Therefore, in our opinion the dynamic MRI community should put effort into developing sequences, reconstruction pipelines and post-processing tools to allow for 3D real time imaging with acceptable temporal resolution.

## Tissue specific imaging

Dynamic MRI in the musculoskeletal field has so far found its main application in determination of bone kinematics. When bone kinematics is the main focus, Computed Tomography (CT) could be more conveniently used, due to the better visualization of bone segments and the much easier bone segmentation and data processing pipeline (11). On the other hand, MRI offers great advantages over CT in terms of contrast and soft tissue characterization. Therefore, new dynamic approaches should be introduced in order to exploit the full potential of MRI in visualization of soft tissue structures.

Accurate information on strain in ligaments is needed in order to get a better insight into disease and injury mechanisms, to design more efficient prevention strategies and to optimize (surgical) treatment. A number of methods to measure strain in ligaments and tendons exist, both *ex vivo* and *in vivo*. Ultrasound-based and MRI-based methods are gaining popularity as tools to measure strain *in vivo* (27). However, most MRI-based methods available only provide an indirect measurement of strain, as they do not take into account the ligament directly, but exploit the change in distance in the attachment sites on the bones to infer tissue deformation. Direct visualization and strain quantification is desired, but it is currently hampered by the difficulties in signal manipulation in these structures due to the typical very short transverse relaxation



times (few ms or less) of collagen-rich structures such as ligaments and tendons. Ultrashort echo times approaches (UTE), already used in dynamic imaging of the heart (45), could be viable approaches to solve this limitation and could provide benefits for dynamic imaging of the musculoskeletal system. In particular, the combination of UTE imaging with Phase Contrast methods (36) could provide tools to assess strain and strain rate in tendons and at the myotendinous junction, which is currently not possible since tendons appear as areas of signal void in conventional PC images (57). Direct strain imaging *in vivo* could be a useful tool for clinicians to quantitatively assess the tissue quality of tendons and ligaments and to follow longitudinal changes, like the process of graft maturation following Anterior Cruciate Ligament reconstruction. Furthermore, accurate information on tissue strain is also desirable in the field of biomechanics. In fact, due to the high sensitivity of computation musculoskeletal models on tendon (slack) length (10), the ability of measuring strain in tendinous structures and to define an accurate slack length could potentially further improve the accuracy of computational models.

**9**

## Higher resolution

Although our work on dynamic imaging, presented in chapter 6, is a first important step towards dynamic imaging in 3D of moving joints, further advances are needed. First, the spatial resolution needs to be improved, in order to be able to appreciate the motion of small structures (i.e. ligaments and tendons). MRI acquisition always requires some compromises between achievable Signal to Noise Ratio (SNR), image resolution (in both space and time) and the acquisition time. Ideally the image acquisition process should be as fast as possible, in order to minimize costs and subject burden/discomfort. At the same time, higher resolution is also highly desired for dynamic imaging of the musculoskeletal system due to the presence of very small structures and to appreciate small lesions at an early stage.

While we think that recent advances in the field of image reconstructions could allow for much better image quality, high-resolution 3D imaging and scan time optimization will probably imply the need for increased SNR. In general, higher SNR can be achieved using MRI scanner with higher field strength (i.e. 7T), which are becoming increasingly popular in research settings. However, 7T scanners typically have a smaller bore size, which would decrease even further the possible range of motion that a joint can undergo. Additionally, the effect of field distortions due to movement of a joint within the bore, together with strong inhomogeneity of the  $B_1$  field, is expected to be worse at 7T as compared to 3T. For these reasons, we do not foresee a big role of 7T scanners

in the field of dynamic imaging. Furthermore, 7T MRI is currently limited to research, and not suitable in a clinical setting.

In order to achieve higher SNR with a clinically available 3T, we will need better acquisition sequences and better coils for data collection. Balanced Steady State Free Precession sequences (bSSFP) are highly SNR efficient and highly useful for diagnostic purposes, and would be a suitable candidate for dynamic 3D imaging of joints. However, they suffer from strong artifacts (called banding artifacts) as a consequence of inhomogeneous  $B_0$ . Better artifact reduction methods, as the one presented by Benkert et al. (5) could be useful for reducing banding artifacts while keeping very high SNR and could be make 3D dynamic imaging with bSSFP sequences possible.

In our study, and in the one by d'Entremont et al. (15), a custom built multi-element coil was used (46) to allow for the use of parallel imaging techniques, for higher SNR due to the close proximity of the coil elements and the body part to be imaged, and for reduced hindrance to the range of motion. Improved coil designs could further improve SNR in future studies, and multichannel coils could facilitate the use of higher parallel imaging acceleration factors, thus leading to increased SNR and higher temporal resolution.

## Dynamic imaging in biomechanical models

Dynamic MRI techniques have shown the ability to provide information of interest for the biomechanics community. Parameters of interest that can be retrieved using dynamic imaging include tissue motion and strain (21, 62), joint kinematic (16) and cartilage contact patterns (33).

Previous dynamic MRI studies suggested that the measured knee kinematics depend on the type of applied load (22, 61). Therefore, in order to retrieve accurate information, the applied load should be quantifiable, highly reproducible, and standardized in order to facilitate comparison between different studies. To this aim, new MRI compatible loading devices should be designed, which allow to apply a controlled load over a large range of motion.

## Dynamic imaging as a diagnostic tool

In addition, the field of diagnostic imaging would greatly benefit from appropriate loading devices. In fact, due to the load dependent kinematic and deformation patterns highlighted in previous studies, the data collection procedure should be performed during specifically designed activities that can highlight best differences between normal and pathological cases.

As we mentioned previously, functional MRI of the lower extremities suffers from many limitations, such as generally low image resolution that does not allow to appreciate small lesions or abnormalities. Therefore, we do not expect functional protocols to replace conventional high-resolution static imaging. However, the addition of dynamic or loaded scanning to existing clinical protocols may add important clinical information to modify treatment decisions in particular applications (i.e. patellofemoral pain, impingement, etc.). Obviously, patient studies in which dynamic MRI are complemented to conventional clinical protocols will be needed in the future to assess what the real value of dynamic MRI is from a diagnostic standpoint.

In addition to patient studies, more effort is also needed in order to assess normative values for the parameters derived from dynamic MRI. For instance, reference values of strain in muscle and other soft tissues could be obtained and used as a complimentary diagnostic tool to high-resolution static imaging. To this aim, interaction between radiologists and basic scientist is of paramount importance, and software tools that allow for fast visualization of 4D data, together with easy extraction of quantitative parameters, should be developed.

## Stress MRI

Many musculoskeletal pathologies are strongly linked to abnormal loading patterns. For instance excessive load on the joints in obese subjects creates an increased risk factor for OA in the knee and hip (1).

Due to the strong connection between load and onset of musculoskeletal disorders (24), the idea of imaging patients while their joints are loaded seems attractive in order to better elucidate the connection between load, pain and underlying physiology. Furthermore, scans under load could be useful to extract useful information for diagnosis. For instance, earlier studies have shown a significant increase in meniscal extrusion under the application of axial load and significant strong correlation between the amount of extrusion and OA grade (50), suggesting that stress MRI could be an useful tool to provide imaging biomarkers of the disease. However, despite these promising results and the general expansion of the field of stress MRI, no consensus has been reached on the utility of imaging joint in atypical positions or under load in clinical practice (17, 42, 54). Further investigation on bigger patient populations is required to assess the value of stress MRI in helping to identify early biomarkers of musculoskeletal diseases.

Although the field of MRI is progressively moving towards higher field strength (7T and higher), interest is growing in low field MRI scanners for musculoskeletal application. Portable scanner characterized by low field strength exist, and they allow for tilting of the subject together with the scanner, therefore enabling imaging of joint under weight-bearing conditions, as well as in the unloaded configuration. These portable, low-cost scanners are very promising diagnostic tools to evaluate joint narrowing, meniscal extrusion, cartilage thinning or other effects of weight-bearing (53). Further research is warranted to investigate the use of these low field systems for diagnosis and follow up of musculoskeletal diseases.

Besides the interest in Stress MRI as a potential diagnostic tool, we believe that Stress MRI could also play a role in the field of biomechanics, provided that the loading conditions during the MRI examination are known in detail. Structures such as cartilage and meniscus are compressed when load is applied on the knee. Using appropriate post-processing techniques on the images obtained with and without load, meaningful parameters such as displacement and strain can be quantified (29). These information can then subsequently be coupled with FE-models to derive material properties of the tissues of interest (28). These MR-based approaches, although currently in an early stage, are promising tools for generating patient specific models, as they can be used *in vivo*, are not invasive, and can provide information on the individual subject/patient.

Another promising field of research is stress MRI in combination with quantitative imaging. The ability of measuring quantitative imaging parameters ( $T_1$ ,  $T_{1\rho}$ ,  $T_2^*$ ,  $T_2$ , etc.) before and during the application of a given load on the human joint could potentially allow to extract more mechanical parameters as compared to a purely anatomical scan. There is in fact growing interest in the possibility of estimating mechanical properties from MRI.  $T_2$  and  $T_{1\rho}$  in cadaveric menisci have already been shown to correlate with water content and mechanical properties (compression module and shear module) in the unloaded configuration (59). Furthermore  $T_2^*$  has been shown to correlate with mechanical properties of native anterior cruciate ligament (ACL) and ligament draft. Although no systematic investigation has been carried out yet on this topic, we expect stress MRI in combination to MR relaxometry to increase the amount of biomechanical information on the tissue status, as compared to relaxometry performed in a single static position. Further work on quantitative MRI in cadavers, followed by mechanical testing of the specimens is needed in order to assess the real value of quantitative MRI in the evaluation of the mechanical status of soft tissues in the lower extremities. Cadaveric experiments will also help to isolate possible confounding effects that can be present *in vivo* (i.e. different dipolar interaction effects as a consequence of inconsistent patient positioning). The ability of accurately and

non-invasively estimate mechanical properties of musculoskeletal tissues could allow in the future for the creation of subject specific models of individual patients purely from MRI data, since both geometrical characteristics and tissue mechanical properties could be estimated within a single scan session.

While most relaxometry Stress MRI studies have been performed at 3T, portable low-field MRI scanners are gaining growing interest in this area of research, and relaxation times at lower field strength have been suggested to provide additional information with respect to joint status under load, as compared to conventional 1.5 or 3T systems (52). Furthermore, the possibility of imaging a joint in different loading conditions and in different orientations with respect to the static magnetic field  $B_0$  could help elucidating signal characteristics related to the “*magic angle*” effect.

MR relaxometry usually requires long scan time, because of the need of acquiring multiple images with different contrast to fit the expected signal model and derive quantitative parameters. While this is a general problem in every application (neuro, cardiovascular, abdominal, etc.), it is particularly problematic in the musculoskeletal field. In fact, the long acquisition time that can lead to fatigue and pain and prevents the use of high loads. In order to reduce motion artifacts induced by involuntary subject motion during the application of the load, motion correction techniques have been successfully applied (37). Despite the improved image quality that can be achieved, further research is needed in terms of optimization of scan time and post-processing time.

Finally, the long-term goal of stress MRI should be to provide a more accurate diagnostic tool by combining morphological and relaxometric information. To this aim, the underlying physical mechanism leading to the (change in) measured MRI parameters should be better understood. This thesis showed a small contribution towards the understanding of load-induced changes in relaxation times in the meniscus, but better designed experiments are needed. As it was previously mentioned for dynamic MRI, stress MRI will also greatly benefit from better loading devices that are able to apply well controller and reproducible loads.

## **Conclusions**

In summary, in this thesis we presented several technical developments in the field of Magnetic Resonance Imaging to obtain functional information of the human musculoskeletal system. Although further technical development will be needed in the future, together with well-designed studies to assess the added value over conventional MRI techniques, the tools presented in this thesis could facilitate a broader use of functional MRI in biomechanical models. Furthermore, the described method are likely to present added clinical value, as they consider motion, deformation and loaded conditions, which are important aspects to diagnose pathologies of the musculoskeletal system.

## References

1. **Anandacoomarasamy A, Catterson I, Sambrook P, Fransen M, March L.** The impact of obesity on the musculoskeletal system. *Int J Obes* 32: 211–222, 2008.
2. **Aprovitola A, Gallo L.** Knee bone segmentation from MRI: A classification and literature review. *Biocybern Biomed Eng* 36: 437–449, 2016.
3. **Arnold EM, Delp SL.** Fibre operating lengths of human lower limb muscles during walking. *Philos Trans R Soc Lond B Biol Sci* 366: 1530–9, 2011.
4. **Baudin P, Azzabou N, Carlier PG, Paragios N.** Automatic skeletal muscle segmentation through random walks and graph-based seed placement. *2012 9th IEEE Int. Symp. Biomed. Imaging.* .
5. **Benkert T, Eheses P, Blaimer M, Jakob PM, Breuer FA.** Dynamically phase-cycled radial balanced SSFP imaging for efficient banding removal. *Magn Reson Med* 73: 182–194, 2015.
6. **Blemker SS, Asakawa DS, Gold GE, Delp SL.** Image-based musculoskeletal modeling: Applications, advances, and future opportunities. *J Magn Reson Imaging* 25: 441–451, 2007.
7. **Blemker SS, Pinsky PM, Delp SL.** A 3D model of muscle reveals the causes of nonuniform strains in the biceps brachii. *J Biomech* 38: 657–665, 2005.
8. **Bolsterlee B, D’Souza A, Gandevia SC, Herbert RD.** How does passive lengthening change the architecture of the human medial gastrocnemius muscle? *J Appl Physiol* 61: jap.00976.2016, 2017.
9. **Bolsterlee B, Veeger HEJ, Van Der Helm FCT, Gandevia SC, Herbert RD.** Comparison of measurements of medial gastrocnemius architectural parameters from ultrasound and diffusion tensor images. *J Biomech* 48: 1133–1140, 2015.
10. **Carbone V, van der Krogt MM, Koopman HFJM, Verdonschot N.** Sensitivity of subject-specific models to Hill muscle-tendon model parameters in simulations of gait. *J Biomech* 49: 1953–1960, 2016.
11. **Carelsen B, Jonges R, Strackee SD, Maas M, Van Kemenade P, Grimbergen CA, Van Herk M, Streekstra GJ.** Detection of in vivo dynamic 3-D motion patterns in the wrist joint. *IEEE Trans Biomed Eng* 56: 1236–1244, 2009.
12. **Chen X, Delp SL.** Human soleus sarcomere lengths measured using in vivo microendoscopy at two ankle flexion angles. *J Biomech* 49: 4164–4167, 2016.
13. **Chen X, Sanchez GN, Schnitzer MJ, Delp SL.** Changes in sarcomere lengths of the human vastus lateralis muscle with knee flexion measured using in vivo microendoscopy. *J Biomech* 49: 2989–2994, 2016.
14. **D’Entremont AG, McCormack RG, Horlick SGD, Stone TB, Manzary MM, Wilson DR.** Effect of opening-wedge high tibial osteotomy on the three-dimensional kinematics of the knee. *Bone Jt J* 96B: 1214–1221, 2014.
15. **D’Entremont AG, Nordmeyer-Massner JA, Bos C, Wilson DR, Pruessmann KP.** Do dynamic-based MR knee kinematics methods produce the same results as static methods? *Magn Reson Med* 69: 1634–1644, 2013.
16. **D’Entremont AG, Wilson DR.** Joint mechanics measurement using magnetic resonance imaging. *Top Magn Reson Imaging* 21: 325–334, 2010.

17. **Dahabreh IJ, Hadar N, Chung M.** Emerging magnetic resonance imaging technologies for musculoskeletal imaging under loading stress: Scope of the literature. *Ann Intern Med* 155: 616–624, 2011.
18. **Damon BM, Buck AKW, Ding Z.** Diffusion-Tensor MRI Based Skeletal Muscle Fiber Tracking. *Imaging Med* 3: 675–687, 2011.
19. **Damon BM, Froeling M, Buck AKW, Oudeman J, Ding Z, Nederveen AJ, Bush EC, Strijkers GJ.** Skeletal muscle diffusion tensor-MRI fiber tracking: rationale, data acquisition and analysis methods, applications and future directions. *NMR Biomed* 3: e3563, 2017.
20. **Damon BM, Heemskerk AM, Ding Z.** Polynomial fitting of DT-MRI fiber tracts allows accurate estimation of muscle architectural parameters. *Magn Reson Imaging* 30: 589–600, 2012.
21. **Deligianni X, Pansini M, Garcia M, Hirschmann A, Schmidt-Trucksäss A, Bieri O, Santini F.** Synchronous MRI of muscle motion induced by electrical stimulation. *Magn Reson Med* 0: 1–9, 2016.
22. **Draper CE, Besier TF, Fredericson M, Santos JM, Beaupre GS, Delp SL, Gold GE.** Differences in patellofemoral kinematics between weight-bearing and non-weight-bearing conditions in patients with patellofemoral pain. *J Orthop Res* 29: 312–317, 2011.
23. **Englund EK, Elder CP, Xu Q, Ding Z, Damon BM.** Combined diffusion and strain tensor MRI reveals a heterogeneous, planar pattern of strain development during isometric muscle contraction. *Am J Physiol Regul Integr Comp Physiol* 300: R1079–R1090, 2011.
24. **Felson DT.** Osteoarthritis as a disease of mechanics. *Osteoarthr Cartil* 21: 10–15, 2013.
25. **Fieremans E, Lemberskiy G, Veraart J, Sigmund EE, Gyftopoulos S, Novikov DS.** In vivo measurement of membrane permeability and myofiber size in human muscle using time-dependent diffusion tensor imaging and the random permeable barrier model. *NMR Biomed* 30, 2017.
26. **Fiorentino NM, Epstein FH, Blemker SS.** Activation and aponeurosis morphology affect in vivo muscle tissue strains near the myotendinous junction. *J Biomech* 45: 647–652, 2012.
27. **Fleming BC, Beynon BD.** In vivo measurement of ligament/tendon strains and forces: A review. *Ann Biomed Eng* 32: 318–328, 2004.
28. **Freutel M, Galbusera F, Ignatius A, Dürselen L.** Material properties of individual menisci and their attachments obtained through inverse FE-analysis. *J Biomech* 48: 1343–1349, 2015.
29. **Freutel M, Seitz AM, Galbusera F, Bornstedt A, Rasche V, Tate MLK, Ignatius A, Dürselen L.** Medial meniscal displacement and strain in three dimensions under compressive loads: MR assessment. *J Magn Reson Imaging* 40: 1181–1188, 2014.
30. **Infantolino BW, Ellis MJ, Challis JH.** Individual Sarcomere Lengths in Whole Muscle Fibers and Optimal Fiber Length Computation. *Anat Rec* 293: 1913–1919, 2010.
31. **Jin KH, McCann MT, Froustey E, Unser M.** Deep Convolutional Neural Network for Inverse Problems in Imaging [Online]. <http://arxiv.org/abs/1611.03679>.



32. **Kaiser J, Bradford R, Johnson K, Wieben O, Thelen DG.** Measurement of tibiofemoral kinematics using highly accelerated 3D radial sampling. *Magn Reson Med* 69: 1310–1316, 2013.
33. **Kaiser J, Vignos MF, Liu F, Kijowski R, Thelen DG.** American Society of Biomechanics Clinical Biomechanics Award 2015: MRI Assessments of Cartilage Mechanics, Morphology and Composition Following Reconstruction of the Anterior Cruciate Ligament. *Clin Biomech* 34: 38–44, 2016.
34. **Kim Y-C, Lebel RM, Wu Z, Ward SLD, Khoo MCK, Nayak KS.** Real-time 3D magnetic resonance imaging of the pharyngeal airway in sleep apnea. *Magn Reson Med* 71: 1501–10, 2014.
35. **Kolk S, Klawer EME, Schepers J, Weerdesteyn V, Visser EP, Verdonschot N.** Muscle Activity during Walking Measured Using 3D MRI Segmentations and [18F]-Fluorodeoxyglucose in Combination with Positron Emission Tomography. *Med Sci Sports Exerc* 47: 1896–1905, 2015.
36. **Krämer M, Motaal AG, Herrmann K, Löffler B, Reichenbach JR, Strijkers GJ, Hoerr V.** Cardiac 4D phase-contrast CMR at 9 . 4 T using self-gated ultra-short echo time ( UTE ) imaging. (2017). doi: 10.1186/s12968-017-0351-9.
37. **Lange T, Maclaren J, Herbst M, Lovell-Smith C, Izadpanah K, Zaitsev M.** Knee cartilage MRI with in situ mechanical loading using prospective motion correction. *Magn Reson Med* 71: 516–523, 2014.
38. **LeCun Y, Yoshua B, Hinton G.** Deep learning. *Nature* 521: 436–444, 2015.
39. **Llewellyn ME, Barretto RP, Delp SL, Schnitzer MJ.** Minimally invasive high-speed imaging of sarcomere contractile dynamics in mice and humans. *Nature* 454: 784–788, 2008.
40. **Lustig M, Donoho D, Pauly JM.** Sparse MRI: The application of compressed sensing for rapid MR imaging. *Magn Reson Med* 58: 1182–1195, 2007.
41. **Marra MA, Vanheule V, Rasmussen J, Verdonschot NJJ, Andersen MS, Fluit R, Koopman BHFJM, Rasmussen J, Verdonschot NJJ, Andersen MS.** A Subject-Specific Musculoskeletal Modeling Framework to Predict in Vivo Mechanics of Total Knee Arthroplasty. *J Biomech Eng* 137: 20904, 2014.
42. **Marsh M, Souza RB, Wyman BT, Hellio Le Graverand MP, Subburaj K, Link TM, Majumdar S.** Differences between X-ray and MRI-determined knee cartilage thickness in weight-bearing and non-weight-bearing conditions. *Osteoarthr Cartil* 21: 1876–1885, 2013.
43. **Mazzoli V, Oudeman J, Nicolay K, Maas M, Verdonschot N, Sprengers AM, Nederveen AJ, Froeling M, Strijkers GJ.** Assessment of passive muscle elongation using Diffusion Tensor MRI: Correlation between fiber length and diffusion coefficients. *NMR Biomed* : 1–12, 2016.
44. **Moo EK, Fortuna R, Sibole SC, Abusara Z, Herzog W.** In vivo sarcomere lengths and sarcomere elongations are not uniform across an intact muscle. *Front Physiol* 7: 1–9, 2016.
45. **Nierop BJ Van, Bax NAM, Nelissen JL, Arslan F, Motaal AG, Graaf L De, Zwanenburg JJM, Luijten PR, Nicolay K.** Assessment of Myocardial Fibrosis in Mice Using a T2\*-Weighted 3D Radial Magnetic Resonance Imaging Sequence. (2015). doi: 10.1371/journal.pone.0129899.
46. **Nordmeyer-Massner JA, De Zanche N, Pruessmann KP.** Stretchable coil arrays:

- Application to knee imaging under varying flexion angles. *Magn Reson Med* 67: 872–879, 2012.
47. **Oudeman J, Mazzoli V, Marra MA, Nicolay K, Maas M, Verdonschot N, Sprengers AM, Nederveen AJ, Strijkers GJ, Froeling M.** A novel diffusion-tensor MRI approach for skeletal muscle fascicle length measurements. *J Magn Reson* 4: 1–12, 2016.
  48. **Oudeman J, Nederveen AJ, Strijkers GJ, Maas M, Luijten PR, Froeling M.** Techniques and applications of skeletal muscle diffusion tensor imaging: A review. *J Magn Reson Imaging* 43: 773–788, 2016.
  49. **Paproki A, Engstrom C, Chandra SS, Neubert A, Fripp J, Crozier S.** Automated segmentation and analysis of normal and osteoarthritic knee menisci from magnetic resonance images—data from the Osteoarthritis Initiative. *Osteoarthritis Cartilage* 22: 1259–1270, 2014.
  50. **Patel R, Eltgroth M, Souza R, Zhang CA, Majumdar S, Link TM, Motamedi D.** Loaded versus unloaded magnetic resonance imaging (MRI) of the knee: Effect on meniscus extrusion in healthy volunteers and patients with osteoarthritis. *Eur J Radiol Open* 3: 100–107, 2016.
  51. **Pedoa V, Majumdar S, Link TM.** Segmentation of joint and musculoskeletal tissue in the study of arthritis. *Magn Reson Mater Physics, Biol Med* 29: 207–221, 2016.
  52. **Reynaud O, Winters KV, Hoang DM, Wadghiri YZ, Novikov DS, Kim SG.** Pulsed and oscillating gradient MRI for assessment of cell size and extracellular space (POMACE) in mouse gliomas. *NMR Biomed* 29: 1350–1363, 2016.
  53. **Rössler E, Mattea C, Saarakkala S, Lehenkari P, Finnilä M, Rieppo L, Karhula S, Nieminen MT, Stäpf S.** Correlations of low-field NMR and variable-field NMR parameters with osteoarthritis in human articular cartilage under load. *NMR Biomed* 30: 1–14, 2017.
  54. **Shapiro LM, Gold GE.** MRI of weight bearing and movement. *Osteoarthr Cartil* 20: 69–78, 2012.
  55. **Shemesh N, Álvarez GA, Frydman L.** Size distribution imaging by non-uniform oscillating-gradient spin echo (NOGSE) MRI. *PLoS One* 10: 1–19, 2015.
  56. **Shin DD, Hodgson JA, Edgerton VR, Sinha S.** In vivo intramuscular fascicle-aponeuroses dynamics of the human medial gastrocnemius during plantarflexion and dorsiflexion of the foot. *J Appl Physiol* 107: 1276–1284, 2009.
  57. **Silder A, Reeder SB, Thelen DG.** The influence of prior hamstring injury on lengthening muscle tissue mechanics. *J Biomech* 43: 2254–2260, 2010.
  58. **Sinha U, Malis V, Csapo R, Moghadasi A, Kinugasa R, Sinha S.** Age-related differences in strain rate tensor of the medial gastrocnemius muscle during passive plantarflexion and active isometric contraction using velocity encoded MR imaging: Potential index of lateral force transmission. *Magn Reson Med* 73: 1852–1863, 2015.
  59. **Son M, Goodman SB, Chen W, Hargreaves BA, Gold GE, Levenston ME.** Regional variation in T1rho and T2 times in osteoarthritic human menisci: Correlation with mechanical properties and matrix composition. *Osteoarthr Cartil* 21: 796–805, 2013.

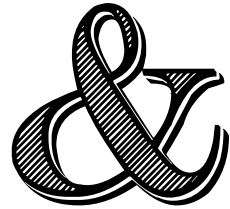
60. **Wang S, Su Z, Ying L, Peng X, Zhu S, Liang F, Feng D, Liang D, Technologies I.** ACCELERATING MAGNETIC RESONANCE IMAGING VIA DEEP LEARNING. *Isbi 2016* (2016). doi: 10.1109/ISBI.2016.7493320.
61. **Westphal CJ, Schmitz A, Reeder SB, Thelen DG.** Load-dependent variations in knee kinematics measured with dynamic MRI. *J Biomech* 46: 2045–2052, 2013.
62. **Zhong X, Epstein FH, Spottiswoode BS, Helm PA, Blemker SS.** Imaging two-dimensional displacements and strains in skeletal muscle during joint motion by cine DENSE MR. *J Biomech* 41: 532–540, 2008.
63. **Zhu Y, Toutios A, Narayanan S, Nayak K.** Faster 3D Vocal Tract Real - time MRI Using Constrained Reconstruction. In: *Interspeech*. 2013, p. 1292–1296.

# Appendix

List of Publications

Acknowledgements

Curriculum Vitae





# List of publications

## Publications

**Water and fat separation in real-time MRI of joint movement with Phase Sensitive bSSFP**

**V Mazzoli**, AJ Nederveen, J Oudeman, AM Sprengers, K Nicolay, GJ Strijkers, N Verdonschot

Magn Reson Med. 2017;78(1):58-68. doi:10.1002/mrm.26341

**A novel diffusion-tensor MRI approach for skeletal muscle fascicle length measurements**

J Oudeman\*, **V Mazzoli\***, MA Marra, K Nicolay, M Maas, N Verdonschot, AM Sprengers, AJ Nederveen, GJ Strijkers, M Froeling

Physiological Reports 2016 Vol. 4 no. e13012. doi: 10.14814/phy2.13012

**Assessment of passive muscle elongation using Diffusion Tensor MRI: Correlation between fiber length and diffusion coefficients**

**V Mazzoli\***, J Oudeman\*, K Nicolay, M Maas, N Verdonschot, AM Sprengers, AJ Nederveen, M Froeling, GJ Strijkers

NMR in Biomedicine, 2016;29(12):1813-1824. doi: 10.1002/nbm.3661.

**Diffusion-prepared neurography of the brachial plexus with a large field-of-view at 3T**

J Oudeman, BF Coolen, **V Mazzoli**, M Maas, C Verhamme, WM Brink, AG Webb, GJ Strijkers, AJ Nederveen

J. Magn. Reson. Imaging, 2016;43:644–654. doi:10.1002/jmri.25025

**Accelerated 4D self-gated MRI of tibiofemoral kinematics**

**V Mazzoli\***, J Schoormans\*, M Froeling, AM Sprengers, BF Coolen, N Verdonschot, GJ Strijkers, AJ Nederveen

NMR in Biomedicine, 2017;e3791. doi: 10.1002/nbm.3791

\* *These authors contributed equally*



## Submitted articles

### **Accelerated 4D phase contrast MRI in skeletal muscle contraction**

**V Mazzoli**, LM Gottwald, ES Peper, M Froeling, BF Coolen, N Verdonschot, AM Sprengers, P van Ooij, GJ Strijkers, AJ Nederveen

### **T1 $\rho$ mapping in the assessment of cartilage integrity of the knee in juvenile idiopathic arthritis – a feasibility study**

AM Barendregt, **V Mazzoli**, EC van Gulik, JM van den Berg, KM Dolman, D Schonenberg-Meinema, TW Kuijpers, M Maas, AJ Nederveen, R Hemke

### **On the origin of changes in T2 and T1 $\rho$ in the meniscus under loading conditions**

**V Mazzoli**, D Tsui, L de Graaf, D Janssen, A Sprengers, N Verdonschot, AJ Nederveen, GJ Strijkers

### **An advanced magnetic resonance imaging perspective on the etiology of deep tissue injury**

JL Nelissen WA Traa, HH de Boer, L de Graaf, **V Mazzoli**, CD Savci-Heijink, K Nicolay, M. Froeling, DL Bader, A.J. Nederveen, CWJ Oomens, and GJ Strijkers



## In preparation

### **Crossing Muscle Fibres of the Tongue Can Be Resolved Using Constrained Spherical Deconvolution**

L Voskuilen, **V Mazzoli**, J Oudeman, LE Smeele, AJM Balm, F van der Heiden, M Froeling, GJ Strijkers, AJ Nederveen

## Presentations in scientific meetings (first author only)

### **Real Time Fat Suppressed MRI of the Knee Joint During Flexion/extension allows the study of PCL motion**

**V Mazzoli**, AM Sprengers, AJ Nederveen, GJ Strijkers, K Nicolay, N Verdonschot

- Poster presentation at ISMRM Benelux 2015, Gent, Belgium
- Poster presentation at ISMRM 2015, Toronto, Canada

### **In vivo skeletal muscle fiber length measurements using a novel MRI diffusion tensor imaging approach: reproducibility and sensitivity to passive stretch**

J Oudeman, **V Mazzoli**, MA Marra, K Nicolay, M Maas, N Verdonschot, AM Sprengers, AJ Nederveen, GJ Strijkers, M Froeling

- Oral presentation at ISMRM Benelux 2016, Eindhoven, The Netherlands
- Oral presentation at ISMRM 2016, Singapore

**Assessment of passive muscle elongation using DTI: Correlation between fiber length and diffusion coefficients**

*V Mazzoli, J Oudeman, MA Marra, AJ Nederveen, K Nicolay, N Verdonschot, AM Sprengers, M Froeling, GJ Strijkers*

- Poster presentation at ISMRM Benelux 2016, Eindhoven, The Netherlands
- Oral presentation at ISMRM 2016, Singapore

**Passive stretch of muscle fibers measured in vivo using a novel MRI diffusion tensor imaging based approach**

*V Mazzoli, J Oudeman, MA Marra, GJ Strijkers, AJ Nederveen, K Nicolay, N Verdonschot, AM Sprengers, M Froeling*

- Oral presentation at ORS 2016, Orlando, Florida

**Dynamic knee imaging using 4D self-gated MRI with compressed sensing reconstruction**

*V Mazzoli, J Schoormans, M Froeling, AM Sprengers, K Nicolay, BF Coolen, N Verdonschot, AJ Nederveen, GJ Strijkers*

- Poster presentation at ISMRM Benelux 2017, Tilburg, The Netherlands
- Oral presentation at ISMRM 2017, Honolulu, Hawaii, **Summa cum Laude**
- Poster presentation at ORS 2017, San Diego, California

**The magic angle effect can (partially) explain load-induced increases in meniscal T2 and T1 $\rho$**

*V Mazzoli, D Tsui, L de Graaf, K Nicolay, AM Sprengers, D Janssen, N Verdonschot, AJ Nederveen, GJ Strijkers*

- Oral presentation at ISMRM 2017, Honolulu, Hawaii

**Compressed Sensing accelerated time-resolved 3D phase contrast MRI of the lower leg muscles during active dorsi- and plantarflexion**

*LM Gottwald, V Mazzoli, ES Peper, Q Zang, BF Coolen, P van Ooij, GJ Strijkers, AJ Nederveen*

- Oral presentation at ISMRM 2017, Honolulu, Hawaii
- Poster presentation at QuantiVision 2017, Amsterdam, The Netherlands







## Acknowledgements

It seems it was just yesterday that I moved to the Netherlands for my Master at TU/e. At that time, I was truly convinced I would go back to Italy right after that. Well, life proved me terribly wrong! Four years have passed and it seems I am about to become “Dr. Vale”. Of course, I would not have been able to get this far without the help and support of many people. So here is my chance to give a well-deserved thanks to all of you who made it possible.

I feel very fortunate for having had the chance to do my PhD in the Biomedical NMR group of Prof. Klaas Nicolay. Dear **Klaas**, I want to express my gratitude for everything you did for me. Thanks for welcoming me to the Biomedical NMR group for my master thesis and thanks for trusting me and offering me a PhD position afterwards. Thanks for always having time for a chat or scientific discussion and for always being so present with me and with all the other lab members. We all miss you. Working with you was always a pleasure and a great honor, and I’ll always be very proud of being one of your students.

Dear **Gustav**, the first time I heard the letters ‘MRI’ was during one of your lectures and I was with you the first time I saw and touched a real MR scanner (we scanned a cherry tomato, I still remember). Thank you for transmitting your passion for MRI, and for keeping that flame burning throughout the last 4 years. I really appreciate your positivity and enthusiasm in everything you do, the great care you take of all your PhD students and the high level of conciseness of your emails. You truly are a great supervisor!

Dear **Aart**, there are so many reasons you deserve a giant “Thank you!”. First of all, thank you for your endless patience, and for all the encouragement you gave me in the darkest moments of my PhD. I really enjoyed our frequent meetings, talking about science and life. I feel very privileged for spending (a lot of) time in your wonderful group at the AMC in Amsterdam, and to have you as a daily supervisor.

Dear **Nico**, your passion for your work and enthusiasm for research is contagious. Thanks for giving me the chance to join the BiomechTools team and for introducing me to the world of biomechanics. Thanks for trusting me and providing me with enough research freedom to follow my interests during the last 4 years.

Dear **Jos**, you are the person with whom I collaborated the most during the last 4 years. Working with you was really enjoyable, and I really appreciated your thinking outside the box. Thanks a lot for your friendly and continuous support and also thanks for the many serious scientific discussions we had over a couple of beers, which ended up being in Chapter 3 and Chapter 4 of my thesis. Also, thank you for being my paranymp.

Dear **Valentina #2**, thanks for sharing the struggles of being a PhD student in the land of the “blond and tall people”. It means a lot to me to have you as a paranymp. Good



luck with the very last bit of your PhD, and with all the great adventures that life will offer you afterwards.

I would also like to thank Prof. **Peter Hilbers**, Prof. **Keita Ito**, Prof. **Bruce Damon**, Prof. **Arend Heerschap**, and Dr. **Jeanine Prompers** for their willingness to serve in my PhD thesis committee.

Pursuing a PhD is an emotional rollercoaster for many, and for me it was no exception. Nonetheless, I am really grateful to life and to my PhD for giving me the chance to meet so many valuable people.

Dear **Andre**, disagreeing with you was by far one of the biggest pleasures during my PhD times. I really hope we will keep having occasions to disagree with each other in the future. **Martijn**, I learnt so much from you that I cannot even put it in words! You were a great supervisor during my master thesis and I am really glad I had the opportunity to work with you again during my PhD. I hope we will have the chance to collaborate again in the future. **Pim**, thanks for being my moral coach during the last year and for guiding me through the wonderful world of Phase Contrast MRI.

A big “thank you!” to all the colleagues at the Radboud UMC involved in the BiomechTools project: **Kaj**, **Kenan**, **Hao**, **Hamid**, **Marco** and **Dennis**. Working with you was fun!



A special thanks to the ladies who made sure all administrative issues would always be solved quickly, and who provided invaluable support: thank you **Floortje**, **Joena**, **Ineke**, and **Joke**.

Dear colleagues and friends at Z0: thank you for the great times we had during the years and for the very stimulating work environment.

Dear **Jasper**, our collaboration resulted in Chapter 6 of this thesis. I learnt a lot about image reconstruction from you. Dear **Lukas**, without your help chapter 7 of this thesis would not exist. Working with you both was very enjoyable and I'll miss the many coffees and afternoon walks we had together. Good luck to both in finishing your PhD. You'll do great!

Dear **Lena**, thank you for all the nice chats we had over a pint. And thank you also for providing a very nice and cozy shelter for all the nights I spent in Amsterdam during the past 4 years.

Thanks to the girls “next door” (**Michelle**, **Claudia**, **Geor**, **Melissa**, and **Esther**) for providing lots of candies and moral support.

Thanks to all the (past) group members at Z0, for the Friday borrels, music quizzes, conferences and all kind of enjoyable moments we shared over the years: **Bada**, **Anne Marije**, **Anouk**, **Bram**, **Dennis**, **Eva**, **Hyke**, **Irene**, **Jithsa**, **Paul DH**, **Jordi**, **JP**, **Kerry**, **Kevin**, **Luuk**, **Martin**, **Matthan**, **Ot**, **Antonia**, **Paul G**, **Raschel**, **Remy**, **Sandra**, **Sofieke**, **Tanja** and **Wouter**.

Thanks also to **Mario Maas** for providing nice clinical insights. **Laura** and **Anouk**, I really enjoyed our collaborations. **Josien** and **Chiel**, I really value our scientific brainstorming in the last months of my PhD.

Although nice things sometimes come to an end, I am still very happy and proud that I was part of the Biomedical NMR team.

Dear **Jules**, having you as office mate at the TU/e campus was lovely. Best of luck with your PhD thesis and defense. **Esther**, thank you for all the nice cakes and cookies you baked for us. **Tom**, I really enjoyed your company in the office over the last 4 years. Organizing ISMRM Benelux together was great.

Dear **Danny**, I was lucky enough to have you as one of my students. I would not have been able to finish Chapter 8 without your help. Best of luck with everything. Whatever you will do, I am sure you will do it very well!

I would also like to thank all the (former) lab members of the Biomedical NMR group: **Desiree, Sin Yuin, Larry, Sharon, Bart, Lukas, Leonie, Stefanie, Emmy, Rik, Willeke, Miranda, Wolter, Marloes, Igor, Siem, Katrien, Lukas, Juan, and Raffa**. I really enjoyed working with you.

A special thanks to my friends in Eindhoven, Italy and around the world that always supported me during the past 4 years: **Cesar, Cara, Martina, Luca DM, Simona, Edu, Stefano, Maria Chiara, Alberto, Daniela, Raluca, Ram, Borko, Federico, Simone, Gabriele, Luca S, Sara, Michele, Irene, Hasret, Victor, Stephanie, Florian, Maro, Sergio, Maria, Michalis, Salvatore, Emilio, Noemi, Paolo, Oliwia, Matteo, Anna, Yuri, Federica, Chicca, Alice, Melissa, Miriam, Veronica, and Barto**. Thanks for always being there and for making my little world a much nicer place. You contributed to my PhD much more than you may think!

I will now switch to Italian for the final thanks:

Un ringraziamento speciale alla mia fantastica famiglia. **Papa'**, il mio radiologo preferito, grazie per aver sempre dimostrato una fiducia incondizionata nelle mie scelte. **Mamma**, grazie per esserti sorbita tutte le mie lementele durante il dottorato, per avermi insegnato la nobile arte del "dar tempo al tempo" e per avermi sempre spronato a dare il meglio di me. **Sara**, la tua presenza e il tuo entusiasmo sono sempre stati fondamentali per me nel portare a termine questo traguardo.

Senza il vostro incessante supporto questa tesi non sarebbe mai esistita. Grazie famiglia. Vi voglio bene.

I met and shared moments with so many people during my PhD years that I might have forgotten someone. If so, don't be mad at me and please accept my apologies.

*Valentina*



## Curriculum Vitae



Valentina Mazzoli was born on July 19<sup>th</sup>, 1988 in Sassocorvaro, Italy. She grew up in Pietrarubbia and obtained her high school diploma in 2007.

In 2010, she graduated in Physics from the University of Bologna, Italy. The following year she moved to Eindhoven, the Netherlands, for a master in Applied Physics at the Eindhoven University of Technology. In the final year of her master, she joined the Biomedical NMR group of Prof. Klaas Nicolay at the department of Biomedical Engineering for an MSc project on *ex vivo* characterization of the porcine heart using Diffusion Tensor Imaging and higher order diffusion models. She

obtained her master in Applied Physics in 2013.

At the end of 2013, she started her PhD project under the supervision of Prof. Klaas Nicolay (Biomedical NMR, Eindhoven University of Technology, Eindhoven), Prof. Gustav Strijkers (Biomedical Engineering and Physics, Academic Medical Center, Amsterdam), Dr. Aart Nederveen (Department of Radiology, Academic Medical Center, Amsterdam), and Prof. Nico Verdonschot (Orthopaedic Research Laboratory, Radboud UMCN, Nijmegen). The results of Valentina's PhD are described in this thesis. The research described in Chapter 6 was awarded with a "Summa cum Laude Merit Award" at the 25<sup>th</sup> annual meeting of ISMRM in 2017.

During her PhD study, Valentina was involved in the organization of the 8<sup>th</sup> annual meeting of the ISMRM Benelux chapter in Eindhoven.

In early 2018, she will start a postdoctoral fellowship at Stanford University, Palo Alto, CA, to work on the development of novel musculoskeletal MRI techniques.



